



Universidade do Minho
Escola de Engenharia

**Rail Power Conditioners Based on Modular Multilevel
Converter in AC Railway Networks**

Mohamed Tanta

Mohamed Tanta

**Rail Power Conditioners Based on Modular
Multilevel Converter in AC Railway
Networks**

UMinho | 2020

November 2020



Universidade do Minho

Mohamed Tanta

**Rail Power Conditioners Based on
Modular Multilevel Converter in AC
Railway Networks**

Doctoral Thesis

Doctoral Program in Electronics and Computer Engineering

Thesis submitted under the supervision of:

Professor João Luiz Afonso

(University of Minho)

Professor António Pina Martins

(University of Porto)

November 2020

COPYRIGHTS AND TERMS OF USE BY THIRD PARTIES

This is an academic work that can be used by third parties under the internationally accepted rules and good practices with regard to the copyright of the authors.

This work can be used under the terms underlined in the license below.

If the user needs permission to be able to use of this work under not provided conditions in the indicated licensing, the user should contact the author, through the RepositóriUM of the University of Minho.

The license granted to users of this work



**Attribution-NonCommercial-NoDerivs
CC BY-NC-ND**

<https://creativecommons.org/licenses/by-nc-nd/4.0/>

DIREITOS DE AUTOR E CONDIÇÕES DE UTILIZAÇÃO DO TRABALHO POR TERCEIROS

Este é um trabalho académico que pode ser utilizado por terceiros desde que respeitadas as regras e boas práticas internacionalmente aceites, no que concerne aos direitos de autor e direitos conexos.

Assim, o presente trabalho pode ser utilizado nos termos previstos na licença abaixo indicada.

Caso o utilizador necessite de permissão para poder fazer um uso do trabalho em condições não previstas no licenciamento indicado, deverá contactar o autor, através do RepositóriUM da Universidade do Minho.

Licença concedida aos utilizadores deste trabalho



**Atribuição-NãoComercial-SemDerivações
CC BY-NC-ND**

<https://creativecommons.org/licenses/by-nc-nd/4.0/>

ACKNOWLEDGEMENT

First, I would like to express my sincere gratefulness to my Ph.D. supervisors, prof. João Luiz Afonso, prof. António Pina Martins and prof. Adriano Silva Carvalho, for their continuous support during the Ph.D. research, for their immense knowledge, inspiration, motivation and the endless patience. Their helpful supervision, explanations and comments helped me to complete and submit of this Ph.D. thesis, as an outcome after four consecutive years of research and development.

I would like to thank my fellow colleagues in the Group of Power Electronics and Energy – GEPE (in Portuguese: Grupo de Eletrónica de Potência e Energia – GEPE), especially to Eng. José Cunha for his massive support regarding the implementation part. I would also like to thank Dr. Gabriel Pinto, Dr. Vítor Monteiro, Dr. Bruno Exposto, Dr. Delfim Pedrosa, Eng. Luis Cardoso, Eng. Tiago Sousa, Eng. Luis Barros, Eng. Luis Machado, Eng. Manuel Silva, Eng. Ana Rodrigues and Eng. Catia Oliveira for their availability, knowledge shared, providing a great work environment of respect and friendship and dealing with all needs in the laboratory during the past years.

I am also thankful to the technicians of the Department of Industrial Electronics and Computer Engineering at the University of Minho, especially to Carlos Torres who always supports with great sympathy and commitment. I am grateful to all the people not mentioned, who helped directly and indirectly in the submission of this doctoral thesis, including my family, my friends and my relatives who have been beside me in the past years for the support and stability provided throughout this academic journey.

A special thanks to Dr. Helena Barroco, the diplomatic adviser of the Portuguese ex-president Dr. Jorge Sampaio, for the encouragement and the moral support provided during this academic journey.

And last but not least, the Portuguese foundation for science and technology (in Portuguese: Fundação para a Ciência e a Tecnologia – FCT), which allowed me to continue my studies with the PD/BD/127815/2016 Ph.D. scholarship under the Innovation in Railway Systems and Technologies Doctoral Program – *iRail*.



STATEMENT OF INTEGRITY

I hereby declare having conducted this academic work with integrity. I confirm that I have not used plagiarism or any form of undue use of information or falsification of results along the process leading to its elaboration. I further declare that I have fully acknowledged the Code of Ethical Conduct of the University of Minho.

DECLARAÇÃO DE INTEGRIDADE

Declaro ter atuado com integridade na elaboração do presente trabalho académico e confirmo que não recorri à prática de plágio nem a qualquer forma de utilização indevida ou falsificação de informações ou resultados em nenhuma das etapas conducente à sua elaboração. Mais declaro que conheço e que respeitei o Código de Conduta Ética da Universidade do Minho.

University of Minho, **November, 08, 2020**

Nome: **Mohamed Tanta**

Mohamed Tanta



Assinatura: _____

Abstract

Railway systems have progressively been developed since James Watt presented a technique of converting steam power into a circular movement back in 1763. With the novelty of steam engines at that time and the increasing of railway networks, railway industry quickly became an economic catalyst throughout the world due to the advantages of passenger and freight transport. In 1879, Siemens & Halske company introduced the world's first electric train in the city of Berlin, consisting of a locomotive and three wagons, and supplied via an insulated third rail with 150 V direct current (DC). From that time, the world has begun to recognize the important transition from steam power to electric power, and the potential of the electrified railway as a mode of mass transport.

Due to the plenty of fuel in the last century, Diesel trains were not only common, but they also dominated the railway sector for a few decades. Consequently, the development in the infrastructures of electric trains decelerated, and the path to having fully electrified trains was long enough. In this context, electric trains have introduced progressively, in which Diesel and electric power have been combined to create hybrid locomotives. However, and with the increased demand for transportation and the higher fuel prices in the last decades, electric trains can substantially offer lower operating costs and lower emissions compared with the Diesel-powered trains.

Nowadays, most of the high-speed electric trains use alternating current (AC) power supply for their traction power systems, which provide better performance under long-distance power transmission than DC power supply. However, as the need for railway transportation increases due to more passengers and higher mobility requirements, more flexible and efficient traction systems are always needed.

In Europe, AC traction power systems are mainly classified according to the voltage and frequency parameters (15 kV, 16.7 Hz) or (1×25 kV or 2×25 kV, 50 Hz). In all cases, railway operators have an absolute interest to run the electrified trains with the lowest possible operation and maintenance costs. In this context, power quality improvement at the three-phase power grid, associated with the AC electrified railway has drawn more attention in the last decades, especially after the evolution in the Power Electronics field. Subsequently, various solutions based on Power Electronics converters have been proposed to improve power quality in the electrified railway, e.g., the flexible AC transmission systems (FACTS).

The rail power conditioner (RPC) is one of the FACTS devices that can be used to improve power quality by compensating harmonic contents, reactive power and negative sequence components of currents generated by the railway system. Among the other possible multilevel power converters, the modular multilevel converter (MMC) is an attractive solution for medium-voltage applications due to harmonics reduction, lower switching losses, and higher flexibility, scalability and reliability. Therefore, the MMC has been enhanced to be combined with the FACTS family.

Taking into consideration the existing opportunities in the railway industry, not only in the development of the electric train itself, but also on the power quality improvement in the electrified railway, there is a strong investment in technological development for electrified railway systems. Therefore, this work presents a new topology of Power Electronics converter (RPC based on MMC) that compensates power quality problems associated with traction power systems, thus, reducing the operating costs of the electrified trains and increasing the power capacity of the electric traction grid.

The main innovations of the RPC based on MMC are the integration of the MMC topology to operate as a railway power quality conditioner, benefiting from the advantages of the MMC in the traction power supply system. In this context, the research work proposed and developed in this Ph.D. thesis aimed to design, develop and validate a reduced-scale laboratory prototype of the RPC based on MMC, including all the necessary control algorithms and simulation models that are important to support the correct operation of the proposed system.

Under simulation conditions, this work developed control algorithms for different RPC topologies, (full-bridge, half-bridge, three-wire, etc.) for demonstrating the general capabilities of the RPC system, and also for two different transformers connections (V/V and Scott). The most favorable RPC based on MMC topology (based on half-bridge MMC) was deeply and extensively simulated, namely employing predictive control approach. The experimental results obtained from a developed reduced-scale prototype confirm the validity of the presented control theory, as well as the power quality improvement capability of the proposed solution.

Keywords: Electrified Railway Systems, Flexible AC Transmission Systems (FACTS), Harmonic Distortion, Modular Multilevel Converter (MMC), Negative Sequence Component (NSC), Power Electronics, Electric Power Quality, Rail Power Conditioner (RPC), Traction Power System (TPS).

Resumo

Os sistemas ferroviários foram progressivamente desenvolvidos desde que James Watt apresentou uma técnica de conversão da energia a vapor para um movimento circular em 1763. Com a novidade dos motores a vapor e a sua implementação nas redes ferroviárias, a indústria ferroviária rapidamente se tornou um catalisador econômico em todo o mundo devido às vantagens no transporte de passageiros e mercadorias. Em 1879, a empresa Siemens & Halske introduziu o primeiro comboio elétrico do mundo na cidade de Berlim, consistindo numa locomotiva com três vagões, alimentado por um terceiro trilho isolado alimentado com corrente contínua em 150 V (CC). A partir desse momento, o mundo começou a reconhecer a importante transição da energia a vapor para a energia elétrica e o potencial na ferrovia eletrificada como um meio de transporte de massa.

Devido à abundância de combustível fóssil no século passado, os comboios a Diesel não eram apenas comuns, mas também dominaram o setor ferroviário. Consequentemente, o desenvolvimento das infraestruturas dos comboios elétricos desacelerou, e o caminho para haver comboios totalmente eletrificados tornou-se bastante longo. Nesse contexto, os comboios elétricos começaram a impor-se progressivamente, inicialmente pela combinação do motor Diesel e do motor elétrico, resultando numa locomotiva híbrida. No entanto, com o aumento da demanda pelo transporte, e com o aumento do preço dos combustíveis nas últimas décadas, os comboios elétricos afirmaram-se por poderem oferecer custos operacionais mais baixos, assim como melhor desempenho ambiental.

Atualmente, a maioria dos comboios elétricos de alta velocidade utilizam sistema de tração em corrente alternada (CA), que oferece melhor desempenho na transmissão de energia a longa distância do que sistema de tração em corrente contínua CC. No entanto, o aumento do transporte ferroviário requer a melhoria da eficiência energética devido a haver mais passageiros e maiores requisitos de mobilidade. Na Europa, os sistemas de tração elétrica são classificados principalmente de acordo com os parâmetros de tensão e frequência (15 kV, 16,7 Hz) ou (1×25 kV ou 2×25 kV, 50 Hz). Em ambos os casos, os operadores ferroviários têm interesse absoluto em otimizar os custos. Nesse contexto, a melhoria da qualidade de energia elétrica na ferrovia suscitou mais atenção nas últimas décadas, principalmente pela introdução da eletrônica de potência. Posteriormente, várias soluções baseadas em conversores de eletrônica de potência foram propostas para melhorar a qualidade de energia elétrica na ferrovia, como por exemplo, os sistemas flexíveis de transmissão CA (FACTS – Flexible AC Transmission Systems).

O condicionador ativo de potência ferroviário (RPC – Rail Power Conditioner) é um dos dispositivos FACTS que pode ser usado para melhorar a qualidade da energia elétrica, compensando o conteúdo harmônico, a potência reativa e os componentes de sequência negativa das correntes. Por outro lado, o conversor multinível modular (MMC – Modular Multilevel Converter) é uma solução atraente para aplicações de média tensão, devido à redução dos harmônicos e das perdas de comutação, e ao aumento da flexibilidade, confiabilidade e escalabilidade. Deste modo, o MMC foi aprimorado para ser integrado na família FACTS.

Levando em consideração as oportunidades existentes no setor ferroviário, não apenas no desenvolvimento do próprio comboio elétrico, mas também na melhoria da qualidade de energia elétrica na ferrovia, existe um forte investimento no desenvolvimento tecnológico para os sistemas ferroviários eletrificados. Assim sendo, este trabalho apresenta uma nova topologia de conversor de eletrônica de potência (RPC baseado em MMC) que compensa os problemas de qualidade de energia elétrica associados aos sistemas de tração, reduzindo os custos operacionais dos comboios elétricos e otimizando a qualidade de energia da rede elétrica.

As inovações principais do RPC baseado em MMC são a integração da topologia do MMC para operar como condicionador de qualidade de energia elétrica na ferrovia, beneficiando das vantagens do MMC. Neste contexto, o trabalho de investigação proposto e desenvolvido nesta tese apontou como objetivo projetar, desenvolver e validar um protótipo laboratorial em escala reduzida do RPC baseado em MMC, incluindo todos os algoritmos de controlo necessários e os modelos de simulação que são importantes para suportar a operação correta do sistema.

Sob condições de simulação, este trabalho desenvolveu algoritmos de controlo para diferentes topologias do RPC (ponte completa, meia ponte, três fios, etc.), para demonstrar as capacidades gerais do sistema do RPC, e também para dois transformadores diferentes (V/V e Scott). O RPC mais favorável baseado na topologia do MMC (baseado no MMC de meia ponte) foi profunda e extensivamente simulado, nomeadamente utilizando uma abordagem de controlo preditivo. As simulações e os resultados experimentais confirmam a validade da teoria de controlo apresentada, bem como a capacidade de melhoria da qualidade de energia elétrica na solução proposta.

Palavras-chave: Condicionador Ativo de Potência Ferroviário (RPC), Conversor Modular Multinível (MMC), Componente de Sequência Negativa (NSC), Distorção Harmônica, Eletrônica de Potência, Qualidade de Energia Elétrica, Sistemas Flexíveis de Transmissão CA (FACTS), Sistema de Tração (TPS), Sistemas Ferroviários Eletrificados.

Table of Contents

COPYRIGHTS AND TERMS OF USE BY THIRD PARTIES	i
DIREITOS DE AUTOR E CONDIÇÕES DE UTILIZAÇÃO DO TRABALHO POR TERCEIROS	i
ACKNOWLEDGEMENT	ii
STATEMENT OF INTEGRITY	iii
DECLARAÇÃO DE INTEGRIDADE	iii
Abstract	iv
Resumo	vi
Table of Contents	viii
List of Figures	xi
List of Tables	xviii
Acronyms and Abbreviations	xx
Nomenclature	xxiii
Chapter 1 Introduction	1
1.1 Electrified Railway Systems in Europe	1
1.1.1 History of Railway Electrification in Europe	1
1.1.2 Railway Challenges in Europe	2
1.1.3 Portuguese Railway Network	4
1.1.4 Portuguese Railway Locomotives	8
1.1.5 Shift2Rail – Achieving a Notable Shift from Road to Rail	10
1.1.6 Timeframe of the Fastest Trains in the World	12
1.2 Thesis Main Motivations	16
1.3 Thesis Main Contributions	16
1.4 Thesis Organization	17
1.5 List of Publications	19
1.5.1 Publications in International Journals	19
1.5.2 Publications in Book Chapters	19
1.5.3 Publications in International Conferences	19
Chapter 2 Power Quality Phenomena in Electrified Railway Systems	21
2.1 Introduction	21
2.2 Power Quality in AC Railway Electrification	22
2.2.1 System Imbalance	22
2.2.2 Harmonic Distortion	24
2.2.3 Reactive Power	26
2.2.4 Low-Frequency Voltage Fluctuations	27
2.2.5 Voltage Arcing	27
2.2.6 Poor Utilization of Supply Network	28
2.3 Hazards of Power Quality Phenomena in AC Railway Electrification	29
2.3.1 Impacts on Electric Power Systems	29
2.3.2 Impacts on Signaling and Communication Systems	30
2.4 Power Quality Improvements: Traditional-Based Methods	30
2.4.1 Three-Phase Electric Trains	30
2.4.2 Phase Shifting Using Adjacent Single-Phase Power Transformers	31
2.4.3 Three-Phase Balanced Power Transformers	32

2.4.4	Passive Power Filters	34
2.4.5	Steinmetz Compensation Circuit	35
2.5	AC Feeding Methods of Traction Power System	36
2.5.1	Simple Feeding with a Return Rail	36
2.5.2	Boost Transformers with a Return Rail	37
2.5.3	Boost Transformers with a Return Wire	37
2.5.4	Auto-Transformers System	38
2.5.5	Coaxial Power Cable	39
2.6	Conclusion	39
Chapter 3 Active Power Compensators in Electrified Railway Systems		41
3.1	Introduction	41
3.2	Static VAr Compensator (SVC)	42
3.3	Static Synchronous Compensator (STATCOM)	43
3.4	Static Frequency Converter (SFC)	45
3.4.1	Single DC-Link Static Frequency Converter (SDLC)	47
3.4.2	Multiple DC-Link Static Frequency Converter (MDLC)	49
3.5	Static Frequency Converter Based on Modular Multilevel Converter (SFC Based on MMC)	50
3.5.1	Modular Multilevel Converter Operation Principle	51
3.5.2	Direct Modular Multilevel Converter	55
3.5.3	Indirect Modular Multilevel Converter	57
3.5.4	Case Study: Using Indirect MMC / Direct MMC as SFC for the 15 kV, 16.7 Hz Electrified Railway	59
3.6	Rail Power Conditioner	61
3.6.1	Case Study: Comparison between Static Frequency Converter and Rail Power Conditioner Based on Indirect Modular Multilevel Converter for Railway Applications	64
3.7	Conclusion	66
Chapter 4 Rail Power Conditioners in Electrified Railway Systems		68
4.1	Introduction	68
4.2	Rail Power Conditioner (RPC) Operation Modes	69
4.2.1	Rail Power Conditioner Traditional Operation Mode	69
4.2.2	Static VAr Compensator Operation Mode	71
4.2.3	Catenary Voltage Regulator Operation Mode	71
4.2.4	Interface Converter Between Two Collateral Substations	72
4.3	RPC Based on Full-Bridge Back-to-Back Two-Level Converter and V/V Power Transformer	73
4.3.1	Control Algorithm	77
4.3.2	Simulation Results	79
4.4	RPC Based on Two-Phase Three-Wire Converter and V/V Power Transformer	83
4.4.1	Control Algorithm	85
4.4.2	Simulation Results	86
4.5	Simplified RPC Based on Half-Bridge Two-Level Converter and V/V Power Transformer	88
4.5.1	Control Algorithm	89
4.5.2	Simulation Results	90
4.6	Hybrid Co-Phase RPC Based on Full-Bridge Back-to-Back Two-Level Converter and Single-Phase Power Transformer	92
4.6.1	Control Algorithm	95
4.6.2	Simulation Results	95
4.7	RPC Based on Scott Power Transformer	98
4.7.1	Control Algorithm	101
4.7.2	Simulation Results	102
4.8	Modular RPC Based on Full-Bridge Back-to-Back Converters and V/V Power Transformer	105
4.8.1	Control Algorithm	106
4.8.2	Simulation Results	107
4.9	RPC Based on Modular Multilevel Converter and V/V Power Transformer	109
4.9.1	RPC Based on Full-Bridge Indirect Modular Multilevel Converter	110
4.9.2	RPC Based on Two-Phase Three-Wire Indirect Modular Multilevel Converter	119
4.9.3	Simplified RPC Based on Half-Bridge Indirect Modular Multilevel Converter	128
4.10	Comparison Between the RPC Topologies	142
4.11	Conclusion	146

Chapter 5	Implementation of a Simplified Rail Power Conditioner Based on Modular Multilevel Converter.....	148
5.1	Introduction.....	148
5.2	Parameters Design.....	149
5.3	Simulation of the Reduced-Scale HB-MMC2 RPC.....	152
5.3.1	Simulation Model.....	152
5.3.2	Simulation Results.....	153
5.4	Supplementary Power Equipment.....	155
5.5	Implementation of a Reduced-Scale MMC.....	157
5.5.1	Driver Circuit PCB.....	158
5.5.2	Protection Circuit PCB.....	162
5.5.3	Power Circuit PCB.....	169
5.5.4	Final SM Structure.....	175
5.5.5	MMC Filter Inductor.....	176
5.5.6	MMC Main DC-link Capacitors.....	177
5.6	Control System Hardware.....	178
5.6.1	Central Control Unit.....	180
5.6.2	Sensors.....	182
5.6.3	Digital to Analogue Converter.....	183
5.6.4	Analogue to Digital Converter and Signal Conditioning.....	184
5.6.5	Command Circuit PCB.....	187
5.6.6	PWM Adapter PCB.....	189
5.7	Conclusion.....	189
Chapter 6	Experimental Results of a Simplified Rail Power Conditioner Based on Modular Multilevel Converter.	191
6.1	Introduction.....	191
6.2	Enhanced Phase-locked Loop (E-PLL) and Moving Average Low-Pass Filter (LPF).....	192
6.3	Testing One MMC Leg/Phase Using an Open-loop Control.....	195
6.4	Testing One MMC Leg/Phase Using a Closed-loop Control.....	196
6.5	Testing Two MMC Legs/Phases Using a Closed-loop Control.....	199
6.6	Experimental Results of the HB-MMC2 RPC.....	202
6.6.1	Experimental Results when Both Load Sections are Loaded.....	204
6.6.2	Experimental Results when One Load Section is Loaded.....	208
6.7	Conclusion.....	212
Chapter 7	Conclusion.....	214
7.1	Introduction.....	214
7.2	General Conclusions.....	214
7.3	Significant Contributions.....	221
7.4	Suggestions for Future Work.....	221
List of References	223

List of Figures

Figure 1.1. Railway maps in EU: (a) The used gauge width; (b) The used voltage level for railway electrification [10].	3
Figure 1.2. Portuguese railway network map in 2015 [16].Source: [<i>Infraestruturas de Portugal</i>].	5
Figure 1.3. The length of active and abandoned Portuguese railway during the last 50 years. Source: [<i>Pordata</i>].....	6
Figure 1.4. Number of Portuguese train stations during the last 15 years. Source: [<i>Pordata</i>].....	6
Figure 1.5. Railway network in north of Portugal plus the already abandoned rail lines (in brown) [15]. Source: [<i>Infraestruturas de Portugal</i>].....	6
Figure 1.6. Electrified and non-electrified Portuguese railway during the last 15 years. Source: [<i>Pordata</i>].	7
Figure 1.7. Portuguese railway based on the running mode in 2012 [18]. Source: [<i>Thorsten Bucker</i>].	7
Figure 1.8. <i>Shift2Rail</i> members map in Europe (red points) [20]. Source: [<i>Shift2Rail</i>].	11
Figure 1.9. The ICE high-speed German train [25]. Source: [https://www.westtours.de].	13
Figure 1.10. The <i>Transrapid</i> German magnetic levitation train [27]. Source: [https://www.hochgeschwindigkeitszuege.com].	13
Figure 1.11. TGV French high-speed trains: (a) 1 st TGV generation (TGV <i>Sud-Est</i>); (b) 2 nd TGV generation (TGV <i>Atlantique</i>); (c) 3 rd TGV generation (TGV <i>Duplex</i>)[28]. Source: [https://socialcompare.com/en/comparison/high-speed-trains].	13
Figure 1.12. <i>Fuxing Hao</i> Chinese high-speed train [31]. Source: [https://www.scmp.com].	14
Figure 1.13. <i>Shanghai</i> Chinese magnetic levitation train [33]. Source: [http://www.digitaljournal.com/image/188575].	14
Figure 1.14. AVE train in <i>Atocha</i> train station, in <i>Madrid</i> [36]. Source: [https://www.abc.es].	15
Figure 1.15. E5 series of <i>Shinkansen</i> Japanese high-speed train [37]. Source: [https://www.railway-technology.com].	15
Figure 1.16. <i>Chuo Shinkansen</i> Japanese Maglev train (still under construction) [39]. Source: [https://www.theguardian.com/].	15
Figure 2.1. E330 three-phase Italian locomotive in the period 1914–1963 [69]. Source: [https://books.google.com/books/about/Italian_Railways.html?id=JFcSAAAAMAAJ].	31
Figure 2.2. Three-phase locomotives: (a) Corcovado Rack train in Rio de Janeiro [70]; (b) French train of La Rhunein [71]. Sources: (a) [https://www.wikiwand.com/en/Corcovado], (b) [https://www.rhune.com/].	31
Figure 2.3. Phase shift method to alternate between PPS phases [49].	32
Figure 2.4. Balanced three-phase power transformers used in railway substations: (a) Scott transformer; (b) LeBlanc transformer; (c) Impedance matching transformer.	33
Figure 2.5. Various types of passive filters used in railway electrification.	35
Figure 2.6. The configuration of Steinmetz compensation circuit.	35
Figure 2.7. Simple direct feeding with a return rail and return wire configuration.	36
Figure 2.8. Boost transformers with a return rail configuration.....	37
Figure 2.9. Boost transformers with a return wire configuration.	37
Figure 2.10. Auto-transformers configuration.	38
Figure 2.11. Coaxial power cable feeding system.	39
Figure 3.1. SVC installation via a step-down power transformer in railway electrification.....	43
Figure 3.2. Static synchronous compensator (STATCOM) in railway electrification.....	45
Figure 3.3. Static frequency converter (SFC).	46
Figure 3.4. Parallel connection of the SFC substations.	47
Figure 3.5. SFC based on a single DC-link converter (SDLC).....	48
Figure 3.6. SFC based on a multiple DC-link converter (MDLC).	49

Figure 3.7. Catenary voltage and load current under a DC-link fault in SDLC and MDLC: $u_o(m)$ and $i_o(m)$ are the output voltage and current of the MDLC topology; $u_o(s)$ and $i_o(s)$ are the output voltage and current of the SDLC topology.	50
Figure 3.8. Operation approach of the 5-level MMC: (a) Representation of the MMC; (b) Simplified representation of the MMC.	52
Figure 3.9. States of the 5-level MMC (state 1 to state 2 example).	53
Figure 3.10. States of the 5-level MMC (state 2 to state 3 example).	53
Figure 3.11. States of the 5-level MMC (state 3 to state 4 example).	54
Figure 3.12. States of the 5-level MMC (state 4 to state 5 example).	54
Figure 3.13. Direct AC/AC MMC topology.	55
Figure 3.14. Indirect AC/DC/AC MMC topology.	57
Figure 3.15. Positions of half-bridge SM switching devices: (a) SM switched on; (b) SM switched off; (c) SM blocked during the deadtime.	58
Figure 3.16. Conventional AC/DC/AC back-to-back two-level converter in 15 kV, 16.7 Hz traction power system.	60
Figure 3.17. Rail Power Conditioner (RPC).	62
Figure 3.18. RPC based on MMC.	63
Figure 3.19. Comparison between SFC and RPC based on an indirect MMC: the estimated cost of implementation.	66
Figure 4.1. Principles of the RPC system.	70
Figure 4.2. RPC operating in the SVC mode (RPC based SVC).	71
Figure 4.3. RPC operating in the catenary voltage regulator mode.	72
Figure 4.4. RPC operating as an interface converter between two substations.	73
Figure 4.5. FB-RPC system with a V/V power transformer.	75
Figure 4.6. PPS phasors diagram: (a) Without compensation; (b) After shifting the active power difference; (c) After shifting the active power difference and compensate reactive power [57].	76
Figure 4.7. Phasors diagram on the secondary windings of the V/V transformer after compensation [57].	77
Figure 4.8. Control strategy of the FB-RPC converter.	78
Figure 4.9. Locomotive equivalent circuit used in the simulation model.	80
Figure 4.10. FB-RPC simulation results: (a) Three-phase currents before compensation; (b) Three-phase currents after compensation (when both of the load sections are loaded).	80
Figure 4.11. FB-RPC simulation results: (a) Load section currents; (b) Currents at the secondary windings of the V/V power transformer after compensation (when both of the load sections are loaded).	81
Figure 4.12. FB-RPC simulation results: (a) DC-link voltage; (b) Compensation currents (when both of the load sections are loaded).	81
Figure 4.13. FB-RPC simulation results: (a) Three-phase currents before compensation; (b) Three-phase currents after compensation (when the load section x is loaded).	82
Figure 4.14. FB-RPC simulation results: (a) Load section current; (b) Currents at the secondary windings of the V/V power transformer after compensation (when the load section x is loaded).	83
Figure 4.15. FB-RPC simulation results: (a) DC-link voltage; (b) Compensation currents (when the load section x is loaded).	83
Figure 4.16. TW-RPC system with a V/V power transformer.	84
Figure 4.17. Control strategy of the TW-RPC converter.	85
Figure 4.18. TW-RPC simulation results: (a) Three-phase currents before compensation; (b) Three-phase currents after compensation (when both of the load sections are loaded).	86
Figure 4.19. TW-RPC simulation results: (a) Load section currents; (b) Currents at the secondary windings of the V/V power transformer after compensation (when both of the load sections are loaded).	87
Figure 4.20. TW-RPC simulation results: (a) DC-link voltage; (b) Compensation currents (when both of the load sections are loaded).	87
Figure 4.21. HB-RPC system with a V/V power transformer.	88
Figure 4.22. Control strategy of the HB-RPC.	90
Figure 4.23. HB-RPC simulation results: (a) Three-phase currents before compensation; (b) Three-phase currents after compensation (when both of the load sections are loaded).	91

Figure 4.24. HB-RPC simulation results: (a) Load section currents; (b) Currents at the secondary windings of the V/V power transformer after compensation (when both of the load sections are loaded).....	91
Figure 4.25. HB-RPC simulation results: (a) DC-link voltage; (b) Compensation currents (when both of the load sections are loaded).	92
Figure 4.26. Co-HRPC with a single-phase power transformer.	93
Figure 4.27. Double-side feeding co-HRPC substations.	94
Figure 4.28. Control strategy of the co-HRPC.	95
Figure 4.29. Co-HRPC simulation results: (a) Three-phase currents before compensation; (b) Three-phase currents after compensation.....	96
Figure 4.30. Co-HRPC simulation results: (a) Load section current; (b) Compensation currents.....	97
Figure 4.31. Co-HRPC simulation results: (a) Passive filter capacitor voltage; (b) DC-link voltage.	97
Figure 4.32. RPC system with a Scott power transformer.	98
Figure 4.33. Phasors of the RPC system with a Scott power transformer: (a) Scott transformer connection points; (b) Phasors diagram of the primary windings; (c) Phasors diagram of the secondary windings.....	99
Figure 4.34. Phasors of the RPC system with a V/V power transformer: (a) V/V transformer connection points; (b) Phasors diagram of the primary windings; (c) Phasors diagram of the secondary windings.....	100
Figure 4.35. RPC output voltages: (a) Output equivalent circuit of the RPC; (b) Phasors of the RPC output voltages in V/V power transformer; (c) Phasors of the RPC output voltages in Scott power transformer.....	100
Figure 4.36. Control strategy of the RPC system with a Scott power transformer.....	101
Figure 4.37. Load section voltages: (a) Using the V/V power transformer; (b) Using the Scott power transformer.	101
Figure 4.38. Public grid currents, PSC and NSC when the load sections are equally loaded before compensation: (a), (b) Using the V/V power transformer; (c), (d) Using the Scott power transformer.....	103
Figure 4.39. Public grid currents, PSC and NSC when load sections are unequally loaded before compensation: (a), (b) Using the V/V power transformer; (c), (d) Using the Scott Power transformer.	103
Figure 4.40. RPC based on a Scott transformer (RPC is turned on after 0.1 s): (a) Three-phase grid currents; (b) Currents at the secondary windings of the Scott transformer; (c) PSC and NSC of three-phase grid currents.	104
Figure 4.41. RPC based on a Scott transformer (RPC is turned on after 0.1 s): (a) Load section currents; (b) Compensation currents synthesized by the RPC; (c) DC-link voltage.....	105
Figure 4.42. MRPC system with a V/V power transformer.	106
Figure 4.43. Control strategy of the MRPC.	107
Figure 4.44. MRPC simulation results: (a) Three-phase currents after compensation; (b) Load section currents; (c) Compensation currents synthesized by an RPC module; (d) DC-link voltage for one RPC module.....	108
Figure 4.45. FB-MMC4 RPC system with a V/V power transformer.....	111
Figure 4.46. AC equivalent circuit of the FB-MMC4 RPC system.	111
Figure 4.47. FB-MMC4 RPC: (a) Output equivalent circuit; (b) Phasors of output voltages when using V/V transformer.	112
Figure 4.48. Block diagram for establishing the compensation current references.	114
Figure 4.49. DC-link voltage control and the calculation of the voltage reference signals of the FB-MMC4 RPC.	114
Figure 4.50. SM capacitors voltage control of the FB-MMC4 RPC: (a) MMC leg averaging voltage control; (b) MMC arm averaging voltage control; (c) MMC SM individual voltage control.	115
Figure 4.51. Voltage command generation of each SM applied to a phase-shifted PWM.....	116
Figure 4.52. FB-MMC4 RPC simulation results: (a) Three-phase currents before compensation; (b) Three-phase currents after compensation; (c) Currents at the secondary windings of the V/V power transformer after compensation.....	117
Figure 4.53. FB-MMC4 RPC simulation results: (a) Load section currents; (b) Compensation currents.	118
Figure 4.54. FB-MMC4 RPC simulation results: (a) Arm currents of the positive leg of the section x converter; (b) Arm currents of the positive leg of the section y converter.	118
Figure 4.55. FB-MMC4 RPC frequency spectrum: (a) Compensation currents; (b) Upper and lower arm currents of converter x; (c) Upper and lower arm currents of converter y.	119

Figure 4.56. FB-MMC4 RPC SM voltages: (a) Positive leg of converter x ; (b) Negative leg of converter x ; (c) Positive leg of converter y ; (d) Negative leg of converter y	119
Figure 4.57. TW-MMC3 RPC system with a V/V power transformer.	120
Figure 4.58. AC equivalent circuit of the TW-MMC3 RPC system.	121
Figure 4.59. TW-MMC3 RPC: (a) Output equivalent circuit; (b) Phasors of output voltages when using V/V power transformer.	121
Figure 4.60. DC-link voltage control and the calculation of the voltage reference signals of the TW-MMC3 RPC.....	124
Figure 4.61. SM capacitors voltage control of the TW-MMC3 RPC: (a) MMC leg averaging voltage control; (b) MMC arm averaging voltage control; (c) MMC SM individual voltage control.	125
Figure 4.62. TW-MMC3 RPC simulation results: (a) Load section currents; (b) Compensation currents.....	126
Figure 4.63. TW-MMC3 RPC simulation results: (a) Arm currents of phase x ; (b) Arm currents of phase y ; (c) Arm currents of phase z	127
Figure 4.64. TW-MMC3 RPC frequency spectrum: (a) Compensation currents; (b) Arm currents of phase x ; (c) Arm currents of phase y ; (d) Arm currents of phase z	127
Figure 4.65. TW-MMC3 RPC SM voltages: (a) Phase x ; (b) Phase y ; (c) Phase z ; (d) Main DC-link voltage.	128
Figure 4.66. HB-MMC2 RPC system with a V/V power transformer.	129
Figure 4.67. Number of SMs connected to the output terminals: (a) FB-MMC4 RPC; (b) HB-MMC2 RPC.	129
Figure 4.68. AC equivalent circuit of the HB-MMC2 RPC system.	130
Figure 4.69. HB-MMC2 RPC: one phase equivalent circuit.	132
Figure 4.70. DC-link voltage control and calculation of the voltage reference signals of the HB-MMC2 RPC.	135
Figure 4.71. SM capacitors voltage control of the HB-MMC2 RPC: (a) MMC leg averaging voltage control; (b) MMC arm averaging voltage control; (c) MMC SM individual voltage control.	136
Figure 4.72. HB-MMC2 RPC simulation results: (a) Three-phase grid currents before compensation; (b) Three-phase grid currents after compensation; (c) Catenary section (x and y) currents.	138
Figure 4.73. HB-MMC2 RPC currents when using the proposed predictive current controller (I) and when using the conventional PI controllers (II): (a) Compensation currents; (b) Upper and lower arm currents of section x converter; (c) Upper and lower arm currents of section y converter; (d) MMC circulating currents.	138
Figure 4.74. HB-MMC2 RPC frequency spectrum of currents when using the proposed predictive current controller (I) and when using the conventional PI controllers (II): (a) Compensation current of section x converter; (b) Compensation current of section y converter; (c) Circulating current of section x converter; (d) Circulating current of section y converter.	139
Figure 4.75. HB-MMC2 RPC frequency spectrum of currents when using the proposed predictive current controller (I) and when using the conventional PI controllers (II): (a) Upper arm current of section x converter; (b) Lower arm current of section x converter; (c) Upper arm current of section y converter; (d) Lower arm current of section y converter.	140
Figure 4.76. HB-MMC2 RPC DC-link voltages when using the proposed predictive current controller (I) and when using the conventional PI controllers (II): (a) Main DC-link voltages; (b) SM voltages of section x converter; (c) SM voltages of section y converter.	140
Figure 4.77. Comparison of RPC topologies based on MMC: (a) V/V power transformer; (b) Scott power transformer.	146
Figure 5.1. HB-MMC2 RPC simulation model using the <i>PSIM</i> V.9.1.	152
Figure 5.2. HB-MMC2 RPC control blocks using the <i>PSIM</i> V.9.1.	153
Figure 5.3. HB-MMC2 RPC reduced-scale prototype simulation results: (a) Three-phase grid currents before compensation; (b) Three-phase grid currents after compensation; (c) Catenary section (x and y) currents.	154
Figure 5.4. HB-MMC2 RPC reduced-scale prototype currents (a) Compensation currents; (b) Upper and lower arm currents of section x converter; (c) Upper and lower arm currents of section y converter; (d) MMC circulating currents.	155
Figure 5.5. HB-MMC2 RPC reduced-scale prototype DC-link voltages: (a) Main DC-link voltages; (b) SM voltages of section x converter; (c) SM voltages of section y converter.	155
Figure 5.6. Supplementary power equipment diagram.	156
Figure 5.7. Supplementary power equipment setup.	156

Figure 5.8. User interface of <i>PADS</i> PCB design tool: (a) <i>PADS Logic</i> ; (b) <i>PADS Layout</i>	158
Figure 5.9. Driver circuit PCB scheme: internal schematic of <i>Si8244</i> and the connections with the IGBT terminals.	159
Figure 5.10. Driver circuit PCB layout design: (a) Top layout; (b) Bottom layout.	159
Figure 5.11. Driver circuit PCB (developed under the scope of this Ph.D. thesis).	160
Figure 5.12. Driver circuit PCB experimental results: (a) Unipolar PWM; (b) Bipolar PWM; (<i>VOA</i> , <i>VOB</i> : 5 V/div; <i>VPWM</i> : 2 V/div).....	161
Figure 5.13. Driver circuit PCB experimental results: (a) Deadtime results; (b) Results when <i>Si8244</i> is disabled; (<i>VOA</i> , <i>VOB</i> , <i>DISABLE</i> : 5 V/div; <i>VPWM</i> : 2 V/div).....	161
Figure 5.14. MMC faults: (a) External origin faults; (b) (c) Internal origin faults.....	162
Figure 5.15. Half-bridge SM with the proposed protection scheme.	164
Figure 5.16. Flowchart diagrams of the proposed protection scheme: (a) Overcurrent protection flowchart; (b) Overvoltage protection flowchart.	165
Figure 5.17. Protection circuit PCB layout design: (a) Top layout; (b) Bottom layout.	165
Figure 5.18. Protection circuit PCB: (a) Top; (b) Bottom (developed under the scope of this Ph.D. thesis).	166
Figure 5.19. Schematic of the circuit implemented for testing the overcurrent protection.	166
Figure 5.20. Protection circuit PCB experimental results (overcurrent protection): Test current (<i>i_{test}</i> : 20 A/div, 100 mV per 1 A); Overcurrent protection actuation signal (<i>v_{pr}</i> : 5 V/div); Differential output voltage of the current sensor (<i>v_{diff}</i> : 1 V/div); Differential output voltage of the current sensor after using a differential amplifier (<i>v_{amp}</i> : 2 V/div).....	167
Figure 5.21. Schematic of the circuit implemented for testing the overvoltage protection.	168
Figure 5.22. Protection circuit PCB experimental results (overvoltage protection): Test voltage (<i>v_{test}</i> : 50 V/div); Voltage protection actuation signal (<i>v_{pr}</i> : 2 V/div); Differential output voltage of the voltage sensor after using a differential amplifier (<i>v_{amp}</i> : 2 V/div); Reference voltage signal (<i>v_{ref}</i> : 2 V/div).	168
Figure 5.23. Half-bridge SM with the proposed power circuit PCB scheme.....	169
Figure 5.24. Power circuit PCB layout design: (a) Top layout; (b) Bottom layout.	170
Figure 5.25. Power circuit PCB: (a) Top; (b) Bottom (developed under the scope of this Ph.D. thesis).	170
Figure 5.26. Testing scheme of the half-bridge SM.....	171
Figure 5.27. Power circuit PCB experimental results without using TVS diodes or snubber capacitors: Collector-emitter voltage of IGBT top (<i>V_{CE1}</i> : 50 V/div); Collector-emitter voltage of IGBT bottom (<i>V_{CE2}</i> : 50 V/div); DC voltage source (<i>V_{dc}</i> : 50 V/div).	173
Figure 5.28. Power circuit PCB experimental results: Output current (<i>i_o</i> : 2 A/div); Collector-emitter voltage of IGBT top (<i>V_{CE1}</i> : 50 V/div); Collector-emitter voltage of IGBT bottom (<i>V_{CE2}</i> : 50 V/div); DC voltage source (<i>V_{dc}</i> : 50 V/div).	173
Figure 5.29. Power circuit PCB experimental results during the deadtime: Collector-emitter voltage of IGBT top (<i>V_{CE1}</i> : 50 V/div); Collector-emitter voltage of IGBT bottom (<i>V_{CE2}</i> : 50 V/div); DC voltage source (<i>V_{dc}</i> : 50 V/div).	174
Figure 5.30. Power circuit PCB experimental results when an overcurrent condition is detected by the protection circuit PCB: Collector-emitter voltage of IGBT top (<i>V_{CE1}</i> : 50 V/div); Collector-emitter voltage of IGBT bottom (<i>V_{CE2}</i> : 50 V/div); Overcurrent protection actuation signal (<i>v_{pr}</i> : 5 V/div); Output current (<i>i_o</i> : 5 A/div).	174
Figure 5.31. Final SM structure.	175
Figure 5.32. Single MMC leg/phase (four SMs).....	175
Figure 5.33. Filter inductor used in MMC.	176
Figure 5.34. Filter inductor saturation test: Pulse voltage (<i>V_{pulse}</i> : 5 V/div); Coil current (<i>i_L</i> : 10 A/div); Coil voltage (<i>v_L</i> : 5 V/div).	176
Figure 5.35. Main DC-link capacitor (developed under the scope of this Ph.D. thesis).	177
Figure 5.36. Control system hardware fitted in a metallic box.	178
Figure 5.37. Global communication structure of the HB-MMC2 RPC reduced-scale prototype.....	179
Figure 5.38. Interface board to support the <i>TMDSCNCD28335</i> control card.	181
Figure 5.39. User interface of the programming tool <i>Code Composer Studio</i> v5.5.0 from <i>Texas Instruments</i>	181
Figure 5.40. PCB of the <i>CYHVS025A</i> voltage sensor.	183
Figure 5.41. PCB of the <i>LA 100-P</i> current sensor.....	183

Figure 5.42. Interface PCB between the DSC and the DAC.....	184
Figure 5.43. Signal conditioning PCB for the external ADC.	185
Figure 5.44. Signal conditioning PCB for the internal ADC: (a) Top; (b) Bottom (developed under the scope of this Ph.D. thesis).....	186
Figure 5.45. Voltage sense application by using <i>Si8920</i> , including the signal conditioning.	187
Figure 5.46. Operation principle of the command circuit PCB.	187
Figure 5.47. Command circuit PCB (developed under the scope of this Ph.D. thesis): (a) Top; (b) Bottom.....	188
Figure 5.48. The overall delay at no load conditions: (a) When using normal optocouplers; (b) When using <i>Si8710</i> isolator from <i>Silicon labs</i> ; (v_{pr} , $v_{disable}$, PWM: 5 V/div).	189
Figure 5.49. PWM PCB adapter (developed under the scope of this Ph.D. thesis).	189
Figure 6.1. MMC workbench developed in GEPE.	192
Figure 6.2. Enhanced phase-locked loop (E-PLL) results: Phase x voltage (u_x : 30 V/div); Phase y voltage (u_y : 30 V/div); Phase x voltage angle (θ_x : 10 ms \leftrightarrow 180°); Phase y voltage angle (θ_y : 10 ms \leftrightarrow 180°).	193
Figure 6.3. Results of the digital moving average LPF at $M = 200$ samples: Load section x current (i_{Lx} : 5 A/div); Load section y current (i_{Ly} : 5 A/div); Moving average LPF output signal (i_{LFP} : 5 A/div).....	194
Figure 6.4. Results of the digital moving average LPF at $M = 600$ samples: Load section x current (i_{Lx} : 5 A/div); Load section y current (i_{Ly} : 5 A/div); Moving average LPF output signal (i_{LFP} : 5 A/div).....	194
Figure 6.5. Results of the digital moving average LPF at $M = 800$ samples: Load section x current (i_{Lx} : 5 A/div); Load section y current (i_{Ly} : 5 A/div); Moving average LPF output signal (i_{LFP} : 5 A/div).....	194
Figure 6.6. Testing of one MMC leg/phase in an open-loop control.....	195
Figure 6.7. Testing of one MMC leg/phase in an open-loop control experimental results: Output voltage (v_o : 10 V/div); Upper arm voltage (v_1 : 10 V/div); Lower arm voltage (v_2 : 10 V/div).	196
Figure 6.8. Test of one MMC leg/phase using a closed-loop control.	197
Figure 6.9. MMC SM voltages when testing of one MMC leg/phase without commutation: SM1 voltage (V_{SMx1} : 20 V/div); SM2 voltage (V_{SMx2} : 20 V/div); SM3 voltage (V_{SMx3} : 20 V/div); SM4 voltage (V_{SMx4} : 20 V/div).....	198
Figure 6.10. MMC SM voltages when testing of one MMC leg/phase with commutation: SM1 voltage (V_{SMx1} : 20 V/div); SM2 voltage (V_{SMx2} : 20 V/div); SM3 voltage (V_{SMx3} : 20 V/div); SM4 voltage (V_{SMx4} : 20 V/div).....	198
Figure 6.11. Testing of one MMC leg/phase in a closed-loop control: DC-link voltage of the upper capacitor (V_{dca} : 10 V/div); DC-link voltage of the lower capacitor (V_{dcb} : 10 V/div); Reference current waveform (i_{ref} : 2 A/div); Output current waveform (i_{rx} : 2 A/div).	199
Figure 6.12. Testing of one MMC leg/phase in a closed-loop control: MMC leg/phase output current (i_{rx} : 2 A/div); Upper arm current (i_{rxu} : 2 A/div); Lower arm current (i_{rxl} : 2 A/div).....	199
Figure 6.13. Testing two MMC legs/phases using a closed-loop control.....	200
Figure 6.14. SM voltages of phase x under operation, when testing two MMC legs/phases: SM1 voltage (V_{SMx1} : 20 V/div); SM2 voltage (V_{SMx2} : 20 V/div); SM3 voltage (V_{SMx3} : 20 V/div); SM4 voltage (V_{SMx4} : 20 V/div).....	201
Figure 6.15. SM voltages of phase y under operation, when testing two MMC legs/phases: SM1 voltage (V_{SMy1} : 20 V/div); SM2 voltage (V_{SMy2} : 20 V/div); SM3 voltage (V_{SMy3} : 20 V/div); SM4 voltage (V_{SMy4} : 20 V/div).....	201
Figure 6.16. Testing two MMC legs/phases using a closed-loop control: Phase x output current (i_{rx} : 2 A/div); Phase y output current (i_{ry} : 2 A/div).	202
Figure 6.17. Testing two MMC legs/phases using a closed-loop control: Phase x upper and lower arm currents (i_{rxu} , i_{rxl} : 2 A/div); Phase y upper and lower arm currents (i_{ryu} , i_{ryl} : 2 A/div).	202
Figure 6.18. Schematic of the HB-MMC2 RPC experimental setup.	203
Figure 6.19. HB-MMC2 RPC experimental results (when both load sections are loaded): Phase x current before compensation (i_x : 10 A/div); Phase y current before compensation (i_y : 10 A/div); Phase z current before compensation (i_z : 10 A/div).	204

Figure 6.20. HB-MMC2 RPC experimental results (when both load sections are loaded): Phase x current before compensation (i_x : 5 A/div); Phase y current before compensation (i_y : 5 A/div); Phase A voltage (u_A : 100 V/div).....	204
Figure 6.21. HB-MMC2 RPC experimental results (when both load sections are loaded): Phase x current after compensation (i_x : 10 A/div); Phase y current after compensation (i_y : 10 A/div); Phase z current after compensation (i_z : 10 A/div).....	205
Figure 6.22. HB-MMC2 RPC experimental results (when both load sections are loaded): Phase x current after compensation (i_x : 5 A/div); Phase y current after compensation (i_y : 5 A/div); Phase A voltage (u_A : 100 V/div).....	205
Figure 6.23. Frequency spectrum of the three-phase currents at the secondary windings of the V/V transformer (when both load sections are loaded): (a) Before compensation; (b) After compensation.	206
Figure 6.24. Harmonic contents value of the three-phase currents at the secondary windings of the V/V transformer (when both load sections are loaded): (a) Before compensation; (b) After compensation.	206
Figure 6.25. Unbalance ratio and phasors diagram of the three-phase currents at the secondary of the V/V transformer (when both load sections are loaded): (a) Before compensation; (b) After compensation.	207
Figure 6.26. HB-MMC2 RPC experimental results (when both load sections are loaded): Phase x compensation current (i_{rx} : 5 A/div); Phase y compensation current (i_{ry} : 5 A/div).....	207
Figure 6.27. HB-MMC2 RPC experimental results – SM voltages of section x converter (when both load sections are loaded): SM1 voltage (V_{SMx1} : 20 V/div); SM2 voltage (V_{SMx2} : 20 V/div); SM3 voltage (V_{SMx3} : 20 V/div); SM4 voltage (V_{SMx4} : 20 V/div).....	208
Figure 6.28. HB-MMC2 RPC experimental results - SM voltages of section y converter (when both load sections are loaded): SM1 voltage (V_{SMy1} : 20 V/div); SM2 voltage (V_{SMy2} : 20 V/div); SM3 voltage (V_{SMy3} : 20 V/div); SM4 voltage (V_{SMy4} : 20 V/div).	208
Figure 6.29. HB-MMC2 RPC experimental results (when load section y is loaded): Phase x current before compensation (i_x : 5 A/div); Phase y current before compensation (i_y : 5 A/div); Phase z current before compensation (i_z : 5 A/div).....	209
Figure 6.30. HB-MMC2 RPC experimental results (when load section y is loaded): Phase x current after compensation (i_x : 5 A/div); Phase y current after compensation (i_y : 5 A/div); Phase z current after compensation (i_z : 5 A/div).....	209
Figure 6.31. Frequency spectrum of the three-phase currents at the secondary of the V/V transformer (when load section y is loaded): (a) Before compensation; (b) After compensation.....	210
Figure 6.32. Harmonic contents value of the three-phase currents at the secondary of the V/V transformer (when load section y is loaded): (a) Before compensation; (b) After compensation.	210
Figure 6.33. Unbalance ratio and phasors diagram of the three-phase currents at the secondary of the V/V transformer (when load section y is loaded): (a) Before compensation; (b) After compensation.	211
Figure 6.34. HB-MMC2 RPC experimental results (when load section y is loaded): Phase x compensation current (i_{rx} : 5 A/div); Phase y compensation current (i_{ry} : 5 A/div).....	211
Figure 6.35. HB-MMC2 RPC experimental results – SM voltages of section x converter (when load section y is loaded): SM1 voltage (V_{SMx1} : 20 V/div); SM2 voltage (V_{SMx2} : 20 V/div); SM3 voltage (V_{SMx3} : 20 V/div); SM4 voltage (V_{SMx4} : 20 V/div).	212
Figure 6.36. HB-MMC2 RPC experimental results – SM voltages of section y converter (when load section y is loaded): SM1 voltage (V_{SMy1} : 20 V/div); SM2 voltage (V_{SMy2} : 20 V/div); SM3 voltage (V_{SMy3} : 20 V/div); SM4 voltage (V_{SMy4} : 20 V/div).	212

List of Tables

Table 1.1. Portuguese railway locomotives in the last 5 decades (part I) [7]. Source: [<i>Comboios de Portugal</i>].	8
Table 1.2. Portuguese railway locomotives in the last 5 decades (part II) [7]. Source: [<i>Comboios de Portugal</i>].	9
Table 1.3. Portuguese railway locomotives in the last 5 decades (part III) [7]. Source: [<i>Comboios de Portugal</i>].	10
Table 1.4. Future trends on high-speed locomotives [40].	16
Table 2.1. Voltage harmonics at the point of power delivery, expressed as a percentage of the nominal voltage amplitude U_c ($1 \text{ kV} \leq MV \leq 36 \text{ kV}$, $36 \text{ kV} \leq HV \leq 150 \text{ kV}$, $150 \text{ kV} \leq EHV \leq 400 \text{ kV}$).	25
Table 2.2. Comparison between several types of power transformers used in railway applications [77].	34
Table 3.1. Full-bridge SM switch operation.	56
Table 3.2. Operating states of the half-bridge SM.	58
Table 3.3. Traction power system, public power system and MMC parameters.	60
Table 3.4. Comparison of SFC based MMC topologies for the application of rail electrification [118].	61
Table 3.5. Comparison between different compensator topologies in railway electrification [49].	63
Table 3.6. Comparison between SFC and RPC based on an indirect MMC: different inherent benefits and the abilities for each system.	65
Table 4.1. Capabilities of the RPC operation mode.	70
Table 4.2. Capabilities of the RPC operating in the SVC mode.	71
Table 4.3. Capabilities of the RPC operating in the catenary voltage regulator mode.	72
Table 4.4. Capabilities of the RPC operating as an interface converter between two substations.	73
Table 4.5. Components quantities of the FB-RPC.	75
Table 4.6. Load parameters of the FB-RPC converter.	79
Table 4.7. Parameters of the FB-RPC simulation model.	80
Table 4.8. Components quantities of the TW-RPC.	84
Table 4.9. Parameters of the TW-RPC simulation model.	86
Table 4.10. Comparison between the HB-RPC and the FB-RPC.	88
Table 4.11. Components quantities of the HB-RPC.	88
Table 4.12. Parameters of the HB-RPC simulation model.	90
Table 4.13. Components quantities of the co-HRPC.	93
Table 4.14. Simulation parameters of the FB-RPC and the co-HRPC models.	96
Table 4.15. Technical comparison between Scott and V/V power transformers.	102
Table 4.16. Components quantities of the MRPC.	106
Table 4.17. Simulation parameters for the FB-RPC model and the MRPC model.	108
Table 4.18. Components quantities of the FB-MMC4 RPC.	111
Table 4.19. Parameters of the FB-MMC4 RPC simulation model.	117
Table 4.20. Components quantities of the TW-MMC3 RPC.	120
Table 4.21. Parameters of the TW-MMC3 RPC simulation model.	126
Table 4.22. Components quantities of the HB-MMC2 RPC.	129
Table 4.23. Load parameters of the HB-MMC2 RPC converter.	137
Table 4.24. Parameters of the HB-MMC2 RPC simulation model.	137
Table 4.25. IGBT characteristics of the RPC topologies [150].	142
Table 4.26. Quantitative comparison of the RPC topologies [150].	143
Table 4.27. Characteristics of the RPC topologies in V/V and Scott transformer [150].	145
Table 5.1. Reduced-scale MMC parameters.	151
Table 5.2. Power circuit PCB components.	170
Table 5.3. Parameters of single half-bridge SM test.	172

Table 6.1. Parameters of testing one MMC leg/phase in an open-loop control.	195
Table 6.2. Parameters of testing one MMC leg/phase using a closed-loop control.	197
Table 6.3. Experimental parameters of the HB-MMC2 RPC.	203

Acronyms and Abbreviations

Acronym	Significance
AC	Alternating Current
ADC	Analogue-to-Digital Converter
AVE	Alta Velocidade Española (in Spanish)
CAN	Controller Area Network
CMOS	Complementary Metal-Oxide-Semiconductor
CO ₂	Carbon Dioxide
Co-HRPC	Hybrid co-phase Rail Power Conditioner
CP	Comboios de Portugal (in Portuguese)
DAC	Digital-to-Analogue Converter
DC	Direct Current
DSC	Digital Signal Controller
EHV	Extra High-Voltage
E-PLL	Enhanced Phase-Locked Loop
ERA	European Railway Agency
ERTMS	European Railway Traffic Management System
EU	European Union
FACTS	Flexible AC Transmission Systems
FB-MMC4 RPC	RPC Based on Full-Bridge Indirect Modular Multilevel Converter
FB-RPC	Full-Bridge Back-to-Back RPC
FPGA	Field-Programmable Gate Array
GEPE	Grupo de Eletrónica de Potência e Energia (in Portuguese)
GPIO	General-Purpose Input/Output
GTO	Gate Turn-Off Thyristor

HB-MMC2 RPC	RPC Based on Half-bridge Indirect Modular Multilevel Converter
HB-RPC	Half-Bridge Back-to-Back RPC
HF	Harmonic Filter
HP	Horse-power
HV	High-Voltage
ICE	Inter-City Express Train
IC	Integrated Circuit
IEGT	Injection-Enhanced Gate Transistor
IGBT	Insulated-Gate Bipolar Transistor
LPF	Low-Pass Filter
MDLC	Multiple DC-Link Static Frequency Converter
MMC	Modular Multilevel Converter
MRPC	Modular Rail Power Conditioner
MSC	Mechanically Switched Capacitor
MSR	Mechanically Switched Reactor
MV	Medium-Voltage
NPC	Neutral Point Clamp
NSC	Negative Sequence Component
PCB	Printed Circuit Board
PI	Proportional-Integral
PPS	Public Power System
PR	Proportional-Resonant
PSC	Positive Sequence Component
PWM	Pulse Width Modulation
RMS	Root Mean Square
RPC	Rail Power Conditioner
S2R	Shift2Rail

SDLC	Single DC-Link Static Frequency Converter
SFC	Static Frequency Converter
SiC	Silicon Carbide
SM	Submodule
SNCF	Société Nationale des Chemins de Fer Français (in French)
SPI	Serial Peripheral Interface
STATCOM	Static Synchronous Compensator
SVC	Static VAr Compensator
TCR	Thyristor controlled reactor
TGV	Train à Grande Vitesse (in French)
THD	Total Harmonic Distortion
TPS	Traction Power System
TSC	Thyristor Switched Capacitor
TVS	Transient Voltage Suppressor
TW-MMC3 RPC	RPC Based on Two-phase Three-wire Indirect Modular Multilevel Converter
TW-RPC	Three Wire Back-to-Back RPC
ZOH	Zero-order Hold

Nomenclature

The symbol “ σ ” belongs to the phases (x, y, z)

ΔV_{out}	Voltage difference between mid-neutral point DC-link capacitors	V
$\Delta I_{r\sigma}$	Current ripples in the MMC arm	A
a	Complex number operator with a unitary magnitude and an angle of 120°	–
A_σ	Output of MMC leg averaging voltage control	V
C_{de}	Decoupling capacitor	F
C_{DSM}	Capacitance of direct AC/AC MMC SM	F
C_{I2SM}	Capacitance of indirect DC/AC MMC SM	F
C_{I3SM}	Capacitance of indirect AC/DC MMC SM	F
C_x	LC passive filter capacitance that used in the co-phase RPC	F
C_{SM}	MMC SM capacitance value	F
f	Electrical grid fundamental frequency	Hz
f_d	DC-link voltage ripple frequency	Hz
f_{isw}	Individual SM switching frequency	Hz
f_{sw}	Equivalent switching frequency	Hz
h_n	Amplitude of the n -order harmonic	A
I_2, I_3, I_4	2 nd , 3 rd and 4 th order current harmonic contents	A
I_A, I_B, I_C	Phase A , phase B and phase C RMS currents of PPS before compensation	A
I_{A1}, I_{B1}, I_{C1}	Phase A , phase B and phase C RMS currents of PPS after active power balance	A
I_{A2}, I_{B2}, I_{C2}	Phase A , phase B and phase C RMS currents of PPS after active power balance and reactive power compensation	A
I_{An}, I_{Bn}, I_{Cn}	Negative sequence component of phase A , phase B and phase C currents	A
I_{Ap}, I_{Bp}, I_{Cp}	Positive sequence component of phase A , phase B and phase C currents	A
$i_{cir\sigma}$	MMC instantaneous circulating current	A
i_{dca}, i_{dcb}	HB-MMC2 RPC main DC-link currents	A
$i_{L\sigma}$	Load section instantaneous currents	A

$I_{L\sigma a}$	RMS load section active currents	A
$I_{L\sigma h}$	RMS h^{th} order harmonic current contents for both load sections	A
$I_{L\sigma r}$	RMS load section reactive currents	A
i_o	AC output instantaneous current	A
$i_{r\sigma}$	Instantaneous compensation currents synthesized by RPC system at the primary windings of the single-phase step-down coupling transformer	A
$i_{r\sigma}^*$	Instantaneous compensation current references	A
$i_{r\sigma 1}$	Instantaneous compensation currents synthesized by RPC system at the secondary windings of the single-phase step-down coupling transformer	A
$I_{r\sigma a}$	Active RMS compensation currents synthesized by RPC	A
$I_{r\sigma n}$	Compensation currents provided by one RPC module when using MRPC.	A
$i_{r\sigma nu}, i_{r\sigma nl}$	Instantaneous upper and lower arm currents of MMC negative legs for section x and section y converter	A
$I_{r\sigma r}$	Reactive RMS compensation currents synthesized by RPC	A
$i_{r\sigma u}, i_{r\sigma l}$	Instantaneous upper and lower arm currents of MMC positive leg for section x and section y converter	A
$i_{r\sigma u_err}, i_{r\sigma l_err}$	Error in the upper and lower arm currents of the MMC	A
i_{sm}	MMC SM instantaneous output current	A
I_{st}	IGBT current stress	p.u.
I_{x2m}	The peak current of phase x current after active power balance and reactive power compensation	A
i_σ	Phase x , phase y and phase z instantaneous currents of the secondary windings of V/V or Scott power transformer	A
$I_{\sigma 1}$	Phase x , phase y and phase z RMS currents of TPS after active power balance	A
$I_{\sigma 2}$	Phase x , phase y and phase z RMS currents of TPS after active power balance and reactive power compensation	A
k	Number of MRPC modules	–
K	Present sample interval of the deadbeat predictive control	–
K_D	Turns ratio of the single-phase step-down coupling transformer	–
K_V	Turns ratio of the V/V power transformer	–
L_{au}, L_{al}	Upper and lower inductances of the MMC leg phase a converter	H
L_{bu}, L_{bl}	Upper and lower inductances of the MMC leg phase b converter	H

L_{cu}, L_{cl}	Upper and lower inductances of the MMC leg phase c converter	H
L_o	Catenary line inductance	H
L_σ	Filter inductance of the RPC system	H
$L_{\sigma nu}, L_{\sigma nl}$	Upper and lower inductances of the MMC negative leg for section x and section y converter	H
$L_{\sigma u}, L_{\sigma l}$	Upper and lower inductances of the MMC positive leg for section x and section y converter	H
M	Number of samples for the moving average low-pass filter	–
n	Single module order in the MRPC	–
N	MMC Voltage Level	–
$N-1$	Number of SMs in one MMC arm	–
N_1, N_2	Number of windings at the primary / secondary of the power transformer	–
p_{ac}	MMC AC power	W
P_C	Shifted active power by RPC	W
p_{dc}	MMC DC-link power	W
p_{losses}	Power losses in MMC converter	W
P_σ	Active power RMS value of load sections x and y	W
Q_σ	Reactive power RMS value of load sections x and y	VAR
R	Electrical resistance	Ω
$R_{\sigma u}, R_{\sigma l}$	Electrical resistance of the upper and lower MMC arm	Ω
T_s	Sampling period	sec
U_{AC}, U_{BC}	Line-to-line RMS voltage of PPS	V
$u_{L\sigma}$	Instantaneous voltage across the MMC filter inductors	V
u_{no}	Zero-sequence voltage	V
$u_{r\sigma}^*$	Instantaneous voltage reference signals	V
$u_{\sigma u}^*, u_{\sigma l}^*$	Instantaneous voltage reference signals resulting from the deadbeat control	V
u_σ	Phase x and phase y instantaneous load section voltages	V
$u_{\sigma 1}$	Phase x and phase y instantaneous voltages at the secondary windings of the single-phase step-down coupling transformer	V
$u_{\sigma n}$	Phase-to-neutral voltages of the TW-MMC3 RPC / HB-MMC2 RPC	V

$u_{\sigma nu}, u_{\sigma nl}$	Instantaneous upper and lower arm voltages of the negative MMC leg	V
$U_{\sigma o}$	RMS AC output voltage of the RPC based on MMC	V
$u_{\sigma o}$	Instantaneous AC output voltage of the RPC based on MMC	V
$u_{\sigma u}, u_{\sigma l}$	Instantaneous upper and lower arm voltages of the positive MMC leg	V
U_{σ}	RMS value of the feeder voltages	V
V_{arm}^*	MMC arm DC-link voltage reference	V
V_{dc}	DC voltage of a DC-link	V
V_{dc}^*	DC voltage reference of a DC-link	V
$V_{i\sigma u}, V_{i\sigma l}$	Output of MMC SM individual voltage control	V
$V_{r\sigma u}, V_{r\sigma l}$	Output of MMC arm averaging voltage control	V
V_{SM}	MMC SM DC-link voltage	V
V_{st}	Voltage stress across the IGBT	p.u.
W_{dc}	Energy stored in the DC-link capacitor	J
X_C	Electrical capacitive reactance	Ω
X_L	Electrical inductive reactance	Ω
Z	Electrical impedance	Ω
Z_L	Catenary lumped impedance	Ω
$\Delta I_{r\sigma}$	Active RMS compensation currents synthesized by RPC	A
ΔV_{dc}	DC-link voltage ripples (peak-to-peak)	V
θ_{σ}	Phase angle shift of phase x and phase y	degree
$\phi_{\sigma h}$	The corresponded phase angles of the h^{th} order harmonic current contents for both load sections	rad
ω	Angular frequency	rad/sec

Chapter 1

Introduction

1.1 Electrified Railway Systems in Europe

European Union (EU) aims to get a major reduction in pollution and carbon dioxide (CO₂) emissions, then, European railway industry is supporting the challenge to develop alternatives of Diesel locomotives. This European strategy is adopted since the rail sector can offer substantial advantages for the energy sector as well as for the environment, preventing catastrophic climate change. The future of rail will be determined by how it responds to the rising transport demand, then using different energy sources, including the renewable green energy, and providing more efficient mobility are the main keys to reduce energy demand by the rail [1].

Nowadays, the regions with the highest contribution in electrified railway systems are Europe and East Asia. In this framework, this chapter presents a summary of the electrified railway systems in Europe, including history, challenges and opportunities. In addition, the case of Portuguese railways has been taken into consideration to present an overview including some statistics.

1.1.1 History of Railway Electrification in Europe

Railway electrification has begun at the end of the 19th century for urban and suburban rail transport [2]. Any curious observer who would like to get knowledge about railways could ask why there are different railway electrification systems in Europe, and if they could be integrated in the near future. The reason for these different electrification systems was based on historical origins, such as the development of electrical equipment throughout the last century. Due to the absence of a unified electrification policy in Europe and as every single country was prepared to introduce the rail electrification at a time different from the other European countries, the best obtainable system for rail electrification at that time was approved to be implemented.

In the 19th century, locomotives were equipped with series-wound Direct Current (DC) motors and supplied at a voltage between 600 V and 750 V DC. The main reason for using these types of motors was the high starting-torque, besides the simple speed control by adding some resistors connected in series with the motor [2], [3]. In the 20th century and within the emergence of railway intercity lines,

the electrification voltage level was increased to reach 3 kV DC. However, and since the DC electrification systems were suffering from the high currents flowing in the overhead catenary line and the limitation in locomotive power, the Alternating Current (AC) electrification of 15 kV was introduced at the beginning of the 20th century. The early designs of series-wound motors were impractical to use under the normal distribution frequency 50 Hz, due to the sparks generated in commutators [4]. Therefore, it was essential to decrease the power supply frequency to 16.7 Hz and then to establish an exclusive generation and distribution power grid for railway electrification. Although the many advantages of this traction system at that time, the low-frequency value led to slightly increase the size of transformers, motors and the locomotive itself [5]. Also, this type of electrification demanded to use a special transmission power system. Consequently, the implementation costs could be high.

In 1951, the French national railway company, called SNCF (*Société Nationale des Chemins de Fer Français*) succeeded to build the first railway line that operated on 20 kV, 50 Hz and in 1953, the voltage was increased to 25 kV. As a conclusion, using the low-frequency of 16.7 Hz was no longer necessary after the evolution in semiconductors and Power Electronics that could perform the power conversion. The locomotives of this system could be equipped with different traction motors, such as DC motors or asynchronous motors. In fact, this system has become the most widely used for high-speed railway electrification [2], even in the European countries that mainly use the DC electrification (e.g., Spain and Italy), the high-speed railway lines in those countries were constructed under 25 kV, 50 Hz [6].

1.1.2 Railway Challenges in Europe

European railway sector needs to be more competitive than the other transport modes. In this context, the European railway transport mode must become more efficient, integrated, modernistic and responsive to customer demand. Building a modern railway network in the EU is needed as a priority that helps for the economic growth and development in Europe. This can smoothly transport the goods between EU countries, besides the development to construct a sustainable transport system. The European efforts in this regard focus on the following criteria [1].

- Opening the rail markets between EU countries for greater competition;
- Achieving the technical standards between rail networks inside EU;
- Modernizing the rail's infrastructure, including the use of new technologies.

EU legislation gives the rail operators the permission to run services between EU countries, introducing a competitive rail transportation with other transport modes. The liberalization in rail freight transport has been achieved in EU since the beginning of 2007 for both international and national services. In

addition, the EU has liberalized the market for the international rail passenger services since January 2010. Harmonizing the hardware and the software between the EU rail operators is a real challenge to accomplish the rail integration in the EU, especially after realizing the differences in the technical specifications of rail infrastructure. For instance, different gauge width is applied between some EU countries as shown in Figure 1.1(a). Portugal and Spain (Iberian gauges) gauge width is 1668 mm [7], higher than the standard gauge in the rest of Europe which is 1435 mm.

The electrification standards are different in the EU countries as shown in Figure 1.1(b). Owing principally to historical reasons, Germany, Sweden, Norway, Switzerland and Austria are using the 15 kV, 16.7 Hz for rail electrification, while the north part of France, Portugal, Denmark and Finland are using the 25 kV, 50 Hz for rail electrification [8]. Italy, Belgium, Poland and Spain are mainly using the 3 kV DC system for rail electrification when the train speeds are lower than 250 km/h [8]. Netherland and south of France are electrified with a 1.5 kV DC system. The southern part of the United Kingdom is electrified with a 0.65/0.75/1.2 kV DC [9]. This problem of five different electrification systems can be fixed by using multisystem or hybrid locomotives equipped with Power Electronics devices, hence the locomotives manufacturers should have the foreknowledge of the multisystem concept. The safety conditions and the signaling systems are also different among some EU countries.

All previous reasons complicate the efforts to run trains from different EU countries. Therefore, specific EU legislations exist to promote the rail specifications in a way to make them under a unified standard. As a conclusion of these challenges, the *European Railway Agency* (ERA) was established in 2004 to coordinate and to harmonize the technical standards between EU countries [1]. The name of this agency changed in 2016 to the European Union agency for railways and it is located in *Valenciennes* and *Lille* cities in France.

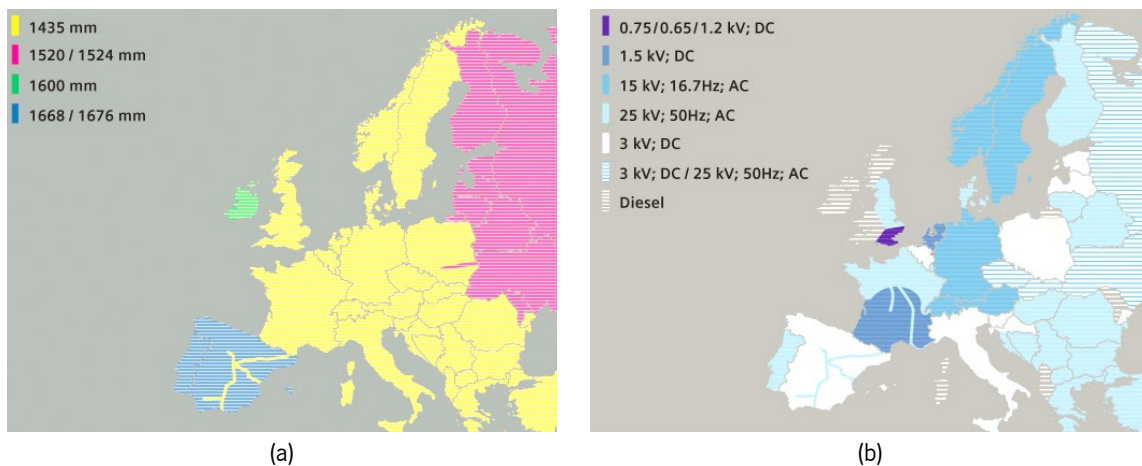


Figure 1.1. Railway maps in EU: (a) The used gauge width; (b) The used voltage level for railway electrification [10].

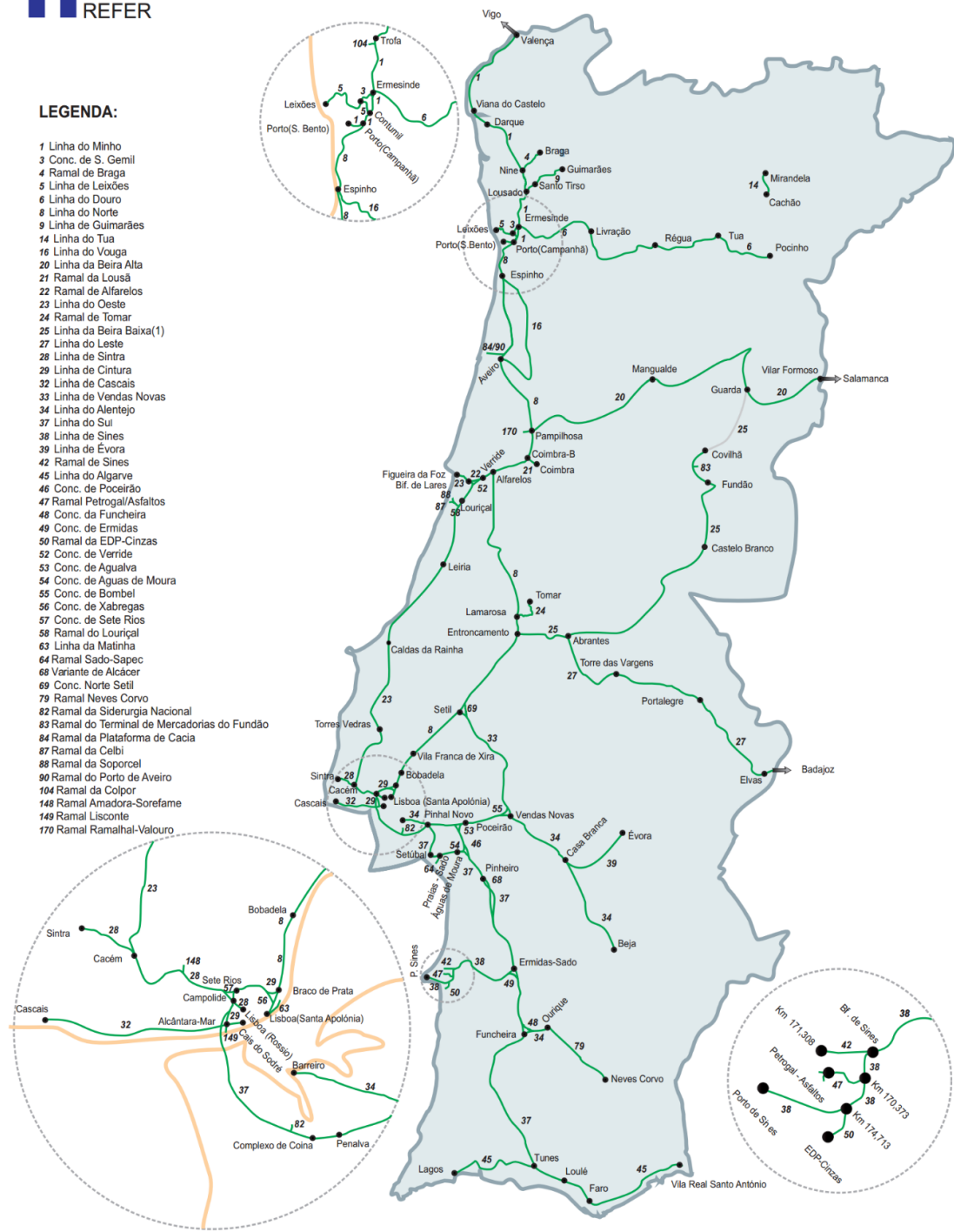
Source: [Siemens mobility]

1.1.3 Portuguese Railway Network

The first train journey in Portugal took place 164 years ago, precisely on 28 October 1856 between Lisbon and Carregado. The railway line between Lisbon and Carregado was initially built in a standard gauge of 1435 mm, then it was substituted by the Iberian gauge of 1668/1676 mm due to the noted developments in Spain [11]. The railway network was gradually expanded in the first-half of the 20th century (1900–1950) to reach north of Portugal besides some of the southern parts. The current Portuguese railway network is shown in Figure 1.2, where nowadays, more than half of the Portuguese railway lines are electrified, but the total length of the railway network has decreased during the last decades. The interior cities of the country were the most affected area of this decrement. Out of the 3.750 km of railway lines in service in the 1960, today Portugal has only 2.630 km of railways [12].

The second half of the 20th century has carried the cars industrial revolution in Europe, then from the 1980s and later, Portugal has observed a high demand for the highway roads as an easy way of transport, and at the same time, railway infrastructure suffered from aging and neglecting. As a result, there was a lower demand for railway freight and transport, leading to a significant reduction in railway investment sector. In such cases, hundreds of railway lines and stations have been closed. In this context, Figure 1.3 shows the active and the abandoned Portuguese railway during the last 50 years [13]. Figure 1.4 shows the reduction in Portuguese railways stations number during the last 15 years. According to *Pordata* the contemporary database for Portugal, the number of Portuguese train stations has decreased from 669 in 2001 to only 571 stations in 2015 [14].

Figure 1.5 shows the abandoned railway lines in the north of Portugal in the last five decades. The most affected areas from the abandoned railway lines were the interior districts of the country [15]. Progressively, railway electrification started in Portugal in 1975, then a plan to finally link all the district capitals by fully electrified trains was to be performed in 2010. The electrified trains nowadays (2016-2017) cover about 1634 km according to *Infraestruturas de Portugal*. In addition, a plan called *Ferrovias 2020* is in the execution phase to promote the Portuguese rail freight transport. For instance, railway network will tend to be fully electrified with a voltage of 25 kV, 50 Hz. Moreover, the network will be equipped with control commands and signaling systems according to the European Railway Traffic Management System (ERTMS) standard.



(1) Troço Covilhã - Guarda encerrado à exploração em 2015

Directório da Rede 2015

Figure 1.2. Portuguese railway network map in 2015 [16].Source: [*Infraestruturas de Portugal*].

Figure 1.6 shows the developments achieved in Portuguese electrified railway lines during the last 15 years [17]. Although the total length of Portuguese railway lines has decreased in the last 50 years, the electrified Portuguese railway lines are composing nowadays around 62% of the total railway length in Portugal. The old electrified lines are operating under 1.5 kV or 3 kV DC, whereas the new high-speed electrified railway lines operate with overhead AC power systems of 25 kV, 50 Hz.

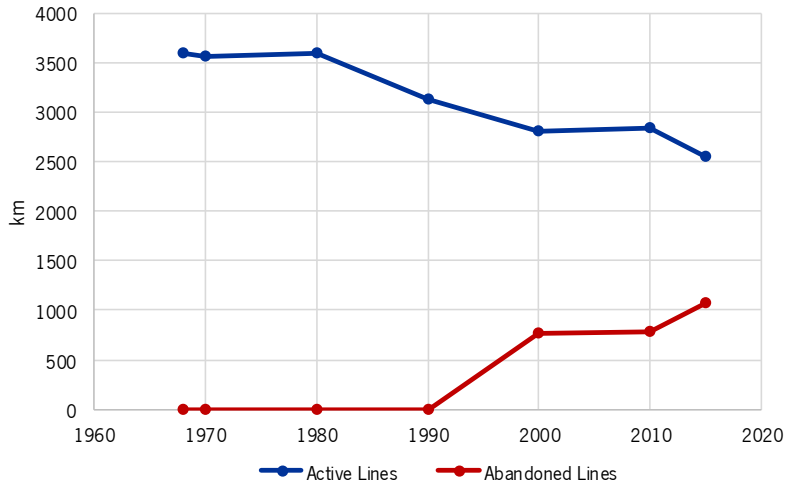


Figure 1.3. The length of active and abandoned Portuguese railway during the last 50 years. Source: [Pordata].

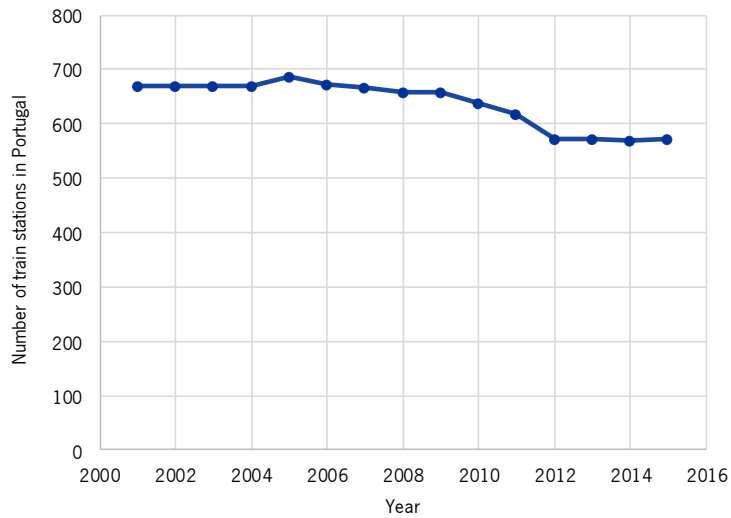


Figure 1.4. Number of Portuguese train stations during the last 15 years. Source: [Pordata].



Figure 1.5. Railway network in north of Portugal plus the already abandoned rail lines (in brown) [15]. Source: [Infraestruturas de Portugal].

Figure 1.7 shows the different voltage levels of the electrified Portuguese railways (such as 25 kV AC, 3 kV DC and 1.5 kV DC), besides the lines that are still using the Diesel locomotives (mainly the internal lines). *Cascais* line was the first electrified Portuguese line with a voltage level around 1.5 kV DC. The data presented in Figure 1.7 correspond to the year of 2012.

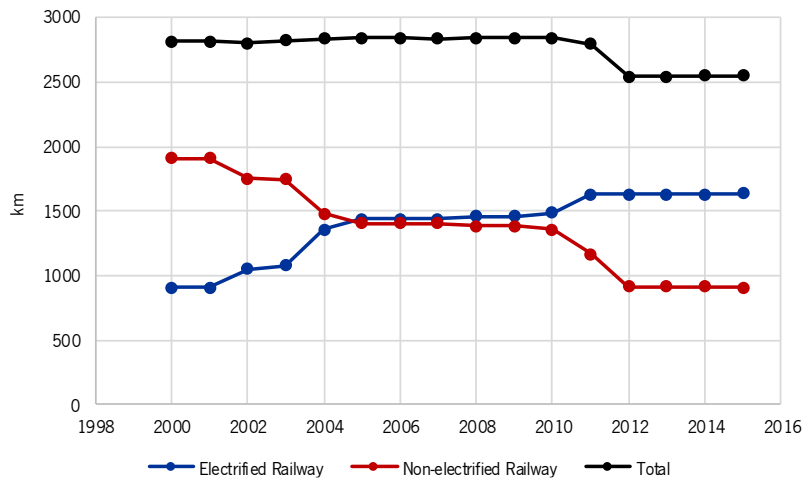


Figure 1.6. Electrified and non-electrified Portuguese railway during the last 15 years. Source: [Pordata].

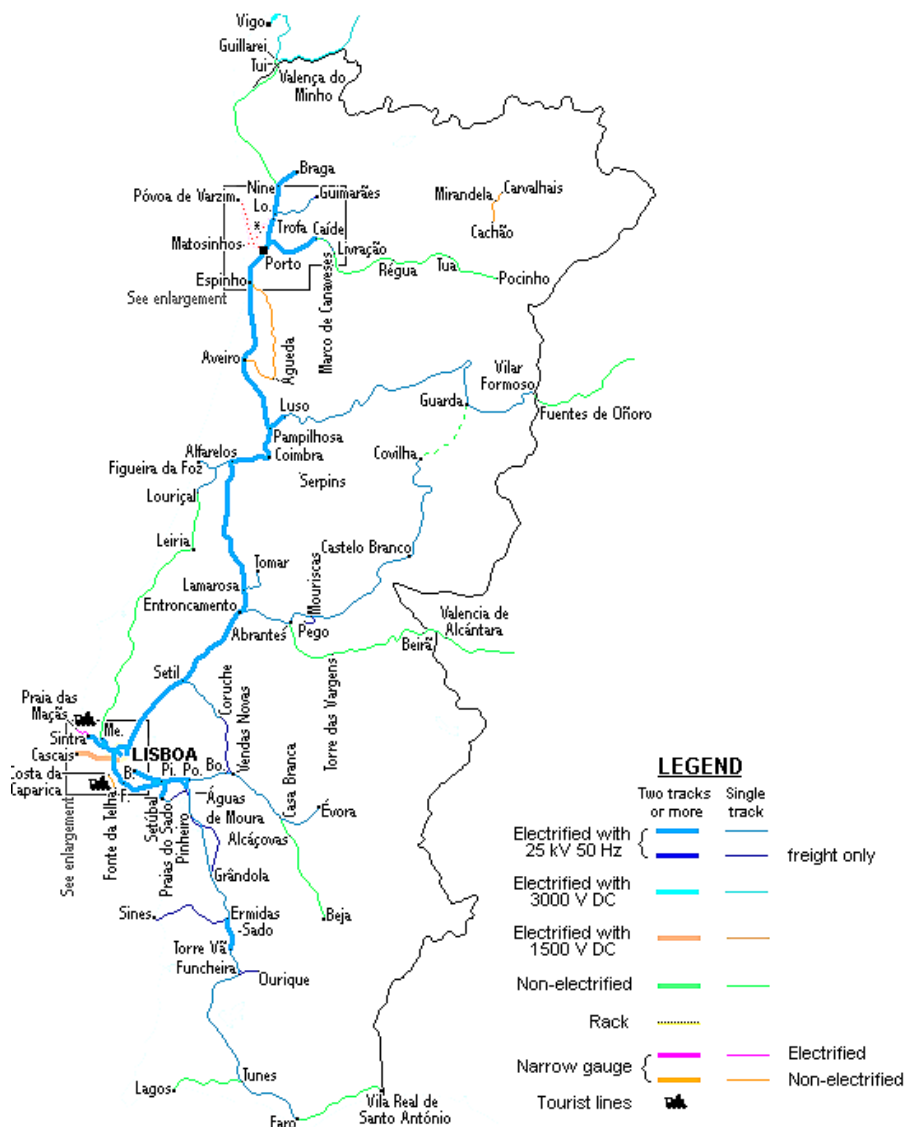


Figure 1.7. Portuguese railway based on the running mode in 2012 [18]. Source: [Thorsten Bükler].

1.1.4 Portuguese Railway Locomotives

Locomotives are the single units responsible to provide the kinetic energy to the train. The source of this kinetic energy can be the fossil fuels (e.g., coal and Diesel fuel), the electrical energy or the Hydrogen (converting the chemical energy of the hydrogen to a kinetic energy- Germany launched in September 2018 the world's first hydrogen-powered train). Despite the importance of the locomotives, these units have no capability to carry passengers for several reasons:

- The easier maintenance of a single power vehicle (locomotive);
- Keeping the power source far from the passengers in case of any dangerous situation;
- Replacing the locomotive and not the whole train in case of failure;
- No necessary to change all the train vehicles, even when the locomotives become old.

Table 1.1, Table 1.2 and Table 1.3 present the used locomotives in Portugal in the last 5 decades. The use of electric locomotives has been increased since the electrification of the Portuguese railway network has taken place many decades ago.

Table 1.1. Portuguese railway locomotives in the last 5 decades (part I) [7]. Source: [*Comboios de Portugal*].






Power	Proprieties	Locomotive
Diesel	Class:1151–1186 Entered Service: 1966–1967 Maximum Speed: 58 km/h Power: 187 kW	
Diesel-Electric	Class: 1401–1467 Entered Service: 1967–1969 Maximum Speed: 105 km/h Power: 992 kW	
Diesel-Electric	Class: 1551–1570 Entered Service: 1973 Maximum Speed: 120 km/h Out of service: 2012 Power: 1268 kW	
Diesel-Electric	Class: 1901–1913 Entered Service: 1981 Maximum Speed: 100 km/h Out of service: 2002 Power: 1686 kW	
Diesel-Electric	Class: 1931–1947 Entered Service: 1981 Maximum Speed: 120 km/h Out of service: 2002–2005 Power: 1640 kW	

Table 1.2. Portuguese railway locomotives in the last 5 decades (part II) [7]. Source: [Comboios de Portugal].










Power	Proprieties	Locomotive
Diesel-Electric	Class: 1961–1973 Entered Service: 1979 Maximum Speed: 120 km/h Out of service: 2012 Power: 1655 kW	
Electric	Class: 2501–2515 Entered Service: 1956–1957 Out of service: 2009 Maximum Speed: 120 km/h Power: 2080 kW	
Electric	Class: 2551–2570 Entered Service: 1963–1964 Out of service: 2009 Maximum Speed: 120 km/h Power: 2080 kW	
Electric	Class: 2602–2612 Entered Service: 1974–1975 Out of service: 2012 Maximum Speed: 160 km/h Power: 2870 kW	
Electric	Class: 2621–2629 Entered Service: 1987 Maximum Speed: 160 km/h Power: 2870 kW	
Diesel	Class: 9601–9637 Entered Service: 1976 Out of service: 2002 Maximum Speed: 90 km/h Power: 286 kW	
Diesel	Class: 0451–0469 Entered Service: 1999 Maximum Speed: 120 km/h Power: 544 kW	
Diesel-Electric	Class: 0351–0371 Entered Service: 2000 Maximum Speed: 100 km/h Power: 269 kW	
Electric	Class: 2301–2342 Entered Service: 1992 Maximum Speed: 120 km/h Power: 3100 kW	

Table 1.3. Portuguese railway locomotives in the last 5 decades (part III) [7]. Source: [*Comboios de Portugal*].

Power	Proprieties	Locomotive
Electric	Class: 5601–5630 Entered Service: 1993 Maximum Speed: 220 km/h Power: 5600 kW	
Electric	Class: 2451–2664 Entered Service: 1997 Maximum Speed: 120 km/h	
Electric	Class: 3151–3163, 3255, 3261–3263 Entered Service: 1998 Maximum Speed: 90 km/h Voltage: 1.5 kV DC	
Electric	Class: 3519–3530, 3569–3580 Entered Service: 1999 Maximum Speed: 140 km/h Power: 3475 kW	
Electric	Class: 4001–4010, 4051–4060 Entered Service: 1999 Maximum Speed: 220 km/h Power: 4000 kW	
Electric	Class: 3401–3434, 3451–3484 Entered Service: 2002 Maximum Speed: 140 km/h Power: 1400 kW	
Electric	Class: 2241–2297 Entered Service: 2004 Maximum Speed: 120 km/h Power: 1230 kW	
Electric	Class: 4701–4725 Entered Service: 2009 Maximum Speed: 140 km/h Power: 4684 kW	

1.1.5 Shift2Rail – Achieving a Notable Shift from Road to Rail

This Ph.D. research project belongs to the *Shift2Rail* (S2R) main objectives, namely the innovation program under the smart power supply framework (IP3). Therefore, this item presents an overview

about S2R, which is the first European rail organization aimed to support rail product solutions, carry on the major innovation and creativities for the European railway industry, besides applying some policies in railway sector for a larger share of transport demand in the next few decades. Creating an unified European railway area is one of the European commission objectives to achieve a notable shift from road to rail in terms of freight and passenger transport. This will accomplish a competitive and an effective European transport system. However, rail's share in the European freight and passenger transport is still unsatisfying. Therefore, one of the main S2R tasks is to push forward the European research and innovation projects in a way that helps the rail of playing a broader role in global transportation. S2R also contributes to reduce the life-cycle cost of railway transports by 50%, obtaining twice the existing railway capacity, reducing congestion and CO2 emissions, retaining Europe's leadership in the global rail market and increasing the trustworthiness and the punctuality by 50% [19]. Figure 1.8 shows the S2R members map in Europe with overall 11 participants from Portugal shared between academic institutions and companies as follow [20]:

- Universidade do Minho;
- Universidade do Porto;
- Instituto Superior Técnico de Lisboa;
- Comboios de Portugal (CP);
- Fertagus Travessia do Tejo Transportes SA;
- Infraestruturas de Portugal SA;
- EMEF SA - Empresa de Manutenção de Equipamento Ferroviário SA;
- STRA LDA;
- Thales Portugal SA;
- IP Patrimonio - administracao e gestao imobiliaria SA;
- Evoleo Technologies LDA.



Figure 1.8. *Shift2Rail* members map in Europe (red points) [20]. Source: [*Shift2Rail*].

The S2R joint undertaking is a new public-private corporation in the rail sector, providing a platform to support future innovations. The founding members of S2R joint undertaking are the EU plus eight agents of the rail industry like *Alstom*, *Ansaldo STS*, *Bombardier*, *Construcciones y Auxiliar de Ferrocarriles*, *Siemens* and *Thales*, as well as infrastructure managers like *Network Rail* and *Trafikverket*. The estimated budget of the S2R joint undertaking for the period between 2014-2020 will be at least €920 million. The EU contributes to the budget of €450 million that will come from the *Horizon 2020* program. Other members from the rail industry sector should contribute with at least €470 million to proceed with the main objectives of the S2R joint undertaking [21].

This partnership will keep track of the research and innovation activities in a way to achieve a unified European railway area. These activities include five aspects as follow [22]:

- Cost-efficient and reliable trains, including high-speed trains and high-capacity trains;
- Advanced traffic management and control systems;
- Cost-efficient and reliable high capacity infrastructure;
- Information technology Solutions for Attractive Railway Services;
- Technologies for Sustainable & Attractive European Freight.

1.1.6 Timeframe of the Fastest Trains in the World

Nowadays, high-speed trains are not only considered as a fast transport mode but also as a representation of the companies/operators and the belonging countries. In other words, the actual development level in the railway sector in any country could prove the ongoing rail improvements and the alignment with new technology.

Thirty years ago, the Germans trains were the fastest, but today Germans retreated from the competition in this race [23]. The high-speed trains are classified according to the maximum operating speed. The 1st generation of the high-speed trains could reach a maximum speed of 250 km/h. The 2nd generation of high-speed trains was designed at an operational speed between 300 km/h and 350 km/h. The last 3rd generation of the high-speed trains nowadays can reach a maximum speed of 500 km/h. In this context, Japan has spent around three decades in the 1st generation and 16 years in the 2nd generation. France has spent 20 years and 10 years, while Germany has spent 12 years and 8 years for the 1st and the 2nd generation of the high-speed trains respectively [23]. The German high-speed train *InterCity-Express* (ICE) as shown in Figure 1.9 was the fastest train in the world 30 years ago, reaching a speed of 406.9 km/h in 1988 and has a power higher than 11,000 hp / 8.2 MW. At present, there are many trains that have exceeded this speed [24].



Figure 1.9. The ICE high-speed German train [25]. Source: [<https://www.westtours.de>].

In 1980, the first experimental line of the Magnetic Levitation Train (*Transrapid*) was constructed in the district of Emsland in Germany. This train can reach a speed of 450 km/h. Billions of Euros were spent on the development of this train. However, the experimental line stopped in 2006 after a tragic accident (twenty-three people lost their lives, while several were injured) [26]. The *Transrapid* German magnetic levitation train is shown in Figure 1.10.



Figure 1.10. The *Transrapid* German magnetic levitation train [27]. Source: [<https://www.hochgeschwindigkeitszuege.com>].

Only two years later, France broke the ICE maximum speed and they designed a version of the TGV (*train à grande Vitesse*) train at a speed of 515 km/h. The new models of the TGV can reach a speed of 574 km/h. Figure 1.11 shows three different generations of the TGV train. The 1st, 2nd and the 3rd generation of *SNCF* high-speed trains entered to the service in 1981, 1989 and 1995 respectively [28].

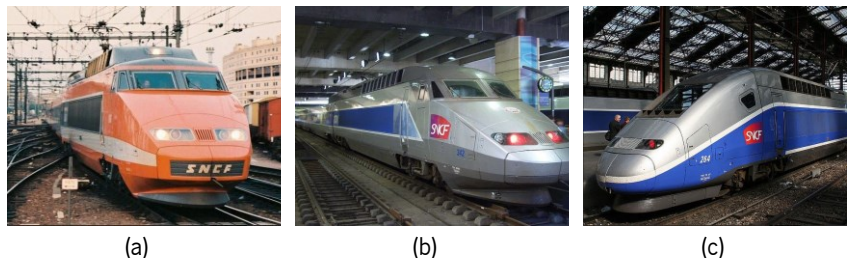


Figure 1.11. TGV French high-speed trains: (a) 1st TGV generation (TGV *Sud-Est*); (b) 2nd TGV generation (TGV *Atlantique*); (c) 3rd TGV generation (TGV *Duplex*) [28]. Source: [<https://socialcompare.com/en/comparison/high-speed-trains>].

Although China has started to evolve the high-speed railway industry not long ago, namely in 2007, the evolution process in the Chinese high-speed railway sector is very prominent [23]. Chinese railways needed only five years in order to reach the world-class level of high-speed railway technology. Some

Chinese trains have reached a speed of 500 km/h. For instance, the new Chinese "*Fuxing Hao*" train, that is shown in Figure 1.12, covers the distance between *Shanghai* and *Beijing* cities (1318 km) by 3.5 hours at a speed of up to 400 km/h [29]. Besides that, it is noteworthy to mention that nowadays, China has the most intense high-speed railway network in the world with a total length of around 25000 km [30].



Figure 1.12. *Fuxing Hao* Chinese high-speed train [31]. Source: [<https://www.scmp.com>].

In China, the development of the magnetic levitation train has been continued. The magnetic train connects *Shanghai* city with its airport. The estimated distance of this journey is 30.5 km and it can be accomplished in just eight minutes. It is the fastest commercial train in the world at present, and the train speed can reach to 430 km/h [32]. *Shanghai* Chinese magnetic levitation train is shown in Figure 1.13.



Figure 1.13. *Shanghai* Chinese magnetic levitation train [33]. Source: [<http://www.digitaljournal.com/image/188575>].

Spain has the longest high-speed railway network in Europe with a total length of 3240 km and the second longest in the world after China. The AVE (*Alta Velocidad Española*) or the "bird" train network as shown in Figure 1.14 links different Spanish cities with the capital city of *Madrid* and Barcelona the center of Spain economy. The maximum speed of AVE can reach up to 310 km/h [34]. On the other hand, the rail line from Madrid to Barcelona and onward to the French border is the longest high-speed line in Europe and the fifth-longest high-speed line in the world, with a total of 804 km. The first connection between the Spanish AVE and the French TGV high-speed trains opened in 2009 [35].



Figure 1.14. AVE train in *Atocha* train station, in *Madrid* [36]. Source: [<https://www.abc.es>].

Japan was the first country in the world to manufacture high-speed trains with a speed of more than 300 km/h. The *Shinkansen* network of high-speed railway lines was primarily built to link the Japanese regions with *Tokyo*. For instance, *Tohoku Shinkansen* train line is able to reach a speed of 320 km/h. The train shown in Figure 1.15 is the E5 series of *Shinkansen* train. It has a long forefront like a nose that extends 15 meters to the front, so the train can reduce the acoustic shock and its high-speed does not cause high noise levels inside the tunnels [37].



Figure 1.15. E5 series of *Shinkansen* Japanese high-speed train [37]. Source: [<https://www.railway-technology.com>].

Japan aspires to develop the world's fastest Maglev train, which is scheduled to begin in 2027 and connect the cities of *Tokyo* and *Nagoya*. The Maglev will rise up for about 10 centimeters above the rail and it will pass the distance between the two cities in 40 minutes instead of 90 minutes via the *Shinkansen* Expressway [38].



Figure 1.16. *Chuo Shinkansen* Japanese Maglev train (still under construction) [39]. Source: [<https://www.theguardian.com>].

Special importance was given to the new concepts of emerging locomotives. In this context, Table 1.4 shows the 10 fastest locomotives to be commercialized in the near future.

Table 1.4. Future trends on high-speed locomotives [40].

Locomotive (Country, Manufacture)	Start Service (Year)	Maximum Speed	Power (kW)
Hemu-430x (South Korean, Hyundai Rotem)	2015	430 km/h	8200
CRH3X (China, <i>CRRC Tangshan</i>)	2020	350 km/h	1017–2034
Talgo Avril (Spain, <i>Talgo</i>)	2020	365 km/h	8800–10000
Avelia Liberty (USA, <i>Alstom</i>)	2021	350 km/h	–
CRRC Maglev (China, <i>CRRC Qingdao Sifang</i>)	2021	600 km/h	24000
Avelia horizon (France, <i>Alstom</i>)	2023	350 km/h	8000
Velaro novo (Germany, <i>Siemens</i>)	2023	360 km/h	8000
LO series Maglev (Japan, <i>Mitsubishi Industries</i>)	2027	603 km/h	–
Alfa-x e956 <i>Shinkansen</i> (Japan, <i>Hitachi</i>)	2030	400 km/h	–
Hyperloop (USA, <i>Hyperloop-one</i>)	2030	1200 km/h	21000

1.2 Thesis Main Motivations

Although there is a great amount of research in the area of power quality and power filters to compensate for power quality problems in electrified railway systems, the use of power quality compensators in this area can be further expanded. On the other hand, in the Department of Industrial Electronics of the University of Minho, several works related to the power quality improvement have been carried out [41], [42]. However, none of the works developed have been orientated for the purpose of power quality improvement in the electrified railway systems. Taking this framework into account, this Ph.D. thesis intends to develop a reduced-scale Power Electronics converter, for power quality improvement in electrified railway systems, and so its main motivations are:

- To study the power quality phenomena in electrified railway systems.
- To fill the gaps that exist in terms of research of active power conditioners in electrified railway systems.
- To present the methods that have been used to overcome power quality problems in electrified railway systems.
- To find alternative solutions for power quality improvement in electrified railway systems, including the Flexible AC Transmission Systems (FACTS), based on Power Electronics technology.
- To use multidisciplinary technology, including hardware and software development.

1.3 Thesis Main Contributions

The main objective of this Ph.D. thesis is to carry out the research work that results from the original contributions in the area of the electrified railway systems, namely through the development of a Rail

Power Conditioner (RPC) based on a Modular Multilevel Converter (MMC). Thus, the main contributions are:

- To assess and compare the performance of different RPC topologies by developing simulation models to overcome the power quality deterioration.
- To study and focusing on the simplified RPC topology based on a half-bridge indirect MMC, including the control algorithms, the simulation model and the parameters design for a laboratory workbench.
- To Validate and implementing an MMC half-bridge submodule, considering protection circuit, driver circuit and power circuit boards.
- To implement a laboratory reduced-scale workbench of the simplified RPC based on a half-bridge indirect MMC to overcome the power quality problems, such as the current harmonics and the negative sequence components (NSCs) of currents.
- To show the main advantages and characteristics of the implemented reduced-scale prototype. The validation of this prototype helps to predict the RPC performance under high-voltage application.

1.4 Thesis Organization

Along this Ph.D. thesis, several strategies were taken in order to ensure that the indicated contributions were successfully achieved. In addition, the covered subjects were simply transmitted. For this purpose, illustrations were used to clarify ideas and to simplify the concepts. The developed work in this thesis was organized in seven chapters as follows:

In Chapter 1, Introduction, the main framework of this thesis is presented to give a brief overview of the electrified railway sector in Portugal, including the motivations and the main contributions that led to the development of the proposed solution. This chapter finishes by presenting thesis main structure showing its chapter organization.

In Chapter 2, named Power Quality phenomena in Electrified Railway Systems, the main parameters that cause the power quality deterioration in electrified railway systems are presented, giving also an overview about the hazards and the impacts of these parameters on both the public power system (PPS) and the traction power system (TPS). This chapter has been completed after presenting the traditional methods to improve the power quality. These methods were mainly based on passive compensators.

In Chapter 3, named Active Power Compensators in Electrified Railway Systems, power quality compensation technology in electrified railway systems based on Power Electronics converters (FACTS devices) are presented. In other words, these methods were mainly based on active compensators. The chapter contained different illustrations and explanations to show the difference between the active power compensators when they are designed to suit the railway application. The focusing was also on the MMC explanation to meet the main aims and contributions of this thesis. This chapter has been accomplished after giving an overview of the RPC to prepare the reader for the next chapter which discusses the RPC technology in detail.

In Chapter 4, named Rail Power Conditioners in in Electrified Railway Systems, different RPC topologies are presented, including the simulation results and the control algorithm for each topology. In addition, a detailed comparative study is accomplished in this chapter to demonstrate the RPC performance when a V/V transformer or a Scott transformer are used to interface between the TPS and the PPS. The RPC based on MMC, which is the main contribution of this thesis, is explained by using mathematical equations and simulation models. The chapter is completed after concluding a comparative table between the presented RPC topologies along the chapter.

In Chapter 5, named Implementation of a Simplified Rail Power Conditioner Based on Modular Multilevel Converter, the different components and subsystems of the implemented laboratory workbench are presented. For instance, the control system design to drive the switching devices and to calculate the reference signals, the protection system design both in hardware and software protection and the power system including the implementation of the V/V power transformer and the load sections. In addition, the developed MMC and the design of SM are presented in this chapter. The aforementioned subsystems are used together in order to build the final RPC based on MMC, which declared as the main contribution for this Ph.D. thesis. All the developed printed circuit boards (PCBs) during this period of doctoral study will be clarified along this chapter.

In Chapter 6, named Experimental Results of a Simplified Rail Power Conditioner Based on Modular Multilevel Converter, the experimental results are presented before and after applying the compensation in order to show the effectiveness of the proposed solution. The DC-link voltage waveforms of MMC SMs are also presented to validate the proposed control strategy that ensured the voltage balancing between all MMC SMs. Additional experimental results are presented along this chapter to confirm the efficiency and the reliability of the designed hardware protection for each MMC SM.

Finally, in Chapter 7, named Conclusion, the main conclusions are presented according to the performed work throughout this Ph.D. thesis, bearing in mind, the suggestions for future work.

1.5 List of Publications

In this item, the publications that have resulted directly from this Ph.D. thesis are presented, namely, publications in international journals, book chapters and indexed international conferences.

1.5.1 Publications in International Journals

1. **M. Tanta**, G. Pinto, V. Monteiro, A. P. Martins, A. S. Carvalho, and Joao. L. Afonso, “Deadbeat Predictive Current Control for Circulating Currents Reduction in a Modular Multilevel Converter Based Rail Power Conditioner”, *Appl. Sci.* 2020, 10, 1849. DOI: 10.3390/app10051849.
2. **M. Tanta**, G. Pinto, V. Monteiro, A. P. Martins, A. S. Carvalho, and Joao. L. Afonso, “Topologies and Operation Modes of Rail Power Conditioners in AC Traction Grids: Review and Comprehensive Comparison”, *Energies.* 2020, 13, 2151. DOI: 10.3390/en13092151.

1.5.2 Publications in Book Chapters

1. **M. Tanta**, J. A. Afonso, A. P. Martins, A. S. Carvalho, and Joao. L. Afonso, “Comprehensive Study for a Rail Power Conditioner Based on a Single–Phase Full–Bridge Back–to–Back Indirect Modular Multilevel Converter,” in *Transactions on Engineering Technologies*, 2019, pp.263-279.

1.5.3 Publications in International Conferences

1. **M. Tanta**, J. A. Afonso, A. P. Martins, A. S. Carvalho, and Joao. L. Afonso, “Rail Power Conditioner Based on Indirect AC/DC/AC Modular Multilevel Converter Using a Three-phase V/V Power Transformer,” in *Lecture Notes in Engineering and Computer Science: Proceeding of the World Congress on Engineering, 5-7 July 2017*, London, UK, pp.289–294.
2. **M. Tanta**, V. Monteiro, J. G. Pinto, A. P. Martins, A. S. Carvalho, and Joao. L. Afonso, “Efficiency and Cost Estimation for a Static Frequency Converter and a Rail Power Conditioner Based on an Indirect Modular Multilevel Converter in Railways Applications,” in *ICEE International Conference on Energy and Environment: Bringing Together Engineering and Economics*, Porto, Portugal, 2017, pp.313–319.
3. **M. Tanta**, V. Monteiro, B. Exposto, J. G. Pinto, A. P. Martins, A. S. Carvalho, and Joao. L. Afonso, “Simplified Rail Power Conditioner Based on a Half-Bridge Indirect AC/DC/AC Modular Multilevel Converter and a V/V Power Transformer,” in *IECON 2017 - 43rd Annual Conference*

- of the *IEEE Industrial Electronics Society*, 2017, pp.6431–6436.
DOI: 10.1109/IECON.2017.8217120.
4. J. G. Pinto, **M. Tanta**, V. Monteiro, L. A. M. Barros, and Joao. L. Afonso, “Active Power Conditioner Based on a Voltage Source Converter for Harmonics and Negative Sequence Components Compensation in Electrified Railway Systems,” presented at the Transport Research Arena TRA 2018, Vienna, Austria, 2018, pp.1–10. DOI: 10.5281/zenodo.1491309.
 5. **M. Tanta**, G. Pinto, V. Monteiro, A. P. Martins, A. S. Carvalho, and Joao. L. Afonso, “A Comprehensive Comparison of Rail Power Conditioners Based on Two-level Converters and a V/V Power Transformer in Railway Traction Power Systems,” presented at the Transport Research Arena 2018, Vienna, Austria, 2018. DOI: 10.5281/zenodo.1483284.
 6. **M. Tanta**, V. Monteiro, T. J. C. Sousa, A. P. Martins, A. S. Carvalho, and Joao. L. Afonso, “Power quality Phenomena in Electrified Railways: Conventional and New Trends in Power Quality Improvement toward Public Power Systems,” in *2018 International Young Engineers Forum (YEF-ECE)*, 2018, pp.25–30. DOI: 10.1109/YEF-ECE.2018.8368934.
 7. **M. Tanta**, G. Pinto, V. Monteiro, A. P. Martins, A. S. Carvalho, and Joao. L. Afonso, “Cost Estimation of Rail Power Conditioner Topologies based on Indirect Modular Multilevel Converter in V/V and Scott Power Transformers,” presented at the 4th International Conference on Energy and Environment: bringing together Engineering and Economics, Guimarães, Portugal, 2019, pp.365–370.
 8. **M. Tanta**, J. Cunha, V. Monteiro, A. P. Martins, A. S. Carvalho, and Joao. L. Afonso, “A Novel Hardware Protection Scheme for a Modular Multilevel Converter Half-Bridge Submodule,” in *IECON 2019 - 45th Annual Conference of the IEEE Industrial Electronics Society*, 2019, vol. 1, pp.6043–6048. DOI: 10.1109/IECON.2019.8927361.
 9. L. A. M. Barros, **M. Tanta**, A. P. Martins, Joao. L. Afonso, and J. G. Pinto, “STATCOM Evaluation in Electrified Railway Using V/V and Scott Power Transformers,” in *Sustainable Energy for Smart Cities*, Cham, 2020, pp. 18–32, DOI: 10.1007/978-3-030-45694-8_2.
 10. L. A. M. Barros, **M. Tanta**, A. P. Martins, Joao. L. Afonso, and G. Pinto, “Opportunities and Challenges of Power Electronics Systems in Future Railway Electrification,” presented at the IEEE CPE - POWERENG 2020, Setúbal-Portugal, 8-10 July, pp. 1–6 (Submitted).
 11. **M. Tanta**, L. A. M. Barros, G. Pinto, A. P. Martins, A. S. Carvalho, and Joao. L. Afonso, “Modular Multilevel Converter in Electrified Railway Systems: Applications of Rail Static Frequency Converters and Rail Power Conditioners” in *2020 International Young Engineers Forum (YEF-ECE)*, 2020, Caparica-Portugal, 3 July, pp. 1–6 (Accepted for publication).

Chapter 2

Power Quality Phenomena in Electrified Railway Systems

2.1 Introduction

Railway electrification has been set out in the early 20th century. It was undertaken in many countries because of its advantages, such as the reduced air pollution, the higher efficiency, and the decreased carbon dioxide (CO₂) emissions [43]. Establishing newly electrified railway lines is not seen enthusiastically by the transmission lines operators as they introduce harmonics and negative sequence components (NSCs) of currents, affecting the power quality of the public power system (PPS).

Power quality has become a very important concept of power delivery especially in the second-half of the 1990s. From the early use of railway electrification, the power quality improvement in alternating current (AC) railway electrification was a significant concern for researchers, and many research studies have been devoted to this purpose. Nowadays, most of the high-speed electric locomotives are using the AC power system for a long-distance electrification [44]. The AC traction power system (TPS) is normally a single-phase system connected through power transformers to the three-phase PPS. Electric trains, especially the old ones that use half-controlled rectifiers usually cause significant distortions in voltage and current waveforms on both three-phase PPS and single-phase TPS. However, the power quality improvement on the single-phase TPS was not under interest by researchers since the electrical traction load has a poor power quality by nature [45]. Consequently, most of the power quality improvement studies in AC railway electrification are focusing on the power quality improvement of the three-phase PPS. The typical power quality problems in high-speed electrified railway systems are; currents imbalance, voltage and current harmonics, reactive power and the low-frequency voltage fluctuations, etc. [46]. Furthermore, the non-linear and the dynamic nature of the high-speed electric locomotives make the improvement of such power quality problems a rather difficult work.

In this context, this chapter presents an overview about the power quality phenomena in electrified railway systems, as well as the power quality improvement methods that can be classified based on traditional power supply systems to interface with the electrified railway systems or based on the flexible AC transmission systems (FACTS) [47].

The traditional power supply-based methods have been used since the beginning of railway electrification for the purpose of improving the PPS power quality. However, the experimental results show that, this choice is only useful in the non-dynamic operation of the locomotives. This led the researchers to search for a solution that can improve the power quality under the transient or the dynamic operation of the electric locomotives. The main contribution of this chapter is to present an overview of the power quality phenomena regarding the AC railway electrification, besides the traditional methods used to overcome the power quality deterioration on the PPS side. This chapter also gives an idea about the hazards resulting from power quality deterioration and it ends with the main conclusion.

2.2 Power Quality in AC Railway Electrification

Railway operators have an absolute interest to run the electrified trains with the lowest possible costs. In this context, power quality improvement is important to guarantee reliability and avoid costly downtime. The traction load is considered as a non-linear load and it is varying dynamically, then voltage arcs may occur because of the pantograph/catenary connection. Harmonics are produced due to the old converter equipment (half-controlled bridges) in the electric locomotives and they have an adverse effect on the three-phase PPS side. On the other side, and since the TPS is a single-phase system connected through power transformers to the three-phase PPS, currents imbalance may occur, resulting in NSC of currents that highly deteriorate the power quality of the three-phase PPS [47]–[49]. Hereafter, power quality phenomena in AC railway electrification are presented in detail.

2.2.1 System Imbalance

The three-phase PPS is considered balanced as long as the three-phase voltage and current waveforms are sinusoidal and have an equal amplitude with a 120° phase shift. However, if these conditions are not met, the system is called imbalanced. In AC railway electrification, the voltage imbalance resulting from a non-linear asymmetrical load is inversely proportional to the PPS short circuit power [50]. Normally, the three-phase PPS with nominal voltage values higher than 110 kV has a high short circuit power (it has a low busbar impedance) and great enough to directly connect the single-side feeding TPS to the PPS [43]. On the other hand, when the primary windings of the traction substation are connected to a voltage level higher than 110 kV, the voltage imbalance issue has less priority to be solved. Also because at extra-high-voltage (EHV) level (higher than 150 kV: e.g., 220 kV, 400 kV), the allowed voltage variation according to the European standard EN-50160:1999 (Voltage characteristics of electricity supplied by public distribution systems) is between $\pm 5\%$, whereas, at a high-voltage (HV) level (between 35 kV and 150 kV), the allowed voltage variation according to the same European

standard is between $\pm 10\%$ [51], [52]. As a result, and in most of the cases, the system imbalance in AC railway electrification mainly refers to the NSC of currents injected into the PPS.

The three-phase currents imbalance will definitely result in three-phase voltage imbalance. In other words, the NSC of currents will produce NSC of voltages as well [45]. The traction motors in the electric locomotives are normally designed to operate appropriately at a reduced voltage amplitude by 24% or at amplitudes 10% higher than the nominal voltage amplitude of the electric locomotives drives based on the IEC-60850 and the EN-50163 [45]. Hence, the power quality deterioration-based currents imbalance has more priority to be solved than the voltage problems in railway electrification. Moreover, using the V/V power transformer to feed a complete line being fed from the same PPS, the voltage imbalance can be reduced in total for all substations. Voltage imbalance is generally measured during 10-period intervals for 50 Hz AC systems (After mitigating the effect of harmonics) according to IEC 61000-4-30 electromagnetic compatibility, testing and measurement techniques, power quality measurement methods.

Currents imbalance is the most serious problem that affects the power quality of the PPS. The imbalance is clearer as long as a huge single-phase load is connected to the PPS, which in electrified railway case, several single-phase electric locomotives consume a huge amount of power estimated by MW. A single-phase load is normally causing the NSC of currents, if they are not compensated, they may cause power perturbation, as well as increasing the operating costs of the electrified trains. An imbalance ratio is usually used to evaluate the potential risks that could appear in the imbalanced system. A higher imbalance ratio indicates a big difference between the three-phase PPS currents and higher NSC of currents injected into the PPS [43]. When the imbalance ratio is close to one, the NSC of currents will have the same magnitude as the positive sequence components (PSCs) but they rotate in a direction opposite to the PSCs. A related point to consider is the zero sequence components of currents have no value in the electrified railway systems as long as the traction power transformers do not have the fourth wire [45].

The European standard EN-50160 describes the main principal characteristics at the point of power delivery to the client under normal operating conditions. The standard refers to characteristics of the three-phase supplied voltage, which states the following regulation for the clients at HV and EHV levels. For a period of one week, 95% of the voltage NSCs effective values, that are obtained for 10 minutes, should not exceed 2% of the corresponding voltage PSCs. In certain regions, the allowed voltage imbalance ratio can reach up to 3% [51] (such as the isolated islands). On the other hand, the European standard EN-50163 specifies the main characteristics of the supply voltages of the TPS side. Under

normal operating conditions, for 25 kV nominal catenary voltage, the voltage value (at the catenary) should always be between 19 kV and 27.5 kV and can reach the minimum of 17.5 kV or the maximum of 29 kV during 2 minutes at most [53].

2.2.2 Harmonic Distortion

Electric locomotives normally use power converters to drive the traction motors. These converters, especially the half-controlled ones, may cause harmonic contents flowing into the three-phase PPS [54]. There will be a series of harmonic orders (load current mainly contains all odd harmonics) that have the double, third, fourth, etc., the fundamental frequency. Among the most critical are the 3rd order harmonic contents that have three-times the fundamental frequency value. The 3rd order harmonics are generated when non-linear loads are under operation [43] (e.g., electric locomotives). Consequently, in order to evaluate the harmonic contents in the PPS, equation (2.1) helps to calculate the total harmonic distortion (THD) in a waveform, and is defined as a percentage ratio between the amplitude of the non-fundamental frequency harmonic contents ($h_2, h_3, h_4, \text{etc.,}$) to the amplitude of the fundamental frequency harmonics (h_1).

$$\text{THD(\%)} = 100 \times \sqrt{\frac{h_2^2 + h_3^2 + h_4^2 + \dots + h_n^2}{h_1^2}} \quad (2.1)$$

Harmonic contents are also remaining in the DC railway electrification, in which some of the urban train locomotives contain some Power Electronics devices, namely, the 12 pulse rectifier that generates a large amount of the 11th and 13th harmonic contents [45]. Harmonic contents are considered as one of the main origins for power quality deterioration in railway electrification. Harmonics suppression could be either by installing passive filters at the load side of each feeder station or by using FACTS devices that are more expensive and more effective for the purpose of harmonics cancellation [43].

On the other hand, the power system may have harmonic resonance frequency because of the interaction between the transmission lines inductance and the distributed capacitances along the power transmission lines. However, a related point to consider is the harmonics problem can be worsened when the harmonic resonance may occur once the harmonic contents injected by the TPS match one or more of the power system natural frequencies (the natural frequency signifies a frequency value at which the electric power system tends to oscillate) [43], [55]. In such situations, the THD value will increase to reach a high level. In other words, the waveforms are being forced to oscillate at the natural frequency and harmonic resonance will happen accompanied by large amplitude oscillations. This scenario must be avoided since it may cause the total collapse of the power devices,

especially on the TPS side, besides the other serious impacts on both PPS and TPS, e.g., power perturbation, power distortion, wrong actuation of the protection relays [55].

According to the standard EN-50160 and under normal operating conditions, for each period of one week, 95% of the obtained voltage values during 10 minutes for each harmonic content should not exceed the values given in the Table 2.1 [51]. As a consequence of the harmonic resonance, higher voltage harmonics may occur, but the THD of the PPS (including the harmonics up to the 40th order) must not exceed 8% at medium-voltage (MV) or HV levels, and 4% at the EHV level [51], [52].

Table 2.1. Voltage harmonics at the point of power delivery, expressed as a percentage of the nominal voltage amplitude U_c ($1 \text{ kV} \leq \text{MV} \leq 36 \text{ kV}$, $36 \text{ kV} \leq \text{HV} \leq 150 \text{ kV}$, $150 \text{ kV} \leq \text{EHV} \leq 400 \text{ kV}$).

Odd Harmonics								Even Harmonics			
Not multiplied by 3				Multiplied by 3							
Harmonic order	Related Voltage %			Harmonic order	Related Voltage %			Harmonic order	Related Voltage %		
	MV	HV	EHV		MV	HV	EHV		MV	HV	EHV
5	6	5	3	3	5*	3*	1	2	2	1.9	1.5
7	5	4	2	9	1.5	1.3	1	4	1	1	1
11	3.5	3	1.5	15	0.5	0.5	0.3	6	0.5	0.5	0.5
13	3	2.5	1.5	21	0.5	0.5	0.2	8	0.5	0.5	0.4
17	2	–**	1	>21	–		0.2	10	0.5	0.5	0.4
19	1.5	–**	1					12	0.5	0.5	0.2
23	1.5	–**	0.7					>12	0.5	0.5	0.2
25	1.5	–**	0.7								

* According to the grid conception, this value of 3rd order harmonic can be much lower.
** These harmonic orders should be in consideration according to the EN-50160 European norm.
Note 1: Harmonic values higher than 25 orders are not indicated in the table due to their small amplitude.
Note 2: THD in percentage, calculated in accordance with EN-50160, should not exceed 4% at the EHV level.

Nowadays, the traction motors are using Power Electronics converters based on the insulated-gate bipolar transistor (IGBT) technology instead of Thyristors. The IGBT can operate at a higher switching frequency (faster commutation), in which a lower amount of harmonics can be injected. On the other hand, silicon carbide (SiC) switches have shown an increase over the last years due to some advantages, e.g., lower power losses, size reduction, improved reliability and switching frequency range. According to *Infineon LDA*, in the next few years, SiC solutions will expand into new applications such as industrial or traction drives. This will result in lower harmonic contents since the SiC semiconductors are prepared to operate at hundreds or thousands of kHz. Using the SiC semiconductors in a multilevel converter topology allows to reach a higher amount of power, then, this innovative solution can be the future but still expensive.

2.2.3 Reactive Power

Reactive power is the part of the complex power that cannot be dissipated in a purely reactive or active loads. This power is alternatively absorbed from and returned to the source. The power factor is normally used to estimate the reactive power amount of the electrical system. A low power factor signifies a large amount of reactive power. However, this power cannot be consumed by the active power components of traction loads, and it should be reduced as possible for lower operating costs of the electrified trains [48].

Power Converters with power factor correction feature that imposing sinusoidal grid currents are nowadays substituting the diode and multi-pulse rectifiers [56], then, modern AC Power Electronics converters of traction motors use the pulse width modulation (PWM) technique, which generates zero reactive power with a unitary power factor since PQ control can be employed [45]. Regarding the TPS side, reactive power is required in order to compensate the NSC of currents, hence, a contradiction between NSCs compensation and the reactive power compensation may occur [57]. Therefore, the NSCs in the single-phase TPS must be in antiphase with the three-phase voltages/currents of the three-phase PPS to eliminate reactive power [45]. As a result, the reactive power compensation, as well as the NSCs compensation should be performed together.

Regarding the compatibility of rolling stocks with the infrastructure, there are some requirements about the power factor of electrified trains. For instance, the power factor of trains should be higher than 0.95 for locomotives having instantaneous power at the pantograph higher than 2 MW. As for those with power below 2 MW, their power factor should be higher than 0.85 over a complete timetable journey. These values are calculated on the basis of the fundamental frequency component only and determined in the standard of EN-50388 [58].

FACTS can be used for the purpose of reactive power compensation. For instance, static VAR compensator (SVC) can be installed into two load sections of the traction substation to improve the power factor and to overcome the NSC of currents [59]. In that case, SVC may increase the total reactive power in the traction substation when it is designed to compensate the NSCs, because there is a trade-off between the power factor correction or the reactive power compensation and the NSCs compensation when using the SVC in traction system [57], [60]. Rail power conditioner (RPC) system consisting in two back-to-back single-phase converters, that can shift active power from one load section to other and send out (or absorb) reactive power to (from) the load sections and, at the same time, achieving NSC compensation. A static synchronous compensator (STATCOM) based a three-phase three-wire AC/DC converter is normally installed at the three-phase PPS side to compensate both of

reactive power and NSC of currents. The three-phase three-wire converter only contains six switching devices, so it saves two switching devices compared with the RPC topology containing eight switching devices [60].

2.2.4 Low-Frequency Voltage Fluctuations

The low-frequency voltage fluctuations indicate the presence of voltages with a low-frequency less than 10 Hz for the 50 Hz railway TPS [43] and less than 5 Hz for the 16.7 Hz railway TPS [61]. In some cases, these fluctuations could trigger the locomotives protection relays, causing an overhead line power-off. This phenomenon affects the power quality of the TPS, as well as the safe operation of the electric locomotives [62]. It is hard to know the direct reason of the low-frequency voltage fluctuations, where this topic still did not get enough attention by the researchers. However, the fluctuation, in fact, could appear as a complicated locomotive-grid interaction problem [62], [63]. These voltage fluctuations can be induced either by impedance variation or by multiple active locomotives in one feeding section [61]. The fluctuations have been worldwide noted in a variety of AC locomotives and at different operating conditions. According to the published literature, this phenomenon, was first noted in a Norwegian railway, where the rotary converters were used in the TPS substations. The fluctuations have been noticed later in Germany, Switzerland, France, China and the USA. Among the aforementioned countries, the problem in France and China occurred for the same reasons, where many electric locomotives in railway stations were under a standstill state with only the auxiliary load powered by the DC-link of AC/DC/AC converters [63]. Another study has been performed on a traction substation in China that suffered from extremely low-frequency voltage fluctuations [62]. Researchers concluded that the fluctuations are caused by the current collectors of the electric Chinese HXD2B locomotives.

2.2.5 Voltage Arcing

Voltage arcing is an unavoidable problem in railway electrification and it is more predominant in high-speed trains [64]. This phenomenon defines electromagnetic interference with a wide frequency spectrum up to several GHz, so it can be induced at wide range of frequencies (kHz to GHz). It occurs as a result of the interaction between the pantograph and the overhead catenary line or between brushes and the third or the fourth rail. Consequently, these arcs have a paramount importance in the high-speed railway lines where the trains run at a speed of over 300 km/h. Then, they may cause power perturbation and power quality deterioration during specific transient periods [64]. Because of the voltage arcs, a transient current component in the TPS is induced, which may trigger one or more of the protection relays, then power-off the main feeder lines of the electric locomotive. In addition, a

transient magnetic field resulting from the produced current component possibly will perturb the locomotives signaling system. The main reason for the voltage arcing in railway electrification is the varied airgap between the feeder line (overhead line/ third rail) and the current collector (pantograph or brush) due to the train mechanical oscillation [45].

The arcs increase at a subzero temperature, where a skinny ice layer prevents the direct contact between the pantograph and the catenary line. Since the voltage level in the DC railway electrification is lower than the one in AC railway, the produced current is always higher, the arcs are stronger and the electromagnetic radiation is more intense in the DC railway electrification [65]. Therefore, visible and bright arcs moving along the pantograph or along the brushes are well noticed in the DC rails underground metros, especially at acceleration conditions or heavy freight trains, in which the train draws heavy current. In addition, recent studies have proved that arc's average duration is longer at a bigger traction load and the arc's duration could be longer at inductive non-linear loads (e.g. traction loads). On the other hand, since the arc's energy is influenced by the arc's duration, the arc's average duration could be shorter and the arc's energy could be lower as long as the locomotives power factor is close to one [66]. The load power factor correction is one of the effective methods in order to reduce the arcs negative impacts in the electrified railway systems.

2.2.6 Poor Utilization of Supply Network

Normally, there is no solution regarding the poor utilization of the TPS, especially in terms of the long-distance between traction substations. However, the irregular utilization of electric locomotives can be as a result of train accelerating/deceleration. For instance, a train going uphill will consume more power, while a train with a constant speed or going downhill will draw a minimal power [46]. Consequently, electric trains have a low electrical load factor or utilization rate by normal (electrical load factor is defined as the average load divided by the peak load in a specified time period). This highly indicates a varied power consumption along a given time (day, month, year). The recent electric locomotives are equipped with regenerative braking. However, if there are no electric trains ready to consume this amount of power, the regenerated power gets back into the supply PPS and will not be consumed by the electric trains [46]. Using the regenerative braking could help to reduce the operating costs of the electrified trains. However, the old locomotives only have unidirectional energy meters and the energy resulting from the regenerative braking cannot be measured. According to the 2017 European railway performance index, railway intensity of use in Portugal was lower than what it was in other European Union countries in both freight and passenger transport, where the prevailing culture

in Portugal continues in use highways instead of railways, especially in villages away from the major cities [67].

2.3 Hazards of Power Quality Phenomena in AC Railway Electrification

Power quality deterioration in the electrical system may happen when one or more of the phenomena presented in the item 2.2 occur. The effects can vary according to the active power quality phenomenon. For instance, the risk is higher in case of currents imbalance between phases, then, NSCs of currents are injected into the PPS side. The following items explain the potential impacts of power quality deterioration on the upstream electric power system and the train signaling and communication system [45].

2.3.1 Impacts on Electric Power Systems

Since the traction load is a huge single-phase non-linear load connected to the three-phase PPS through a V/V or a Scott power transformer or other transformer type, the NSC of currents injected into the PPS exist by nature. In case of no compensation, the NSC of currents will cause power quality deterioration and they may increase the power losses of the transmission lines. On the other hand, the NSCs also have an adverse impact on the synchronous generators, in which the rotor parts will be overheated, resulting in additional losses and mechanical stress of the generators [68]. Moreover, the NSCs may overheat the power transformer windings, leading to a decrease in the total loading capacity of these transformers [68]. The power converters installed in the electric locomotives are the main responsible for the harmonic contents injected into the PPS. A high ratio of THD will cause additional power losses in the transmission lines, synchronous generators, and the power transformers, followed by additional vibration and noise [43]. Thereafter, a failure or a wrong response of the protection relays may occur, especially at high harmonics level. When a harmonic resonance happens, which is the most serious scenario, the resonance may saturate the measuring transformers cores in the power substation, which will decrease the measurement accuracy [43].

A low power factor indicates a high amount of reactive power in both PPS and the TPS. However, the reactive power is very important for the AC electrical machines, e.g., induction motors and power transformers, due to its root factor for establishing a magnetic field in which energy conversion takes place. On the other hand, reactive power in the power systems supports the voltage that must be controlled for higher reliability. If the reactive power ratio in the power system is more than 10%-20 %, this leads to a reduction in the generators loading capacity and reducing the electrical equipment

efficiency [68], besides the higher costs of electricity generation and the transmission lines. Furthermore, the power transmission lines will suffer from an additional voltage drop. The low-frequency voltage fluctuations and the voltage arcing are able to induce the protection relays in the power system, which could wrongly power-off some power equipment in the substation [68].

2.3.2 Impacts on Signaling and Communication Systems

Communication and signaling system circuits are normally designed to operate at a higher frequency different from the power fundamental frequency (50 Hz) in order to avoid electromagnetic interference [45]. However, if the power system suffers from a high THD ratio, the high-order harmonic frequencies may disturb the communication signals, resulting in incorrect signals and false fault detection that affect the train monitoring system [45]. On the other side, voltage arcs are the main reason for the stray currents. However and since the communication cables usually lie in parallel near the power cables, the stray currents may generate magnetic fields in the communication cables and induce voltages that pollute the main communication signals [45], [68].

2.4 Power Quality Improvements: Traditional-Based Methods

From the early use of railway electrification, several methods have been applied and investigated to overcome the power quality deterioration. In this context, the NSC of currents, besides the harmonics, are the most severe phenomena. With the purpose of power quality improvement, the following techniques have put in service several decades ago, and for the time being, they are still used worldwide in several traction substations. In the following items, a brief description of those techniques is provided, concluding to the state-of-the-art for using the FACTS devices for power quality improvement in railway electrification.

2.4.1 Three-Phase Electric Trains

In the last decades, the three-phase asynchronous motors were commonly used in traction applications due to the missing of brushes and commutators, then, they require less maintenance compared to the series-wound DC motors. At that time, some of the TPS have been created under the three-phase AC power with two current collectors, two catenary lines, and third rail. The main complexity of this system was substantial because of using three conductors which highly increased the total costs. Italy was the major user for the three-phase AC TPS under the frequency of 16.7 Hz and a voltage around 3.6 kV for the mountains lines with the advantage of regenerative braking [45], [49].

Figure 2.1 shows the E330 Italian locomotive with two current collectors (Bow collectors) and the third electrified rail. Since the traction load, in this case, is a three-phase one, the main advantage of this system was the negligible NSC of currents injected into the PPS. However, using a second pantograph and electrifying the rails were the main reason to abandon this approach.



Figure 2.1. E330 three-phase Italian locomotive in the period 1914–1963 [69].
Source: [https://books.google.com/books/about/Italian_Railways.html?id=JFcSAAAAMAAJ].

Nowadays, one of the present three-phase railway systems that is still in use is the Corcovado Rack Railway in Rio de Janeiro, Brazil as shown in Figure 2.2(a). The line's length is 3.8 km and it operates under a three-phase voltage of 800 V, 60 Hz. Another three-phase line that still in use in Europe is the French train of La Rhune in the south of France as shown in Figure 2.2(b). The line's length is almost 4.2 km and it operates under a three-phase voltage of 3 kV, 50 Hz.



(a)



(b)

Figure 2.2. Three-phase locomotives: (a) Corcovado Rack train in Rio de Janeiro [70]; (b) French train of La Rhunein [71].
Sources: (a) [<https://www.wikiwand.com/en/Corcovado>], (b) [<https://www.rhune.com/>].

2.4.2 Phase Shifting Using Adjacent Single-Phase Power Transformers

This method is based on alternate the phases that supply each section of the catenary. The overhead catenary lines are sectionized in electrically isolated parts, where the non-electrified zones are called the neutral sections, and their length should be higher than the spacing between the extreme pantographs (the length varies from 5 to tens of meters). Short neutral sections (or inline neutral sections) are formed by inserting electrically-isolated elements, e.g., glass bead insulator, between lengths of live overhead line, and fitting the catenary overhead line with insulators. Long neutral sections

consist of separate insulated lengths of overhead catenary line in which two or more switches in quick succession overlaps between two normal sections [72].

Figure 2.3 shows the phase shifting method in three single-phase traction substations. The loss of power is the major drawback of this solution, where neutral sections are important to avoid short circuits between phases, then, this method prevents load sharing between the single-phase power transformers. Each zone along the catenary line is a single-phase one and the alternation between phases normally occur at each traction substation.

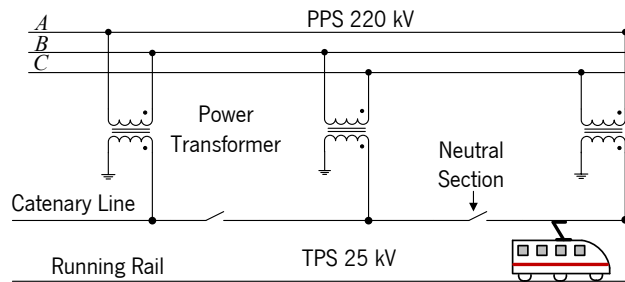


Figure 2.3. Phase shift method to alternate between PPS phases [49].

This is an old method to achieve such a balance between phases. However, it is also the less efficient to eliminate the NSCs effects. When the overhead catenary lines are not equally loaded, the NSCs of currents are relatively reduced but they still remain as a result of the three-phase currents imbalance [45], [49]. The alternation between phases does not totally solve the problem of currents imbalance unless the loads of each electrified section are equal and a balanced power transformer is adopted (e.g., Scott, LeBlanc and Woodbridge) [73], [74].

2.4.3 Three-Phase Balanced Power Transformers

Some special types of the three-phase power transformers are familiar to be used in two-phase power connections and in rail distribution networks. This is due to some technical characteristics that help in power quality improvement, such as the ability to reduce the NSCs and the harmonic contents. Among the most widely used balanced transformers are Scott, Woodbridge, LeBlanc and the impedance matching power transformers. For instance, the Scott connection is used in Japanese *Tokaido-Shinkansen* and the LeBlanc connection is used in Taiwan railway [75]. On the other hand, in Europe, the V/V unbalanced transformer is the mainly used, e.g., in the French TGV and the British rail east coast main line [75]. When using a balanced power transformer, the NSC of currents injected into the PPS are negligible when the electrified sections are equally loaded [76]. Regarding the harmonic distortion, balanced transformers can be an interesting choice, since they lead to some harmonics cancellation due to their special connections [55]. However, and after considering the facts

of complex windings and an unequal number of turns for each phase, these reasons could cause a non-perfect balanced situation even when the load sections are equally loaded [45].

Another factor should be considered when the electric locomotives are passing through the neutral zones. In this case, trains will lose power and velocity. Therefore, the neutral section in such transformers is reflected as the main drawback [55]. Moreover, balanced transformers have some disadvantages in terms of costs and the material (iron and copper) utilization factor. A higher material utilization factor signifies a smaller transformer volume at the same nominal power and lower investment costs for the electric power grid [55]. The material utilization factors of Scott, Le Blanc, Woodbridge and impedance matching power transformers respectively are 81.6%, 84.5%, 82.6% and 91.95%. However, the utilization factor of the unbalance V/V power transformer could reach up to 94% [77]. Further to this, the required voltage insulation level is high for the Scott and LeBlanc power transformers, since there is no neutral point in the primary windings of these transformers [77]. The main difference between Scott and LeBlanc power transformer is the number of cores windings. Dissimilar to Scott transformer, LeBlanc transformer is constructed based on three-legged cores. In addition, the primary windings of LeBlanc transformer are usually delta-connected to suppress the third harmonic current contents injected by the loads [78]. Figure 2.4(a) shows Scott power transformer connections, whereas Figure 2.4(b) presents the LeBlanc power transformer. Woodbridge power transformer requires two additional auto-transformers for the two-phase railway traction power supply [77], [55]. The impedance matching power transformer presented in Figure 2.4(c) is the most used in China for traction applications. This transformer is normally manufactured with a high number of secondary windings that could lead to complicated windings.

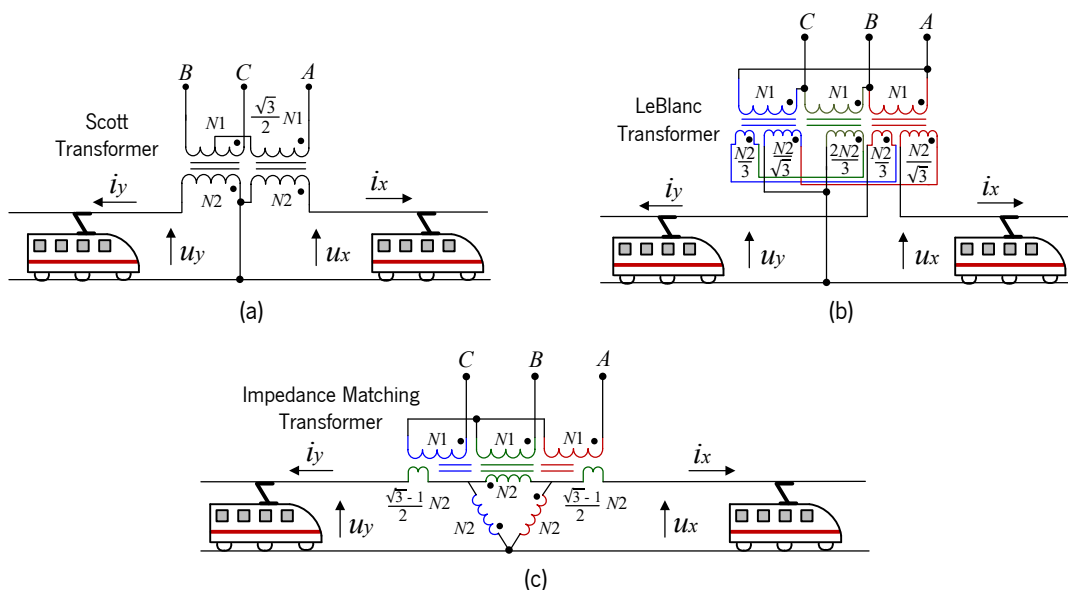


Figure 2.4. Balanced three-phase power transformers used in railway substations: (a) Scott transformer; (b) LeBlanc transformer; (c) Impedance matching transformer.

Table 2.2 presents a brief comparison between the above-mentioned power transformers [77]. The unbalanced V/V power transformer has a high utilization factor of more than 94%. In addition to this, it has a simple structure compared to the balanced power transformers. Therefore, it is widely used for railway applications, particularly for high-speed trains that demand high power consumption.

Table 2.2. Comparison between several types of power transformers used in railway applications [77].

Power transformer	Scott	LeBlanc	Woodbridge	Impedance matching	V/V
Balanced transformer	Yes	Yes	Yes	Yes	No
Auto-transformer need	No	No	Yes	No	No
Utilization factor	81.6%	84.5%	82.6%	91.95%	94%
3 rd Harmonic flow	Yes	No	No	No	Yes
Neutral point	No	No	Yes	Yes	Yes
Complexity	Complex	Complex	Complex	Complex	Simple

2.4.4 Passive Power Filters

The structure of passive power filters is simple containing only passive elements, such as inductors and capacitors. These filters were first used in 1940 to reduce the harmonic contents and reactive power compensation [79]. This was the typically used method for harmonics cancellation and power factor correction in the electrified railway systems. Beyond that, nowadays, these passive power devices are combined with the FACTS devices to reduce the converter power ratings, costs and volume [55], [80].

There are many types of passive power filters, such as resonant and damping filters as shown in Figure 2.5. Resonant filters can be single-tuned, double-tuned or third-tuned ones. In general, resonant filters have the ability to mitigate some of the odd harmonic contents, such as the 5th and the 7th order harmonics, whereas, the damping passive filters have proposed to eliminate higher order harmonics. In resonant passive filters, inductors and capacitors are connected in a way that resonant frequency has almost no impedance. The damping filter type has a low impedance for a wide range of frequency [79]. The electric locomotives power converters produce a variety of harmonic contents that have different frequency orders. As a result, and in order to limit the harmonic distortion to a permissible level, passive filter banks linked in parallel is a practical solution to ensure the full filtering effect. However, this solution may require a large space for installation, besides the higher implementation costs [43]. Another problem related to the change in filter parameters affected by heat or lifetime, which gradually causes misoperations and perturbation in the filter functionality. It is worthy to mention, the compensation system that use passive filters has a poor power factor correction. The

fixed capacitor value in each passive filter cannot totally compensate the reactive power since these devices are not able to follow the load dynamic changes [43]. Therefore and in order to implement a dynamic compensation, FACTS devices put in service since the 1970s [79], especially after the fast evolution in Power Electronics field.

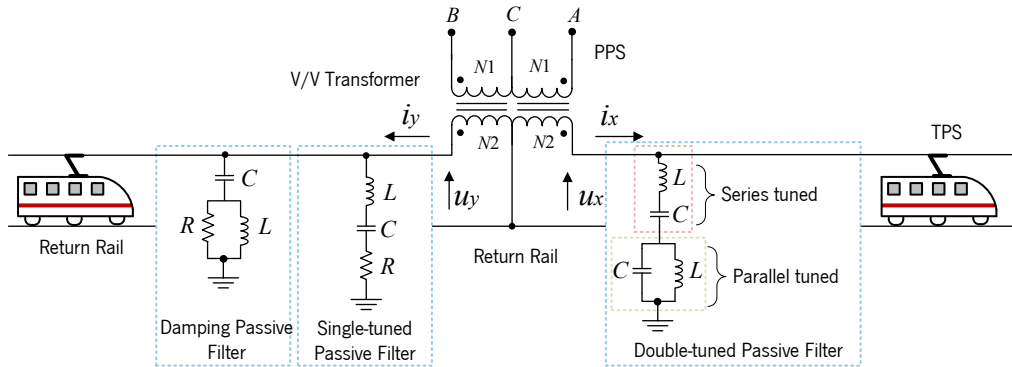


Figure 2.5. Various types of passive filters used in railway electrification.

2.4.5 Steinmetz Compensation Circuit

The Steinmetz compensation circuit indicates one of the power quality solutions when a huge single-phase load (e.g., electric locomotives) is connected to the PPS. This solution is applied to balance the three-phase currents and to compensate reactive power. Figure 2.6 shows the main configuration of the Steinmetz compensation circuit. It is easy to be implemented in practice due to its independent structure and control. This power compensator may contain controlled impedance, both capacitive and inductive, as required. These impedances, connected across the phase voltages of the TPS, draw currents with a NSC that compensates the imbalance of the three-phase currents and the voltage imbalance produced by the locomotive load [81]. Steinmetz compensation circuit is a good solution to balance fixed single-phase loads. However, bearing in mind, if the single-phase load varies over a large range (as the case of electric locomotives), then Steinmetz compensation circuit cannot be an effective solution [82]. In such situations, using Steinmetz compensation circuit equipped with changeable reactive elements (capacitors and inductors) controlled by switching devices sounds a good technique. This solution is known as an active Steinmetz compensator or an SVC, which is presented in chapter 3. On the other hand and since the load in high-speed railway is heavy, the capacitors of the Steinmetz compensation circuit may be too large to achieve full compensation [43].

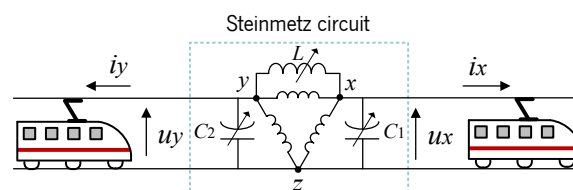


Figure 2.6. The configuration of Steinmetz compensation circuit.

2.5 AC Feeding Methods of Traction Power System

Since the early use of railway electrification, different methods have been adopted to connect the feeding transformers of the overhead catenary lines. Choosing a method is dependent on some fundamental aspects, such as the power transmission capacity as a relation to the line length, besides the generated electromagnetic disturbances near the train's surrounding area. In this context, the next items present the common AC feeding methods of the TPS. The catenaries (overhead lines) are supposed to be used in AC electrification instead of electrifying the rails.

2.5.1 Simple Feeding with a Return Rail

This simple power system transmits the train power through the catenary and the rails. The main drawback of this feeding system is the significant rail-to-earth leakage current due to the unavoidable rail-to-earth impedance [83]. This leakage current is resulting from the difference between the catenary supply line current and the return current through the rails, causing electromagnetic interference with the telecommunication equipment [84]. In addition, the catenary current can induce electromagnetic fields in nearby signal causing interference as well. The leakage current is higher near the locomotive as well as the rail-to-earth voltage value. Reducing the rail-to-earth leakage current is possible by using a return wire connected to the rails at constant intervals as shown in Figure 2.7. This technique helps somewhat to reduce the leakage current [83].

The coupling transformers along the catenary can be connected in single-side feeding or in double-side feeding. The single-side feeding signifies that the neighboring coupling transformers are connected to a different line-to-line voltage, and the electric train draws power from only one traction substation. In this case, a neutral section should be inserted between substations. However, the double-side feeding implies to connect both neighboring coupling transformers to the same line-to-line voltage. In this case, the train draws power from two traction substations, leading to, reducing the required capacities of each individual substation and the voltage drop across the catenary line. However, the double-side feeding is not that common due to the constant current transit between substations [85], [86].

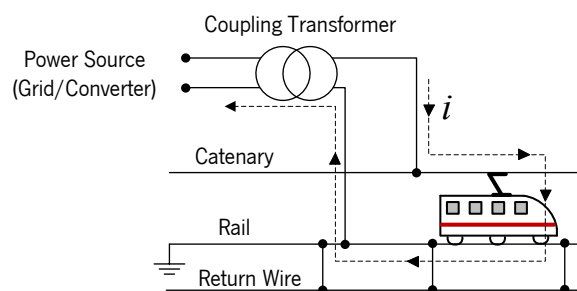


Figure 2.7. Simple direct feeding with a return rail and return wire configuration.

2.5.2 Boost Transformers with a Return Rail

This system contains boost transformers along the catenary line (every 4 km-6 km [87]) to minimize the leakage current to the ground as presented in Figure 2.8. The effects of induction and noise are minimized in this configuration. Boost transformers are used in AC electrified railway systems with overhead catenary lines to collect the return current from the rails to the return wire or to collect the return current from the rail and the earth to the return wire (as in the item 2.5.3.). However, the boost transformers connected in series with the overhead catenary line increase the voltage drop in comparison to the simple direct feeding system with a return rail.

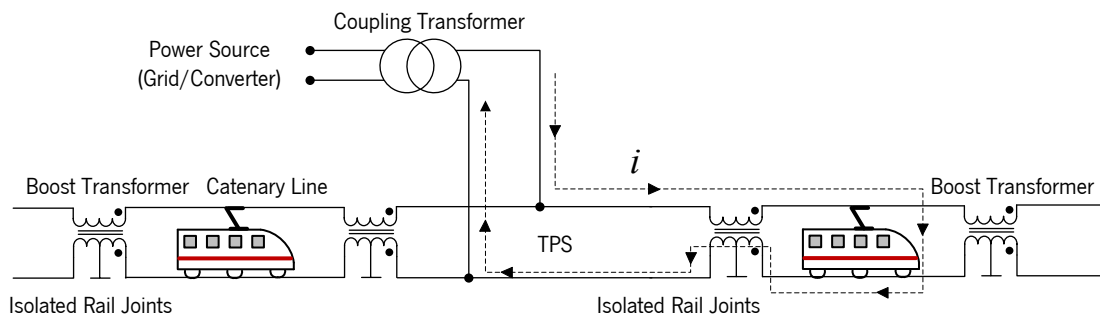


Figure 2.8. Boost transformers with a return rail configuration.

2.5.3 Boost Transformers with a Return Wire

The boost transformers feeding with a return wire provide a way to enforce the return current to flow in the return wire rather than the rails. However, this method has poor voltage regulation as a result of additional boost transformers impedances [83]. In some countries, these types of configuration were necessary to be used due to the high ground resistance of different soils. Therefore, Swedish and Norwegian catenary systems have introduced the Boost transformers in railway electrification [87]. In this scenario as in Figure 2.9, the return current flows to the rail only in partial sections.

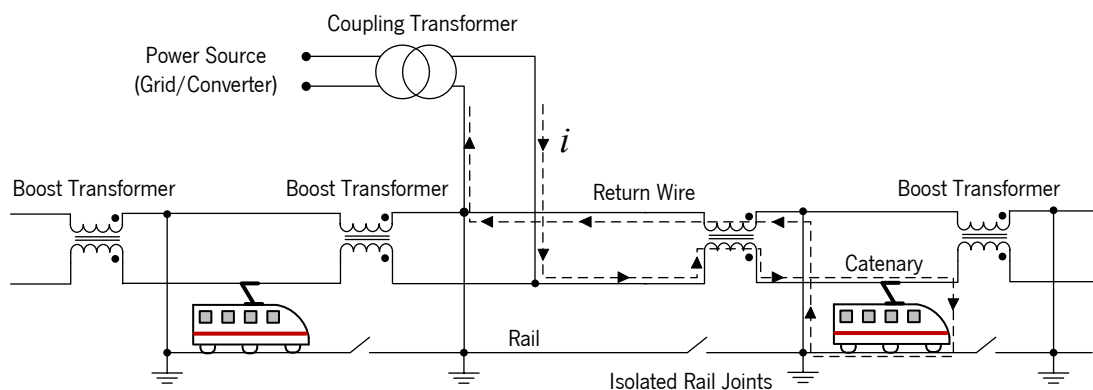


Figure 2.9. Boost transformers with a return wire configuration.

Since the catenary and the return wire are much closer to each other, the induction effects are quite smaller than what they are in the previous cases. In other configurations, series capacitors can be

added to the return wire to reduce the voltage drop along the line and to decrease the arcs generated when the locomotive passes the boost transformer section [9].

2.5.4 Auto-Transformers System

Auto-transformers are designed to obtain voltage balancing, while the boost transformers operate by balancing the currents on the primary and the secondary windings [83]. The interference suppression, besides the improved system efficiency, are the main advantages of using the auto-transformer system. This system has a feeder called a negative feeder so that from the substation connected between the feeder and the catenary line there is a voltage twice the voltage between catenary and rail. The doubling of the voltage is created by a 180 degrees phase shift. This configuration allows transmitting the power at the voltage twice of the operating voltage (25 kV or 15 kV).

Auto-transformers maintain better voltage regulation and a longer interval allowance between transformers around 10–12 km [9], [83]. As known, at a constant power value, a higher voltage leads to smaller currents, then, reducing the power losses and electromagnetic interference [87]. This makes the auto-transformer configuration is preferable one among the other feeding methods. The locomotive is fed by both neighboring auto-transformers as shown in Figure 2.10.

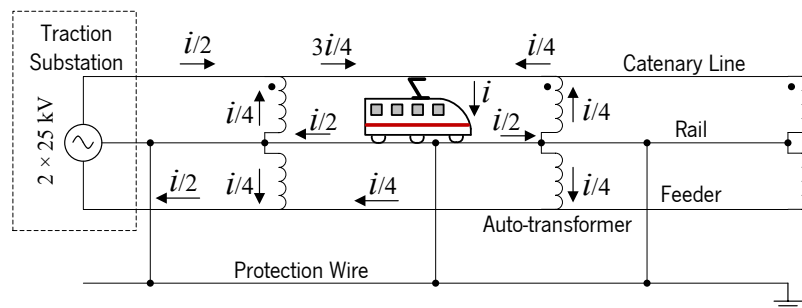


Figure 2.10. Auto-transformers configuration.

The locomotive current distribution varies according to the distance between the locomotive and the respective auto-transformers. The current magnitudes in Figure 2.10 are presented assuming the distance between the locomotive and the respective auto-transformers is the same on the left and the right sides. In some scenarios, series capacitors with the negative feeder line are added to decrease the voltage drop and to stabilize the catenary voltage. A study presented in [84] shows the voltage drop of an auto-transformers system is less than the voltage drop when using a boost transformers system by 40%, at a traction power of 8 MVA, 10 km spacing between auto-transformers and 5 km spacing between boost transformers. On the other hand, rail-to-earth voltage is lower in the auto-transformer system than in systems where the return current flows through the rails. Nowadays, this system is the

most used for AC railway electrification, even some boost transformer systems have been modified into auto-transformer as in Norway and Sweden [87].

2.5.5 Coaxial Power Cable

As shown in Figure 2.11, the coaxial cable feeding system consists of a coaxial cable placed along the train path. Every several kilometers, the inner conductor of the cable is connected to the overhead catenary line and the outer conductor is connected to the rail through parallel connectors. This configuration is expensive compared to the previous feeding ways. However, it can be useful when space is limited.

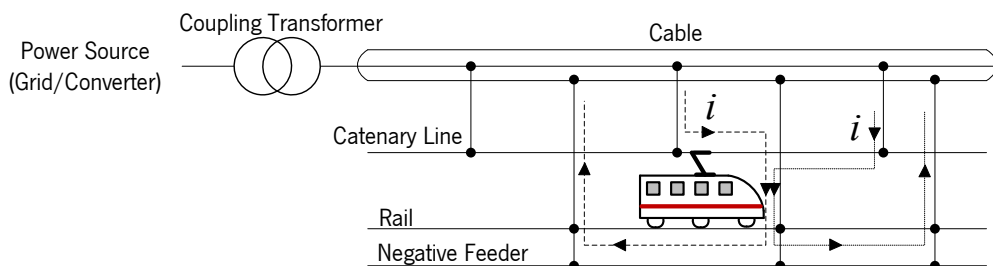


Figure 2.11. Coaxial power cable feeding system.

The *Shinkansen* high-speed train in Japan is using in some sections this way of electrification. The Eurotunnel train is also using this method of electrification. In some situations, the cable small loop impedance makes this solution attractive for some applications as it reduces the electromagnetic interference with other communication devices. In general, the load current is boosted in the cable and the rail current distribution is similar to that of the auto-transformer system [9].

2.6 Conclusion

Power quality phenomena have been discussed in this chapter to demonstrate the effects caused by power quality deterioration in electrified railway systems. In this context, the power quality deterioration has directly adverse impacts either on the electric power system, including the electric locomotive itself, or on the signaling and communication system between trains. Power quality deterioration will result in higher operating costs of electrified trains, as well as in polluting the power system with high total harmonic distortion (THD) levels and negative sequence components (NSCs). Balanced three-phase power transformers can partially solve the problem of system imbalance in the electrified railway systems. However, the effectiveness of this solution is highly relying on the trains loading profile parameters. These transformers provide a better power quality improvement when both load sections are equally loaded. On the other hand, power compensators based on passive components have been presented in this chapter to explain the technology used in the last decades, and even in these days,

to overcome the power quality deterioration. These passive compensators are not able to follow the fast-dynamic changes of non-linear loads, which is the case of the traction load (electric locomotive). This reason has established a high demand for dynamic power compensators that can follow the dynamic changes of non-linear loads. From here, next chapter of this Ph.D. thesis serves that purpose.

Chapter 3

Active Power Compensators in Electrified Railway Systems

3.1 Introduction

Chapter 2 presented an overview of power quality phenomena, besides the traditional-based methods of power quality improvements in electrified railway systems, such as balanced power transformers and passive power compensators. However, these techniques are not able to follow the non-linear load's dynamic changes and they cannot totally compensate harmonics and negative sequence components (NSCs) of currents [88]. Power Electronics converters are increasingly responsible for ensuring operation with high efficiency and for meeting power quality requirements [89]. Therefore, some of the flexible AC transmission systems (FACTS) devices are used for the purpose of power quality improvement of the three-phase public power system (PPS). In this case, these devices operate as active power compensators to increase the efficiency of the long-distance power transmission. Then, providing extra network capacity more economically and much faster than the option of building new transmission lines. They also contribute to enhance power quality, improve grid stability, besides increasing the reliability of AC power grids. Due to the FACTS advantages, nowadays, electrified trains are one of the biggest users of FACTS devices in Japan [90].

In this context, the static VAR compensator (SVC) is used for reactive power compensation and to mitigate active power oscillations. Like the SVC, but with a faster transient response, the static synchronous compensator (STATCOM) is considered as an evolution of the SVC technology. Both solutions are well-known devices and they are broadly used for power quality improvement applications. On the other hand, the static frequency converter (SFC) is used in certain countries to interface the single-phase traction power system (TPS) and the three-phase PPS. The SFC based on the modular multilevel converter (MMC) has been included in this chapter for a better understanding of MMC topology. The SFC solution prevents the harmonics and the NSC of currents passing from the TPS to the PPS side. However, the SFC has some drawbacks regarding the converter power ratings and the need for additional passive filters on the PPS side [91]. The rail power conditioner (RPC) is a recent

technology used in AC electrified railway systems. It has the ability to compensate the NSCs and the current harmonics produced by the locomotives [57].

Both types of power compensators (active and passive) are intended to operate together for the purpose of power quality improvement. This type of combination helps to reduce the power ratings of the active power compensators. In such cases, a considerable part of the reactive power compensation is handled by passive compensators. In this context, and since the previous chapter gave an idea about the passive power compensators, this chapter presents the active power compensators, or the FACTS devices used in electrified railway systems. At the end of this chapter, several case studies are presented to establish a comparative analysis according to the published literature.

3.2 Static VAR Compensator (SVC)

At the end of seventies, with the emergence of new semiconductor materials, a switching devices-based solution was introduced with the objective of improving power quality. At that epoch, Thyristor switching devices have drawn more interest and they were mainly used for dynamic compensation purposes. Since the SVC has the same operation principles of the Steinmetz circuit (presented in the item 2.4.5), this device can be called as an active Steinmetz compensator. SVC is typically modeled as variable three-phase reactive elements (capacitors and inductors), connected in delta or wye scheme [45]. Consequently, the SVC structure involves several reactive elements, in which they could be fixed or controlled by Thyristor switching devices.

SVC systems are used to improve the balance of the PPS by adjusting the three-phase impedance connected to the grid. However, using these devices at the high-voltage (HV) or the extra-high-voltage (EHV) level requires a high number of series connected switches to withstand the high-voltage values. Otherwise, the connections can be accomplished through a step-down power transformer (coupling transformer) as shown in Figure 3.1. Another solution is by installing the SVC devices at the secondary windings of V/V power transformer or at the two feeder sections of the traction substation.

SVC devices are well known as an economical solution for power quality improvement. This category of FACTS compensates both of NSCs and reactive power, leading to three-phase PPS power factor correction and balanced three-phase currents. However, the main drawback of such devices is the huge amount of harmonic contents injected into the PPS due to the slow Thyristors commutation [46]. For this reason, harmonics compensation using the SVC is a weak indicator, as the SVC performance relies entirely on the harmonic impedance of the grid. Moreover, SVC in traction system may reduce the power factor of the traction system when it is designed for NSCs compensation because there is a

trade-off between power factor correction and NSCs compensation when using the SVC in traction system for the purpose of power quality improvement [57]. In other words, the conflict is between NSCs and reactive power compensation. If the three-phase power system carries a high amount of reactive power, the SVC cannot be a helpful solution. Anyway, and regardless of this fact, nowadays, most of the new electric locomotives use pulse width modulation (PWM) technique in the traction drivers. This technology can achieve an almost unitary power factor in the traction system, and the SVC in this case compensates the NSC.

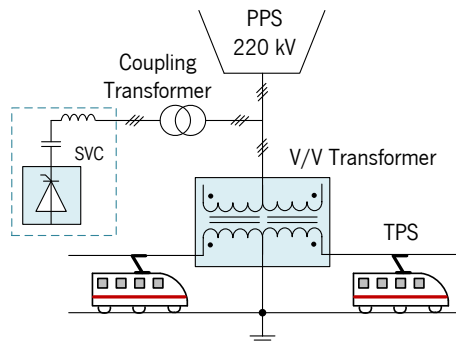


Figure 3.1. SVC installation via a step-down power transformer in railway electrification.

At the present time, SVC is branded as a low cost dynamic compensator and is used in more flexible power systems (e.g., near the giant power plants) which can be technically sufficient and economically effective [45]. Since there are various types of SVC in the market, manufacturers are customizing the SVC to fit each customer with their specific needs. The SVC contains several fixed or switched branches, of which, at least one branch includes thyristors, and the combination of branches can be diversified depending on the customer requirements. Typically, the SVC includes a combination of at least two of the following branches: Thyristor controlled reactor (TCR); Thyristor switched capacitor (TSC); Harmonic filter (HF); Mechanically switched capacitor bank (MSC) and Mechanically switched reactor bank (MSR) [92].

The most common topologies are the ones include the combination of TCR/HF or TCR/TSC/HF. Using the TSC topology is useful to reduce the total SVC losses, where the TSC results in reducing the overall SVC size. On the other hand, the MSR or the MSC topologies are the ones used at the high-voltage and the medium/low-voltage side of the SVC coupling transformer to have extra reactive power support outside the dynamic range [92]. As a result, SVC dynamic performance is poor, and the system occupies a large physical area compared to other active power compensators [93].

3.3 Static Synchronous Compensator (STATCOM)

During the last two decades, the insulated-gate bipolar transistors (IGBTs) have begun replacing the Thyristor based SVC (new SVC IGBT based). This was due to the higher IGBTs switching frequency

compared to the Thyristor switching devices. Consequently, STATCOM devices have been considered as the next-generation of SVC power compensators but with improved performance. Normally, STATCOM devices consist of a voltage-source converter, coupling power transformer and filter inductors installed on the three-phase AC grid. These devices allow reactive power exchange without the need for other passive filters [94]. In some cases and if needed, switched, or fixed air core coils and capacitors can be used with the voltage-source converter as supplementary reactive power components to reach any desired range. In Japan, five sets of 34 MVA to 60 MVA STATCOM devices are available in *Tokaido Shinkansen* [90].

STATCOM devices can be used in medium-voltage levels at a frequency of 50 or 60 Hz. Consequently, they are normally manufactured with a larger volume in comparison to the SVC devices. However, and in some applications (e.g., an extension of the dynamic compensation range and for better overloading performance), combining the best of SVC and STATCOM technologies to create a new solution called hybrid STATCOM (manufactured by ABB Ltd.) in which the TCR and TSC branches are connected in parallel with STATCOM device. On the other hand, the STATCOM based on cascade connected modular multilevel voltage-source converter has low harmonic generation. Therefore, and since the TSC does not add any harmonic contents, there is no need for low-order harmonic filters in the substation. The STATCOM is usually used for power factor correction, current compensation and voltage regulation at the point of power delivery, contributing in electrical PPS stability. However, voltage regulation by the STATCOM is only possible due to the inductive part of the upstream grid line impedance at the point of interconnection between the STATCOM and the PPS [42].

Figure 3.2 depicts the STATCOM device connected in parallel with the PPS. This parallel connection signifies that STATCOM can be connected or disconnected without disturbing the operation of the traction substation. Consequently, the robustness and readiness of the railway substation will not be affected by the STATCOM operation [95]. Moreover, this device does not require an internal power supply, meaning that, the STATCOM has a neutral contribution in terms of active power. By another meaning and after neglecting the STATCOM power losses, STATCOM will not consume or provide active power to the PPS, and the main objective is to exchange only reactive power with the PPS in order to improve the power quality. This is possible by exchanging the instantaneous reactive power among the phases of the PPS since the STATCOM can act as either a source or as a sink of reactive power [96].

As a fully controllable compensator, the STATCOM can dynamically provide reactive power to compensate NSC of currents. Considering another aspect, and since the necessary load active power flows directly to the catenary through the V/V power transformer or any of the balanced transformers

(e.g., Scott power transformer), the STATCOM Volt-Ampere (VA) rate or apparent power can be significantly lower than the traction substation VA rate. However, and according to the published results in [95], STATCOM VA rate when using the Scott power transformer is significantly lower than its VA rate when using the V/V power transformer. Compared with the SVC technology, the STATCOM behaves as a bidirectional reactive power compensator, with a faster time response, higher load capability and lower harmonic contents.

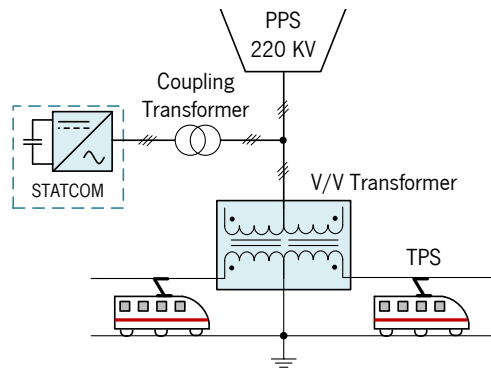


Figure 3.2. Static synchronous compensator (STATCOM) in railway electrification.

3.4 Static Frequency Converter (SFC)

The SFC system consists of a three-phase AC/DC converter connected back-to-back to a single-phase DC/AC converter with a single DC-link as shown in Figure 3.3. Compared to old solutions like the rotary converters (rotary converter: type of electrical machine that acts as a mechanical rectifier), the SFC provides additional benefits in terms of future investments, improved efficiency, lower maintenance costs, faster start-up time and instant response to grid faults. The SFC main feature is the separation between the PPS and the TPS through a regulated DC busbar voltage (DC-link). The last prevents harmonic contents generated by the locomotives passing from the single-phase TPS to the three-phase PPS. In addition to that, the SFC can easily overcome the problem of NSC, since they present the TPS single-phase load as a balanced PPS three-phase load [49]. In other words, the feeder stations equipped with the SFC system draw a nearly sinusoidal balanced current at unitary power factor [44]. Consequently, the harmonics and NSC compensation are considered as an inherent behavior when using the SFC solution.

In case of many SFC devices are supplying an overhead catenary line, then, these SFC devices need to operate in four quadrants and they must have a power capacity that quite enough to supply full power rated electric locomotives. It is important to guarantee the previous condition as the SFC has a limited overloading capability [46].

Compared with other FACTS devices, such as the SVC, the STATCOM and the RPC, the cost of the SFC system is the highest since this converter has to be rated for a full power of traction loads, whereas the rest of FACTS devices have to be rated only for a part of the feeder power stations [91]. This view has been changed recently due to the evolution of new high-speed trains in China, Japan and Europe. On the other side, SFC devices are normally installed at the medium-voltage busbar. This significantly reduces the equipment costs to interface the TPS and the PPS [44].

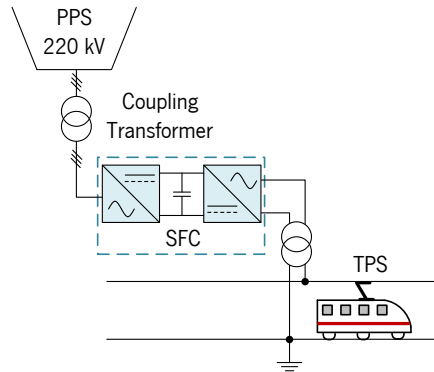


Figure 3.3. Static frequency converter (SFC).

The power system may include many SFC substations linked in parallel without the need for catenary neutral sections as shown in Figure 3.4 (with a continuous overhead catenary line). In this case, parallel SFC substations can simultaneously provide the power in a way that similar to DC TPS. However, the neutral sections between the SFC substations could remain for safety reasons to isolate any fault or equipment malfunctioning. The distance between neutral sections is determined according to the applied authoritative standards and norms. Unlike the DC substations which they only have the DC voltage magnitude to be controlled, AC substations have the voltage magnitude and the phase angle to control active and reactive power, thus droop control is the technique used to link many SFC substations in parallel, where each converter's frequency is a function to the active power and the root mean square (RMS) voltage is a function to the reactive power [91]. The parallel connection of many SFC substations allows a longer feeding distance between the traction substations. It also reduces the neutral sections number according to the distance between the SFC substations and gives a flexible power flow control between substations.

The general SFC topology consists of a three-phase two-level converter connected back-to-back through a DC-link to a single-phase two-level converter. This topology requires step-down coupling transformers to interface the SFC substations and the PPS. However, and within the appearance of advanced multilevel converter topologies, SFC substations based multilevel converters can be directly connected at the medium-voltage levels without using step-down coupling transformers. The SFC based on MMC

is explained in the further sections of this chapter. A study of novel advanced traction power supply system using many SFC based MMC substations is presented in [97].

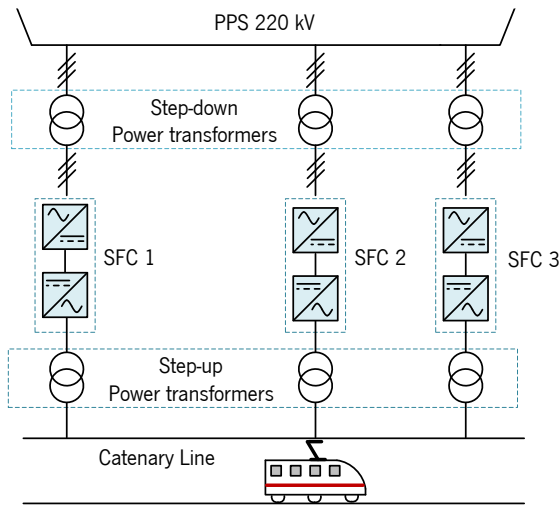


Figure 3.4. Parallel connection of the SFC substations.

The recent commercialized SFC topologies (SFC commercialized by ABB Ltd) are equipped with:

- Quick response to grid faults and fast start-up times;
- Various frequency applications of 60, 50, 25 and 16.7 Hz;
- Better power capabilities with active catenary voltage control;
- Improved system efficiency and fault behavior;
- Reduced SFC active power consumption;
- Better short circuit protection on TPS (no short circuit current is drawn from PPS);
- Complete decoupling ensures low harmonic contents from TPS towards 50 Hz PPS;
- Energy resulting from regenerative braking can be reused;
- Advanced test functionality for locomotives and catenary lines.

Electrified railway systems in Japan are one of the best examples in the world for efficient urban and intercity transportation. In this context, *Tokaido Shinkansen* traction substation in Japan uses 60 Hz frequency in the area around Tokyo to reduce the weight of the locomotives, then, since 2003, an SFC with a nominal power of 60 MVA has been introduced using the Gate Turn-Off Thyristor (GTO). Another three-phase 50 Hz to single-phase 60 Hz SFC with a nominal power of 60 MVA using the Injection-Enhanced Gate Transistor (IEGT) has been available since January 2009 [90].

3.4.1 Single DC-Link Static Frequency Converter (SDLC)

SFC based on a single DC-link converter (SDLC) and a neutral point clamp inverters (NPC) is shown in Figure 3.5. Most of the power converter topologies for railway applications are based on voltage source rectifiers to convert the three-phase AC voltage waveforms to a DC voltage. Afterward, power NPC

inverters convert the DC voltage to a single-phase AC voltage. Since the overhead catenary voltage has a value of 25 kV or 15 kV RMS, single-phase step-up transformers at the AC output voltage are necessary to guarantee the voltage values of 25 kV or 15 kV. This is also useful to avoid high-voltage drop when the TPS is overloaded after respecting the NPC inverters nominal power [4], [44]. However, one of the key elements of this structure is the single-phase transformers which are not only increase the total costs, but also may represent a bulky and noisy structure, especially when the TPS is operating under 15 kV, 16.7 Hz.

In SDLC topology, the three-phase PPS side is connected through a step-down power transformer, where the secondary windings are connected through two rectifiers, then the outputs of these rectifiers are connected in parallel through a single DC-link to several DC/AC converters that also have parallel connections. The output of each DC/AC converter is connected directly to the primary windings of step-up power transformers, then the single-phase output voltage is formed by series-connected secondary windings of single-phase transformers to reach the required output voltage of 25 kV or 15 kV [44] as shown in Figure 3.5.

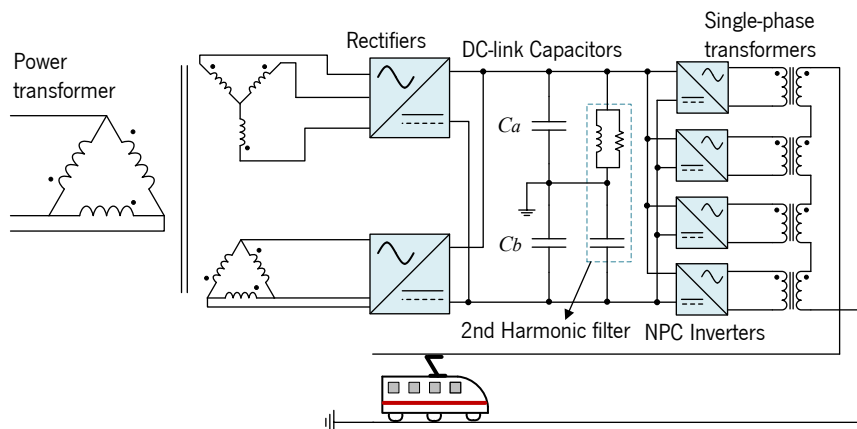


Figure 3.5. SFC based on a single DC-link converter (SDLC).

The step-down power transformer ($\Delta/\Delta/Y$ connection) can improve the power quality of the PPS since the zero sequence components are not allowed to pass into the public grid side due to the delta connection. On the other hand, rectifiers are used and linked in parallel to get the total DC-link voltage that contains high-power capacitors and a 2nd harmonic filter. This is important to have a stable DC-link voltage as an input for the NPC inverters. The main drawback of this topology is the limitation of the fault tolerance, especially when one of the DC-link capacitors collapses or a short circuit fault happens in transistors. In that cases, the SDLC cannot remain in operation and the SFC topology with multiple DC-link capacitors (presented in the next item) has better fault tolerance [44].

3.4.2 Multiple DC-Link Static Frequency Converter (MDLC)

This topology is based on single-phase cascade-connected converters and it has multiple DC-links as shown in Figure 3.6. It is essentially formed by multiple back-to-back converters at the three-phase power grid and single-phase series-connected NPC inverters at the single-phase grid. This topology has better output waveforms, low harmonic distortion and better fault tolerance compared to the SDCL topology. Since all of the single-phase inverters are series-connected, this results in multilevel output voltage waveform which reduces the harmonic distortion [44], [98]. In the case of any faults in the converters, the damaged converter can be bypassed, remaining the normal operation if the remaining converters can withstand the increase in their individual voltage. On the other hand and by using a sufficient number of modules (AC/DC/AC converters), it is possible to dispense the single-phase output transformer, reducing the multiple DC-link static frequency converter (MDLC) total cost and improving the quality of the output voltage waveform [44], [99].

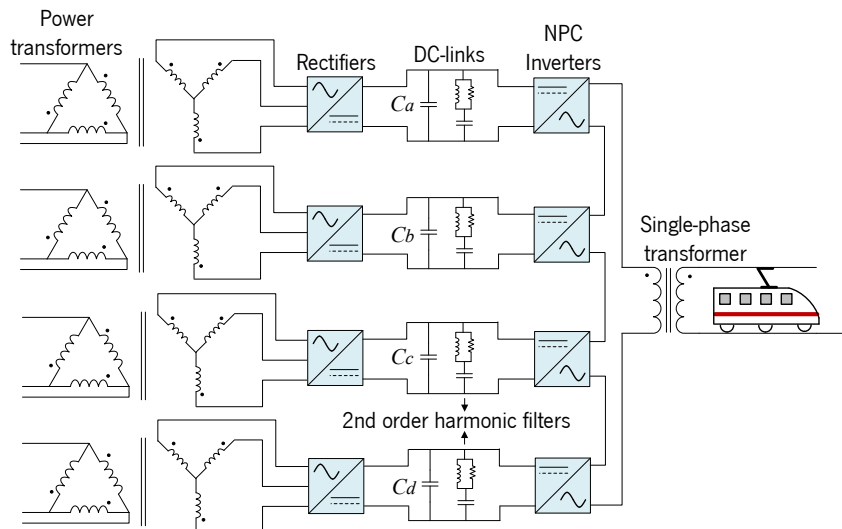


Figure 3.6. SFC based on a multiple DC-link converter (MDLC).

Figure 3.7 presents the difference between the SDLC and the MDLC output waveforms when one of the DC-link capacitors collapses (e.g., C_a , C_b in Figure 3.5 and C_a , C_b , C_c , C_d in Figure 3.6). The simulation models of SDLC and MDLC are exactly as in Figure 3.5 and Figure 3.6 and they were built by using *PSIMV.9.1* simulation tool. Nomenclatures of $u_o(s)$ and $i_o(s)$, respectively refer to the output voltage and current of the SDLC topology. On the other side, the nomenclatures of $u_o(m)$ and $i_o(m)$, respectively refer to the output voltage and current of the MDLC topology.

Simulation results in Figure 3.7 (at 15 kV, 16.7 Hz) show a better DC fault tolerance for the MDLC topology. This is because both of $u_o(s)$ and $i_o(s)$, have completely negative waveforms and higher absolute average values. Therefore, and although the MDLC complex structure and its higher costs

due to the additional DC-links, power transformers and power converters, this solution is recommended over the SDLC topology to operate as an SFC in railway applications [44].

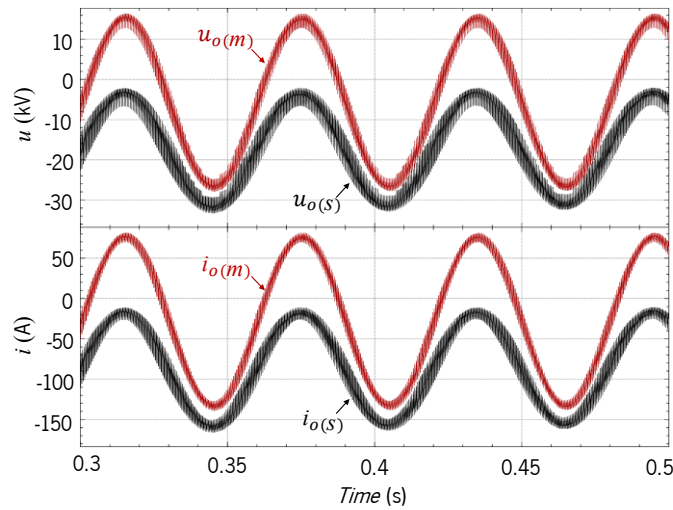


Figure 3.7. Catenary voltage and load current under a DC-link fault in SDLC and MDLC: $u_o(m)$ and $i_o(m)$ are the output voltage and current of the MDLC topology; $u_o(s)$ and $i_o(s)$ are the output voltage and current of the SDLC topology.

Owing to the facts of bulky 16.7 Hz transformer in the MDLC topology, the limitation of the DC-link fault tolerance in the SDLC topology and other drawbacks, strong interests have appeared for solutions that can make the output transformers dispensable. In addition, and since the typical catenary voltage of 25 kV requires a DC-bus voltage in the order of 40 kV, a transformer-less implementation is not applicable unless series-connected switching devices are used or, instead, an MMC topology is employed.

3.5 Static Frequency Converter Based on Modular Multilevel Converter (SFC Based on MMC)

NPC and flying capacitor multilevel converters are quite hard to extend to a higher level, e.g., more than three-level, due to the complications resulting from electrical connections, loss distribution and voltage balance problems [100], then, one of the innovative SFC systems is the one based on the MMC topology which consists of series-connected submodules (SMs). The MMC idea was first introduced in 2001 by *Marquardt Group* for medium-voltage applications [101]. The topology itself was first used for medium-voltage transmission lines because of the scalability and the low harmonic distortion. [44]. After 15 years of evolution and improvement, the MMC has become the most preferable multilevel converter topology for the medium and high-power systems despite the need for reactors to suppress the circulating currents between the MMC phases [102]. MMC phase leg is divided into two equal arms (the number of SMs must be even) to be able to generate an equal number of positive and negative levels at the AC side [103]. In railway applications, features of MMC technology favor its application for the following attractive advantages [104]:

- SFC based on MMC is a transformer-less topology. In other words, power transformers are dispensable devices at the TPS side.
- The power ratings will be divided equally among several SMs. Therefore, there is no need to use switching devices with high power ratings.
- MMC equivalent switching frequency is equal to the SM switching frequency multiplied by the total number of SMs in each arm (each MMC leg contains two arms, the upper and the lower arms). Accordingly, MMC output waveforms contain lower harmonics content and a smaller size of passive filters (higher output voltage level results in minimal use of three-phase grid filters).
- The possibility to increase the total MMC power with ease by inserting extra SMs.
- High reliability due to the MMC flexibility of redundancy.

MMC SMs can be half-bridge or full-bridge according to the application and they sequentially switch during one complete cycle. MMC equipped with full-bridge SMs is an interesting solution in 15 kV, 16.7 Hz traction substations. This technology is called a direct AC/AC MMC. On the other aspect, the other MMC type called an indirect AC/DC/AC MMC consists of several half-bridge SMs and it is the suitable choice for 25 kV, 50 Hz traction substations. The main reasons for such a selection are explained in the further items of this chapter.

3.5.1 Modular Multilevel Converter Operation Principle

Figure 3.8 depicts operation approach of the 5-level MMC, besides a simplified representation of the MMC [105]. The AC output voltage u_o is acquired by inserting or bypassing a specific number of SMs in each MMC leg. The DC-link voltage capacitor of each SM can be inserted (as the case of SM_2 , SM_3 , SM_4 and SM_{1n}) or bypassed (as the case of SM_1 , SM_{2n} , SM_{3n} and SM_{4n}) as shown in Figure 3.8(a). A higher number of DC-link capacitors signifies a higher output voltage level, lower harmonic distortion, and a lower noise to the neighboring electrical equipment [106]. The simplified representation of MMC can be equivalent to a switch that changes its position and connection points with charged floating capacitors during a time cycle as shown in Figure 3.8(b). In that case, a multilevel output voltage u_o is generated [107]. A review of MMC SM topologies and PWM techniques is presented in [108].

Three-phase MMC contains three legs that correspond to the three-phase AC grid. Each phase leg consists of two arms, namely an upper arm and a lower arm. Each arm contains a few tens of cascade-connected SMs. Each SM is an independent voltage-source converter with at least two switching devices and one floating DC-link capacitor. The total DC-link voltages of SMs in one MMC arm should be able to withstand the entire converter DC-link voltage V_{dc} . In other words, each leg must have a total DC-link voltage with a value double the entire MMC DC-link voltage. By adopting an

appropriate switching strategy, each MMC arm voltage (including the filter inductance voltage in the MMC arm) has a sinusoidal output waveform with a DC offset equal to half the entire DC-link voltage.

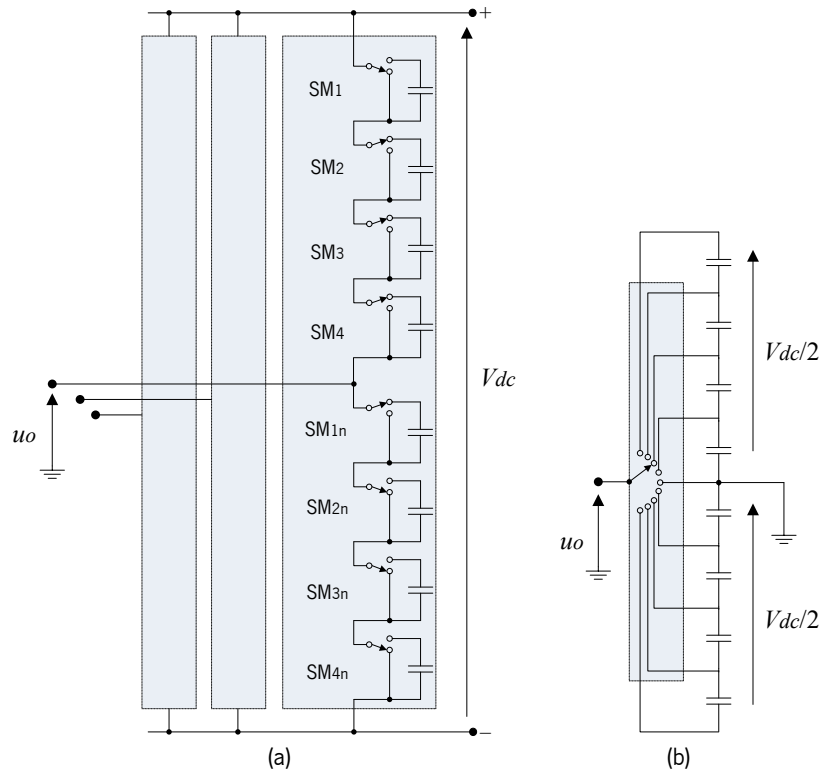


Figure 3.8. Operation approach of the 5-level MMC: (a) Representation of the MMC; (b) Simplified representation of the MMC.

MMC leg output AC voltage is obtained collaboratively through the upper and the lower MMC arms, after considering mid-neutral point capacitors at the DC-link, V_{dc} , to create a neutral point. [109]. States of the 5-level MMC are presented in Figure 3.9, Figure 3.10, Figure 3.11 and Figure 3.12. MMC is structurally scalable and can hypothetically meet any voltage level requirement. The voltage level at the midpoint of the phase leg u_o is defined by the number of SMs that are connected in the upper and lower MMC arms [107].

By considering 5-level MMC, state 1 happens when all the upper arm SMs are inserted and the lower arm SMs are bypassed. In that case, the output voltage u_o has the highest negative value. On the other hand, state 2 is when three SMs in the upper arm and one SM in the lower arm are inserted. State 3 is when two SMs in the upper arm and two SMs in the lower arm are inserted and the output voltage u_o is close to zero. State 4 is when one SM in the upper arm and three SMs in the lower arm are inserted. State 5 is when all the lower arm SMs are inserted and the upper arm SMs are bypassed. In that case, the output voltage u_o has the highest positive value [110].

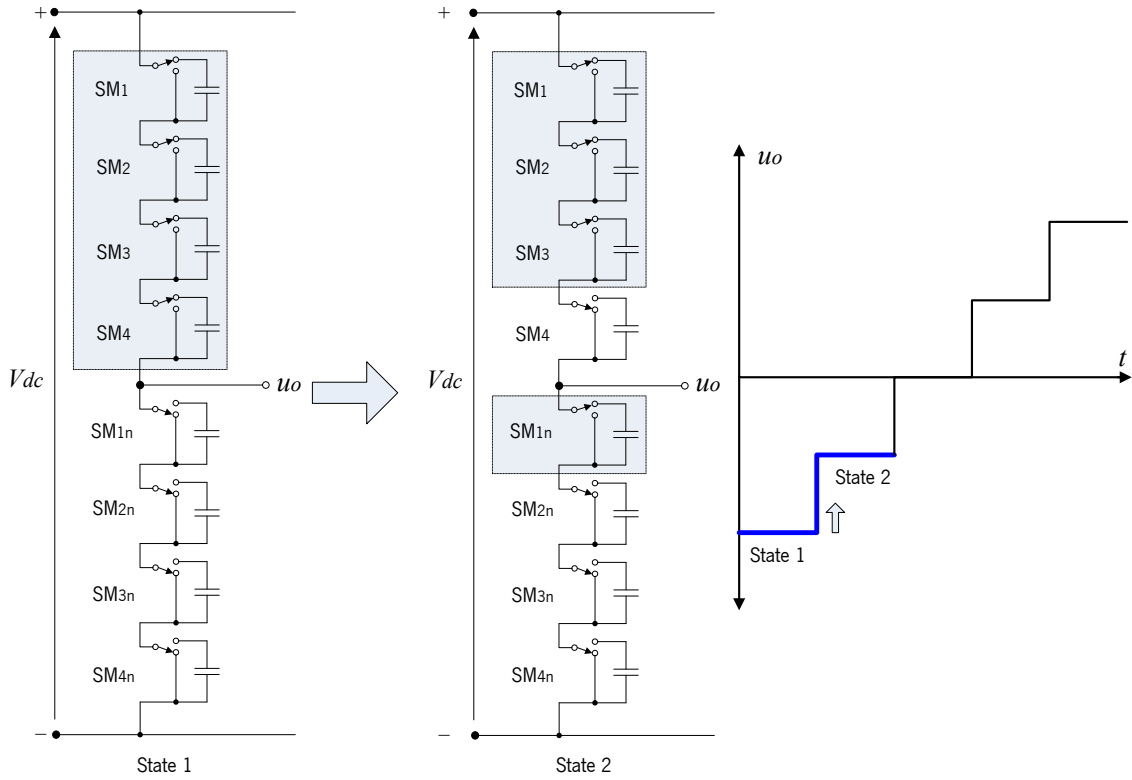


Figure 3.9. States of the 5-level MMC (state 1 to state 2 example).

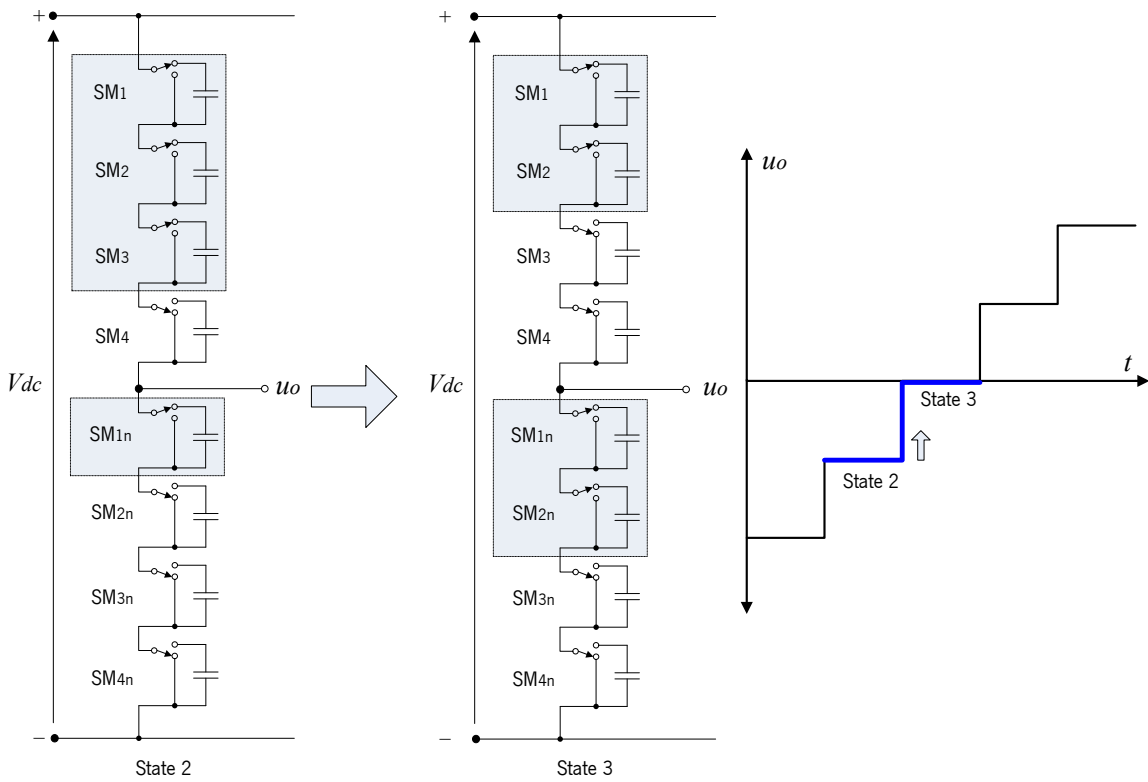


Figure 3.10. States of the 5-level MMC (state 2 to state 3 example).

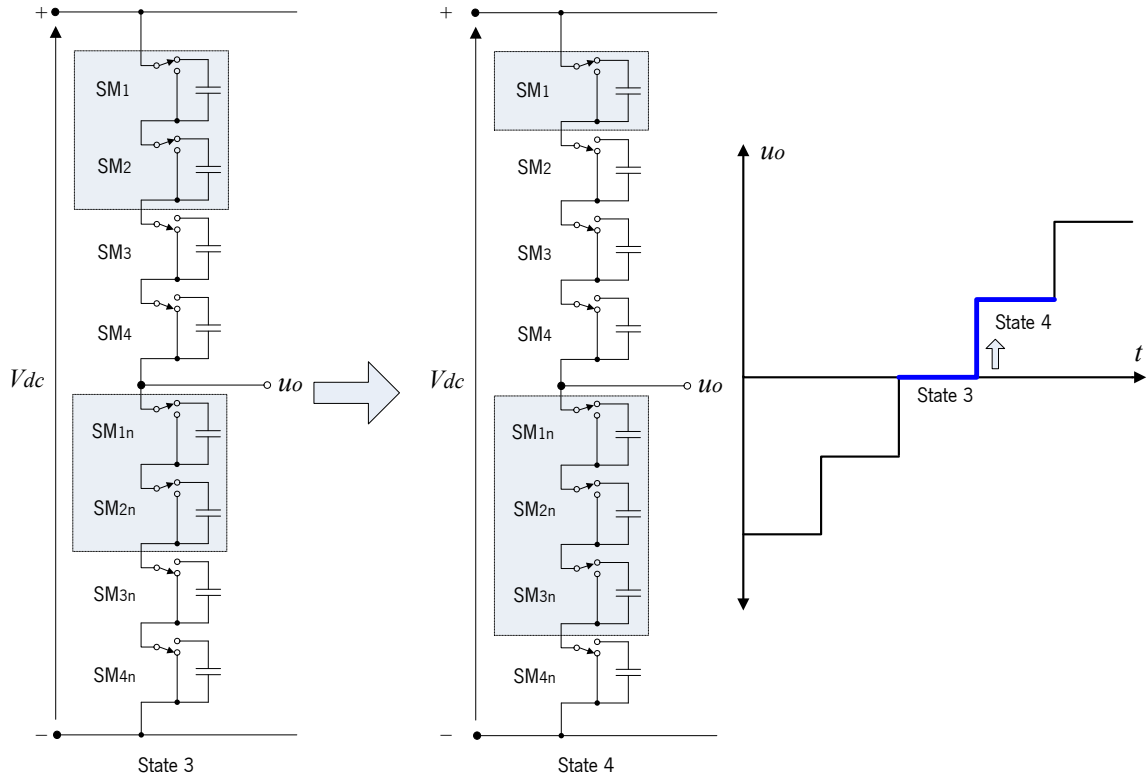


Figure 3.11. States of the 5-level MMC (state 3 to state 4 example).

As a conclusion, the MMC voltage level (N) is always equal to the number of SMs in one MMC arm plus one, then, the number of SMs in one arm is: $(N-1)$. These nomenclatures are the ones used in this Ph.D. thesis.

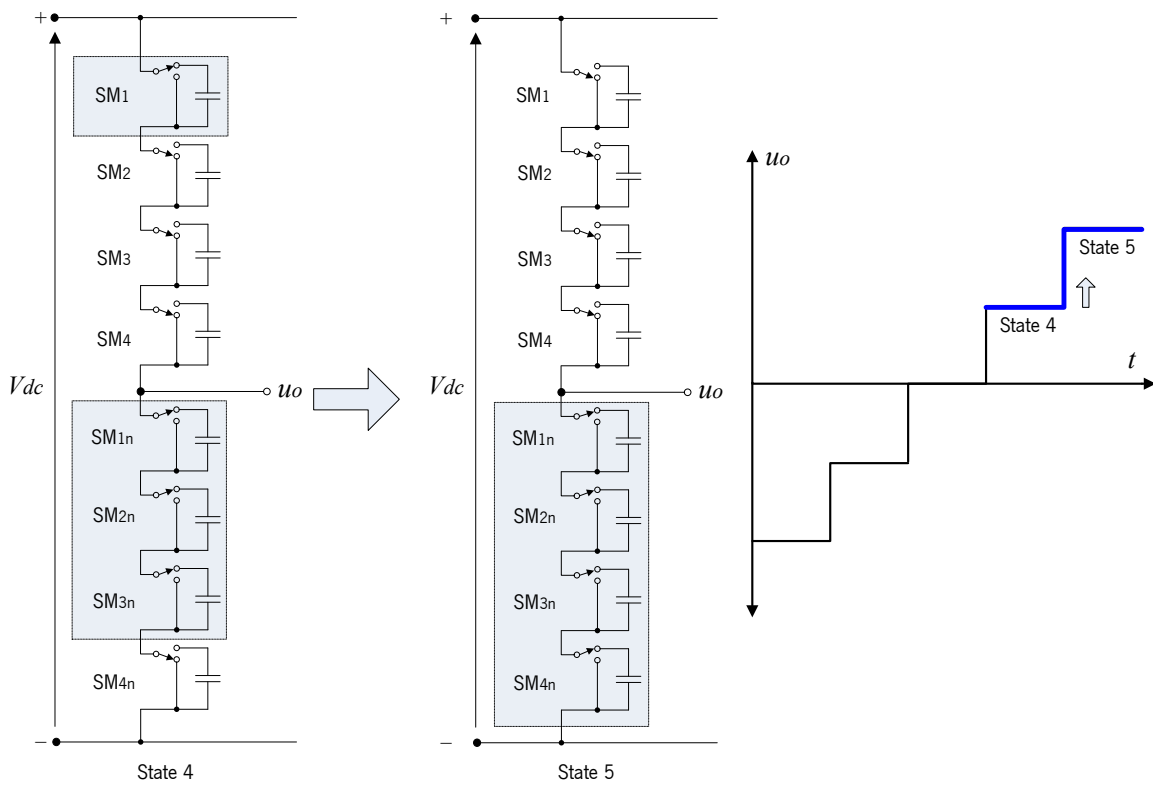


Figure 3.12. States of the 5-level MMC (state 4 to state 5 example).

3.5.2 Direct Modular Multilevel Converter

This MMC type fulfills a direct three-phase to single-phase AC/AC conversion without DC-link connection. The main structure of direct MMC is composed of identical series-connected bipolar full-bridge SMs [111]. Each SM consists of four power electronic modules (IGBTs + freewheeling diodes) and a DC-link capacitor as shown in Figure 3.13. The direct MMC full-bridge SM allows the SM capacitor to be inserted into the circuit in any polarity as presented in Table 3.1 [112]. The MMC leg contains two arms and two reactors to smooth the current waveforms and to limit the circulating currents between the MMC arms.

The main MMC advantage is to have a low actual switching frequency of switching devices [113]. Consequently, the equivalent switching frequency in this case is equal to the actual switching frequency for each SM multiplied by the number of SMs connected in series in each arm (each leg consists of two arms, as shown in Figure 3.13). This leads to lower switching losses and a higher efficiency. Moreover, and compared to the SDLC and the MDLC, there is no need for the step-up power transformer at the TPS side, since the MMC can withstand the catenary medium-voltage of 25 kV or 15 kV. This reduces the total costs, size, and the cooling equipment of the overall system [44].

The number of series-connected SMs in each arm can be defined according to the desired power level. Normally, in SFC railway substation, the number of SMs in each arm is between 10 and 30 with a power level between 20 MVA and 60 MVA. For example and for a catenary voltage of 15 kV, the peak voltage value is around 21 kV could be obtained by seven SMs per arm (14 SMs per MMC leg) with DC-link capacitors each of 3.25 kV [114], [44]. The converter design should guarantee the MMC ability to deal with the voltage oscillations according to the grid norm.

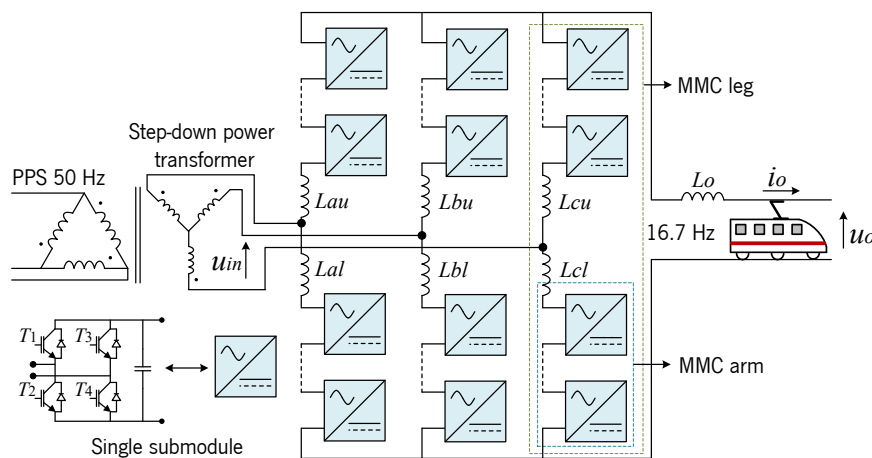


Figure 3.13. Direct AC/AC MMC topology.

Table 3.1. Full-bridge SM switch operation.

Switching devices (IGBTs)	Output voltage
$T_1 + T_4$	$+ V_{out}$
$T_2 + T_3$	$- V_{out}$
$T_1 + T_3$	0
$T_2 + T_4$	0

Under normal operation, the direct AC/AC MMC converter circulates power between the three legs to compensate pulsating power on the catenary line. This circulated power has two frequencies, the sum and the difference between input and output power frequencies. If the input and the output frequencies are the same, so there is no circulating power between legs. This converter is convenient to be used for 16.7 Hz output frequency in railway substations because the circulating power difference frequency between legs is higher than the output frequency, thus this decreases the importance for filters requirement. Nevertheless, using direct MMC topology in practical applications is still limited and has some difficulties as it requires a frequency separation accompanied by a complex control as well. Otherwise, the implementation will result in a harmonic interaction between the power grids (PPS and TPS), especially at low numbers of SMs and low switching frequency values [111].

Arm currents of the direct AC/AC MMC have mainly three different frequency components, the fundamental frequency current component of 50 Hz that has the main responsibility for power exchange between the direct MMC and the PPS, the 16.7 Hz (50/3 Hz) current component that manages the power exchange between the direct MMC and the TPS, and the two-third of (100/3 Hz) fundamental frequency current component (the difference of input and output current frequencies) that controls the power exchange between the direct MMC arms (circulating current between arms). The last component refers to the circulating current flows between the MMC arms, which should be well controlled to avoid high power losses in the converter. The circulating current between arms can also be created from an additional current component that has the frequency of (50+16.7 Hz) (the sum of input and output current frequencies). However, the last indicated component could be ignored since the main part of the circulating current has the two-third of the fundamental frequency. Finally, current waveforms may also contain some additional harmonic contents. The main challenge in direct MMC control system is the simultaneous currents control for the MMC legs in a way to generate AC current reference and also to maintain equal DC-link voltages among the MMC SMs [44].

3.5.3 Indirect Modular Multilevel Converter

This MMC topology comprises series-connected half-bridge SMs as shown in Figure 3.14. Each half-bridge SM contains two power electronic modules (IGBTs + freewheeling diodes) and a DC-link capacitor. Besides the SM DC-links, there is a main DC-link connection between the three-phase AC/DC converter and the single-phase DC/AC converter. Although the indirect MMC can accomplish direct frequency conversion. However, this topology is used when the input frequency and the output frequency are the same since there is no limitation on frequency separation [115]. Concerning the railway applications, indirect MMC is the best choice for 50 Hz catenary supply. On the other side and for 16.7 Hz catenary supply, indirect MMC should be used with larger SM capacitors and higher current rating devices on its single-phase DC/AC converter compared to the direct MMC topology (see the item 0 case study).

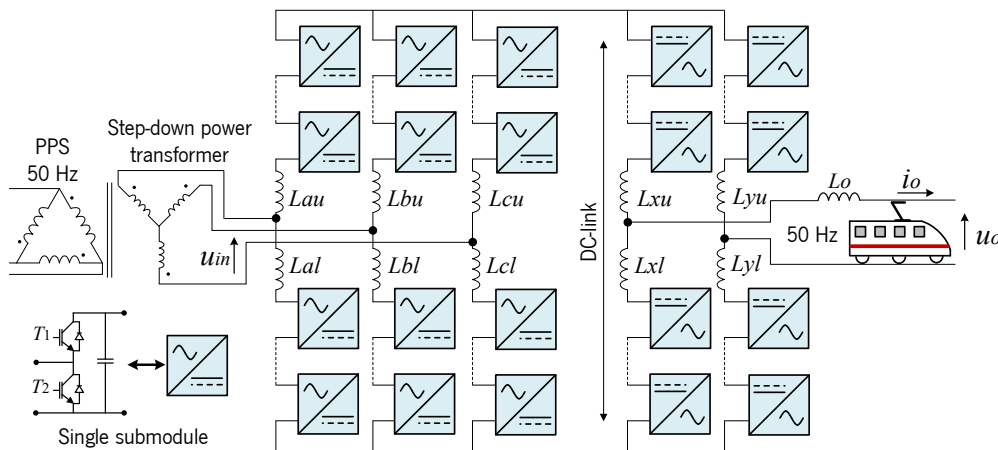


Figure 3.14. Indirect AC/DC/AC MMC topology.

Each SM acts as an independent two-level converter generating a voltage of either 0 V or V_{dc} (SM capacitor voltage). Using an enough number of series-connected SMs increases the converter power capacity. In addition, this makes the power electronic modules synthesize a stepped voltage that varies near a Sine waveform with very low harmonic contents. The main difference between MMC and other converter types is the MMC arm currents that flow continuously in all arm SMs of the converter over the frequency cycle. As a result, concepts such as on-state and off-state in MMC have no physical meaning.

This converter has two principal disadvantages. First, the control is more complex than other converter types, then, balancing the SM voltages is a profound challenge that requires a significant computing power and high-speed communication between central control unit and actuators. Figure 3.15 shows the switching possibilities of indirect AC/DC/AC MMC SM, where the output voltage is either equal to the capacitor voltage when the capacitor is inserted or equal to zero when the capacitor is bypassed.

Among the SM topologies of MMC, half-bridge SM is the most common because of its simple configuration and due to the low number of power electronic modules (switching devices) as shown in Figure 3.15. In addition to that, using the half-bridge SM can reduce the MMC control complexity, hereafter the positions of half-bridge SM switching devices are presented in Figure 3.15 [116]. Switching devices T_1/D_1 represent the upper IGBT/diode of the half-bridge SM and the switching devices T_2/D_2 signify the lower IGBT/diode of the half-bridge SM. At normal operating condition, SM capacitor is either inserted or bypassed and the output voltage is either equal to V_{dc} or 0. Depending on the switches positions of T_1/D_1 , T_2/D_2 and the current direction, there are six switching states, as shown in Figure 3.15 and Table 3.2 [109].

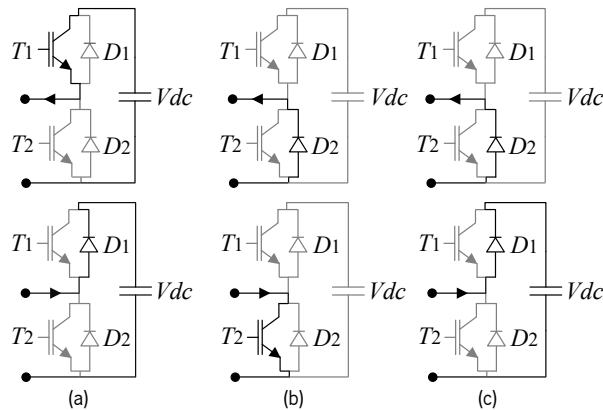


Figure 3.15. Positions of half-bridge SM switching devices: (a) SM switched on; (b) SM switched off; (c) SM blocked during the deadtime.

Table 3.2. Operating states of the half-bridge SM.

States	SM switches positions	T_1 state	T_2 state	Conducting switch	Direction of current	Capacitor state
1	Switch on	On	Off	T_1	←	Inserted
2	Switch on	Off	Off	D_1	→	Inserted
3	Switch off	Off	Off	D_2	←	Bypassed
4	Switch off	Off	On	T_2	→	Bypassed
5	Block (during deadtime)	Off	Off	D_2	←	Bypassed
6	Block (during deadtime)	Off	Off	D_1	→	Inserted

When the SM is required to be switched into MMC arm circuit, T_1/D_1 will switch on and T_2/D_2 will switch off. In this case, SM capacitor is charging or discharging according to the current direction i_{SM} . However, the opposite scenario is when the SM outputs a zero voltage into the MMC arm circuit. In this case, T_2/D_2 will switch on and T_1/D_1 will switch off. As a result, the SM capacitor will be always bypassed regardless the current direction i_{SM} . A deadtime band is required between both actions to avoid a short circuit fault during the switch transient state. Therefore and in such situations, when the system is in the pre-energization state or in deadtime band between switches, SM capacitor can be

either inserted or bypassed according to the current direction i_{SM} , and the current in this case flows only through the diodes D_1 or D_2 as explained in Figure 3.15(c) [97].

3.5.4 Case Study: Using Indirect MMC / Direct MMC as SFC for the 15 kV, 16.7 Hz Electrified Railway

The conventional AC/DC/AC back-to-back two-level converter normally requires a step-up power transformer at the side of 16.7 Hz. In addition, AC filters are required on both AC sides to meet the standards of 50 Hz PPS and 16.7 Hz of TPS. A single-line diagram of such system is presented in Figure 3.16 with two power transformers and AC filters. The converter efficiency is normally high, but the total system efficiency is low because of the filters and the power transformers losses. The overall system is bulky and entails some drawbacks, such as filtering requirement and the low efficiency. Therefore and as a result of the multilevel converter features, these transformer-less power converters are nowadays under interest [44].

SFC devices based on MMC have recently been proposed to interface the TPS (50 Hz or 16.7 Hz) and the PPS (50 Hz or 60 Hz). Normally, the SFC based on an indirect MMC is intended for fixed frequency applications, whereas, the SFC based on a direct MMC is proposed to obtain a lower value of output frequency (16.7 Hz or 25 Hz). In this framework, this item presents a detailed explanation to clarify the main reasons for this selection. Serving that purpose, direct and indirect MMC for 15 kV, 16.7 Hz are compared in terms of SMs energy storage, power losses, and complexity with regard to the number of filters and semiconductors [117].

As mentioned earlier, indirect MMC is equipped with half-bridge SMs and consists of a three-phase AC/DC converter and a single-phase DC/AC converter linked to a DC-link as shown in Figure 3.14. Filter inductors between MMC arms play an important role to limit the circulating currents between MMC arms. In addition, there is no need for using AC filters in both AC sides since the MMC passive components operate as inner filters. The multilevel output voltage waveform contains low harmonic contents [117]. On the other side, direct AC/AC MMC is equipped with full-bridge SMs and consists of a three-phase AC/AC converter without the need for a DC-link as shown in Figure 3.13. As already stated, the filter inductors between MMC arms can effectively reduce the power fluctuations, hence there is no need for using power filters.

A research team from ABB Ltd has accomplished a study about the SFC based on direct and indirect MMC for railway applications. The results have been published in [117] after considering the same rated power and the same parameters for PPS and TPS as presented in Table 3.3. In other words, this

study is performed under the same loading parameters when using the SFC based on direct or indirect MMC.

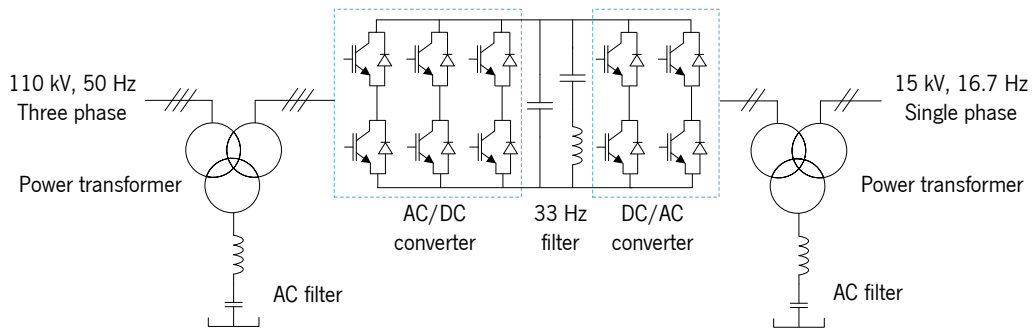


Figure 3.16. Conventional AC/DC/AC back-to-back two-level converter in 15 kV, 16.7 Hz traction power system.

Both converters were designed in ABB Ltd after considering the customer requirements in terms of overvoltage and other operation points. Maximum overvoltage was set to be around 18 kV (catenary voltage). Therefore, the maximum peak output voltage for each converter was around 25.5 kV. Each converter included eleven SMs with a DC-link voltage around 2.6 kV for each SM after assuming a voltage fluctuation around $\pm 10\%$. Both indirect and direct MMC with eleven SMs in each MMC arm create 12-level catenary line voltage. The final results waveforms for both solutions are presented in [117]. The capacitance of the SM capacitor is normally defined by the maximum SM voltage fluctuations, besides the energy fluctuations in MMC arms. The final selected values of the SM capacitors by ABB Ltd are presented in Table 3.3.

Table 3.3. Traction power system, public power system and MMC parameters.

Parameters		Symbols	Values
TPS	Rated power	S_n	15 MVA
	Rated phase voltage	U_n	15 kV
	Rated current	I_n	1000 A
	Rated frequency	f_n	16.7 Hz
PPS	Rated line-to-line voltage	U_{LL}	15 kV
	Rated frequency	f_{Ln}	50 Hz
	Rated current	I_{Ln}	575 A
Indirect and Direct MMC parameters design	Number of SMs in one arm	N_{SM}	11
	SM switching frequency	f_{isw}	250 Hz
	Equivalent switching frequency	f_{sw}	2.75 kHz
Capacitance of the SM Capacitor	Direct MMC	C_{DSM}	2.6 mF
	Indirect MMC (AC/DC side)	C_{I3SM}	1.3 mF
	Indirect MMC (DC/AC side)	C_{I2SM}	10.6 mF

The main power fluctuations in the SM capacitor of DC/AC indirect MMC have a frequency of 16.7 Hz. Therefore, a large capacitance is required for each DC/AC indirect MMC SM. However, the power fluctuations in the SM capacitor of AC/DC indirect MMC have the same PPS frequency of 50 Hz, then, SM capacitors of AC/DC indirect MMC are smaller than the ones of DC/AC indirect MMC as shown in Table 3.3. Reducing the capacitance value of the DC/AC MMC SM capacitor is possible if each SM is equipped with a 16.7 Hz filter. This choice makes the indirect MMC bulky and expensive.

According to a provided study from ABB Ltd in [117], direct AC/AC MMC SMs capacitors have lower values than the case in DC/AC indirect MMC. As a result and by summing the stored energies in the three legs AC/DC MMC SMs, then adding up the stored energies in the two legs DC/AC MMC SMs, this gives a very high stored energy in the SMs capacitors, especially after knowing the DC/AC indirect MMC SMs capacitors are the highest among the other capacitors [117]. The direct AC/AC MMC requires less than third of the stored energy compared to the indirect AC/DC/AC MMC at the same load conditions. In addition, all of the AC/AC direct MMC SMs have the same capacitance value, then the full-bridge SMs operate under the same conditions. On the contrary, half-bridge SMs of the AC/DC/AC indirect MMC operate under two different conditions. Subsequently, SMs with different nominal values are required for the AC/DC/AC indirect MMC which is the main disadvantage of using that system under 15 kV, 16.7 Hz. As a conclusion, direct AC/AC MMC is an adequate solution in 15 kV, 16.7 Hz and more relevant than the indirect AC/DC/AC MMC. The last requires higher number of Power devices (SMs, coupled inductor, etc.,) and a larger volume for installation. On the other aspect, indirect MMC may demand more periodical maintenance and higher power losses as a result of the extra components, then, direct AC/AC MMC is a convenient solution to interface the PPS and the TPS.

Table 3.4. Comparison of SFC based MMC topologies for the application of rail electrification [118].

Parameter	Indirect MMC	Direct MMC
Energy storage	Higher	Lower
Device utilization	Unequal	Equal
Switching devices count	0.8 p.u.	1 p.u.
Power losses	Higher	Lower
Production and maintenance	Harder	Easier
Control complexity	Higher	Lower

3.6 Rail Power Conditioner

RPC is one of the FACTS devices to overcome the negative effects of NSCs and current harmonics in electrified railway systems. RPC also compensates the voltage fluctuation by exchanging power

between the load sections. It is sometimes regarded as a two-phase STATCOM [88]. Its structure contains single-phase back-to-back converters with a single DC-link in between, as shown in Figure 3.17. Each converter is connected to a load section through a step-down coupling transformer. The first implemented proposal of 60 kV, 20 MVA RPC for *Tohoku Shinkansen* railway in Japan was in 2004 [119]. The implemented RPC at that time was based on multilevel converters and a Scott power transformer [120]. Another project was implemented in March 2009, RPC systems with gate-commutated thyristors were installed in four substations of the *Tokaido Shinkansen* in Japan: the *Shimizu* substation, *Shin-Kikugawa* substation, *Shin-Biwajima* substation and *Ritto* substation. Detailed information of that project can be found in [121].

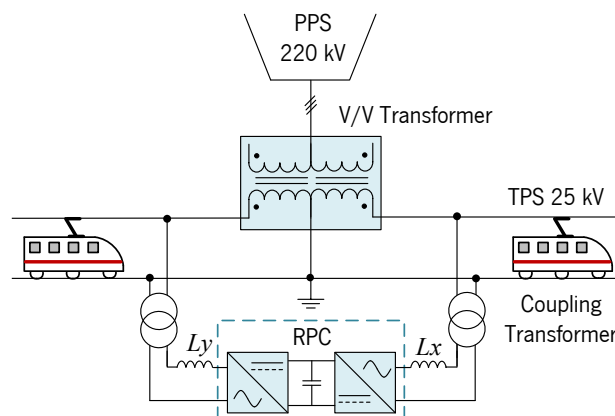


Figure 3.17. Rail Power Conditioner (RPC).

The RPC can balance the active power drawn by the main feeder two-phases of the TPS. This is possible by shifting half of the load active power difference from the highly loaded section to the lightly loaded one [49]. However, balancing the active power drawn by the two-phases is not enough to achieve balanced three-phase currents of the PPS. Therefore, the RPC also compensates the reactive power, where one of the RPC converters provides a capacitive reactive power while the other converter compensates an inductive reactive power [122]. Normally and when using V/V power transformer, the section x converter compensates a quantity of a capacitive reactive power and the section y converter compensates a quantity of an inductive reactive power [122]. When using Scott power transformer, the reactive power compensation is not a vital factor, then, the RPC in that case can be designed with lower power ratings. Since the load power is mainly provided by the PPS through a V/V or a Scott power transformer, unlike the SFC, RPC cannot perform a direct frequency conversion but, on the other hand, the load sections can be overloaded as an advantage of the RPC partial contribution in load power delivery [57]. The SFC provides catenary voltage regulation due to the AC/DC/AC power conversion but the disadvantage is that SFC should transmit all the load power, which sometimes makes this solution bulky and expensive. Also, the problem of the neutral sections can be reduced by using a co-phase RPC system (explained in the item 4.6) [45]. In that case, neutral sections for only

safety reasons can be added between the substations. The new recommended RPC topologies are the ones based on the MMC, so the step-down coupling power transformers can be avoided as shown in Figure 3.18 [122].

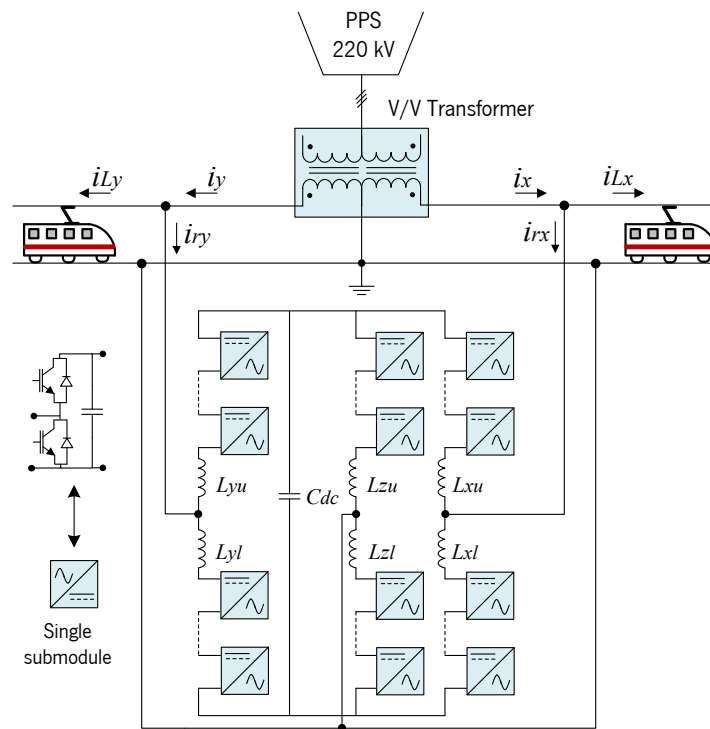


Figure 3.18. RPC based on MMC.

Table 3.5 shows a comparison between the active power compensators that can be used for railway electrification, including the potential capabilities for each power compensator (e.g., Harmonics and NSC compensation capability, the ability of frequency conversion, overloading capability). For more details and since the RPC is the main interest of this Ph.D. thesis, chapter 4 presents more extensive information about the RPC system, including the operation principle, the control algorithm, and the simulation results for different RPC topologies.

Table 3.5. Comparison between different compensator topologies in railway electrification [49].

Characteristics	SVC	STATCOM	SFC	RPC
Harmonics Filtering	No	Yes	Yes	Yes
NSC Compensation	Yes	Yes	Yes (inherent)	Yes
Frequency Conversion	No	No	Yes	No
Catenary voltage regulation	No	No	Yes	No
Neutral Sections	Yes	Yes	Can be reduced but maintained for safety reasons	Can be reduced but maintained for safety reasons
Overload Capability	No	Yes	No	Yes
Power Rating (p.u. Load) [44]	≈ 0.58	≈ 0.58	$= 1.00$	$\approx 0.50 \div 0.58$
Passive Filter Size on PPS	Large	Small	Medium	Small

3.6.1 Case Study: Comparison between Static Frequency Converter and Rail Power Conditioner Based on Indirect Modular Multilevel Converter for Railway Applications

A comparative study between two different active power compensators is presented in this item, namely, the SFC based on an indirect MMC as in Figure 3.14 and the RPC based on an indirect MMC as in Figure 3.18. Both systems of the SFC and the RPC operate at medium-voltage levels to feed the catenary line partially (e.g. RPC) or totally (e.g. SFC) and to overcome the harmonics and NSC of currents. This study mainly evaluates the estimated cost of implementation between solutions, besides the inherent benefits [91].

Different abilities and inherent benefits for both systems have been presented in Table 3.6 Both of the SFC and the RPC based on MMC can achieve balanced three-phase currents. However, each system has some advantages over the other. For instance, the SFC has a better fault current limitation at the TPS because of the coupled inductors connected directly to the catenary line [46], [91]. In addition, SFC can perform direct frequency conversion, in which, the TPS frequency can be different from the one of PPS [104], [114]. On the other hand, and because of using a V/V power transformer, RPC system has a better overloading capability than the SFC. RPC can be temporarily overloaded and at those conditions, it will only balance three-phase currents and dynamically filter harmonics up to its power capacity. This scenario likely to be acceptable in most of the cases as the limits associated with load balancing, NSC and harmonic compensation are usually statistical and temporary events [46]. On the contrary, SFC overloading is not recommended because it may damage the MMC power SMs [49].

Since the SFC can freely control voltage amplitudes, angles and the frequency of TPS [123], catenary voltage at such case has a direct relation with the indirect MMC performance. Therefore, the SFC is less robust than the RPC. Moreover, the SFC accepts load sharing with other power systems, namely, other neighboring substations linked to the SFC [46], [91]. It also prevents harmonics from passing to the PPS and it represents a balanced load without NSCs. However, RPC reacts in a different way through compensating these phenomena, and it also represents a balanced three-phase load [91], [123]. On the other hand, in case of SFC, the required passive filters at the PPS side to compensate the additional harmonics resulting from the low switching frequency are indispensable. Nevertheless, a higher MMC level signifies a higher equivalent switching frequency that entails a smaller size of passive filters at PPS side [116].

RPC system normally contains a neutral section that separates the catenary line for two load sections. However, using the SFC eliminates the neutral sections along the catenary line. Nevertheless, these neutral sections can be added for safety and security purposes when many SFC substations are linked

or when a combination of SFC substations and power transformers are linked in the form of a double-side feeding. Anyway, the latest RPC topologies, namely, the co-phase RPC system eliminates the neutral section in front of the substations but the one between the neighboring substations should remain for safety and security reasons. Hence, the number of total neutral sections could be reduced by half on the whole line compared to the normal RPC topology [124].

The estimated costs of the SFC and the RPC based on indirect MMC are close to each other and they have been analyzed in Figure 3.19. Cost estimation analysis took in to account the same output voltage level of MMC and eight factors to make the comparison: The number of switching devices or IGBTs; number of SMs capacitors; the coupled inductors between MMC arms; the size of passive filters at PPS to compensate harmonics; the required sensors that are important to obtain the control signal; the power ratings of the switching devices; the control implementation for each system; and the need of a power transformer [91].

The SFC system requires more switching devices (IGBTs), SM capacitors and coupled inductors between MMC arms than the RPC system based on MMC as shown in Figure 3.14 and Figure 3.18. Consequently, that entails for extra sensors in the SFC system. In addition, IGBTs power rating is a very important factor to estimate the costs of each system. For instance, and as has mentioned before, the locomotive's energy in case of the SFC is mainly handled by the MMC IGBTs, while in the case of RPC, this energy passes through the V/V power transformer and the MMC, in this case, compensates harmonics and NSCs. As a result, using the SFC system obligates to use higher IGBTs power ratings, which will definitely increase the total SFC costs [91].

Table 3.6. Comparison between SFC and RPC based on an indirect MMC: different inherent benefits and the abilities for each system.

Properties	SFC based on MMC	RPC based on MMC
Fault current limitation	Good	Fair
Frequency conversion	Good	Not possible
Overload capability	Not possible	Good
Power factor correction	Good	Good
Sharing other loads	Good	Not possible
NSC compensation/prevention	Good	Good
Harmonic compensation	Good	Good
Reducing the number of neutral sections	Good	Fair

V/V power transformer is a vital part of the RPC system to step-down the input voltage and to obtain two load sections. A step-down power transformer is not a part of essential equipment in the SFC based

on MMC system, especially when the last is connected directly to the power grid and the Power Electronics devices can withstand the medium-voltage levels. The step-down power transformer is only useful if the Power Electronics devices cannot withstand the high-voltage values. However, an isolation power transformer can be used for the protection and safety purposes between the SFC based on MMC and the three-phase PPS. As a conclusion, V/V transformer may increase the total costs of RPC system, but at the same time, it may enhance the overloading capability of the RPC, making this solution more reliable and robust than the SFC system [125].

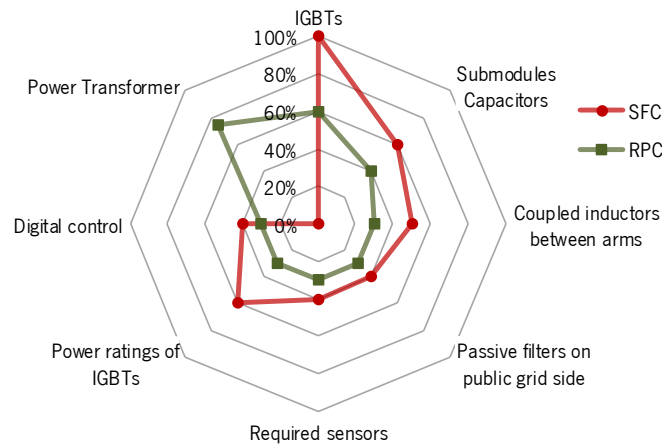


Figure 3.19. Comparison between SFC and RPC based on an indirect MMC: the estimated cost of implementation.

On the other aspect, passive filters are often required on the PPS to compensate some additional harmonics resulting from the low switching frequency. As a result, both systems of the SFC and the RPC have almost a close estimated cost of implementation, considering that the cost highly depends on the required MMC voltage level since a higher level demands an extra number of SMs, then, additional capacitors and power modules. Due to of some restrictions, Figure 3.19 does not present in detail the relative costs of each analyzed parameter but it gives a percentage ratio of the estimated cost for each equipment, after considering the total price of IGBTs in the SFC system as a reference to estimate the costs of other power devices [91].

3.7 Conclusion

The non-linear and the dynamic characteristics of the traction loads make the power quality improvement quite a difficult work. In this context, this chapter presented some of the flexible AC transmission systems (FACTS) devices that are used for the purpose of power quality improvement of the three-phase public power system (PPS). These devices could be controlled to follow the dynamic behavior of the non-linear traction loads. Along the chapter, the FACTS were described and compared to each other, giving a general overview of the main characteristics of each system. These FACTS were mainly based on voltage-source converters controlled by current to achieve compensation of harmonics

and negative sequence components (NSCs) of currents. The static VAR compensator (SVC), the static synchronous compensator (STATCOM), the static frequency converter (SFC) and the rail power conditioner (RPC) were the main FACTS introduced along the chapter. The focus has been more on the modular multilevel converter (MMC) topology with comprehensive introductory information, since it is one of the main topics of this Ph.D. thesis. In this term, comparative case studies between the SFC and the RPC based on MMC have been under the scope of this chapter. The direct AC/AC MMC and the indirect AC/DC/AC MMC, besides the half-bridge and the full-bridge MMC submodules, have been described to understand the MMC operation principle, which is significant to perceive the RPC based on MMC system that will be explained in the next chapter.

Chapter 4

Rail Power Conditioners in Electrified Railway Systems

4.1 Introduction

Electric locomotives in the AC traction power system (TPS) represent a huge single-phase non-linear load and detrimentally affect the power quality and the efficiency of the three-phase public power system (PPS) [46]. Some drawbacks are related to the continuous variations of the traction load, the harmonics distortion produced by the electric locomotives and the negative sequence components (NSCs) created by the three-phase currents imbalance [126]. Many power quality conditioners and compensation strategies have been developed and investigated in the last decades to overcome such phenomena and to guarantee an advantageous interface with the three-phase PPS. However, and within the appearance of high-speed electrified railway systems, those compensation strategies and power compensators have been recently enhanced to follow the latest technology and developments in the high-speed electrified railway systems that use the 25 kV, 50 Hz supply voltage [46].

Power quality improvement determines to use flexible AC transmission systems (FACTS) installed either at the PPS or at the TPS. For instance, static VAR compensators (SVC) are normally used to compensate the NSCs, but they have a limited tracking ability and a poor power factor correction. In addition, the SVC systems generate some harmonic contents [127]. The static synchronous compensator (STATCOM) devices are normally used to be installed at the three-phase PPS. Therefore, the cost is usually high compared with their compensation capacity.

In this framework, the rail power conditioner (RPC) is basically used to overcome the power quality deterioration, then maintaining balanced the three-phase power grid currents, without NSCs and with lower harmonic distortion. Usually, the RPC system is installed near the catenary neutral section of the traction substation (close to the secondary windings of the traction power transformer), which has two load sections with the same frequency and RMS voltage magnitude [44], [128].

Over the last decades, some railway substations, especially the ones in East Asia countries (Japan and China), have been equipped with RPC systems for their beneficial utilization with the balanced power

transformers (Scott, Woodbridge, LeBlanc and impedance-matching transformers) that are commonly used in that region. In that case, the RPC nominal power ratings will be lower since the RPC mainly shifts active power between load sections, and the reactive power compensation requirement is lower.

By considering the V/V transformer features presented in Table 2.2, the RPC with the V/V unbalanced power transformer can be an interesting solution, and therefore, this chapter presents a comprehensive analysis of the RPC systems with V/V power transformer at 25 kV, 50 Hz. The RPC topologies based on two-level converters can use single-phase full-bridge back-to-back converters, or two-phase three-wire converters, or even half-bridge back-to-back converters, sharing a DC-link in between [54].

This chapter also explains the RPC topologies based on the indirect AC/DC/AC modular multilevel converters (MMC), which is one of the main interests of this Ph.D. thesis. In addition to that, and along the chapter, it is explained the RPC operation principle and the associated control algorithms. In the final analysis, a comparative study between the RPC topologies under interest is executed in terms of the number of power component, control complexity, costs, volume, reliability and overall performance.

4.2 Rail Power Conditioner (RPC) Operation Modes

High-speed trains are single-phase non-linear loads that usually cause NSCs, current harmonics, imbalance of the three-phase currents, and low power factor in the three-phase PPS [129]. These power quality phenomena occur regardless of the used power transformers (unbalanced transformers or balanced transformers) that interface the PPS and the TPS. However, the effect of power quality distortion is higher when using unbalanced transformers. For instance, and to solve the problem of poor power factor, reactive power exchange should not be between the traction loads and the three-phase PPS, then, traction loads have to exchange reactive power with a third party (e.g., power compensator) [49]. The key feature of the RPC is the potential of different operation modes, in which each operation mode can be implemented by using the same converter hardware, but the converter control is quite different. The operation modes can be either implemented to increase the power capacity of the traction substation or to solve one or more of the power quality problems. When the two terminals of the RPC are connected to a single-phase traction power grid, the RPC can operate as an SVC. On the other hand, when the two terminals of the RPC are connected to two-phase traction power grid, the RPC can transfer active power between the two-phases [121].

4.2.1 Rail Power Conditioner Traditional Operation Mode

RPC devices are very effective in compensating the NSC of currents and the harmonic contents in electrified railway systems. The presented RPC schemes, in this chapter, are based on the split of the

TPS into two load sections separated by isolators, known as catenary neutral sections. The pantograph may produce arcs when it crosses over the neutral sections due to the electric current interruption. To avoid such circumstances, the speed limit is usually applied when the locomotive moves from a load section to another [129]. RPC devices are designed to tolerate the overloading circumstances that could happen when several locomotives operate at the same load section. The RPC system should deal with harmonics compensation, presenting a balanced load seen by the PPS and correcting the three-phase grid power factor to unitary. Figure 4.1 shows the RPC system basic operation principles when both load sections (x and y) are unequally loaded ($P_x > P_y$) and when using V/V power transformer. In this case, the RPC system shifts half of the active power difference from the highly loaded section (section x) to the lightly loaded one (section y). Table 4.1 presents the capabilities of the RPC operation mode.

The shifted active power by the RPC, P_C , is presented as in (4.1). The power factor of PPS is close to one since the required reactive power for both load sections is always provided by the RPC compensator. The reactive power exchange between the TPS and the RPC is bidirectional according to the loading conditions and the used power transformer to interface the three-phase PPS and the single-phase TPS. It is noteworthy to mention, the power consumption losses of the TPS equipped with RPC are higher due to the additional losses in the RPC components [130].

$$P_C = 0.5 (P_x - P_y) \quad (4.1)$$

Table 4.1. Capabilities of the RPC operation mode.

Active power shifting	Reactive power compensation	Harmonics cancelation	Catenary voltage stability
✓	✓	✓	✗

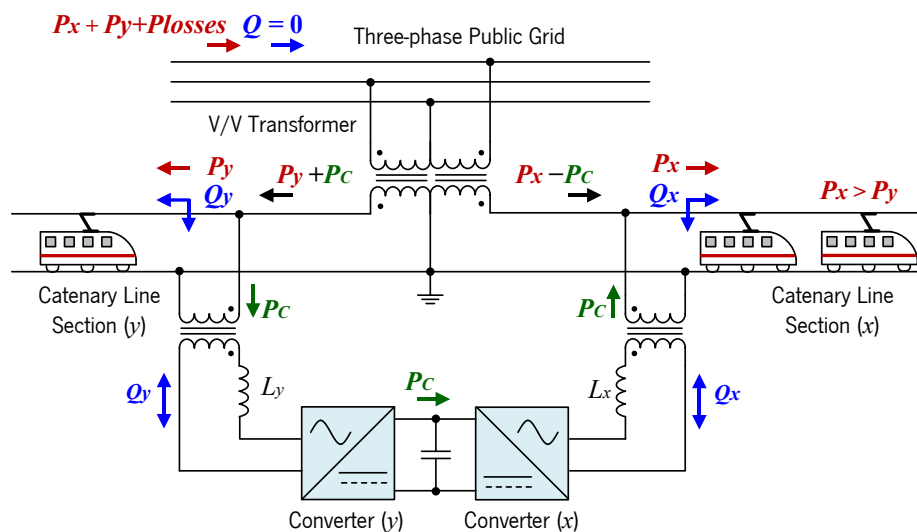


Figure 4.1. Principles of the RPC system.

4.2.2 Static VAR Compensator Operation Mode

Normally, the traction power transformers, such as the V/V and the Scott, are constituted by a three-phase input and two-phase output. When one of the traction transformer output phases is disconnected due to the periodic maintenance, in this case, the SVC mode based on a single-phase power transformer is implemented, as shown in Figure 4.2. Accordingly, the active power cannot be shifted between the load sections, and the RPC operates as an SVC system only to compensate reactive power and harmonic distortion as presented in Table 4.2. The RPC based on the SVC mode calculates the reactive power of the substation according to the load section currents and voltage deviation, then, the converter controls the reactive power that has a reverse polarity of the calculated reactive power to accomplish reactive power compensation. The converter x and converter y are connected in parallel, and therefore, each converter injects half of the reactive power amount [120], [131].

Table 4.2. Capabilities of the RPC operating in the SVC mode.

Active power shifting	Reactive power compensation	Harmonics cancelation	Catenary voltage stability
×	✓	✓	×

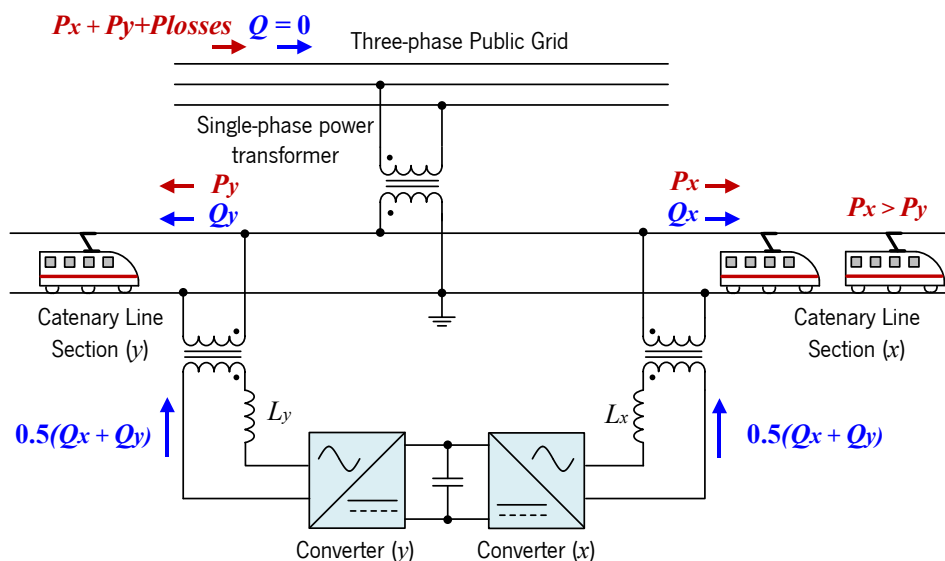


Figure 4.2. RPC operating in the SVC mode (RPC based SVC).

4.2.3 Catenary Voltage Regulator Operation Mode

Additional operation mode is when the RPC is not directly connected to the traction substation, but it is connected to a certain point along the overhead catenary line, as shown in Figure 4.3. In that case, no active power shifting, or reactive power compensation is applied in this scenario. However, the converter, in this case, can produce reactive power to compensate the feeding voltage drop caused by the loads of the catenary load sections, as presented in Table 4.3. The voltage regulation in the overhead catenary lines occurs due to the internal impedance of the line. On the other hand, this

operation mode overcomes the effect of the three-phase power grid voltage oscillations to maintain constant overhead catenary voltages. The catenary voltage adjustment close to the connection point is achieved by controlling the reactive power output, Q_x , Q_y [119], [131]. It is worthy to mention that reactive power compensation can be made instead of catenary voltage stability. On the other side, this scheme is hardly possible. The open-loop voltage in each traction substation is different and high circulating currents can happen.

Table 4.3. Capabilities of the RPC operating in the catenary voltage regulator mode.

Active power shifting	Reactive power compensation	Harmonics cancelation	Catenary voltage stability
×	×	×	✓

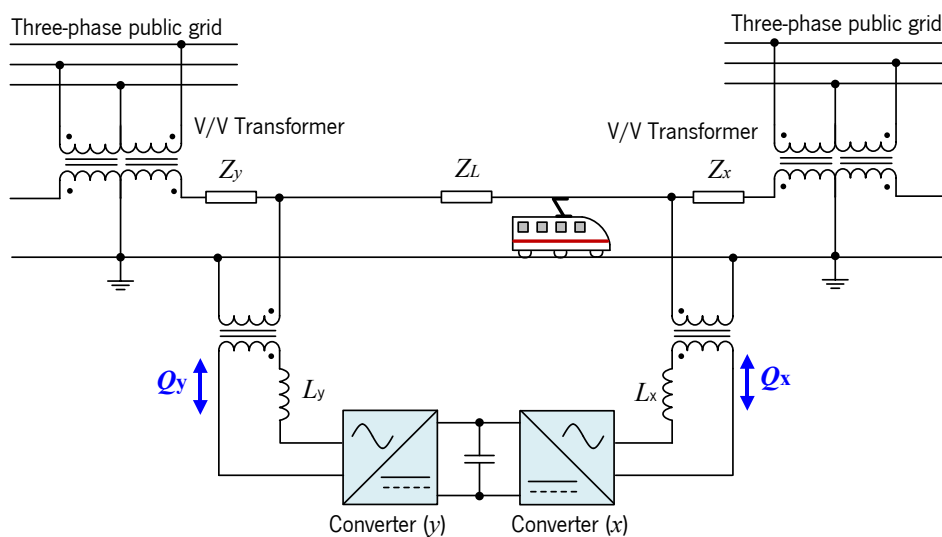


Figure 4.3. RPC operating in the catenary voltage regulator mode.

4.2.4 Interface Converter Between Two Collateral Substations

Additional operation mode is when the RPC operates as an interface converter between two collateral substations, as shown in Figure 4.4. The interface converter, in this case, is used to interface between two phases (with different out-of-phase angles). The control of the interface converter is quite different from the one in the conventional RPC application. The RPC operating as an interface converter, is mainly used for the purpose of power transfer by controlling the converter as a voltage source or current source to extract power from two substations instead of only one substation. In other words, it is possible to shift the active power from one substation to another, but this solution has no ability to compensate the NSC of currents, then, the three-phase currents may suffer from imbalance. Table 4.4 presents the main capabilities of this solution.

In [132], an RPC interface converter located between two traction substations is presented and commercialized by *Hitachi, Japan*. The system commenced operation in 2015 and is designed to shift

active power from one substation to another, including the energy resulting from the regenerative braking of the trains. The RPC converter was manufactured for the 22 kV AC catenary line and installed at the *Ushiku* neutral section between *Tsuchiura* and *Fujishiro* traction substations in Japan. Both traction substations are equipped with arithmetic units that compute the amount of electric power consumed and regenerated. Each of these units transmits the power data to a central control unit of the RPC installed at the neutral section between the traction substations. Digital subscriber line communication technology is used to a range of 10 km-20 km. The RPC was designed with a total capacity around 2.6 MW. However, and since regenerative electric power is frequently generated in large amount over short time duration, the power transformer and cooling system have been adapted by giving the system a one-minute overload capacity of 5.3 MW. A single-phase full-bridge power converter using the insulated-gate bipolar transistor (IGBT) switching devices is used, with a total DC-link of 6 kV. Besides the active power shifting capability, it is worthy to mention that reactive power compensation capability or catenary voltage stability can be implemented (not both simultaneously).

Table 4.4. Capabilities of the RPC operating as an interface converter between two substations.

Active power shifting	Reactive power compensation	Harmonics cancelation	Catenary voltage stability
✓	×	×	×

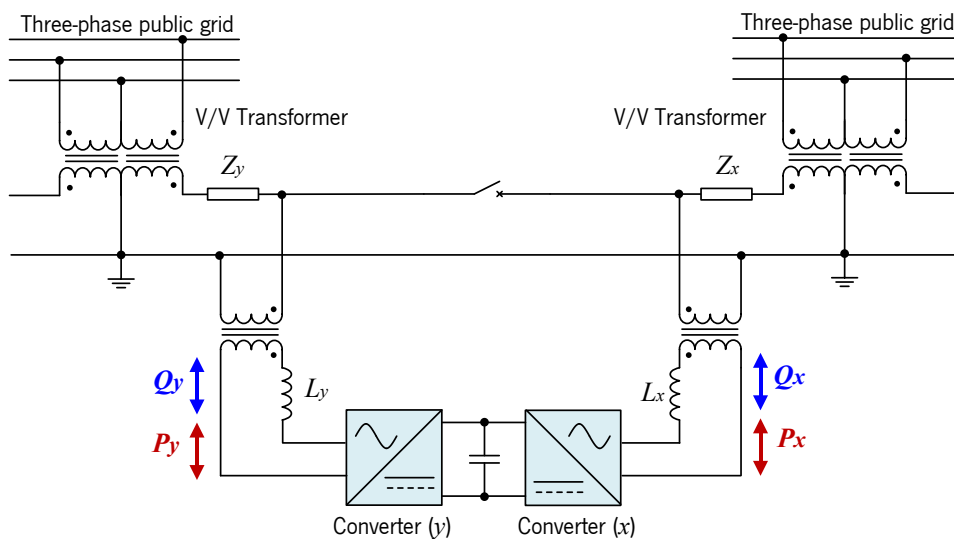


Figure 4.4. RPC operating as an interface converter between two substations.

4.3 RPC Based on Full-Bridge Back-to-Back Two-Level Converter and V/V Power Transformer

In order to eliminate the effects of NSC and harmonic distortion in the three-phase PPS, when a V/V unbalanced power transformer is used to interface the PPS and the TPS, RPC based on full-bridge back-to-back two-level converters (FB-RPC), sharing the same DC-link, can provide power quality improvement. The amount of NSC depends on the TPS topology, particularly, the type of used power

transformer. For instance, V/V transformers are widely used in high-speed railways due to their simple structure, low cost and high overload capacity compared to other power transformers [54].

It is important to declare that when using a balanced power transformer (presented in item 2.4.3), no NSCs of currents are injected into the PPS when both load sections consume the same power. However, when an unbalanced V/V power transformer is in use, the NSCs of currents injected into the PPS are half of the fundamental positive sequence components (PSCs) when both load sections are equally loaded [54]. RPC system is equipped with an ability of energy storage system is presented in [133]. This system uses a supercapacitor that is connected onto the DC-link of the RPC via a bidirectional DC-DC converter. The energy storage system is useful for reducing the peak power demand and the operating costs in a railway substation.

In AC railway electrification, the catenary line system can be modeled in sections with lumped impedances along it. However, in this Ph.D. thesis, these lumped impedances were not added to the figures of RPC leading to some assumptions in the RPC configurations. Nevertheless, different assumed values of lumped impedance were considered in the simulation of RPC systems. According to the European standard EN-50641, the lumped impedance for one tracking line has the value of $Z_L = 0.1 + j 0.1 \Omega/\text{km}$ in the 15 kV, 16.7 Hz system. On the other hand, the lumped impedance for one tracking line has the value of $Z_L = 0.15 + j 0.45 \Omega/\text{km}$ in the 25 kV, 50 Hz system [134]. The lumped parameters utilize the network equivalent impedance and they add more complexity to the RPC models. Therefore, the lumped impedance values in AC railway systems are only informative. The presented control algorithm and studies in this chapter are for the conventional application of RPC (NSC and harmonics compensation). Photos of the RPC devices in Shin-Numakunai substation in Japan, besides some technical aspects, are presented in [135].

Figure 4.5 depicts the RPC system based on full-bridge converters and a V/V power transformer. The line-to-line three-phase voltage of PPS is stepped-down through the V/V power transformer to 25 kV catenary voltage. Since two of the RPC legs are connected to the same grounding point (the rail), step-down coupling transformers are necessary to avoid short circuits in the FB-RPC. In addition, and by considering the maximum voltage blocking of 6.5 kV of the commercially available IGBTs [112], the coupling transformers are important to step-down the catenary medium-voltage value to a lower value. Table 4.5 presents the components quantities of the FB-RPC.

Two filter inductors, L_x, L_y , are added to operate as an RPC filter. Figure 4.5 assumes that the right load section is called phase x and the left one is called phase y . The corresponded phases for \dot{U}_x and \dot{U}_y , are respectively \dot{U}_{AC} and \dot{U}_{BC} . Consequently, phasors diagram of the PPS before compensation

is shown in Figure 4.6(a) after assuming both load sections have a unitary power factor. The turns ratio of the three-phase V/V power transformer and the single-phase step-down coupling transformers are K_V and K_D , respectively. Normally, the three-phase currents of PPS are suffering from current imbalance and harmonic contents, then the three-phase currents are presented in (4.2) [136].

By assuming negligible power losses in the RPC, there will be an active power transfer with an amplitude of half the active power difference between load sections as in (4.3). This active power flows from the highly loaded section to the lightly loaded one. In this context, Figure 4.6(b) presents the phasors diagram when RPC shifts only active power from phase x to phase y [54], [136]. Phase A and phase B currents after active power shifting are as presented in (4.4) and (4.5).

Table 4.5. Components quantities of the FB-RPC.

Number of IGBTs	Number of capacitors	Number of inductors	Isolation/coupling transformer
8	1	2	2

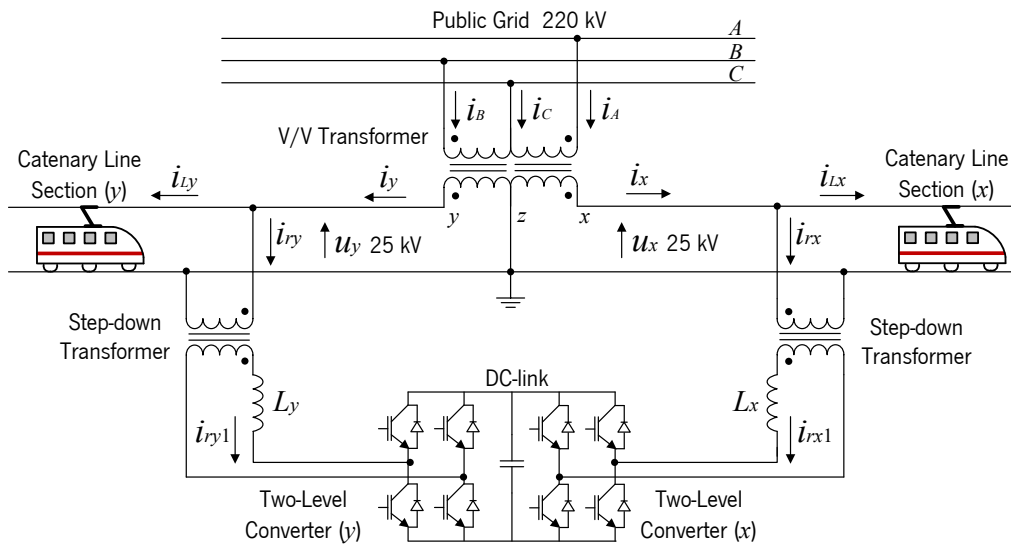


Figure 4.5. FB-RPC system with a V/V power transformer.

$$\dot{i}_A = \frac{I_{Lx}}{K_V} e^{j30^\circ}, \dot{i}_B = \frac{I_{Ly}}{K_V} e^{j90^\circ}, \dot{i}_C = -\frac{I_{Lx}}{K_V} e^{-j30^\circ} - \frac{I_{Ly}}{K_V} e^{-j90^\circ} \quad (4.2)$$

$$\Delta I = \frac{1}{2} (I_{Lx} - I_{Ly}) \quad (4.3)$$

$$\dot{i}_{A1} = \dot{i}_A - \frac{\Delta I}{K_V} e^{j30^\circ} = \frac{1}{2K_V} (I_{Lx} + I_{Ly}) e^{j30^\circ} \quad (4.4)$$

$$\dot{i}_{B1} = \dot{i}_B + \frac{\Delta I}{K_V} e^{j90^\circ} = \frac{1}{2K_V} (I_{Lx} + I_{Ly}) e^{j90^\circ} \quad (4.5)$$

On the TPS side (x, y, z), equation (4.6), Figure 4.6(b) and Figure 4.7 confirm that the RPC equalizes in magnitude between phase x and phase y currents after shifting the active power difference between

load sections. However, the three-phase currents, in that case, do not have equal magnitude as presented in (4.6).

$$I_{x1} = I_{Lx} - \Delta I, I_{y1} = I_{Ly} + \Delta I, I_{z1} = \sqrt{3} I_{y1} = \sqrt{3} I_{x1} \quad (4.6)$$

Phase *A* and phase *B* currents have now the same root mean square (RMS) value, but phase *C* has a different magnitude since the three-phase currents are still imbalanced (different magnitudes and different out-of-phase angles), as presented in Figure 4.6(b). However, phase *C* current is in phase now with its phase voltage, while the other two phases (phase *A* and phase *B* currents) have 30° out-of-phase with the corresponded phase voltages because the reactive power is not yet compensated.

In order to balance the three-phase currents, it is important to add a certain reactive current component to phase *x* and phase *y* as shown in Figure 4.6(c) [54]. Phase *x* generates reactive power because the reactive current component, \dot{I}_{rxr} , that is synthesized by the converter *x* leads the line-to-line voltage \dot{U}_{AC} , and its corresponded phase voltage on the secondary windings of the V/V power transformer, \dot{U}_x . Phase *y* receives reactive power because the reactive current component, \dot{I}_{ryr} , that is received by the converter *y* lags the line-to-line voltage \dot{U}_{BC} , and its corresponded phase voltage on the secondary windings of the V/V power transformer \dot{U}_y , as shown in Figure 4.7. The following equation (4.7) confirms equal RMS reactive components of compensation currents. Equation (4.8) presents the RMS then the instantaneous value of the section *x* current after compensation.

$$I_{rxr} = I_{x1} \tan \frac{\pi}{6} = \frac{1}{2} (I_{Lx} + I_{Ly}) \tan \frac{\pi}{6} \quad (4.7)$$

$$I_{ryr} = I_{y1} \tan \frac{\pi}{6} = \frac{1}{2} (I_{Lx} + I_{Ly}) \tan \frac{\pi}{6}$$

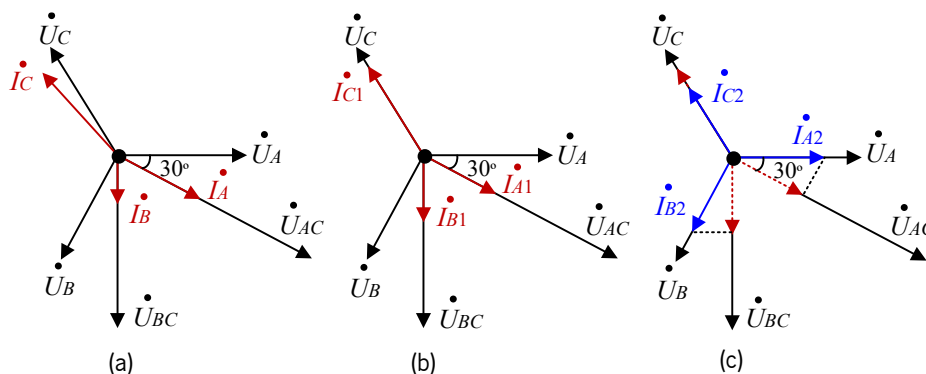


Figure 4.6. PPS phasors diagram: (a) Without compensation; (b) After shifting the active power difference; (c) After shifting the active power difference and compensate reactive power [57].

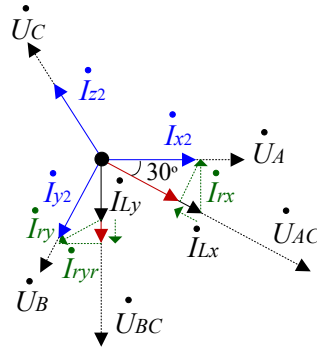


Figure 4.7. Phasors diagram on the secondary windings of the V/V transformer after compensation [57].

$$\dot{i}_{x2} = \dot{i}_{x1} + \dot{i}_{rxr} = \frac{1}{2} (I_{Lx} + I_{Ly}) \left[e^{-j30^\circ} + \tan \frac{\pi}{6} e^{j60^\circ} \right] = \frac{1}{\sqrt{3}} (I_{Lx} + I_{Ly}) e^{j0^\circ} \quad (4.8)$$

$$i_{x2} = i_{x2m} \sin \omega t = \frac{\sqrt{2}}{\sqrt{3}} (I_{Lx} + I_{Ly}) \sin (\omega t + 0)$$

The same previous steps are also applied for the phase y current, then equation (4.9) presents the instantaneous value of the section y current after compensation.

$$i_{y2} = i_{y2m} \sin \left(\omega t - \frac{2\pi}{3} \right) = \frac{\sqrt{2}}{\sqrt{3}} (I_{Lx} + I_{Ly}) \sin \left(\omega t - \frac{2\pi}{3} \right) \quad (4.9)$$

The total compensation currents (reference currents that should be generated by the RPC) of the two RPC converters can be obtained from Figure 4.7 and as in equation (4.10):

$$\begin{aligned} i_{rx}^* &= i_{x2} - i_{Lx} \\ i_{ry}^* &= i_{y2} - i_{Ly} \end{aligned} \quad (4.10)$$

4.3.1 Control Algorithm

RPC control algorithm includes the following parts: the reference signals generation, the DC-link voltage regulation, and the modulation technique to drive the switching devices. The compensation current references, i_{rx}^* and i_{ry}^* , should be synthesized by the RPC system to compensate harmonics, reactive power and NSC of currents. In that case, the three-phase PPS should have almost a unitary power factor, balanced three-phase currents and low harmonic contents. The reference currents can be extracted according to the following steps. The beginning is from the load sections instantaneous currents as in (4.11) [54].

$$\begin{aligned} i_{Lx} &= \sqrt{2} I_{Lxa} \sin \left(\omega t - \frac{\pi}{6} \right) + \sqrt{2} I_{Lxr} \sin \left(\omega t - \frac{2\pi}{3} \right) + \sum_{h=2}^{\infty} \sqrt{2} I_{Lxh} \sin (h\omega t + \phi_{xh}) \\ i_{Ly} &= \sqrt{2} I_{Lya} \sin \left(\omega t - \frac{\pi}{2} \right) + \sqrt{2} I_{Lyr} \sin (\omega t - \pi) + \sum_{h=2}^{\infty} \sqrt{2} I_{Lyh} \sin (h\omega t + \phi_{yh}) \end{aligned} \quad (4.11)$$

Where, I_{Lxa} and I_{Lya} , are the RMS active components of the load section currents. The currents of I_{Lxr} and I_{Lyr} , are the RMS reactive components of the load section currents. The currents components of I_{Lxh} and I_{Lyh} , are the h^{th} order harmonic contents for both sections, then, ϕ_{xh} and ϕ_{yh} , are the corresponded phase angles of the h^{th} order harmonic current.

Multiplying (4.11) of i_{Lx} by $\sin(\omega t - \pi/6)$, gives a DC current component of $\sqrt{2}/2 I_{Lxa}$, as presented in (4.12). On the other side, multiplying (4.11) of i_{Ly} by $\sin(\omega t - \pi/2)$ gives a DC current component of $\sqrt{2}/2 I_{Lya}$ [54]. The sum of the DC components of $\sqrt{2}/2 I_{Lxa}$ and $\sqrt{2}/2 I_{Lya}$, then multiplying the result with the value of $2/\sqrt{3}$ gives the peak value of phase x current after compensation, I_{x2m} , as a DC component after considering a unitary load power factor. This assumption is due to the electric locomotives normally contain power converters, and in such a case, load currents mainly contain active components and harmonics [125]. The RPC control block according to the previous analysis is shown in Figure 4.8. Extracting the DC current component is possible after using a 2nd order low-pass filter (LPF). On the other hand, enhanced phase-locked loop (E-PLL) is important to generate an output waveform whose phase is related to the phase of an input waveform (u_x or u_y).

$$i_{Lx} \sin\left(\omega t - \frac{\pi}{6}\right) = \frac{\sqrt{2}}{2} \left[I_{Lxa} - I_{Lxa} \cos\left(2\omega t - \frac{\pi}{3}\right) - I_{Lxr} \cos\left(2\omega t - \frac{5\pi}{6}\right) \right] + \sum_{h=2}^{\infty} \sqrt{2} I_{Lxh} \sin(h\omega t + \phi_{xh}) \sin\left(\omega t - \frac{\pi}{6}\right) \quad (4.12)$$

$$I_{x2m} = \sqrt{2/3} (I_{Lx} + I_{Ly}) \quad (4.13)$$

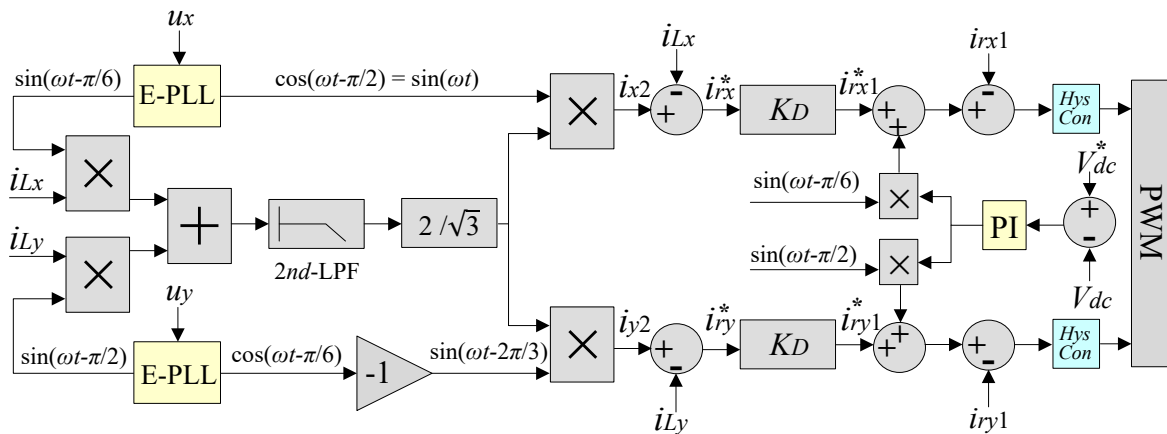


Figure 4.8. Control strategy of the FB-RPC converter.

After acquiring the total compensation current references of i_{rx}^* and i_{ry}^* , the values should be multiplied by the turns ratio factor, K_D , of the single-phase step-down coupling transformers. The total compensation current references, in that case, are i_{rx1}^* and i_{ry1}^* . The proportional-integral (PI) controller is used to regulate the RPC DC-link voltage. The output of this PI controller is then multiplied

by the correspondent Sine waves to synchronize between the PI output signal and the compensation current waveforms. The reference currents, i_{rx1}^* and i_{ry1}^* , include active, reactive, and harmonic components that are important to compensate NSCs, harmonics and reactive power at the three-phase PPS.

Tracking the reference signals is possible by using several types of controllers, such as hysteresis control, PI control, proportional-resonant (PR) control and predictive control for each RPC converter. In case of using the hysteresis controller, the applied switching frequency could be inconstant, then the width of the hysteresis should have a proper value, where a high value may cause low switching frequency and large tracking error. A low value of hysteresis may lead to high switching frequency accompanied by small tracking error [54], [137]. PI controller is simple but is not so efficient for tracking the AC signals due to its steady-state error. However, and as an alternative solution, synchronous frame PI can reduce the steady-state tracking error in AC signals but it requires multiple frame transformations. On the other hand, PR controller has many variables to be adjusted, which adds more complexity when using this type of controller. Predictive control can be a good solution, but it requires to conclude the equivalent mathematical model of the RPC system. In this study, hysteresis controllers are used to follow the compensation current references.

4.3.2 Simulation Results

To verify the presented control strategy of the RPC, high-speed electric locomotive can be modeled as a resistive load R_1 in parallel with an uncontrolled single-phase rectifier connected to the secondary windings of the locomotive transformer. The DC voltage output of the uncontrolled rectifier is connected in series to a resistance R_2 and an inductance L_2 , as presented in Figure 4.9. The locomotive transformer has turns ratio of 25/1.5. The simulation model assumes that both load sections are loaded but section x has twice the load of section y . The load parameters are presented in Table 4.6. On the other hand, parameters of the FB-RPC simulation model are presented in Table 4.7 [54]. Simulation results presented in this chapter are acquired after using the *PSIM*V.9.1 tool for Power Electronics simulation.

Table 4.6. Load parameters of the FB-RPC converter.

Symbols	Section x	Section y
R_1	0.8 Ω	1.6 Ω
R_2	1 Ω	2 Ω
L_2	2 mH	4 mH
P_L	4.8 MW	2.4 MW

Table 4.7. Parameters of the FB-RPC simulation model.

Description	Symbols	Values
Line-to-line PPS voltage	U_{AB}, U_{BC}, U_{CA}	220 kV
Catenary voltage	U_x, U_y	25 kV
RPC filter inductance	L_x, L_y	2.2 mH
Catenary lumped impedance	Z_L	$0.05 + j 0.15 \Omega$
Capacitance of the DC-link capacitor	C_{dc}	80 mF
Turns ratio of the V/V power transformer	K_V	220/25
Turns ratio of the step-down coupling transformer	K_D	25/1

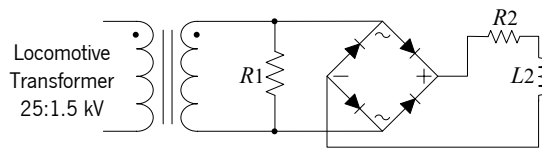


Figure 4.9. Locomotive equivalent circuit used in the simulation model.

Figure 4.10(a) shows the three-phase PPS currents before compensation. These currents are suffering from NSCs and a high harmonics distortion. In other words, there is an imbalance of the three-phase currents, where i_A has double the value of i_B , and phase C current has the maximum value that is resulting from the sum of both waveforms of i_A and i_B . The same description is applicable for the currents at the secondary windings of the V/V power transformer, i_x , i_y , and i_z . Figure 4.10(b) presents the three-phase PPS currents after applying the FB-RPC compensation strategy. In that case, the PPS currents become balanced and sinusoidal.

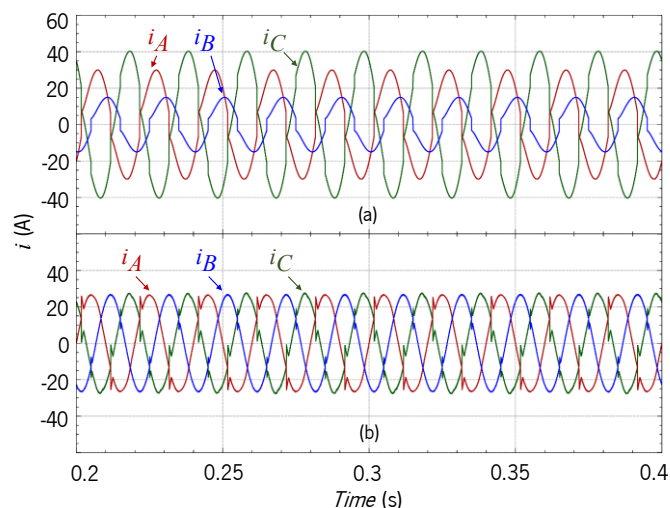


Figure 4.10. FB-RPC simulation results: (a) Three-phase currents before compensation; (b) Three-phase currents after compensation (when both of the load sections are loaded).

Figure 4.11(a) shows the load section currents of i_{Lx} and i_{Ly} , where the current i_{Lx} has double the value of i_{Ly} . The load section currents contain harmonic contents caused by the uncontrolled bridge rectifiers in the locomotives. These current waveforms are very important to calculate the compensation

current references, bearing in mind, the load section currents are not related to the RPC compensation currents. However, they are only related to the applied catenary voltage and the load equivalent impedance. Figure 4.11(b) presents the secondary windings currents of the V/V power transformer after compensation. These currents have 120° out-of-phase (after compensation) instead of 60° out-of-phase (before compensation) due to the reactive power compensation and active power shifting performed by the RPC. It is noteworthy to mention, the used power transformers in the simulation model are considered as ideal ones without considering leakage flux, copper losses and core losses. In other words, the ideal transformer gives an output power exactly equal to its input power.

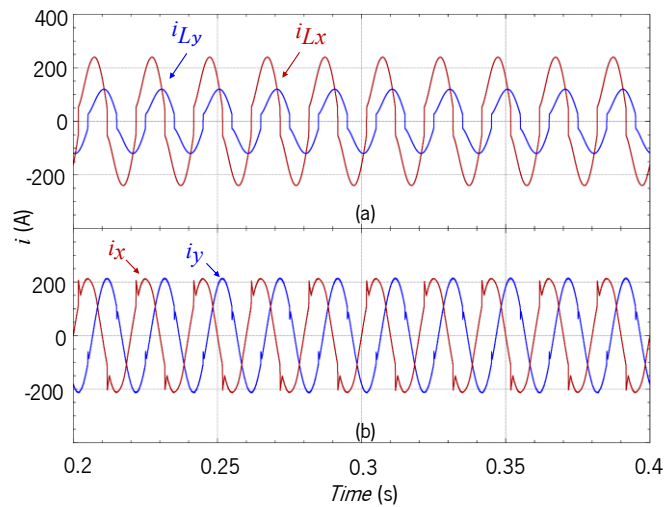


Figure 4.11. FB-RPC simulation results: (a) Load section currents; (b) Currents at the secondary windings of the V/V power transformer after compensation (when both of the load sections are loaded).

Figure 4.12(a) shows the DC-link voltage of the FB-RPC. The applied PI controller operates to keep a constant DC-link voltage close to 2 kV. The RPC converter should synthesize actual currents similar to the compensation currents references. The compensation currents of i_{rx1} and i_{ry1} , synthesized by the RPC to compensate harmonics, reactive power and NSC are presented in Figure 4.12(b).

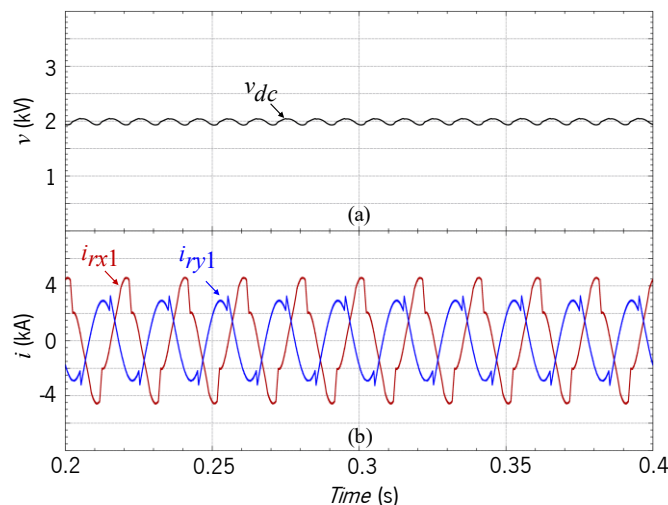


Figure 4.12. FB-RPC simulation results: (a) DC-link voltage; (b) Compensation currents (when both of the load sections are loaded).

Next results are presented when only one load section is loaded. Since the active power difference between sections is higher, this is the worst-case scenario, and the RPC in that case works at higher operating power. This scenario has a greater possibility in the electrified railway systems as long as railway operators cannot ensure a continuous loading profile at both load sections. Therefore, this situation must be considered in order to ensure the reliability of RPC under different loading conditions.

Figure 4.13(a) shows the three-phase PPS currents before compensation, and when section x is the only loaded section. Phase A and phase C currents, i_A and i_C , have the same magnitude but phase B current equals to zero because load section y has no loads. In this case, the NSCs percentage ratio could reach up to 100% of the PSCs of current, which may cause additional power quality deterioration more than the case when both sections were loaded. The three-phase PPS currents after compensation are presented in Figure 4.13(b). Apparently, the three-phase currents after compensation have lower RMS value than the case when both load sections were loaded, as presented in Figure 4.10(b).

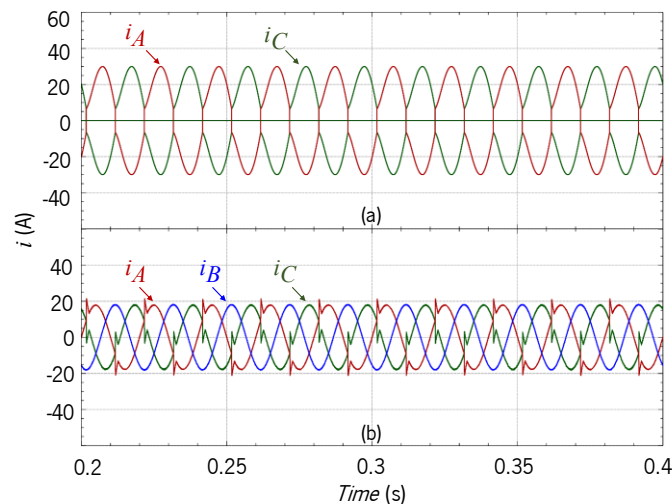


Figure 4.13. FB-RPC simulation results: (a) Three-phase currents before compensation; (b) Three-phase currents after compensation (when the load section x is loaded).

Figure 4.14(a) shows the load current i_{Lx} , that contains harmonic contents caused by the uncontrolled bridge rectifiers in the locomotive. Load section y current, in that case, equals to zero. Figure 4.14(b) presents the secondary windings currents of the V/V power transformer after compensation when only load section x is loaded.

Figure 4.15(a) shows the DC-link voltage of the FB-RPC when only load section x is loaded. This voltage follows its reference value of 2 kV as the PI controller functions to reduce the error between the actual and the reference value of the DC-link voltage. The compensation currents synthesized by the FB-RPC are shown in Figure 4.15(b). Section y compensation current waveform is, in this case, a pure sinusoidal as long as there is no load connected to the section y .

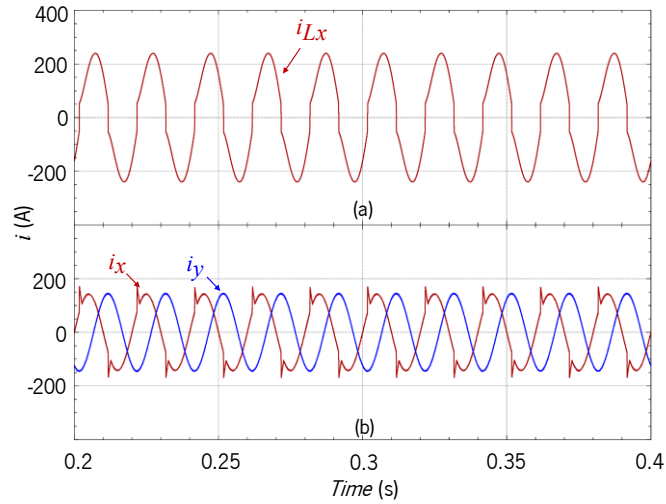


Figure 4.14. FB-RPC simulation results: (a) Load section current; (b) Currents at the secondary windings of the V/V power transformer after compensation (when the load section x is loaded).

On the other hand and although the three-phase PPS currents after compensation have a smaller RMS value than the case when both load sections were loaded, the compensation currents synthesized by the RPC in this case, as shown in Figure 4.15(b), are higher than the case when both load sections were loaded, as shown in Figure 4.12(b). This signifies higher operating power demand for the RPC system, including capacitors, inductors and power switching devices. As a conclusion, the design of the RPC system should always consider the worst-case scenario when only one load section is loaded.

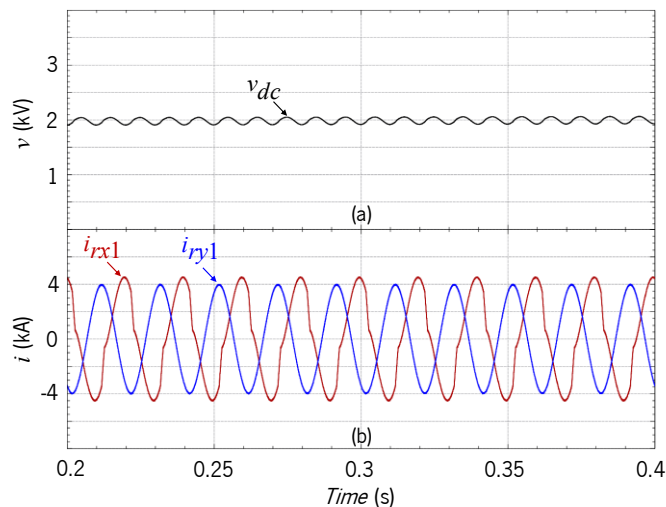


Figure 4.15. FB-RPC simulation results: (a) DC-link voltage; (b) Compensation currents (when the load section x is loaded).

4.4 RPC Based on Two-Phase Three-Wire Converter and V/V Power Transformer

This RPC system consists of two-phase three-wire converter (TW-RPC), which is fed by single-phase step-down coupling transformers connected to the TPS. There are six bidirectional switching devices, where one of the TW-RPC wires is connected to the grounded rail of the TPS. Hence, a leg with two switching devices are saved compared to the FB-RPC as shown in Figure 4.16. In that regard, authors

in [138] propose a three-wire quasi-Z-source RPC and authors in [139] propose a three-wire Z-source RPC to decrease the ratings of the RPC converter. It is worthwhile to mention that using a lower number of switching devices does not affect the TW-RPC power ratings, which is similar to the power ratings of the FB-RPC [60]. In other words, the TW-RPC topology has the same characteristics of the FB-RPC. Therefore, it can be considered as two single-phase converters merged together and sharing the same DC-link voltage [140]. Since each leg of the TW-RPC is connected to different phase or wire, it is not essential to have isolation transformers between the converter and the traction feeders. However, step-down coupling transformers are indispensable in this topology [48]. Also, the outer legs generate the compensation currents for phase x and phase y , respectively. In turn, the inner leg generates the compensation current of the common ground phase. Then, all the IGBTs in the TW-RPC topology have homogeneous stress. Table 4.8 presents the components quantities of the TW-RPC.

Table 4.8. Components quantities of the TW-RPC.

Number of IGBTs	Number of capacitors	Number of inductors	Isolation/coupling transformer
6	1	2	2

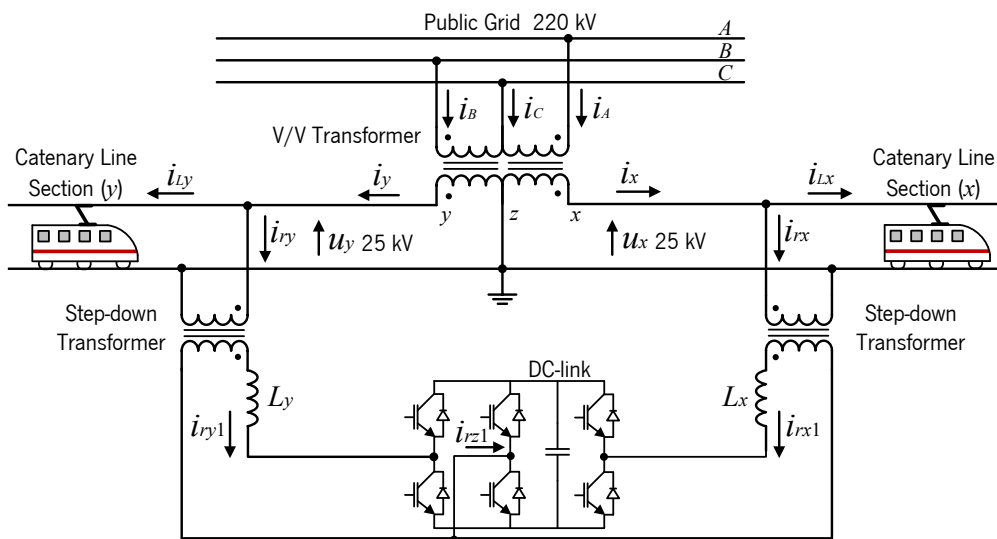


Figure 4.16. TW-RPC system with a V/V power transformer.

In some applications, the TW-RPC converter can be connected through three-phase step-down coupling transformer to the PPS instead of the single-phase TPS [95]. In that case, the solution is called shunt active power conditioner, which does not offer the operation modes flexibility that the RPC presents. Due to the use of the three-phase coupling power transformer, the shunt active power conditioner can be bulkier and more expensive converter than the TW-RPC converter.

The phasors diagram presented in Figure 4.6 and Figure 4.7 can be applied in the case of TW-RPC [60]. This results in obtaining the compensation current equations in (4.10), (4.14) and (4.15), where (4.14) shows the compensation currents in the phases after considering the turns

ratio of the step-down single-phase coupling transformer K_D . However, summing the vectors of \dot{I}_{rx} and \dot{I}_{ry} , in Figure 4.7, gives the compensation current of phase z , \dot{I}_{rz} , as presented in (4.15). The compensation current of phase z has an amplitude very close to the phase x and phase y compensation current amplitudes. Consequently, current ratings of the two switching devices connected to the grounded leg or phase are not increased. This is one of the main advantages of the TW-RPC topology [60], [140].

$$I_{rx1} = K_D I_{rx}, \quad I_{ry1} = K_D I_{ry}, \quad I_{rz1} = K_D I_{rz} \quad (4.14)$$

$$i_{rz1}^* = -(i_{rx1}^* + i_{ry1}^*) \quad (4.15)$$

4.4.1 Control Algorithm

The control strategy of the TW-RPC has the details presented in the item 4.3.1 but with adding the leg z control, as shown in Figure 4.17. The load section currents of i_{Lx} and i_{Ly} , are the main keys to calculate the compensation current references of i_{rx}^* and i_{ry}^* . Two single-phase E-PLL are used to create a signal whose phase angle is adaptively tracking the variations in the voltage x and the voltage y waveforms. In addition, 2nd order (LPF) is used to extract the peak value of $i_{Lx} \sin(\omega t - \pi/6) + i_{Ly} \sin(\omega t - \pi/2)$. Subtracting the waveforms of i_{x2} and i_{y2} (secondary windings of the V/V power transformer currents after compensation) from the waveforms of i_{Lx} and i_{Ly} , gives the required compensation currents synthesized by the TW-RPC as presented in (4.10) [60].

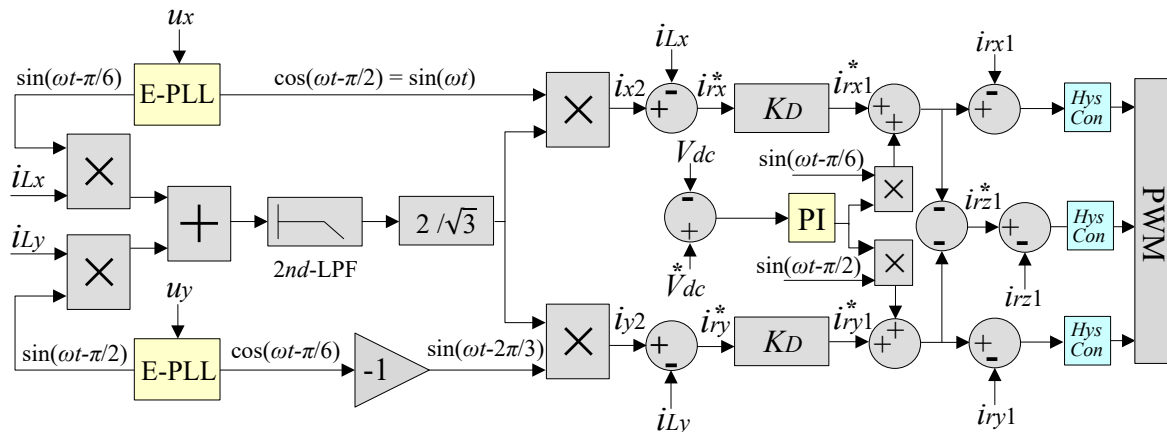


Figure 4.17. Control strategy of the TW-RPC converter.

The DC-link voltage control is similar to the one presented in Figure 4.8. In addition, three hysteresis controllers are used to correct the error resulting from the difference between the reference and the measured compensation currents. The final three-phase compensation current references have the values as in (4.10) and (4.15). It is worth noting that, using the TW-RPC instead of the FB-RPC does not increase the number of sensors required but additional current tracking controller is mandatory to drive the leg z switching devices [60].

4.4.2 Simulation Results

The overhead catenary lines of the load section x and the load section y are loaded with electric locomotives, which can be modeled using the equivalent circuit of the electric locomotive, as in Figure 4.9. The simulation model assumes that both load sections are unequally loaded. In this study, the overhead catenary line of phase x is loaded with a higher load, which has a value of 4.8 MW. On the other side, the overhead catenary line of phase y is loaded with a value of 2.4 MW (half of the loading value of phase x), as presented in Table 4.6. The parameters of the TW-RPC simulation model are presented in Table 4.9.

Table 4.9. Parameters of the TW-RPC simulation model.

Description	Symbols	Values
Line-to-line PPS voltage	U_{AB}, U_{BC}, U_{CA}	220 kV
Catenary voltage	U_x, U_y	25 kV
RPC filter inductance	L_x, L_y	2 mH
Catenary lumped impedance	Z_L	$0.03 + j 0.12 \Omega$
Capacitance of the DC-link capacitor	C_{dc}	80 mF
Turns ratio of the V/V power transformer	K_V	220/25
Turns ratio of the step-down coupling transformer	K_D	25/1

Figure 4.18(a) presents the three-phase PPS currents before compensation. These currents are imbalanced and contain harmonics and NSCs. There is 60° out-of-phase between the phase A and phase B currents. Under other conditions, Figure 4.18(b) presents the three-phase PPS currents after compensation when the TW-RPC balances the active power between the load sections, and compensates the reactive power. In that case, the three-phase PPS has a unitary power factor.

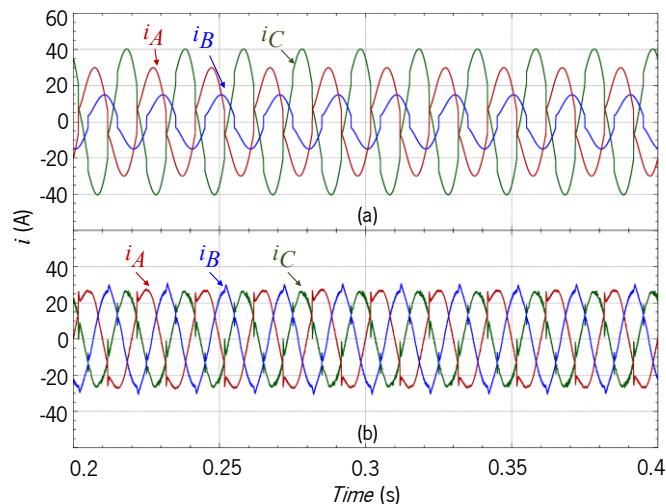


Figure 4.18. TW-RPC simulation results: (a) Three-phase currents before compensation; (b) Three-phase currents after compensation (when both of the load sections are loaded).

Figure 4.19(a) shows the same load section currents of i_{Lx} and i_{Ly} , that have been presented in Figure 4.11(a), where the load section x has double the value of the load section y . Figure 4.19(b) presents the currents at the secondary windings of the V/V power transformer after compensation. These currents have 120° out-of-phase (after compensation) instead of 60° (before compensation). In general, the simulation results presented in Figure 4.18 and Figure 4.19 confirm that the TW-RPC has a similar performance to the FB-RPC.

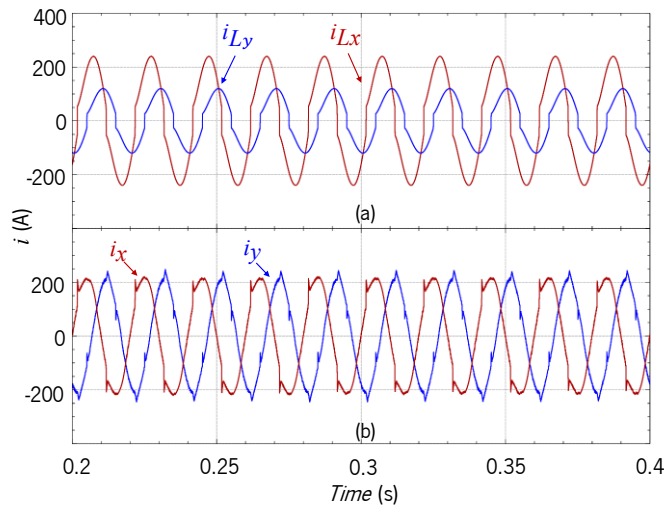


Figure 4.19. TW-RPC simulation results: (a) Load section currents; (b) Currents at the secondary windings of the V/V power transformer after compensation (when both of the load sections are loaded).

The DC-link voltage waveform of the TW-RPC is presented in Figure 4.20(a), where the waveform has voltage ripples with a frequency equals to 100 Hz. The DC-link voltage, in this case, follows its reference value of 2 kV, as was the case in the FB-RPC. The compensation currents synthesized by the TW-RPC to compensate NSC and harmonic contents are presented in Figure 4.20(b).

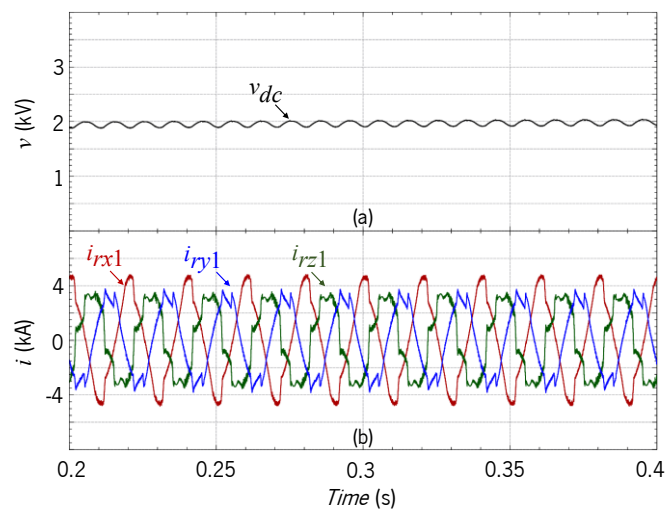


Figure 4.20. TW-RPC simulation results: (a) DC-link voltage; (b) Compensation currents (when both of the load sections are loaded).

The voltage stress across each of the power switching devices is similar to the one when using the FB-RPC as both of the topologies have the same DC-link voltage value. As a conclusion, the

compensation capacity of the TW-RPC is similar to the FB-RPC topology but with a lower number of power components for the TW-RPC [60].

4.5 Simplified RPC Based on Half-Bridge Two-Level Converter and V/V Power Transformer

This system consists of two half-bridge back-to-back converters connected by two capacitors with a mid-neutral point (HB-RPC), as presented in Figure 4.21. This RPC can reduce half of the required switching devices compared to the FB-RPC [130], which can decrease the power losses, complexity and the total costs of the HB-RPC system. However, the voltage stress of each switching device in the HB-RPC is double compared with the FB-RPC and with the TW-RPC as presented in Table 4.10. This determines to use switching devices with a higher voltage stress capability [140]. Table 4.11 presents the components quantities of the HB-RPC.

Table 4.10. Comparison between the HB-RPC and the FB-RPC.

Characteristics	FB-RPC	HB-RPC
IGBTs number	8	4
Voltage stress	1 p.u.	2 p.u.
Current stress	1 p.u.	1 p.u.
Switching frequency of IGBTs	f_{sw}	$2f_{sw}$

Table 4.11. Components quantities of the HB-RPC.

Number of IGBTs	Number of capacitors	Number of inductors	Isolation/coupling transformer
4	2	2	2

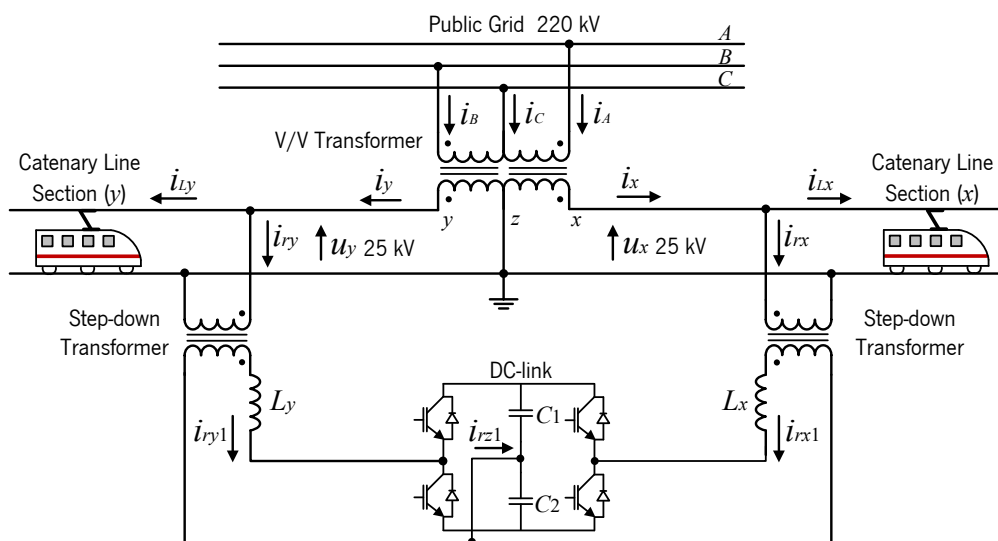


Figure 4.21. HB-RPC system with a V/V power transformer.

To have a similar performance between the RPC topologies under interest (FB-RPC, TW-RPC and HB-RPC), and by considering identical filter inductors in these topologies, the switching stress for each

switching device in the HB-RPC should be twice the value of the applied switching frequency in the FB-RPC and the TW-RPC topologies. Otherwise, a higher value of filter inductance is required for the HB-RPC because of the high current ripple as a result of the half-bridge schematic. On the other hand, using high switching frequency increases the switching losses of the switching devices. Simulation results, presented in [130], confirm that HB-RPC has a good performance regarding the power quality improvement in electrified railway systems, including NSC and harmonic contents compensation. Although the HB-RPC has some drawbacks as previously indicated but it provides one of the attempts to accomplish power quality improvement in the high-speed electrified railway systems [130].

4.5.1 Control Algorithm

The control algorithm of the HB-RPC is very similar to the ones of the FB-RPC and the TW-RPC topologies with some differences in the DC-link voltage control due to the mid-neutral point configuration [130]. This control algorithm is presented in Figure 4.22 after considering the equations introduced in the item 4.3. As was the case of the FB-RPC, there are only two hysteresis current tracking controllers. If the voltages of the DC-link capacitors are imbalanced, this will cause current distortion and waveforms fluctuation. Therefore, two PI controllers are important to achieve the voltage balancing between the capacitors. The first PI controller is used to compare the actual value of the DC-link voltage with its reference value ($V_{dc}^* = 4$ kV). The output of this PI controller is synchronized by multiplying the output signal with the correspondent waveforms. The second PI controller is mainly used to achieve the balance between DC-link voltages. One of the capacitor DC-link voltage is considered as a reference for the second capacitor voltage. Then, the input signal of the second PI controller is $\Delta V_{out} = V_{dc2} - V_{dc1}$, while the output signal is subtracted or added to the compensation current references i_{rx1}^* and i_{ry1}^* [130].

When the control system is at the positive half-cycle of $i_{r\sigma 1}^*$, $\sigma \in \{x, y\}$, and in order to get an increase in the reference current value to $|i_{r\sigma 1}^* + \Delta V_{out}|$, capacitor C_2 should discharge with more time in the control cycle to make the current increase, so the voltage of the capacitor C_2 will decrease. In a similar procedure, when the control system is at the negative half-cycle of $i_{r\sigma 1}^*$, and in order to get a reduction in the reference current value to $|i_{r\sigma 1}^* + \Delta V_{out}|$, the capacitor C_2 should charge with more time in the control cycle to make the current decrease, so the voltage of the capacitor C_2 will increase, making ΔV_{out} reduce to zero [48]. This control attempts to overcome the high fluctuations in the DC voltage waveforms of the DC-link capacitors [130].

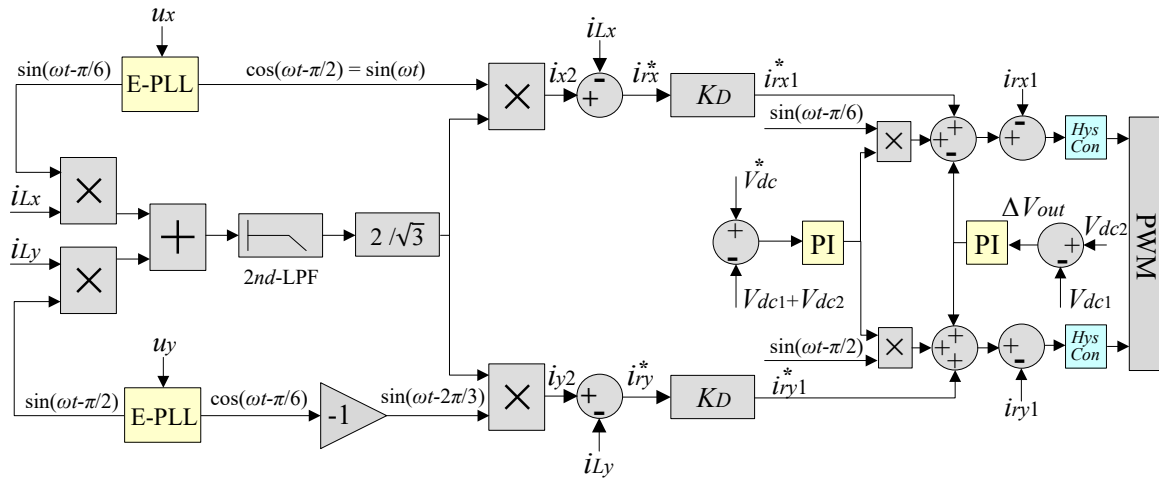


Figure 4.22. Control strategy of the HB-RPC.

4.5.2 Simulation Results

Parameters of the HB-RPC simulation model are presented in Table 4.12. The same load parameters presented in Table 4.6 are used in this simulation after considering a unitary load power factor for both load sections. It is worthwhile to mention how the HB-RPC requires a higher value of filter inductance, L_x and L_y , at the same switching frequency applied in the FB-RPC and the TW-RPC (using the same width of the hysteresis). However, it is possible to reduce the filter inductance value of the HB-RPC if the switching frequency is higher (by reducing the width of hysteresis). Higher switching frequency can increase the switching losses and the temperature of the power switching devices. Otherwise, the current waveforms of the three-phase PPS may contain higher harmonic contents. This is the main disadvantage of using the HB-RPC, besides the higher voltage stress across the power switching devices. Therefore, parameters of the HB-RPC should be carefully selected according to the aforementioned trade-off.

Table 4.12. Parameters of the HB-RPC simulation model.

Description	Symbols	Values
Line-to-line PPS voltage	U_{AB}, U_{BC}, U_{CA}	220 kV
Catenary voltage	U_x, U_y	25 kV
RPC filter inductance	L_x, L_y	3 mH
Catenary lumped impedance	Z_L	$0.03 + j 0.12 \Omega$
Capacitance of the DC-link capacitors	$C_1 = C_2$	50 mF
Turns ratio of the V/V power transformer	K_V	220/25
Turns ratio of the step-down coupling transformer	K_D	25/1

Figure 4.23(a) presents the waveforms of the three-phase currents before compensation. These currents are imbalanced and contain harmonic contents and NSCs of currents. Figure 4.23(b) shows the three-phase currents after compensating the reactive power and shifting half of the active power

difference from the highly to the lightly loaded section (from section x to section y). In that case, the imbalance ratio is lower since the three-phase currents are balanced and have sinusoidal waveforms.

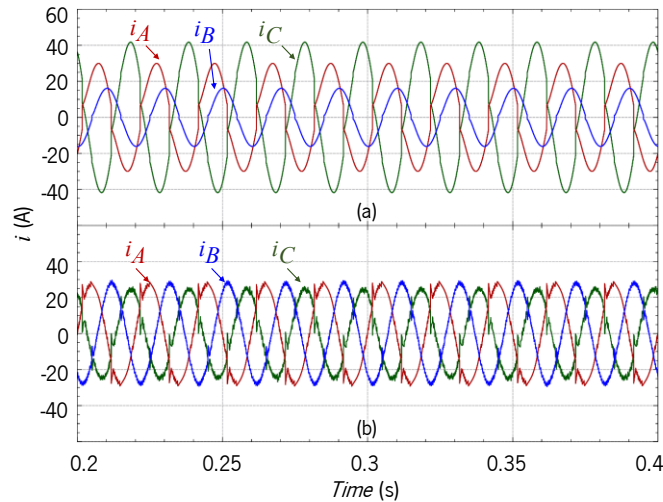


Figure 4.23. HB-RPC simulation results: (a) Three-phase currents before compensation; (b) Three-phase currents after compensation (when both of the load sections are loaded).

Figure 4.24(a) shows the load section currents of i_{Lx} and i_{Ly} , where the load section x has double the value of the load section y . The currents at the secondary windings of the V/V power transformer, i_x and i_y , are presented in Figure 4.24(b). After compensation, there is 120° out-of-phase between the currents of i_x and i_y . However, this phase difference was 60° before applying the compensation strategy. The results introduced in the Figure 4.24 are very similar to the ones presented in the Figure 4.11 (the case of the FB-RPC) and the Figure 4.19 (the case of the TW-RPC).

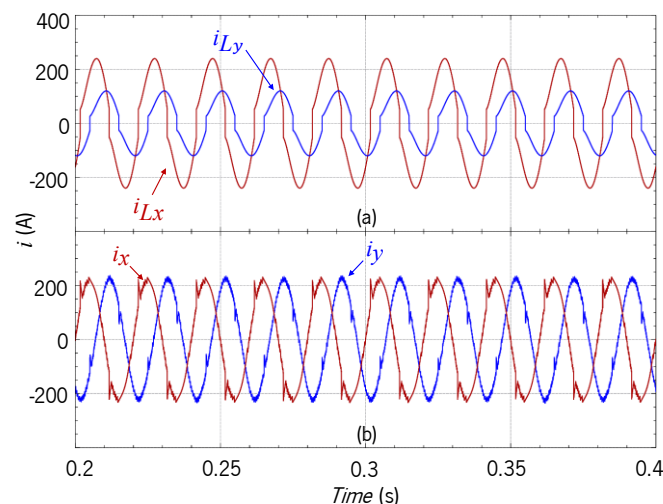


Figure 4.24. HB-RPC simulation results: (a) Load section currents; (b) Currents at the secondary windings of the V/V power transformer after compensation (when both of the load sections are loaded).

Figure 4.25(a) shows the total DC-link voltage of the HB-RPC. The PI controllers maintain the DC-link voltage around its reference value of $V_{dc}^* = 4$ kV. The higher the value of the stored energy in the HB-RPC DC-link capacitors, the better the dynamic response of the HB-RPC compensator. This is important to match the same dynamic performance of the FB-RPC and the TW-RPC compensators

[140]. The voltage waveforms of v_{dc1} and v_{dc2} , show that there is always one DC-link capacitor is charging while the other one is discharging, as has been previously explained in the item 4.5.1. The frequency of the total DC-link voltage ripples has a value close to 100 Hz. However, the voltage ripples across each capacitor have the frequency value close to 50 Hz, which implies using capacitors with high capacitance value, making the solution of the HB-RPC bulky and expensive.

Figure 4.25(b) presents the compensation currents synthesized by the HB-RPC to compensate the NSCs and the current harmonics. These currents are calculated by using the control strategy presented in Figure 4.22. The results are very similar to the ones presented in Figure 4.12(b) and Figure 4.20(b), but the current ripples are higher which demands to use a higher switching frequency or a higher value of filter inductors.

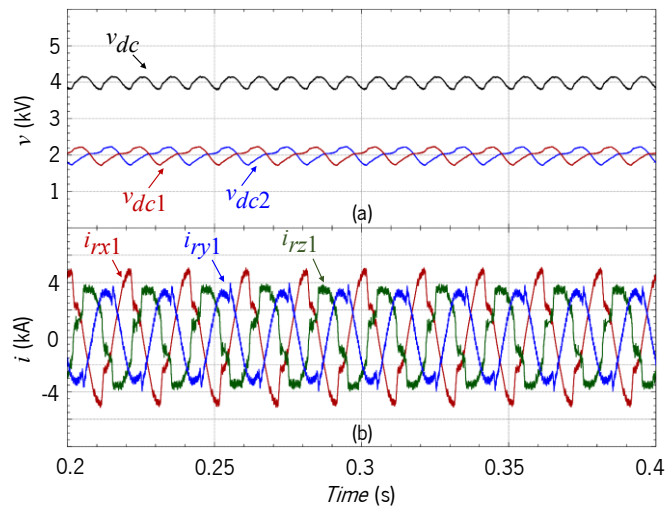


Figure 4.25. HB-RPC simulation results: (a) DC-link voltage; (b) Compensation currents (when both of the load sections are loaded).

4.6 Hybrid Co-Phase RPC Based on Full-Bridge Back-to-Back Two-Level Converter and Single-Phase Power Transformer

The aforementioned RPC topologies are connected to the TPS with an inductive coupling structure, bearing in mind that most of the traction loads are inductive in nature, this will increase the voltage drop across the coupling structure, leading to a higher RPC DC-link voltage. However, this voltage can be decreased by using a capacitive-inductive coupled structure such as a series LC branch [88]. The LC passive filter is used to compensate harmonics, besides its main role in minimizing the DC-link voltage. In that regard, a developed system, called hybrid co-phase RPC (co-HRPC) eliminates the needs for a neutral section at the TPS side when using a single-phase traction substation as shown in the Figure 4.26. Table 4.13 presents the components quantities of the co-HRPC.

Table 4.13. Components quantities of the co-HRPC.

Number of IGBTs	Number of capacitors	Number of inductors	Isolation/coupling transformer
8	2	2	2 or 1

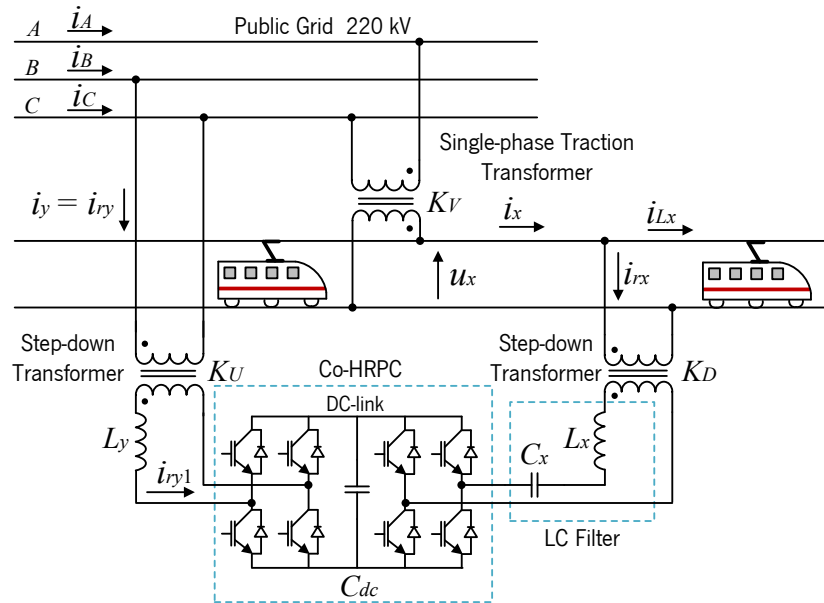


Figure 4.26. Co-HRPC with a single-phase power transformer.

However, and although the advantage of neutral section elimination in the co-phase connection (only the neutral sections in front of the traction substations), this is the worst operation scenario for the RPC converter. In the V/V transformer, RPC shifts half of the active power difference from the highly to the lightly loaded section and provides all the reactive power. However, in a single-phase traction transformer, this active power magnitude is equal to half of the total load active power, which is the active power magnitude that the RPC should always shift when using this type of transformer. Hence, the RPC power ratings can be higher [46]. In order to avoid this problem, it is possible to include a capacitor in one coupling branch. In that case, RPC operational voltage is significantly reduced when compared to the conventional RPC solutions. Then, a lower DC-link voltage is required for the back-to-back converter which reduces the power ratings of the switching devices as well.

The capacitive coupling phase of the hybrid RPC is connected to the secondary windings of the step-down power transformer with turns ratio of K_D . The other phase is connected to the three-phase power grid through a step-down power transformer with turns ratio of K_U . It is noteworthy to mention that, some studies recommend to insert double asymmetric capacitive-inductive structure in the two coupling branches of the RPC for a better heavy-load compensation capacity and lower DC-link voltage [141]. In that regard, a study of the co-phase RPC rated at 10 MVA in Meishan city in China is presented in [142].

In some applications, it is possible to dispense the step-down power transformer (the one with turns ratio of K_D) when a partial compensation is implemented [143]. This is a more economical solution, in which the compensation currents are expressed as a function of the power factor at the three-phase power grid. The use of the partial compensation helps to reduce the co-HRPC power ratings but it does not totally solve the problem of power quality deterioration [143]. Other studies introduce a partial compensation to reduce both the current and voltage ratings in which the hybrid RPC compensation currents vary with the converter operational voltage as well [93]. On the other hand, a flexible DC-link voltage control for the co-HRPC system is proposed in [144] to reduce the power losses during the RPC operation, besides reducing the RPC ratings.

Hybrid RPC can increase the loading capacity of the traction substation by transferring active power from the three-phase PPS to the single-phase TPS. Moreover, and when a full compensation is applied, all the reactive power is supplied by the co-HRPC, maintaining a unitary power factor of the three-phase power grid [93]. The hybrid RPC system may contain additional power filters to reduce the volume and power ratings of the system. In this context, a combination of RPC and SVC is presented in [145]. However, a coordinative control is necessary for two subsystems of RPC and SVC [146].

By using double-side feeding co-phase substations, as shown in Figure 4.27, this eliminates the neutral sections in front of the substations but the ones between the neighboring substations should remain for safety and security reasons. The double-side feeding system is applied when the load is always fed by two neighboring traction substations.

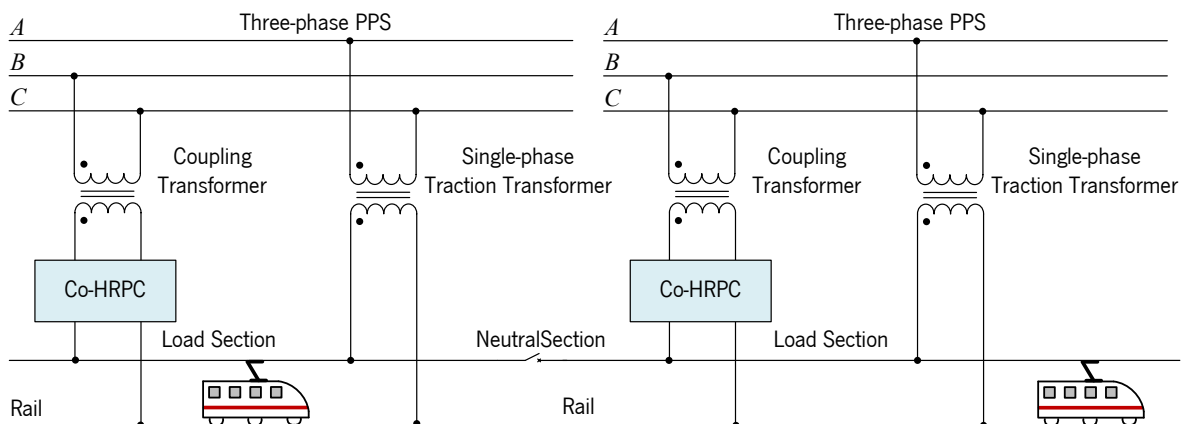


Figure 4.27. Double-side feeding co-HRPC substations.

When using double-side feeding V/V or Scott substations, the neutral sections in front of the substations besides the ones between the neighboring substations should remain. As a result, the total number of neutral sections could be reduced by half on the whole catenary line when using co-phase traction substations [124]. This allows the locomotives to reach a higher speed since they lose power and velocity when they are passing through the neutral sections [144]. The locomotives need fewer times

to pass through the neutral sections. Co-HRPC system improves the traction performance by increasing the power capacity. Consequently, the Co-phase system is more appropriate for supplying the high-speed railway than other traction schemes [147]. The first co-phase RPC was implemented in China, namely, in Meishan traction substation in 2010 [148], [88].

4.6.1 Control Algorithm

Since the co-HRPC only contains one load section, the input signal for the control algorithm is only the load section current, i_{Lx} , then, the load section y current is equal to zero ($i_{Ly} = 0$). The co-HRPC control algorithm is presented in Figure 4.28. As was the case of the FB-RPC. Two hysteresis controllers are used to correct the error resulting from the difference between the reference and the measured compensation currents. The final compensation current references have the values as in (4.10). The DC-link voltage control is similar to the one presented in the FB-RPC and the TW-RPC.

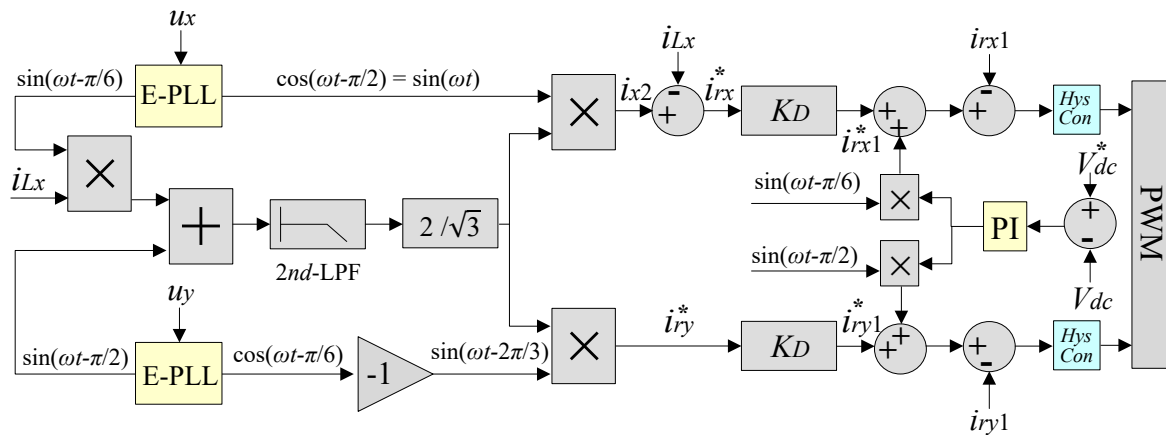


Figure 4.28. Control strategy of the co-HRPC.

4.6.2 Simulation Results

In order to study the effect of inserting the LC passive filter and to compare the co-HRPC system with the FB-RPC, simulation model of the co-HRPC will consider the same total load power when the load sections of the FB-RPC were unequally loaded, as presented in Table 4.6, with a total active load power value around $P_x + P_y = 4.8 \text{ MW} + 2.4 \text{ MW} = 7.2 \text{ MW}$. The results have been obtained after considering a unitary load power factor. Simulation parameters of the co-HRPC model are presented in Table 4.14. In addition, simulation parameters of the FB-RPC at the same loading conditions are also presented to compare and demonstrate the advantages of the co-HRPC system.

Simulation results show that, using the LC passive filter leads to a detected reduction in the DC-link voltage value of the co-HRPC, then reducing the size of the overall power compensator [44]. Some

hybrid RPC schemes are based on RPC+SVC to reduce the RPC required power capacity. However, in that case, a coordinative control is essential for both subsystems of RPC and SVC [146].

Table 4.14. Simulation parameters of the FB-RPC and the co-HRPC models.

Description	Symbols	FB-RPC	Hybrid RPC
Line-to-line PPS voltage	U_{AC}, U_{BC}	220 kV	220 kV
Catenary voltage	U_x	25 kV	25 kV
RPC filter inductance	L_x, L_y	2.2 mH	1.7 mH
Catenary lumped impedance	Z_L	$0.05 + j 0.15 \Omega$	$0.05 + j 0.15 \Omega$
Capacitance of the DC-link capacitor	C_{dc}	80 mF	50 mF
Capacitance of the passive filter capacitor	C_x	–	30 mF
Load power of the section x	P_x	4.8 MW	7.2 MW
Load power of the section y	P_y	2.4 MW	–
DC-link voltage	V_{dc}	2 kV	1.5 kV
Turns ratio of step-down transformer	K_V	220/25	220/25
Turns ratio of adjacent step-down transformer	K_U	–	220/1
Turns ratio of coupling step-down transformer	K_D	25/1	25/1

Simulation results of the three-phase PPS currents before and after compensation are presented in Figure 4.29. The three-phase currents before compensation were imbalanced and contained high harmonic contents, as well as the NSC of currents. Figure 4.29(b) shows the same currents after balancing the active power between load sections and compensating the reactive power. The three-phase currents after compensation, presented in Figure 4.10 and Figure 4.29, show the same RMS value because the total loading power is the same in both of the cases.

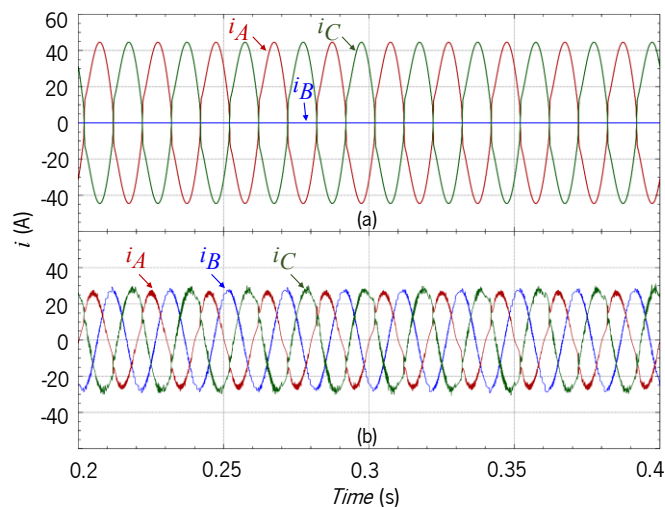


Figure 4.29. Co-HRPC simulation results: (a) Three-phase currents before compensation; (b) Three-phase currents after compensation.

Figure 4.30(a) shows the load section current, i_{Lx} , that causes the harmonic contents and the imbalance in the three-phase currents. The compensation currents synthesized by the co-HRPC converter are presented in Figure 4.30(b). The compensation current provided by the unloaded section converter (in this case, section y converter), i_{ry1} , has completely a sinusoidal waveform. In that case, the active power is shifted from the section x converter to the section y converter. Moreover, section x converter compensates a quantity of capacitive reactive power, whereas, section y converter compensates a quantity of inductive reactive power.

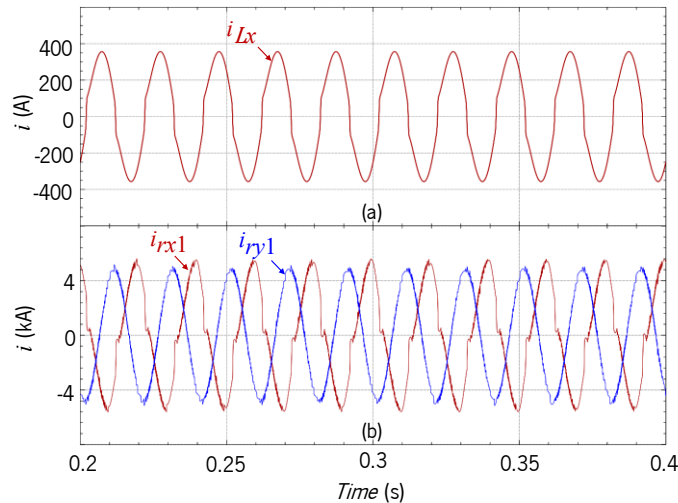


Figure 4.30. Co-HRPC simulation results: (a) Load section current; (b) Compensation currents.

Figure 4.31 shows the DC-link capacitor voltage of the co-HRPC, besides the passive filter capacitor voltage, which has a peak voltage around 200 V. Due to the high capacitance of the passive filter capacitor, the voltage oscillation is between -200 V and 200 V. It is important to note the average value of the passive filter capacitor voltage is equal to zero, and the capacitor is charging/discharging at the same fundamental frequency rate of 50 Hz. The DC-link voltage value is reduced to 1.5 kV in the co-HRPC instead of 2 kV in the FB-RPC system at the same conditions.

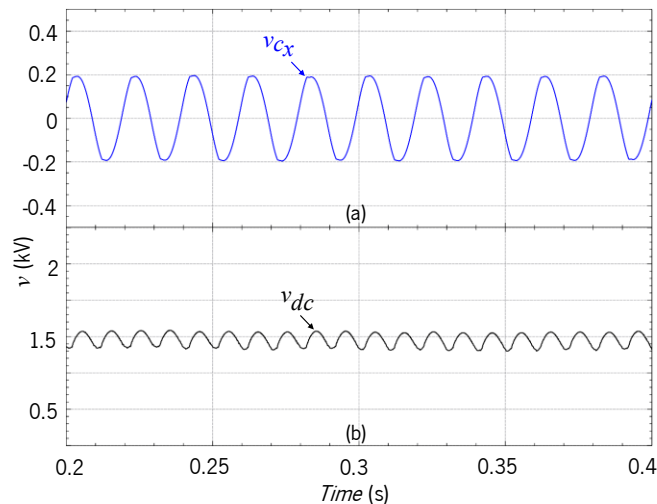


Figure 4.31. Co-HRPC simulation results: (a) Passive filter capacitor voltage; (b) DC-link voltage.

Active power of the High-speed railways varies between 0 MW and 40 MW [93]. As a result and since the previous studies show that RPC shifts half of the load active power difference and it provides all of the reactive power, RPC power ratings could be very high (tens of MW) [140]. Therefore and by inserting a capacitor in one of the coupling branches, the RPC DC-link voltage can be significantly decreased, then, reducing the converter power ratings and the power losses of the co-HRPC [93].

4.7 RPC Based on Scott Power Transformer

This study presents a rail power conditioner based on a Scott power transformer and a full-bridge back-to-back converter. Although the Scott transformer has more complex structure than the V/V power transformer, it has several advantages regarding power quality improvement capability. Normally, the Scott power transformer is used to perform the three-phase to two-phase conversion. Simulation results of this case study confirm the Scott power transformer capability in terms of overcoming the NSC of currents, especially when both load sections, x and y , are equally loaded. Nevertheless, Scott power transformer is also able to reduce the NSC of currents when both load sections, x and y , are unequally loaded. Figure 4.32 depicts the RPC system based on a Scott power transformer. The primary windings currents are denoted as i_A , i_B and i_C , and the secondary windings currents are denoted as i_x , i_y and i_z . The compensation currents provided by the RPC are i_{rx} and i_{ry} [54].

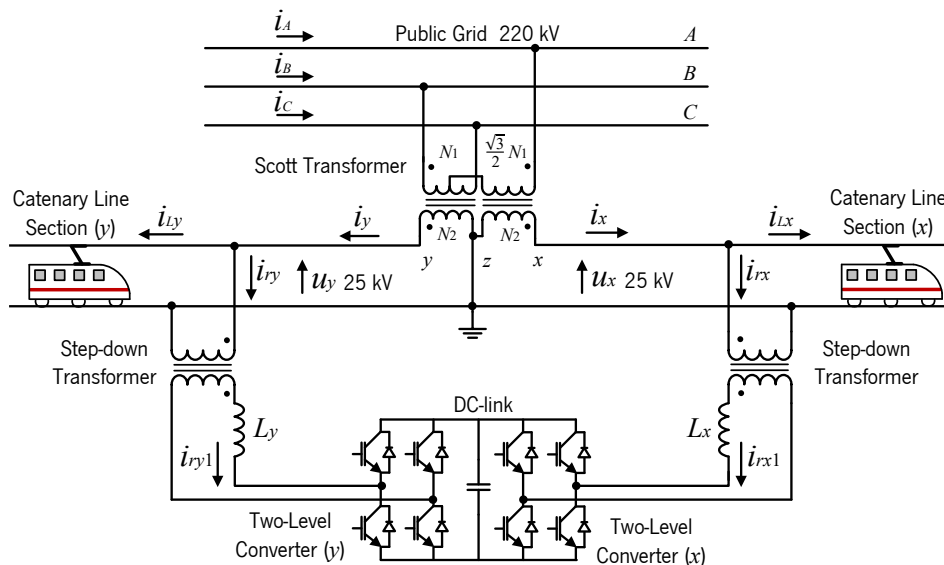


Figure 4.32. RPC system with a Scott power transformer.

Figure 4.33(a) presents the Scott power transformer connection points to create two traction feeders. Figure 4.33(b) shows the phasors diagram of the primary windings of the Scott power transformer. The voltage, \dot{U}_{BC} , is the line voltage which makes 30° out-of-phase with the phase voltage, \dot{U}_B . The voltage, \dot{U}_{AD} , is in phase with the phase voltage, \dot{U}_A , as described in (4.16) and (4.17). Figure 4.33(c) presents the phasors diagram of the secondary windings of the Scott power transformer [149].

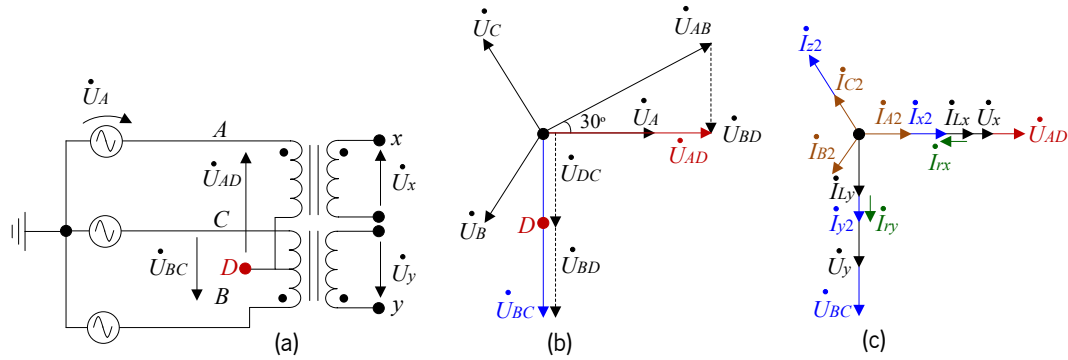


Figure 4.33. Phasors of the RPC system with a Scott power transformer: (a) Scott transformer connection points; (b) Phasors diagram of the primary windings; (c) Phasors diagram of the secondary windings.

$$\dot{U}_{BD} = \frac{1}{2} U_{BC} e^{-j90^\circ}; \quad \dot{U}_{AB} = U_{AB} e^{j30^\circ}; \quad |U_{AB}| = |U_{BC}| \quad (4.16)$$

$$\dot{U}_{AD} = \dot{U}_{AB} + \dot{U}_{BD} = \frac{\sqrt{3}}{2} U_{AB} \quad (4.17)$$

The compensation currents synthesized by the RPC based on the Scott power transformer, in that case, have no reactive components to compensate the NSC of currents, then, there is no need to inject reactive power for NSC compensation. However, a small value of reactive power can be injected by the RPC converter to compensate for the harmonics produced by the electric locomotives. As a result, the Scott power transformer helps to reduce the RPC power ratings for some RPC topologies (see item 4.10 for more information). This is due to the fact that in the RPC based on the Scott power transformer the reactive power compensation is not a vital factor and the compensator mainly shifts the active power difference from the highly loaded section to the lightly loaded one [48], [146].

Figure 4.34 shows the V/V power transformer phasors diagram. In this case, there is a phase shift of 60° between the load section currents of \dot{I}_{Lx} and \dot{I}_{Ly} . The two-phase secondary windings voltages, \dot{U}_x and \dot{U}_y are in phase with the primary windings voltages of \dot{U}_{AC} and \dot{U}_{BC} , respectively. The secondary windings voltages of the V/V power transformer are expressed in (4.18). As a result, in the V/V power transformer, the line-to-line or the voltage between the overhead catenary lines has an RMS voltage equals to the phase-to-neutral voltage. However, in the Scott power transformer, the line-to-line voltage between the overhead catenary lines has a higher RMS value than the traction feeder voltages, which results in a higher DC-link voltage of the RPC. This is only correct in the RPC topologies that are designed with respect to the line-to-line voltage (e.g., TW-RPC, HB-RPC) [150].

The compensation currents synthesized by the RPC based on the V/V power transformer, \dot{I}_{rx} and \dot{I}_{ry} have both of the active and the reactive current components for the compensation of current harmonics and the NSC. It is worth mentioning the RPC rated power, in this case, is higher since the converter mainly shifts the active power and compensates the reactive power [150].

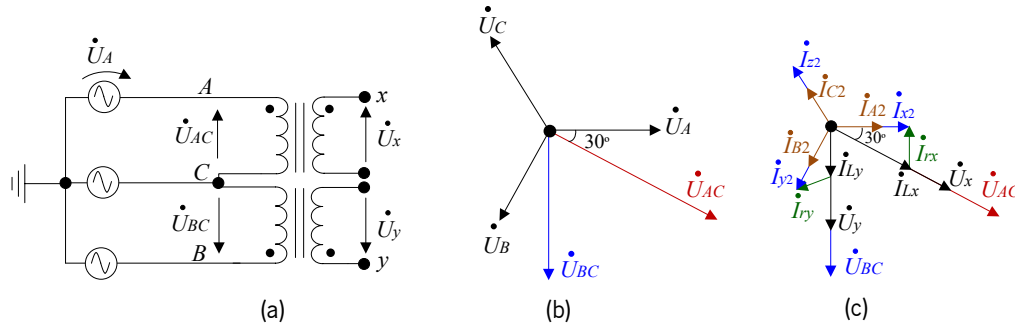


Figure 4.34. Phasors of the RPC system with a V/V power transformer: (a) V/V transformer connection points; (b) Phasors diagram of the primary windings; (c) Phasors diagram of the secondary windings.

$$\dot{U}_x = \frac{\dot{U}_{AC}}{K_V} e^{-j30^\circ}, \quad \dot{U}_y = \frac{\dot{U}_{BC}}{K_V} e^{-j90^\circ} \quad (4.18)$$

The DC-link voltage value when using the Scott power transformer is normally lower in the RPC topologies that are designed with respect to the phase-to-neutral voltage (e.g., FB-RPC). This is an extra advantage of using the RPC based on the Scott power transformer. The justification is presented in Figure 4.35, where the phasors diagram of the RPC output voltages are presented in both of the cases when using the V/V and the Scott power transformers. Figure 4.35(a) presents the equivalent circuit of the single-phase RPC load section converter [150].

The voltage across the filter inductors, L_x and L_y , leads the compensation current synthesized by the RPC, then, when using the Scott power transformer, the RPC phase-to-neutral output voltages, $(\dot{U}_{x0})_{Scott}$ and $(\dot{U}_{y0})_{Scott}$, have almost a similar magnitude since the reactive power compensation is not a critical factor, as shown in Figure 4.35(c). On the other hand, as long as the reactive power compensation is a vital factor when using the V/V power transformer, the phase x output voltage, $(\dot{U}_{x0})_{V/V}$, is higher than the phase y output voltage, $(\dot{U}_{y0})_{V/V}$, and slightly higher than the phase-to-neutral output voltages of the RPC based on the Scott power transformer $(\dot{U}_{x0})_{Scott}$ and $(\dot{U}_{y0})_{Scott}$. In the FB-RPC, the DC-link voltage should at least have the peak value of the phase voltages, u_{x0} and u_{y0} .

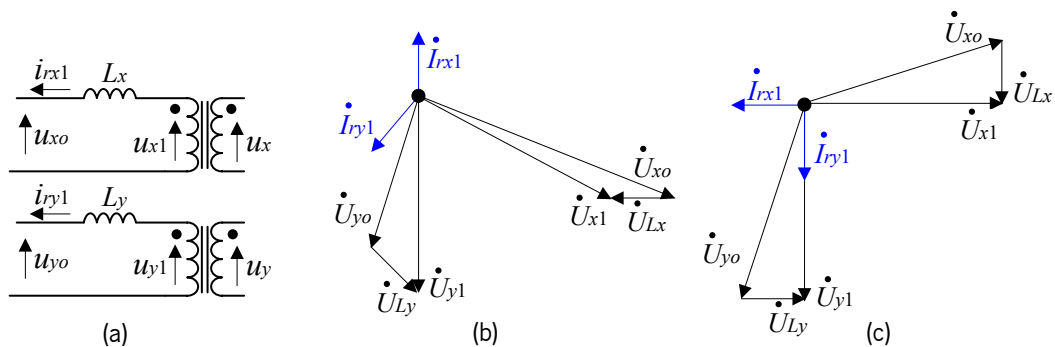


Figure 4.35. RPC output voltages: (a) Output equivalent circuit of the RPC; (b) Phasors of the RPC output voltages in V/V power transformer; (c) Phasors of the RPC output voltages in Scott power transformer.

As a result, the DC-link voltage of the FB-RPC based on a V/V transformer is normally higher than the DC-link voltage when using the Scott power transformer [150]. The previous conclusion is not correct in the RPC topologies that are designed with respect to the line-to-line voltage (e.g., TW-RPC, HB-RPC). In that case, the DC-link voltage value when using the Scott power transformer will be higher since the line-to-line voltage in the Scott power transformer is higher than the line-to-line voltage in the V/V power transformer (The line-to-line voltage is equal to the phase-to-neutral voltage in the V/V power transformer, but it is higher than the phase-to-neutral voltage in the Scott power transformer).

4.7.1 Control Algorithm

The control algorithm of the RPC based on a Scott power transformer is presented in Figure 4.36. Compared to the RPC based on a V/V power transformer control strategy, the main difference is in the phase angles of the correspondent Sine waves. As shown in Figure 4.37, there are $\theta_x = -30^\circ$ and $\theta_y = -90^\circ$ in the RPC based on the V/V power transformer, so there is $\theta = 60^\circ$ out-of-phase between the load section voltages. However, there are $\theta_x = 0^\circ$ and $\theta_y = -90^\circ$ in the RPC based on the Scott power transformer, so there is $\theta = 90^\circ$ out-of-phase between the load section voltages.

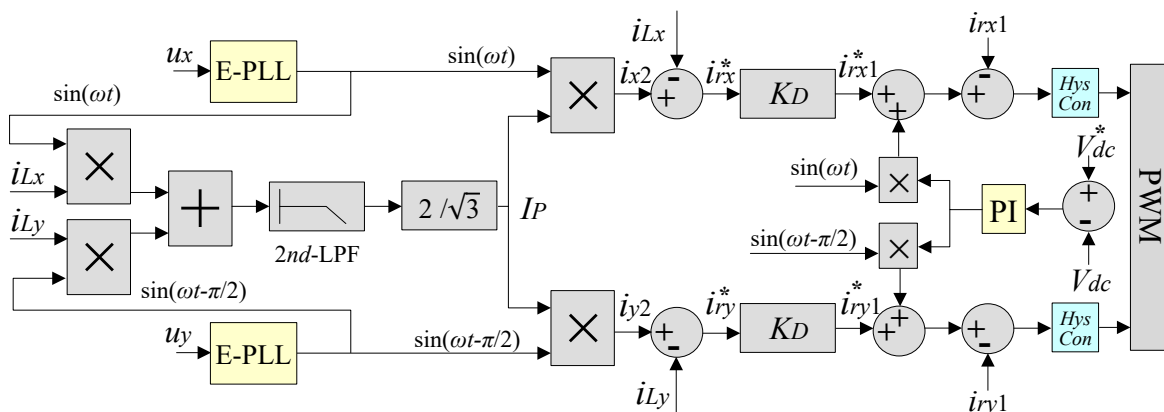


Figure 4.36. Control strategy of the RPC system with a Scott power transformer.

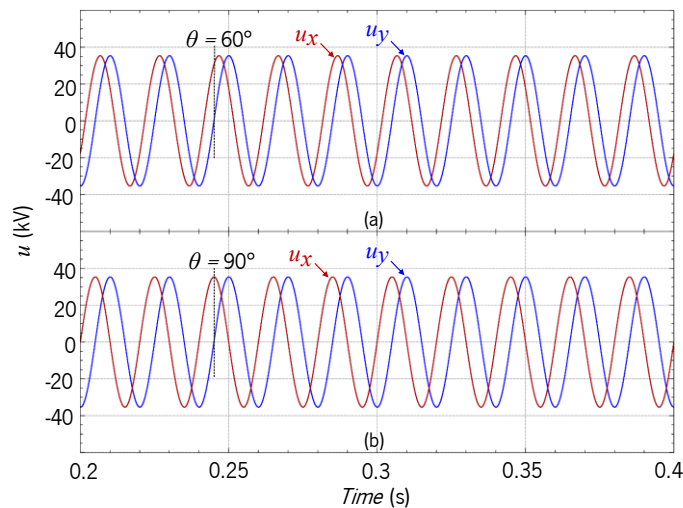


Figure 4.37. Load section voltages: (a) Using the V/V power transformer; (b) Using the Scott power transformer.

Table 4.15 shows a technical comparison between the Scott and the V/V power transformers [151]. The Scott power transformer has more complex structure than the V/V. Moreover, V/V power transformer has a higher material utilization factor, which signifies a smaller transformer volume at the same nominal power. Consequently, the manufacturing costs of the Scott power transformer are higher. Nevertheless, and since the traction power system based on the Scott power transformer exchanges a lower amount of reactive power with the RPC, the Scott power transformer can effectively reduce the costs of the RPC or the power compensator.

Table 4.15. Technical comparison between Scott and V/V power transformers.

Compared Item	V/V Transformer	Scott Transformer
Structure	Simple	Complex
Material utilization factor	High (94%)	Low (81.6%)
Requirement for reactive power compensation	Higher	Lower
Manufacturing costs	Lower	Higher

4.7.2 Simulation Results

A comparative study between the RPC based on a V/V power transformer and the RPC based on a Scott power transformer has been established using the *PSIM*V.9.1 software. *PSIM* advantages for Power Electronics simulation are presented in [152]. Figure 4.38 shows the performance of each traction power transformer (V/V and Scott power transformer) when both of the load sections, x and y , are equally loaded (each load section is loaded with 4.8 MW and the PPS line-to-line voltage is 220 kV). During the simulation, the RPC system is turned-off and there are no compensation currents injected into the PPS. Mathematically, PSC and NSC in a system with ABC rotation are defined as in (4.19) and (4.20), where these equations are implemented in the simulation model by using *C* code.

$$P\dot{S}C = \frac{\dot{I}_A + a \dot{I}_B + a^2 \dot{I}_C}{3}; \quad a = 1 \angle 120^\circ \quad (4.19)$$

$$N\dot{S}C = \frac{\dot{I}_A + a^2 \dot{I}_B + a \dot{I}_C}{3}; \quad a = 1 \angle 120^\circ \quad (4.20)$$

Figure 4.38(a) presents the PPS currents without compensation when using the V/V power transformer. The PSC and the NSC of currents are calculated at the fundamental frequency of 50 Hz, as shown in Figure 4.38(b). In this case, the NSC of currents is almost 50% of the PSC. On the other hand, the simulation results when using the Scott power transformer show a good capability to present balanced PPS currents without compensation, as shown in Figure 4.38(c). The NSC of currents, on these terms, has a value close to zero, as shown in Figure 4.38(d). In addition, the PPS currents only contain harmonic contents without NSC.

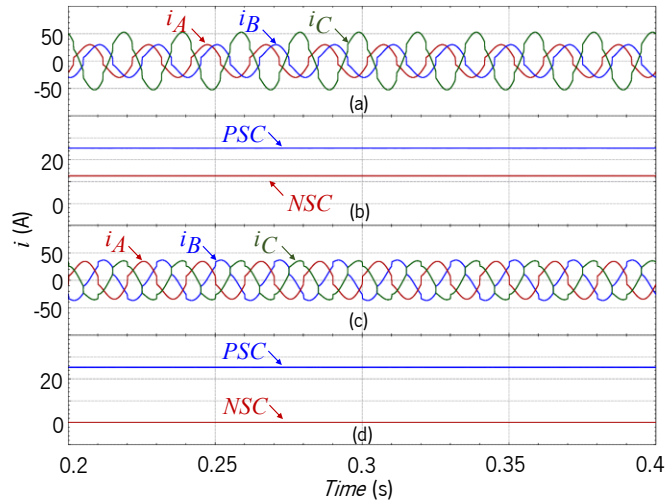


Figure 4.38. Public grid currents, PSC and NSC when the load sections are equally loaded before compensation: (a), (b) Using the V/V power transformer; (c), (d) Using the Scott power transformer.

Consequently, Scott power transformer shows a power quality improvement capability better than the V/V power transformer, even when both of the load sections are unequally loaded (section x is loaded with 4.8 MW and section y is loaded with 2.4 MW), as shown in the Figure 4.39(c) and Figure 4.39(d). In that regard, the NSC of currents at the fundamental frequency of 50 Hz when using the Scott power transformer is lower than the NSC when using the V/V power transformer. The value of NSC of currents has a value more than 50% of the PSC when using the V/V power transformer, as shown in Figure 4.39(b), while its value is lower than 40% of the PSC when using the Scott power transformer, as shown in Figure 4.39(d). As a result, and at similar loading conditions, any of the active power compensators (e.g., RPC and SVC) used to compensate the currents imbalance should have higher power ratings in the V/V traction system [150].

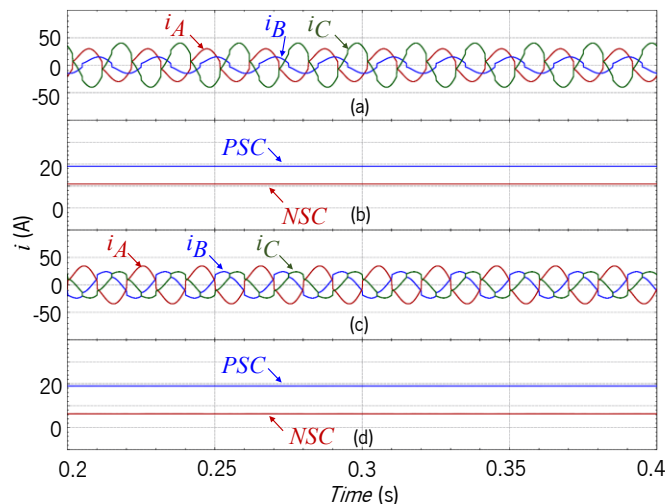


Figure 4.39. Public grid currents, PSC and NSC when load sections are unequally loaded before compensation: (a), (b) Using the V/V power transformer; (c), (d) Using the Scott Power transformer.

Simulation results of the RPC based on a Scott power transformer, after compensation, are shown in Figure 4.40. The same load parameters presented in Table 4.6 and Table 4.7 are used in this

simulation after considering a unitary load power factor for both load sections. The RPC is turned on after 0.1 s to improve the public grid power quality when both load sections are unequally loaded (section x active power is 4.8 MW; section y active power is 2.4 MW). Before the indicated time (0.1 s), the public grid currents are imbalanced and the NSC of currents has a high value (almost 40% of the PSC). After 0.1 s, the RPC is turned on to compensate for both of harmonics and NSC of currents. Consequently, and as shown in Figure 4.40(c), the NSC of currents at the fundamental frequency 50 Hz is reduced to be almost zero, and the PSC of currents is increased. Figure 4.40(b) shows the secondary windings currents of the Scott power transformer. These currents are imbalanced since the primary and the secondary end windings points of the Scott power transformer are different. This imbalance does not appear when using the V/V power transformer since it has common end windings points on the primary and the secondary windings [150].

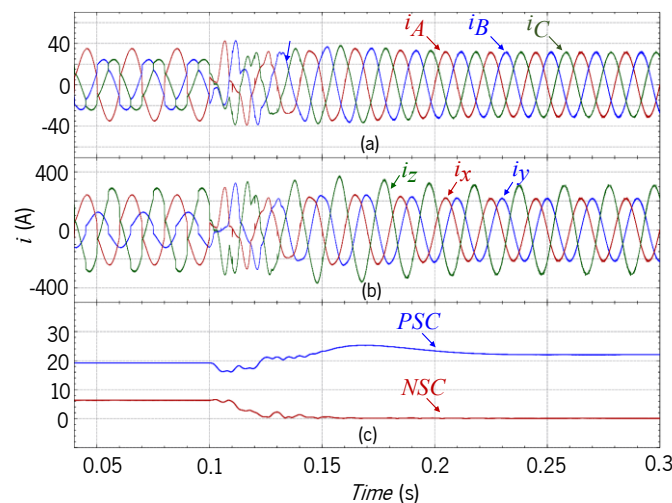


Figure 4.40. RPC based on a Scott transformer (RPC is turned on after 0.1 s): (a) Three-phase grid currents; (b) Currents at the secondary windings of the Scott transformer; (c) PSC and NSC of three-phase grid currents.

Figure 4.41(a) shows the load section currents that are considered as harmonic sources in the power system. During the simulation, the load currents have a constant RMS value. Figure 4.41(b) presents the compensation currents synthesized by the RPC converter. Since the load sections are unequally loaded (load section x has double the value of load section y), section x converter injects an active power component, which is opposite in direction to load section x active power. On the other hand, section y converter injects an active power component which is similar in direction to the load section y active power. The compensation current of the section x converter, i_{rx1} , has 180° out-of-phase with the load section x current, i_{Lx} . In addition, the compensation current of the section y converter, i_{ry1} , is in phase with the load section y current, i_{Ly} . This is also confirmed in the phasors diagram presented in the Figure 4.33(c) [150].

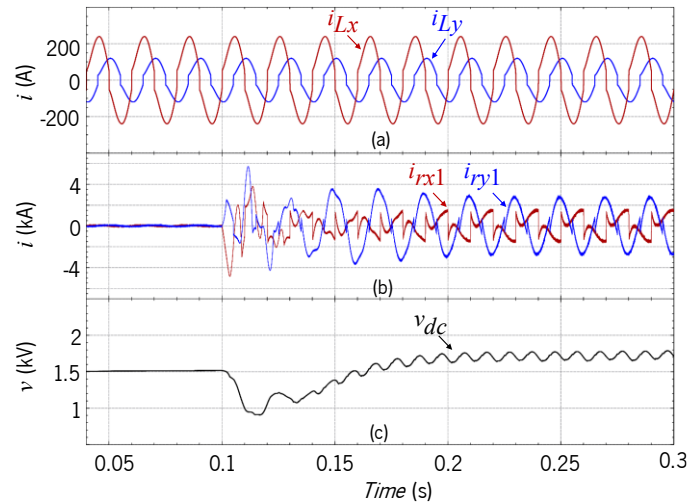


Figure 4.41. RPC based on a Scott transformer (RPC is turned on after 0.1 s): (a) Load section currents; (b) Compensation currents synthesized by the RPC; (c) DC-link voltage.

As has mentioned before, using the Scott power transformer helps to decrease the DC-link voltage in the RPC topologies that are designed with regard to phase-to-neutral voltage (e.g., FB-RPC). Consequently, and as shown in Figure 4.41(c), the initial value of the DC-link voltage is 1.5 kV before compensation. In the steady-state and after introducing the RPC compensation currents, the DC-link voltage reaches a value close to 1.8 kV. The DC-link voltage in the RPC based on the V/V power transformer, at the same loading conditions, reached a value close to 2 kV. In both of the cases, the DC-link voltage is supposed to be controlled in closed-loop with a constant reference. This reference has a lower value in the RPC topologies based on the Scott power transformer that are designed with regard to phase-to-neutral voltage (e.g., FB-RPC). On the other hand, the value of this reference is higher in the RPC topologies based on the Scott power transformer that are designed with regard to line-to-line voltage (e.g., TW-RPC, HB-RPC).

4.8 Modular RPC Based on Full-Bridge Back-to-Back Converters and V/V Power Transformer

Modular rail power conditioner (MRPC), as shown in Figure 4.42, is mainly used to decrease the current stress of the switching devices, in which each RPC module can be considered as an independent single-phase back-to-back full-bridge converter. Using the MRPC topology is more common when a single RPC cannot withstand the high ratings of the compensation currents [146], [153]. The MRPC improves the power grid reliability as one or more of the RPC modules is out of service, the MRPC system can present power quality improvement, allowing full utilization of the installing capacity of the traction power transformer.

On the other hand, the MRPC solution and its control strategy with renewable energy access is presented in [154]. The proposed solution in [154] has a better integration of the distributed renewable

energy sources along the railway, besides the power quality control of the railway system. In addition, authors in [155] present MRPC topology in a co-phase traction power supply system, in which separated DC-links of the back-to-back power converters are used instead of a single DC-link in between, and therefore, the two converters of the RPC can operate independently with a relatively simple controlling method. However and due to the separated DC-links, the main drawback is that the active power cannot be exchanged between the RPC power converters, so the compensation performance is just satisfactory for traction loads at nearly unitary power factor [155]. By considering k is the number of the RPC modules, Table 4.16 presents the components quantities of the MRPC.

The coupling step-down transformer for each load section converter is assumed as an ideal transformer with multiple secondary windings. The turns ratio of the coupling step-down transformer, K_D , is given in the (4.21), where U_x and U_y , are the primary windings voltages. The voltages, U_{xn} and U_{yn} , are the phase n voltages of the secondary windings of the step-down coupling transformer.

$$K_D = U_x / U_{xn} = U_y / U_{yn} \tag{4.21}$$

Table 4.16. Components quantities of the MRPC.

Number of IGBTs	Number of capacitors	Number of inductors	Isolation/coupling transformer
$8*k$	k	$2*k$	2

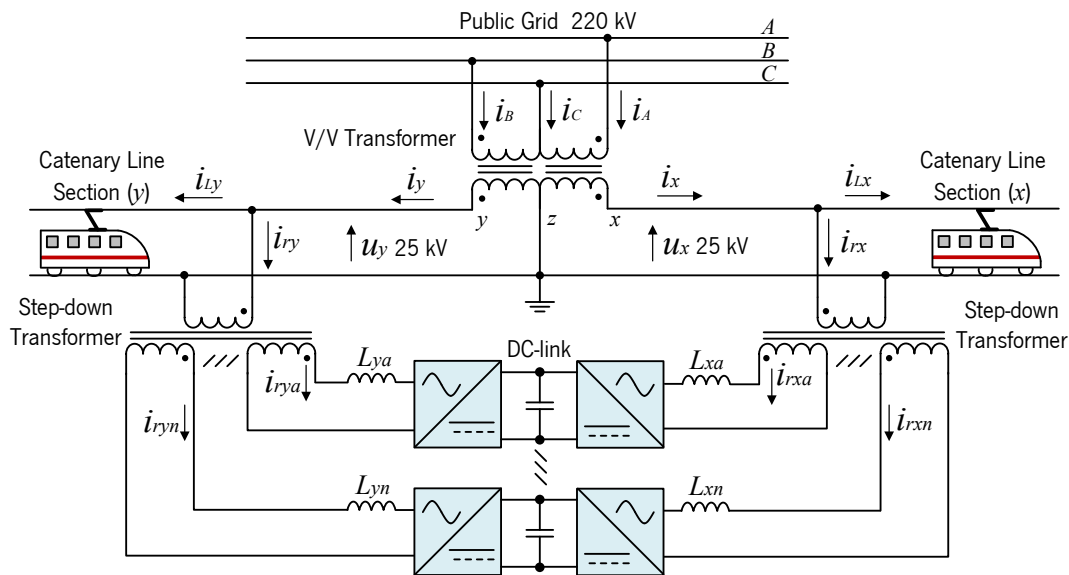


Figure 4.42. MRPC system with a V/V power transformer.

4.8.1 Control Algorithm

Each RPC module can be considered as an independent FB-RPC unit. Consequently, the RPC module compensates a part of the reactive power and shifts a part of the active power difference between the load sections. The RPC module has its independent control in terms of producing the compensation current references and the DC-link voltage control. Therefore, it is not appropriate to use a common

single DC-link for all the RPC modules. Otherwise, this will result in a bulky and expensive DC-link capacitor, besides the necessary coordinative control between the RPC modules in this case.

Control algorithm of MRPC system is very similar to the FB-RPC control algorithm presented in Figure 4.8. However, the main difference is that each RPC module should contribute with a part of the total compensation currents, i_{rx} and i_{ry} . In addition, each RPC module control should guarantee a constant DC-link capacitor voltage. In this context, an averaging control is important to ensure equal DC-link voltage values and similar loading conditions for the RPC modules. In other words, this control improves the MRPC performance to validate the same compensation power contribution among the RPC modules. For that purpose, additional PI controller is used in this topology to perform the averaging control, then equalizing between all the DC-link voltages of the RPC modules. The output signals of the averaging controller, A_x and A_y , are multiplied with the correspondent Sine waves. Finally, these signals are added to the compensation current references for each RPC module. Figure 4.43 presents the control strategy of the MRPC system. Hysteresis controllers are used to track the compensation current references.

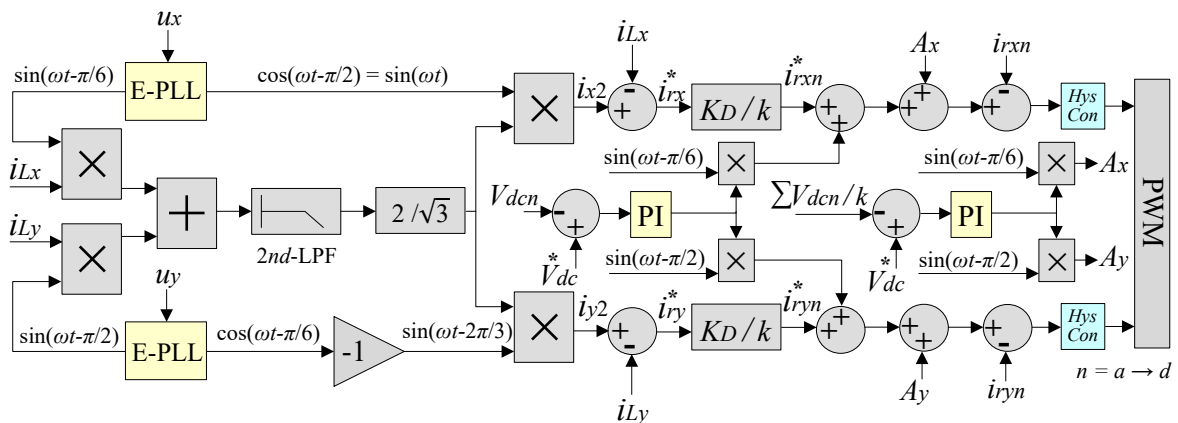


Figure 4.43. Control strategy of the MRPC.

4.8.2 Simulation Results

Simulation parameters of the MRPC model and the FB-RPC are presented in Table 4.17 to show the difference in parameters selection between the MRPC and the FB-RPC. Since the power provided by each RPC module is always lower than the total power provided by the FB-RPC system, the required DC-link capacitor for an RPC module is lower than the one for the FB-RPC. In addition, the IGBTs current stress is reduced by $1/k$. For this case study, it has been considered four RPC modules ($k = 4$) in the simulation model of the MRPC. Consequently, the currents flowing through the RPC modules or the compensation currents synthesized by the RPC modules are given in (4.22).

$$I_{rxn} = I_{rx} (K_D / k), \quad I_{ryn} = I_{ry} (K_D / k); \quad n = a \rightarrow d; \quad k = 4 \quad (4.22)$$

Table 4.17. Simulation parameters for the FB-RPC model and the MRPC model.

Description	Symbols	FB-RPC	MRPC
Line-to-line PPS voltage	U_{AB}, U_{BC}, U_{CA}	220 kV	220 kV
Catenary voltage	U_x, U_y	25 kV	25 kV
RPC filter inductance	L_x, L_y	2.2 mH	2 mH
Catenary lumped impedance	Z_L	$0.05 + j 0.15 \Omega$	$0.05 + j 0.15 \Omega$
Section x load power	P_x	4.8 MW	4.8 MW
Section y load power	P_y	2.4 MW	2.4 MW
Capacitance of the DC-link capacitor	C_{dc}	80 mF	20 mF
DC-link Voltage	V_{dc}	2 kV	2 kV
IGBT Current Stress	–	1 p.u.	$1/k$ p.u.
IGBT Voltage Stress	–	1 p.u.	1 p.u.

Simulation results of the MRPC are presented in Figure 4.44. The three-phase currents after compensation are sinusoidal, and similar to the previous case studies when both of the load sections were unequally loaded, as shown in the Figure 4.44(a). The three-phase currents are balanced without NSCs and with lower harmonic contents. Figure 4.44(b) presents the load section currents at the loading values presented in Table 4.17. These currents cause harmonic contents and imbalance in the currents of the three-phase power grid. Figure 4.44(c) shows the compensation currents synthesized by one RPC module. In comparison to the compensation currents presented in Figure 4.12(b), Figure 4.20(b) and Figure 4.25(b) for the FB-RPC, TW-RPC and HB-RPC, respectively, each RPC module in the MRPC system only carries a portion of the total compensation current. Figure 4.44(d) shows the DC-link voltage for each RPC module. The voltage stress value is similar to the one in the FB-RPC, and the TW-RPC topologies, but the current stress is quite lower.

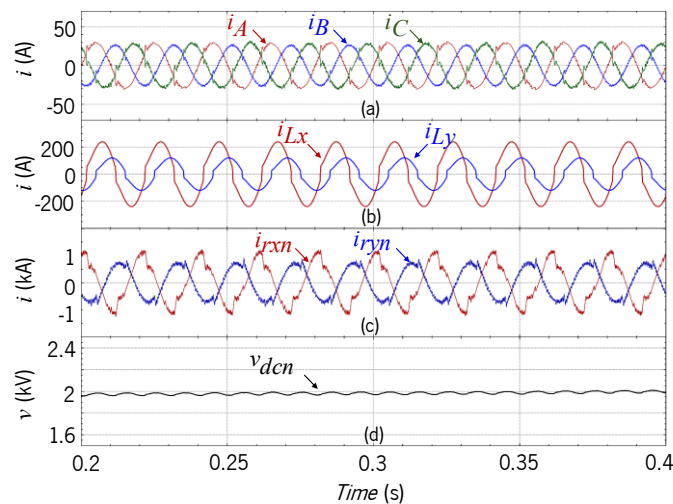


Figure 4.44. MRPC simulation results: (a) Three-phase currents after compensation; (b) Load section currents; (c) Compensation currents synthesized by an RPC module; (d) DC-link voltage for one RPC module.

Although the advantages of the MRPC topology, such as the scalability and better reliability, the main drawback of using this topology is its high implementation cost. The step-down coupling transformer (for each traction feeder) with multiple secondary windings are bulky and expensive solution. Moreover, the RPC modules can be processed independently due to the isolation of multiple secondary windings transformer. This means the number of DC-link voltage controllers, current controllers, and pulse width modulation (PWM) generators are all proportional to the number of RPC modules [146].

4.9 RPC Based on Modular Multilevel Converter and V/V Power Transformer

The FB-RPC system that combined with the two-level converters has some disadvantages in terms of the converter power ratings at medium-voltage levels, besides the high switching frequency applied on the power switching devices. For that reason, single-phase step-down coupling power transformers (one for each single-phase converter) were required to interface the FB-RPC system with the TPS. These step-down coupling power transformers may extremely increase the implementation costs of the FB-RPC, besides the required huge area for installation.

Over the last years, a dramatic change has taken place toward submodules (SMs) based topologies, in which cascade strings of SMs behave as controllable voltage sources [146]. With the purpose of enhancing the voltage and the current ratings of the traditional FB-RPC, several options in a modular manner were developed in the last decade in which the MMC was one of the applied choices. MMC is a relevant solution for the medium-voltage applications due to its modularity and flexibility, where the converter's total power is divided equally between several inner two-level converters (SMs). Therefore, the power switching devices can withstand the medium-voltage levels. Consequently, the RPC based on AC/DC/AC MMC (indirect MMC) can be connected without using step-down coupling transformers. However, other RPC topologies based on indirect MMC may require isolation transformers to interface with the TPS. Furthermore, the MMC power switching devices can operate at a lower switching frequency, which effectively reduce the switching losses of the RPC [122].

All the RPC topologies presented in the item 4.9 are based on a three-phase V/V power transformer and the indirect MMC. At present, the majority of commercialized MMC projects are based on the indirect MMC with half-bridge SMs [156]. This is due to the high efficiency of the half-bridge SM, the low costs, and the simple construction compared to other types of SM.

Voltage and current phasors, besides the compensation strategy, are completely as described in the item 4.3 of the FB-RPC. The half-bridge SM functionality has been described in Chapter 3, item 3.5.3

(Figure 3.15 and Table 3.2). Since the RPC based on MMC contains many Power Electronics equipment, the control strategy of this system is more complex than the FB-RPC, the TW-RPC and the HB-RPC. The RPC based on MMC requires implementing some additional control blocks to guarantee a robust RPC performance, regardless of the loading conditions. The control algorithm should guarantee similar DC-link voltages of MMC SMs. The main objective of the RPC control strategy is to compensate reactive power, NSC of currents, and the harmonic contents. In addition, RPC should shift half of the active power difference from the highly to the lightly loaded section [150].

Many RPC topologies have been proposed using the MMC in the literature with high compensation capacity. In this context, this item mainly discusses the RPC based on indirect AC/DC/AC MMC, which is equipped with unipolar half-bridge SMs. Other RPC based on MMC topologies, such as the RPC based on direct AC/AC MMC, which is equipped with bipolar full-bridge SM is out of the scope of this Ph.D. thesis. However, the discussion on analysis and control strategies for the RPC based on direct AC/AC MMC can be found in [118], [146], [157].

4.9.1 RPC Based on Full-Bridge Indirect Modular Multilevel Converter

The RPC based on a full-bridge indirect modular multilevel converter (FB-MMC4 RPC) is shown in Figure 4.45. The FB-MMC4 RPC consists of two back-to-back single-phase MMC with half-bridge SMs. Each half-bridge SM contains two switching devices (IGBTs) and one capacitor, which can be inserted or bypassed. The arm inductors are important to adjust the circulating current in the MMC phases, then, reducing the second order harmonic content of the MMC output currents. In this topology, isolation transformers with turns ratio 1/1 are needed to interface the converter with the single-phase TPS. This is important to avoid short circuit between the MMC arms since two of the MMC legs are connected to the same ground (each MMC leg consists of two arms, upper and lower arms) [150].

Load sections instantaneous voltages, u_x and u_y , are given by the (4.23), where, U_x and U_y , are the RMS value of the load section voltages. When using the V/V power transformer, the angle, θ_x , is equal to -30° and the angle, θ_y , is equal to -90° , as shown in the phasors diagram of the Figure 4.35(b). However, the angle, θ_x , is equal to zero and the angle, θ_y , is equal to -90° when using the Scott power transformer as shown in the Figure 4.35(c). The AC equivalent circuit of the FB-MMC4 RPC is shown in Figure 4.46. This system is characterized by an inherent DC-link that formed due to the SM voltages of the FB-MMC4 RPC [150]. Considering that, N , is the MMC number of levels, then, $(N-1)$ is the number of SMs in one MMC arm, Table 4.18 presents the components quantities of the FB-MMC4 RPC.

$$u_x = \sqrt{2} U_x \sin(\omega t + \theta_x)$$

$$u_y = \sqrt{2} U_y \sin(\omega t + \theta_y)$$
(4.23)

Table 4.18. Components quantities of the FB-MMC4 RPC.

Number of IGBTs	Number of capacitors	Number of inductors	Isolation/coupling transformer
16(N-1)	8(N-1)	8	2

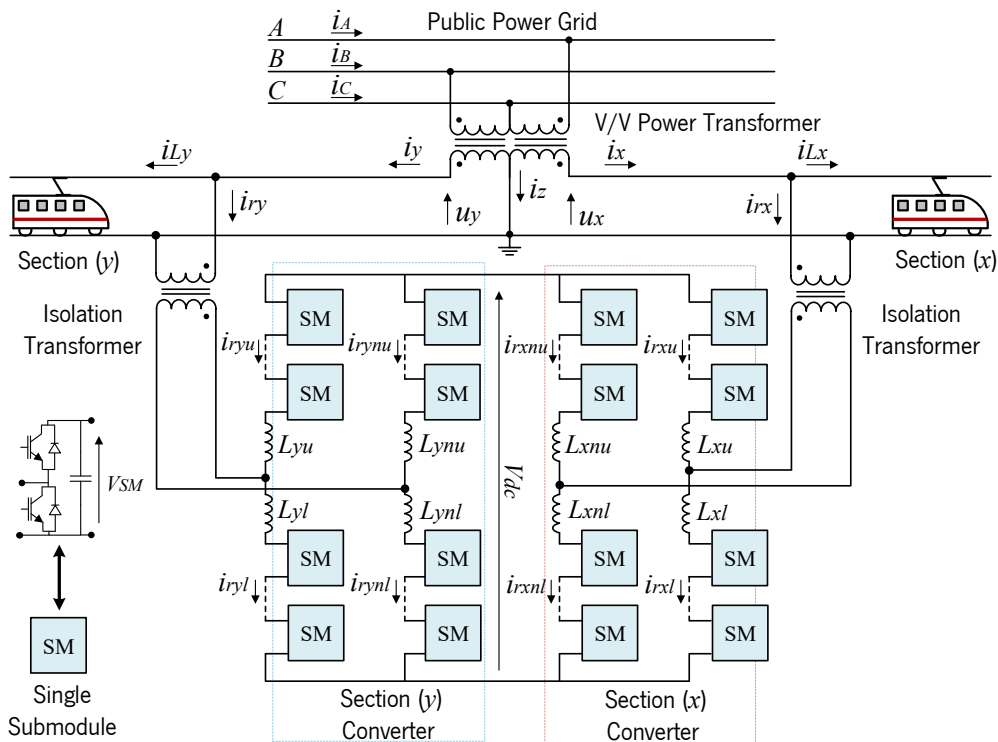


Figure 4.45. FB-MMC4 RPC system with a V/V power transformer.

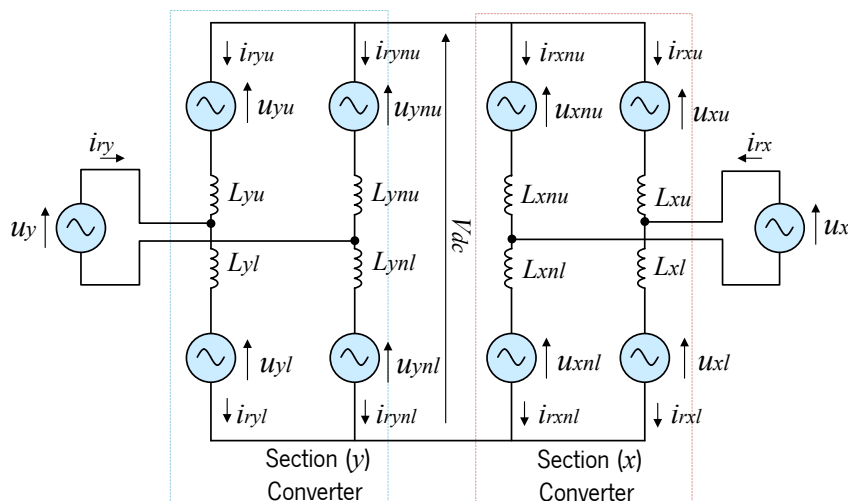


Figure 4.46. AC equivalent circuit of the FB-MMC4 RPC system.

As a result, SM capacitors can effectively substitute the high-voltage DC-link capacitor [158]. Similar to Figure 4.35(a) and Figure 4.35(b), Figure 4.47(a) and Figure 4.47(b) show the output equivalent circuit of single-phase load section converter, and the associated phasors of the FB-MMC4 RPC when

using the V/V power transformer. Consequently, the steady-state circuit equation can be given as in (4.24), where the voltages, u_{xo} and u_{yo} , are the instantaneous AC output voltage of the RPC. The next steps demonstrate the main principles to design the DC-link of the FB-MMC4 RPC in the V/V and the Scott power transformer. The instantaneous compensation currents of section x and section y are given in (4.25) [146]. The active and reactive output compensation currents of section x are, I_{rxa} and I_{rxr} , respectively. The active and reactive output compensation currents of section y are, I_{rya} and I_{ryr} . The values of I_{rxa} , I_{rya} and I_{rxr} , I_{ryr} are presented in (4.3) and (4.7), respectively.

$$\begin{aligned} u_x &= u_{xo} + u_{Lx} \\ u_y &= u_{yo} + u_{Ly} \end{aligned} \quad (4.24)$$

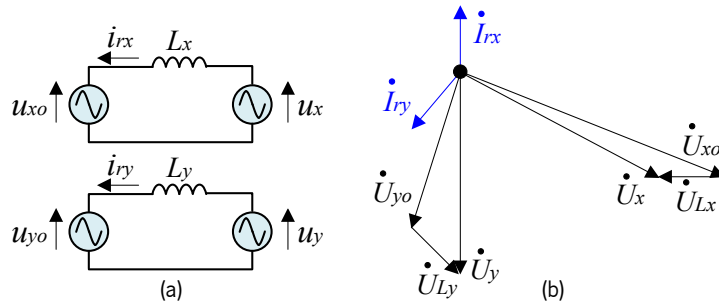


Figure 4.47. FB-MMC4 RPC: (a) Output equivalent circuit; (b) Phasors of output voltages when using V/V transformer.

$$\begin{aligned} i_{rx} &= -\sqrt{2} I_{rxa} \sin(\omega t + \theta_x) + \sqrt{2} I_{rxr} \cos(\omega t + \theta_x) \\ i_{ry} &= +\sqrt{2} I_{rya} \sin(\omega t + \theta_y) - \sqrt{2} I_{ryr} \cos(\omega t + \theta_y) \end{aligned} \quad (4.25)$$

From (4.25), the voltage drop across the filtering inductor of section x converter can be expressed as in (4.26), after supposing that the inductance of the MMC inner filter is 0.1 p.u, namely, $L_x = 0.1 U_x / (I_{rx} \omega)$, where L_x , is the equivalent inductance of the section x converter [146].

$$u_{Lx} = L_x \frac{di_{rx}}{dt} = -\frac{\sqrt{2} U_x}{10 \sqrt{I_{rxa}^2 + I_{rxr}^2}} [I_{rxa} \cos(\omega t + \theta_x) + I_{rxr} \sin(\omega t + \theta_x)] \quad (4.26)$$

Substituting (4.26) into (4.24), the output phase x voltage of the FB-MMC4 RPC can be obtained as in (4.27) [146]. The same analysis is applicable for section y converter as presented in (4.28) and (4.29).

$$u_{xo} = \sqrt{2} U_x \sin(\omega t + \theta_x) + \frac{\sqrt{2} U_x}{10 \sqrt{I_{rxa}^2 + I_{rxr}^2}} [I_{rxa} \cos(\omega t + \theta_x) + I_{rxr} \sin(\omega t + \theta_x)] \quad (4.27)$$

$$u_{Ly} = L_y \frac{di_{ry}}{dt} = +\frac{\sqrt{2} U_y}{10 \sqrt{I_{rya}^2 + I_{ryr}^2}} [I_{rya} \cos(\omega t + \theta_y) + I_{ryr} \sin(\omega t + \theta_y)] \quad (4.28)$$

Substituting (4.28) into (4.24), the output phase y voltage of the FB-MMC4 RPC can be obtained as in (4.29) [146].

$$u_{yo} = \sqrt{2} U_y \sin(\omega t + \theta_x) - \frac{\sqrt{2} U_y}{10 \sqrt{I_{rxa}^2 + I_{rxr}^2}} [I_{rya} \cos(\omega t + \theta_y) + I_{ryr} \sin(\omega t + \theta_y)] \quad (4.29)$$

The peak voltage value of u_{xo} and u_{yo} can be obtained from (4.27) and (4.29), respectively. These are the applied voltages on the SM capacitors, after considering the voltage drop across the filter inductors. Therefore, the DC-link voltage of the FB-MMC4 RPC should meet the condition presented in (4.30) to assure good performance. Hence, the number of half-bridge SMs in one MMC arm should be equal to V_{dc}/V_{sm} . Since the value of $U_{\sigma\sigma}$, presented in (4.30), is a phase voltage (U_{xo} or U_{yo}), then the equation (4.30) is applicable when using the FB-MMC4 RPC in the V/V power transformer or in the Scott power transformer. Other characteristics of the FB-MMC4 RPC according to the previous analysis are presented in the item 4.10, Table 4.25, Table 4.26 and Table 4.27 [146], [150].

$$V_{dc} \geq \sqrt{2} U_{\sigma\sigma} ; \sigma \in \{x, y\} \text{ for the V/V and the Scott power transformers} \quad (4.30)$$

4.9.1.1. Control Algorithm

The control algorithm of FB-MMC4 RPC should guarantee the correct calculation of the compensation currents, maintain a constant MMC DC-link, and balance the DC-link voltages of MMC SMs. The deterioration of one or more of the previous conditions may cause severe impacts on the safety and the efficient operation of MMC. In this context, a control algorithm is proposed and presented in this item to obtain a robust performance of the FB-MMC4 RPC.

As the main purpose of the RPC is to compensate for the NSC of currents, reactive power, and harmonic content, Figure 4.48 shows a block diagram for establishing the compensation current references. A full explanation of this block has been presented in the item 4.3.1. The final reference signals of i_{rx}^* and i_{ry}^* , are compared with the actual compensation currents synthesized by the RPC, i_{rx} and i_{ry} , as shown in the control diagram presented in Figure 4.49. The PR controllers are used to correcting the error and to calculate the voltage reference signals, u_{rx}^* and u_{ry}^* . Tracking the reference currents can be enhanced after using the PR controllers, then, steady-state errors associated with the conventional PI controllers can be alleviated. As an alternative solution, the synchronous frame PI controller can be used, but this type of controllers usually requires multiple frame transformations, and can be difficult to implement using a low cost digital controller [159].

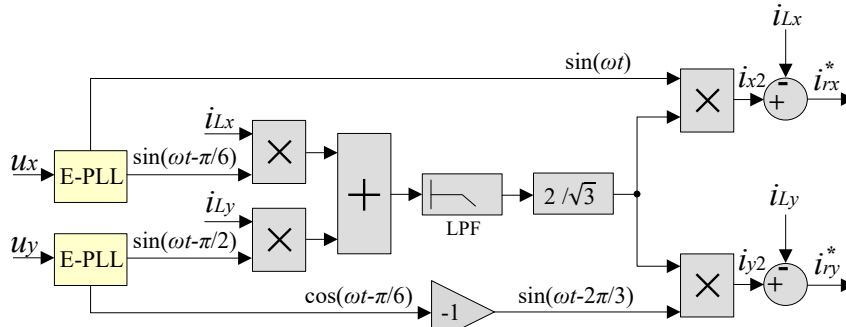


Figure 4.48. Block diagram for establishing the compensation current references.

Since the FB-MMC4 RPC is composed of two back-to-back MMC converters and an inherent DC-link, so this solution does not require to install a bank of capacitors at the DC-link side. However, the DC-link voltage control using PI controller is important to improve the SM capacitors voltage balancing control. The DC-link voltage control is presented in the Figure 4.49, where the PI controller corrects the error between the actual and the reference value of the DC-link voltage. The controller output is multiplied with the correspondent Sine waves. It is noteworthy to mention the relation between the voltage reference of the main DC-link and the voltage reference of the SM DC-link is presented in (4.31) [125].

$$V_{dc}^* = V_{SM}^* (N-1); N: \text{MMC voltage levels} \quad (4.31)$$

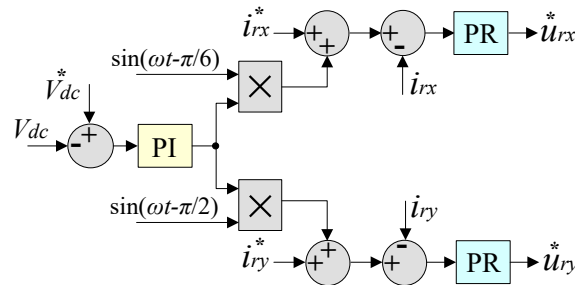


Figure 4.49. DC-link voltage control and the calculation of the voltage reference signals of the FB-MMC4 RPC.

Figure 4.50 shows three control diagrams that are responsible to balance the voltage across the SM capacitors of the MMC. A robust control of SM voltages leads to better MMC performance, then, the control of SM voltages is achieved through three steps:

- MMC leg averaging voltage control, as shown in Figure 4.50(a);
- MMC arm averaging voltage control, as shown in Figure 4.50(b);
- MMC SM individual voltage control, as shown in Figure 4.50(c).

The first control block, presented in Figure 4.50(a), indicates the leg averaging voltage control and the circulating current control, where two PI controllers are used for each MMC leg. The averaging control is implemented by summing the actual voltage values for all SM capacitors, then it compares the average of this actual value with a value provided as a reference [122]. The output of this controller is considered as a reference value for a circulating current controller, which is implemented after

summing the arm currents, $i_{r\sigma u}$ and $i_{r\sigma l}$, where $\sigma \in \{x, y\}$, in the upper and the lower arms that belong to the same MMC leg. The output voltage command of the MMC leg averaging voltage control, nominated as A_σ , will be added to a voltage command generation for each SM, as presented in Figure 4.51 [100].

Circulating current, i_{cir} , presented in (4.32), is considered as a part of the MMC arm current. However, it consists of a DC current component, AC current component that has double of the fundamental frequency (second harmonic order) and other harmonic orders. This current circulates in the MMC loops and it does not contribute to the compensation currents synthesized by the FB-MMC4 RPC, i_{rx} and i_{ry} . Therefore, it should be controlled as it causes extra losses and may increase the ratings of the power components. The DC current component is responsible for the active power flow between the DC-link and the AC side. The second harmonic content, that has double of the fundamental frequency, is mainly responsible for the power exchange between the MMC legs [160].

$$i_{r\sigma l} = i_{r\sigma} + i_{r\sigma u} \Rightarrow i_{cir} = (i_{r\sigma u} + i_{r\sigma l}) / 2 ; \sigma \in \{x, y\} \quad (4.32)$$

The second control block, presented in Figure 4.50(b), indicates the MMC arm averaging voltage control [161]. A proportional controller, KP1, is responsible to adjust the SM voltages in one arm to the reference voltage value, V_{arm}^* . The third control block in Figure 4.50(c) represents the MMC SM individual voltage control. A proportional controller, KP2, is responsible to adjust each SM voltage to its reference voltage value V_{SM}^* . The proportional controllers, KP1 and KP2, act only dynamically in the balancing process in every switching period. The output signal of KP1 and KP2, is multiplied by +1 when the current direction of $i_{r\sigma u}$ and $i_{r\sigma l}$, where $\sigma \in \{x, y\}$, is to charge the SM capacitor, or it can be multiplied by -1 when the current direction is to discharge the SM capacitor.

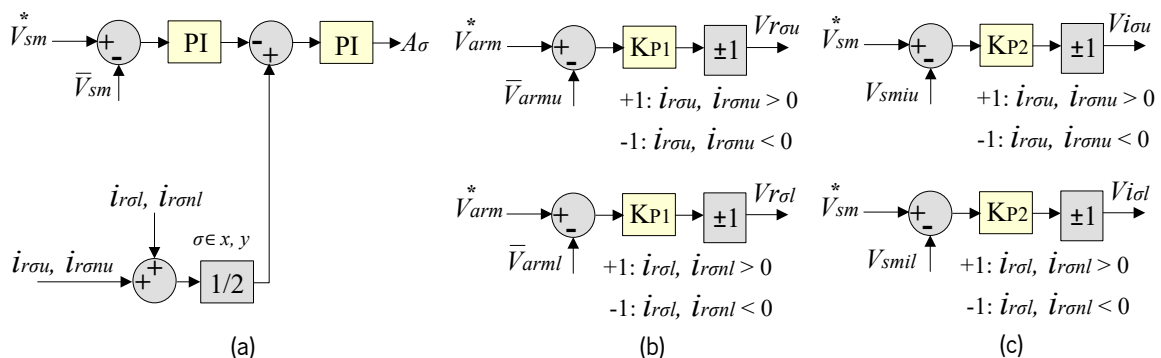


Figure 4.50. SM capacitors voltage control of the FB-MMC4 RPC: (a) MMC leg averaging voltage control; (b) MMC arm averaging voltage control; (c) MMC SM individual voltage control.

The final signals of MMC leg averaging control, A_σ , MMC arm averaging control, $V_{r\sigma u}$ and $V_{r\sigma l}$, MMC SM individual voltage control, $V_{i\sigma u}$ and $V_{i\sigma l}$, where $\sigma \in \{x, y\}$, are added to the voltage reference signals, $u_{r\sigma}^*$, to generate a voltage command (modulating signal) for each SM, which is to be compared

with the phase-shifted PWM triangular carriers, as shown in Figure 4.51. The Phase-shifted PWM can be easily applied after shifting the carriers phase angle in the same MMC arm, consecutively, and with a fixed angle of $360/(N-1)$. It should be declared that, all of the above-mentioned explanation is applicable when using the FB-MMC4 RPC with a V/V power transformer. When using the Scott power transformer, several aspects should be considered in the control blocks, namely in the correspondent Sine waves that have been used to correct the control signals (more details about this case are presented in the item 4.7 and the item 4.10).

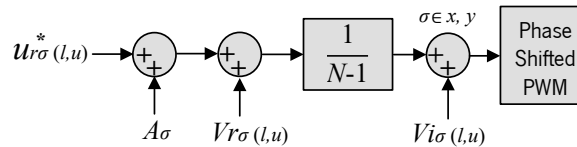


Figure 4.51. Voltage command generation of each SM applied to a phase-shifted PWM.

4.9.1.2. Simulation Results

Simulation model is built by using the *PSIMV.9.1* software for Power Electronics simulation to validate the system of FB-MMC4 RPC and the associated control algorithm. The simulation model consists of 7-levels ($N = 7$) MMC with a total number of 48 SMs. The main parameters of the simulation model are shown in the Table 4.19. In this framework, the same load parameters presented in Table 4.6 are used in this simulation after considering a unitary load power factor for both load sections. Therefore, the locomotives can be modeled as a resistive load connected in parallel with an uncontrolled full-bridge rectifier on the secondary windings of the locomotive transformer [57]. This full-bridge rectifier is considered as a harmonic source, where the full locomotive model is shown in Figure 4.9. The simulation considers that both of the load sections are unequally loaded. Then, in this study, load section x is loaded with a value of 4.8 MW and load section y is loaded with a value of 2.4 MW, as presented in Table 4.6.

The three-phase currents before applying the compensation strategy are presented in Figure 4.52(a) and they are imbalanced currents with high harmonic contents. Figure 4.52(b) shows the same currents after compensation. The three-phase currents are now balanced without NSC and with lower harmonic contents, as shown in the phasors diagram presented in Figure 4.6(c). Figure 4.52(c) shows the currents on the secondary windings of the V/V power transformer after compensation. These currents have 120° out-of-phase and sinusoidal waveforms (after compensation) instead of 60° out-of-phase (before compensation). It is noteworthy to mention, the used power transformers in the simulation model are considered as ideal ones without considering leakage flux, copper losses, and core losses. In other words, the ideal transformer gives an output power exactly equal to its input power.

Table 4.19. Parameters of the FB-MMC4 RPC simulation model.

Description	Symbols	Values
Line-to-line PPS voltage	U_{AB}, U_{BC}, U_{CA}	220 kV
Catenary voltage	U_x, U_y	25 kV
RPC filter inductance	$L_{\sigma u}, L_{\sigma nu}, L_{\sigma l}, L_{\sigma nl}$	3 mH
Catenary lumped impedance	Z_L	$0.05 + j 0.15 \Omega$
SM capacitor	C_{SM}	600 μ F
SM Switching frequency	f_{isw}	3 kHz
Equivalent switching frequency	f_{sw}	18 kHz
SM voltage	V_{SM}	8.3 kV
DC-link voltage	V_{dc}	50 kV
Number of SMs in each arm	$N-1$	6

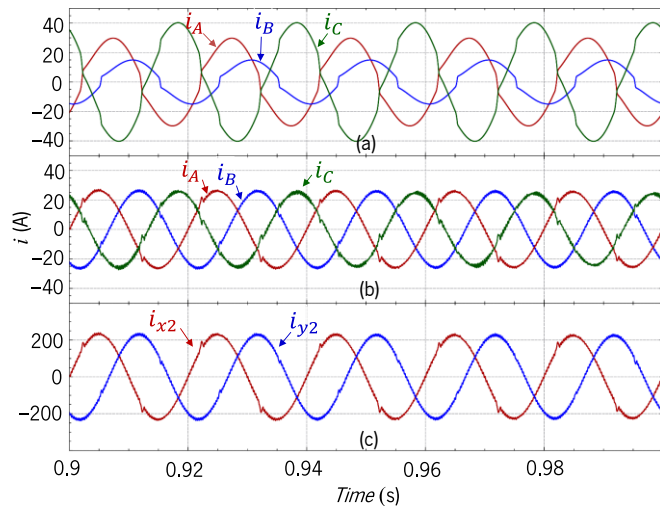


Figure 4.52. FB-MMC4 RPC simulation results: (a) Three-phase currents before compensation; (b) Three-phase currents after compensation; (c) Currents at the secondary windings of the V/V power transformer after compensation.

The load section currents are presented in Figure 4.53(a), where, i_{Lx} has double the value of i_{Ly} . Both currents are considered as harmonic sources because of using uncontrolled rectifiers in the locomotive model. The compensation currents synthesized by the RPC are demonstrated in Figure 4.53(b). These currents are calculated by using the control strategy presented in Figure 4.48. The results are very similar to the ones presented in Figure 4.12(b), but the RMS value of currents, in this case, are lower due to the abandon of the step-down coupling transformers, but isolation transformers with turns ratio 1/1 are used to interface the converter with the single-phase TPS.

The compensation currents, i_{rx} and i_{ry} are shared among the upper and the lower arms of the MMC, where, i_{rxu} is the upper arm current of the positive leg of the section x converter, i_{rxl} is the lower arm current of the positive leg of the section x converter, i_{ryu} is the upper arm current of the positive leg of the section y converter, i_{ryl} is the lower arm current of the positive leg of the section y converter.

In addition, the arm currents presented in the Figure 4.54 contain three current components, as shown the frequency spectrum presented in Figure 4.55. These three components are: the fundamental frequency current component of 50 Hz that contributes to create the compensation currents of i_{rx} and i_{ry} , the double fundamental frequency current component of 100 Hz (second harmonic current) that circulates between the MMC legs, the DC current component that has the responsibility of charging / discharging of the SM capacitors. The DC current component is also responsible for the DC/AC power transfer. This component has a value close to 18 A, as shown in the Figure 4.55.

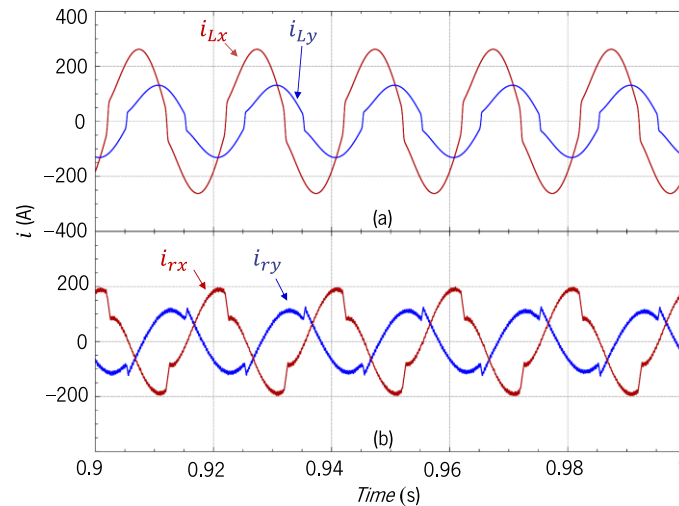


Figure 4.53. FB-MMC4 RPC simulation results: (a) Load section currents; (b) Compensation currents.

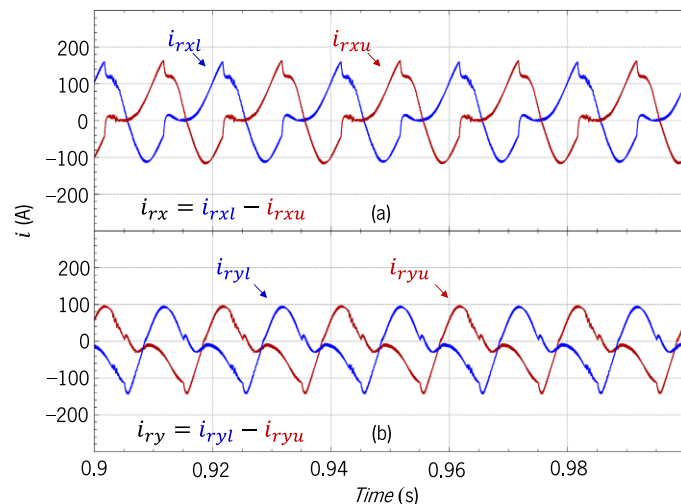


Figure 4.54. FB-MMC4 RPC simulation results: (a) Arm currents of the positive leg of the section x converter; (b) Arm currents of the positive leg of the section y converter.

It should be highlighted that, the circulating currents normally do not affect the AC output of the MMC, since these currents only circulate between the MMC phases. In addition, circulating currents are normally generated because of the inner voltage differences between MMC arms, and they increase the total RMS values of the MMC arm currents, resulting in higher power losses. One of the main applied techniques to suppress the circulating currents in the MMC is by using an inner filter (inductor) between the MMC arms. The effect of the circulating currents can be reduced by adjusting the

circulating current controller (the second PI controller presented in the Figure 4.50(a)). Figure 4.56 shows the simulation results of the FB-MMC4 RPC SM voltages. The main aim of the FB-MMC4 RPC control is to maintain the SMs voltages at their reference value, which is in this case a value close to 8.3 kV, as presented in Figure 4.56. These results confirm the effectiveness of the SM capacitors voltage balancing control presented in Figure 4.50. The SM voltage value of 8.3 kV is not reasonable for today's IGBTs, where the maximum voltage blocking of the commercially available IGBTs is close to 6.5 kV [112], consequently, the MMC should be designed with a higher level to reduce the SM voltage or two IGBTs connected in series have to be used.

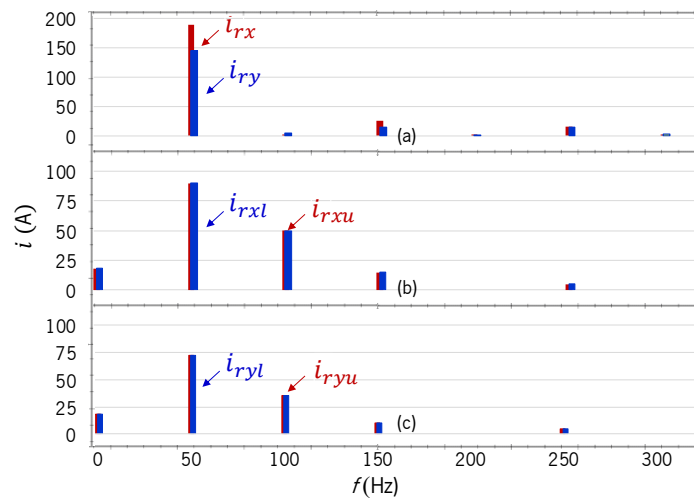


Figure 4.55. FB-MMC4 RPC frequency spectrum: (a) Compensation currents; (b) Upper and lower arm currents of converter x ; (c) Upper and lower arm currents of converter y .

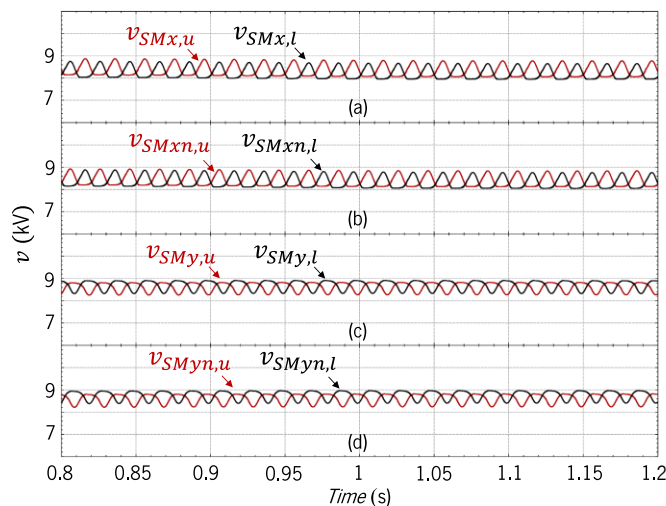


Figure 4.56. FB-MMC4 RPC SM voltages: (a) Positive leg of converter x ; (b) Negative leg of converter x ; (c) Positive leg of converter y ; (d) Negative leg of converter y .

4.9.2 RPC Based on Two-Phase Three-Wire Indirect Modular Multilevel Converter

This RPC topology is quite different from the FB-MMC4 RPC, and it can be considered as a three-phase MMC operating to compensate reactive power, NSC of currents, harmonic contents and balance the

active power. Since the RPC based on two-phase three-wire indirect modular multilevel converter (TW-MMC3 RPC) does not have the potential of an inherent DC-link between the converters as was the case of the FB-MMC4 RPC, it is mandatory to add a DC-link capacitor to ensure a good performance, and to reduce the size of the SM capacitors. On the other hand, the TW-MMC3 RPC solution does not require to install step-down coupling transformers or isolation transformers to interface the converter with the single-phase TPS. The TW-MMC3 RPC based on a V/V power transformer is shown in Figure 4.57. Each half-bridge SM contains two switching devices and one capacitor, which can be inserted or bypassed. The leg inductors are considered as the MMC inner filters, which are important to adjust the circulating current flow between the MMC phases [150].

By using the TW-MMC3 RPC instead of the FB-MMC4 RPC, it is possible to reach the same output voltage level using only 75% of the FB-MMC4 RPC hardware. In other words, the TW-MMC3 RPC topology saves 25% of the SMs required in the FB-MMC4 RPC topology, and at the same RPC power ratings. In addition, Table 4.20 presents the components quantities of the TW-MMC3 RPC [150].

Table 4.20. Components quantities of the TW-MMC3 RPC.

Number of IGBTs	Number of capacitors	Number of inductors	Isolation/coupling transformer
$12(N-1)$	$6(N-1)+1$	6	0

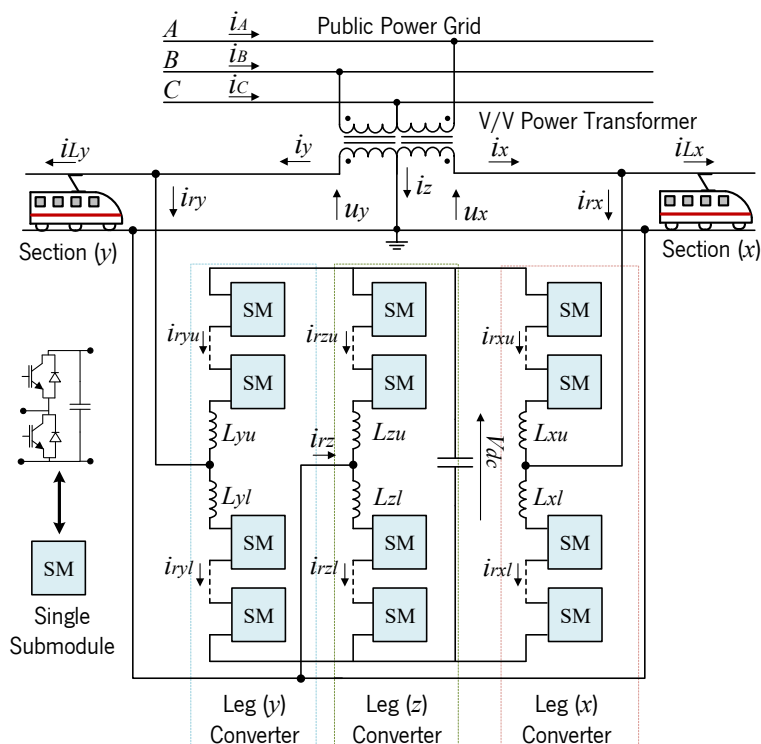


Figure 4.57. TW-MMC3 RPC system with a V/V power transformer.

The load section instantaneous voltages, u_x and u_y , are given in (4.23). In the V/V power transformer, there is 60° out-of-phase between the phasors of the load section voltages. However, in the Scott power transformer, this phase shift is equal to 90° , as demonstrated in the phasors diagram presented

in Figure 4.35(b) and Figure 4.35(c). Figure 4.58 shows the AC equivalent circuit of the TW-MMC3 RPC, where the zero-sequence voltage is given by (4.33), and the voltages of u_{xn} , u_{yn} and u_{zn} are the phase-to-neutral voltages [146].

$$u_{no} = (u_x + u_y) / 3 \quad (4.33)$$

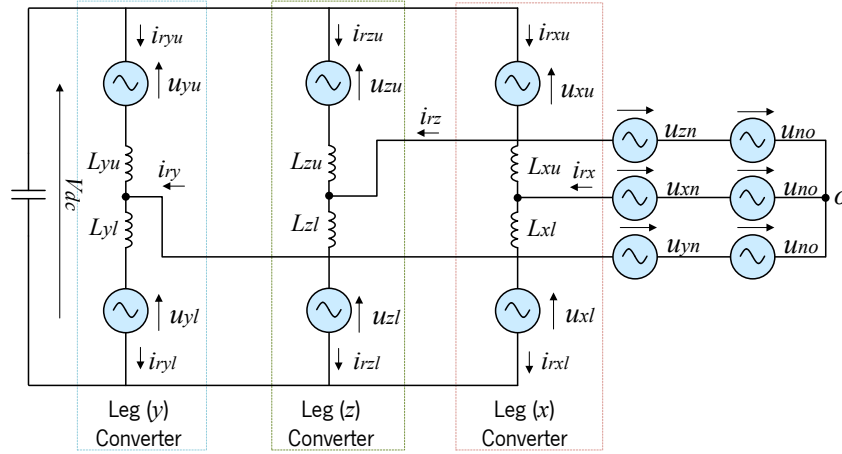


Figure 4.58. AC equivalent circuit of the TW-MMC3 RPC system.

On the other hand, Figure 4.59(a) and Figure 4.59(b) show the output equivalent circuit of single-phase TW-MMC3 RPC converter, and the associated phasors when using the V/V power transformer. Consequently, the load sections instantaneous voltages are calculated as in (4.34), where, u_{no} is the zero-sequence voltage [146].

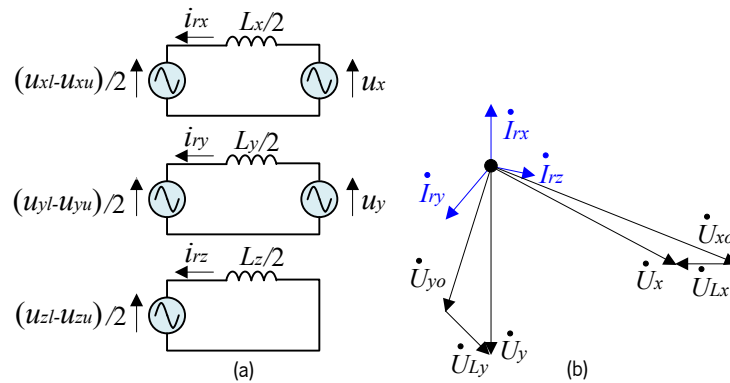


Figure 4.59. TW-MMC3 RPC: (a) Output equivalent circuit; (b) Phasors of output voltages when using V/V power transformer.

$$\begin{aligned} u_x &= u_{xo} + u_{Lx} = u_{xn} + u_{no} \\ u_y &= u_{yo} + u_{Ly} = u_{yn} + u_{no} \\ 0 &= u_{zo} + u_{Lz} = u_{zn} + u_{no} \end{aligned} \quad (4.34)$$

The instantaneous compensation currents synthesized by the TW-MMC3 RPC are given in (4.25) and (4.35). The active and the reactive compensation currents components of the phase x (RMS value) are I_{rxa} and I_{rxr} , respectively. In a similar way, the active and the reactive compensation currents components of the phase y (RMS value) are I_{rya} and I_{ryr} , respectively. The active and the reactive

compensation currents components are presented in (4.3) and (4.7), respectively. From (4.25), the equation that gives the instantaneous values of the compensation currents, it is possible to conclude the voltage drop across the filtering inductance of leg x converter, which can be expressed as in (4.26) after supposing the filtering inductance of the MMC inner filter is 0.1 p.u, namely, $L_x = 0.1 U_x / (I_{rx}^* \omega)$, where L_x , is the equivalent inductance of the leg x converter, and ω is the angular frequency [146].

$$i_{rz} = - (i_{rx} + i_{ry}) \quad (4.35)$$

Substituting (4.26) into (4.34), phase x output voltage of the TW-MMC3 RPC can be obtained as in (4.27). The same analysis is applicable for the leg y converter, as presented in (4.28) and (4.29) [146]. The voltage drop across the filtering inductance of leg z converter can be expressed as in (4.36), after supposing that the inductance of the MMC inner filter is 0.1 p.u, namely, $L_z = 0.1 U_\sigma / (I_{rz}^* \omega)$, where L_z , is the equivalent inductance of the leg z converter, ω is the angular frequency, and U_σ is the RMS value of the feeder voltages U_x or U_y [146].

$$u_{Lz} = L_z \frac{di_{rz}}{dt} = \frac{\sqrt{2} U_\sigma}{10 \sqrt{I_{rza}^2 + I_{rzs}^2}} [I_{rxa} \cos(\omega t + \theta_x) + I_{rxr} \sin(\omega t + \theta_x) - I_{rya} \cos(\omega t + \theta_y) - I_{ryr} \sin(\omega t + \theta_y)] \quad (4.36)$$

Substituting (4.36) into (4.34), the voltage of phase z can be obtained as in (4.37) [146].

$$u_{zo} = - \frac{\sqrt{2} U_\sigma}{10 \sqrt{I_{rza}^2 + I_{rzs}^2}} [I_{rxa} \cos(\omega t + \theta_x) + I_{rxr} \sin(\omega t + \theta_x) - I_{rya} \cos(\omega t + \theta_y) - I_{ryr} \sin(\omega t + \theta_y)] \quad (4.37)$$

The peak voltage values of u_{xo} , u_{yo} and u_{zo} can be obtained from (4.27), (4.29) and (4.37), respectively. These are the output voltages of the TW-MMC3 RPC after taking into consideration the voltage drop across the filter inductors. With regard to the three-phase structure of the TW-MMC3 RPC, the DC-link voltage should not be less than the magnitude of the line-to-line voltage. Since the magnitude of the line-to-line voltage in the V/V power transformer is equal to the amplitude of the phase-to-neutral voltage (this is due to the 60° out-of-phase between the phase voltages, u_x and u_y , as shown in Figure 4.34), then the condition presented in (4.38) is only applicable when using the TW-MMC3 RPC in the V/V power transformer [146], [150].

$$|U_{xo}|, |U_{yo}| > |U_{zo}| \quad (4.38)$$

$$V_{dc} \geq \sqrt{2} U_{\sigma\sigma} ; \sigma \in \{x, y\} \text{ for the V/V power transformer}$$

However, the condition in (4.38) is not applicable when using the Scott power transformer since the magnitude of the line-to-line voltage in the Scott power transformer is higher than the amplitude of the

phase-to-neutral voltage (this is due to the 90° out-of-phase between the phase voltages, u_x and u_y , as shown in Figure 4.33), then the condition presented in (4.39) is applicable when using the TW-MMC3 RPC in the Scott power transformer. Therefore, the TW-MMC3 RPC is the best solution to be used with the V/V power transformer since it demands lower number of hardware power components compared to the FB-MMC4 RPC. The number of half-bridge SMs in one MMC arm should be equal to V_{dc}/V_{sm} . Further characteristics of the TW-MMC3 RPC are presented in the item 4.10, Table 4.25, Table 4.26 and Table 4.27 [146].

The TW-MMC3 RPC has the same parameters design of the FB-MMC4 RPC when using the V/V power transformer. On the other hand, in the Scott power transformer, the TW-MMC3 RPC should have higher SM voltages and a higher main DC-link voltage not less than the magnitude of the line-to-line voltage. The previous conditions obligate to use power switching devices with a higher blocking voltage, which makes this solution expensive and bulky. Therefore, it is not recommended to use the TW-MMC3 RPC topology when using the Scott power transformer instead of the V/V power transformer [146], [150].

$$\begin{aligned} |U_{xo}|, |U_{yo}| &> |U_{zo}| \\ V_{dc} &\geq 2 U_{\sigma o} ; \sigma \in \{x, y\} \text{ for the Scott power transformer} \end{aligned} \quad (4.39)$$

4.9.2.1. Control Algorithm

Control algorithm of the TW-MMC3 RPC should guarantee the correct calculations of the compensation currents to achieve power quality improvement, maintain a constant MMC DC-link voltage, and maintain constant SM voltages. The malfunctioning of one or more of the aforementioned conditions may cause severe impacts on the safety and the efficient operation of MMC. In that regard, control algorithm is proposed in this item to obtain a robust performance of the TW-MMC3 RPC.

Calculations of the reference currents, i_{rx}^* and i_{ry}^* , can be achieved as presented in the Figure 4.48. However, an additional reference voltage signal for the third MMC phase (leg z) is required to assure the correct operation of the TW-MMC3 RPC. The final reference signals, i_{rx}^* , i_{ry}^* and i_{rz}^* are compared with the actual compensation currents synthesized by the TW-MMC3 RPC, i_{rx} , i_{ry} and i_{rz} , as shown in the control diagram presented in Figure 4.60. In that respect, PR controllers are used to correct the error resulting from the difference between the reference and the actual values. Output of the PR controllers gives the voltage reference signals, u_{rx}^* , u_{ry}^* and u_{rz}^* . Although the additional requirement to generate the reference voltage signal, u_{rz}^* , however, using the TW-MMC3 RPC instead of the FB-MMC4 RPC results in lower number of hardware components. Consequently, it leads to simplify the control of the RPC system.

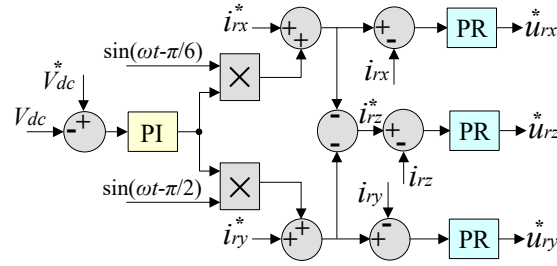


Figure 4.60. DC-link voltage control and the calculation of the voltage reference signals of the TW-MMC3 RPC.

Figure 4.61 shows three control blocks that are responsible to balance the voltage across each of the SM capacitors. A robust SM voltage control leads to better MMC performance and then, this control is achieved through three steps:

- MMC leg averaging voltage control, as shown in Figure 4.61(a);
- MMC arm averaging voltage control, as shown in Figure 4.61(b);
- MMC SM individual voltage control, as shown in Figure 4.61(c).

Figure 4.61 represents the SM capacitors voltage control of the TW-MMC3 RPC after considering that $\sigma \in \{x, y, z\}$. The overall required control blocks to achieve that purpose in the TW-MMC3 RPC are six (two control blocks for each MMC leg), whereas, the required control blocks in the FB-MMC4 RPC are eight control blocks. The first control block, presented in Figure 4.61(a), shows the MMC leg averaging voltage control and the circulating current control, where two PI controllers are used for each MMC leg. The averaging control is implemented by summing the actual voltage values for all SM capacitors, then it compares the average of this actual value with a value provided as a reference [122]. The output of the first PI controller is considered as a reference value for a circulating current controller, which is implemented after summing the arm currents $i_{r\sigma u}$, $i_{r\sigma l}$, where $\sigma \in \{x, y, z\}$, in the upper and the lower arms that belong to the same MMC leg.

Circulating current, i_{cir} , presented in (4.32) is considered as a part of the MMC arm current. However, it consists of a DC current component, AC current component that has double of the fundamental frequency (second harmonic current) and other harmonic currents. This current should be controlled as it causes extra losses and may increase the ratings of the power components. The second control block, presented in Figure 4.61(b), represents the MMC arm averaging voltage control [161]. The same explanation of Figure 4.50(b) and Figure 4.50(c) can be applied for the Figure 4.61(b) and Figure 4.61(c), respectively, where $\sigma \in \{x, y, z\}$ in the TW-MMC3 RPC.

The final signals of MMC leg averaging control, A_σ , MMC arm averaging control, $V_{r\sigma u}$ and $V_{r\sigma l}$, MMC SM individual voltage control, $V_{i\sigma u}$ and $V_{i\sigma l}$, where $\sigma \in \{x, y, z\}$, are added to the voltage reference signals, $u_{r\sigma}^*$, to generate a voltage command (modulating signal) for each SM, which is to be compared

with the phase-shifted PWM triangular carriers, as shown in Figure 4.51. The Phase-shifted PWM can be easily applied after shifting the carriers phase angle in the same MMC arm, consecutively, and with a fixed angle of $360/(N-1)$. It should be declared that all of the above-mentioned explanation is applicable when using the TW-MMC3 RPC with a V/V power transformer. When using the Scott power transformer, several points should be considered in the control blocks and the design parameters of this converter (more details about this case are presented in the item 4.10).

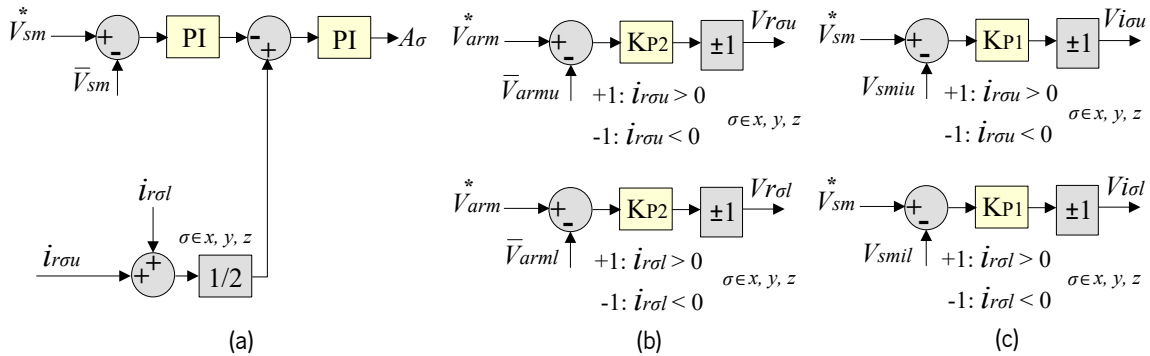


Figure 4.61. SM capacitors voltage control of the TW-MMC3 RPC: (a) MMC leg averaging voltage control; (b) MMC arm averaging voltage control; (c) MMC SM individual voltage control.

4.9.2.2. Simulation Results

Simulation model of the TW-MMC3 RPC based on V/V power transformer is established by using the *PSIM* V.9.1 tool. This is important to validate the TW-MMC3 RPC system and the associated control algorithm. The simulation model consists of 7-levels ($N = 7$) MMC with a total number of 36 SMs. The main parameters of the simulation model are presented in Table 4.21. In this framework, the same load parameters presented in Table 4.6 are used in this simulation after considering a unitary load power factor for both load sections. Therefore, the locomotives can be modeled as a resistive load connected in parallel with an uncontrolled full-bridge rectifier on the secondary windings of the locomotive transformer [57], where the full locomotive model is shown in Figure 4.9. The simulation considers that both of the load sections are unequally loaded. Then, in this study, load section x is loaded with a value of 4.8 MW and load section y is loaded with a value of 2.4 MW, as presented in Table 4.6.

The three-phase currents before and after compensation have the same waveforms presented in Figure 4.52(a) and Figure 4.52(b), respectively. The load section currents are presented in Figure 4.62(a), where the current of i_{Lx} , has double the value of i_{Ly} . The compensation currents provided by the RPC are demonstrated in Figure 4.62(b). These currents are calculated according to the control block presented in Figure 4.48. The used power transformers in the simulation model are

considered as ideal ones, without considering leakage flux, copper losses and core losses. In other words, the ideal transformer gives an output power exactly equal to its input power.

Table 4.21. Parameters of the TW-MMC3 RPC simulation model.

Description	Symbols	Values
Line-to-line PPS voltage	U_{AB}, U_{BC}, U_{CA}	220 kV
Catenary voltage	U_x, U_y	25 kV
RPC filter inductance	$L_{\sigma u}, L_{\sigma nu}, L_{\sigma l}, L_{\sigma nl}$	2.8 mH
Catenary lumped impedance	Z_L	$0.05 + j 0.15 \Omega$
SM capacitor	C_{SM}	500 μ F
Main DC-link capacitor	C_{dc}	4 mF
SM Switching frequency	f_{isw}	3 kHz
Equivalent switching frequency	f_{sw}	18 kHz
SM voltage	V_{SM}	8.3 kV
DC-link voltage	V_{dc}	50 kV
Number of SMs in each arm	$N-1$	6

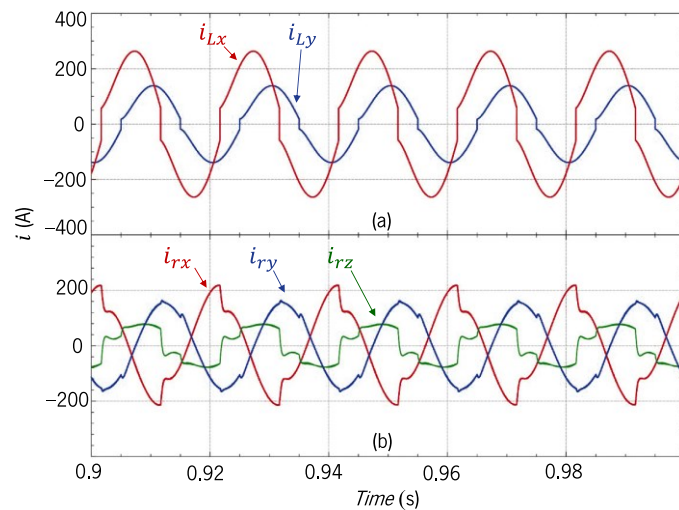


Figure 4.62. TW-MMC3 RPC simulation results: (a) Load section currents; (b) Compensation currents.

Compensation currents synthesized by the TW-MMC3 RPC are shared among the upper and the lower arms, then, currents of the upper arms, $i_{rxu}, i_{ryu}, i_{rzu}$, and currents of the lower arms, $i_{rxl}, i_{ryl}, i_{rzl}$, are presented in Figure 4.63. Apparently, the DC harmonic content, the fundamental frequency harmonic content of 50 Hz, and the double fundamental frequency harmonic content of 100 Hz are introduced, as shown in the frequency spectrum in Figure 4.64.

The DC harmonic content is mainly responsible for the DC power transfer between the MMC phases and the main DC-link (charging and discharging of the SM capacitors), while the fundamental frequency harmonic content composes the compensation currents synthesized by the converter. The double fundamental frequency content indicates the circulating current between the MMC phases. Obviously,

and as shown in Figure 4.64(a), the compensation currents synthesized by the TW-MMC3 RPC do not contain any DC contents or double fundamental frequency contents. In other words, these currents do not contribute to the compensation currents synthesized by the converter. All currents presented in Figure 4.64 have the harmonic contents of the third, fifth, etc. However, high-order harmonic contents are normally neglected, since they have small amplitudes.

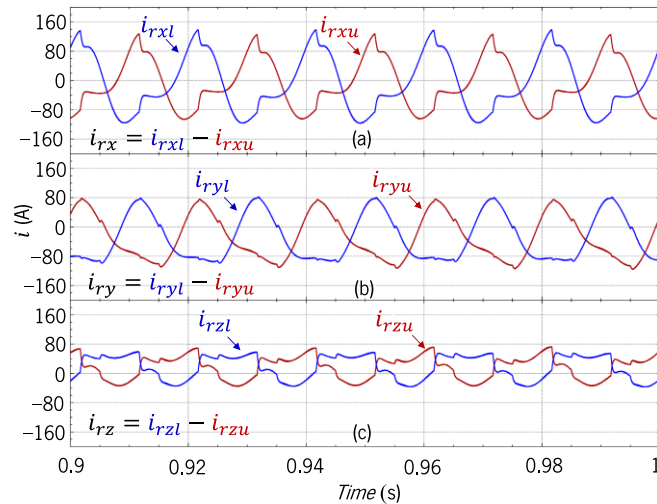


Figure 4.63. TW-MMC3 RPC simulation results: (a) Arm currents of phase x ; (b) Arm currents of phase y ; (c) Arm currents of phase z .

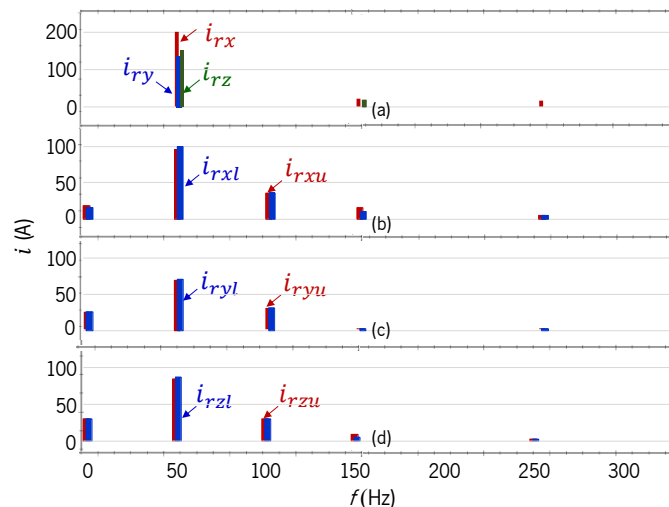


Figure 4.64. TW-MMC3 RPC frequency spectrum: (a) Compensation currents; (b) Arm currents of phase x ; (c) Arm currents of phase y ; (d) Arm currents of phase z .

Figure 4.65 shows the results of the TW-MMC3 RPC SM voltages. These results confirm the effectiveness of the applied voltage balancing control, where the SM voltages maintain a value close to the reference value of 8.3 kV, and the total DC-link voltage follows its reference value of 50 kV. The SM voltage value of 8.3 kV is not reasonable for today's IGBTs, where the maximum voltage blocking of the commercially available IGBTs is close to 6.5 kV [112], then, the MMC should be designed with a higher level to reduce the SM voltage or two IGBTs connected in series have to be used.

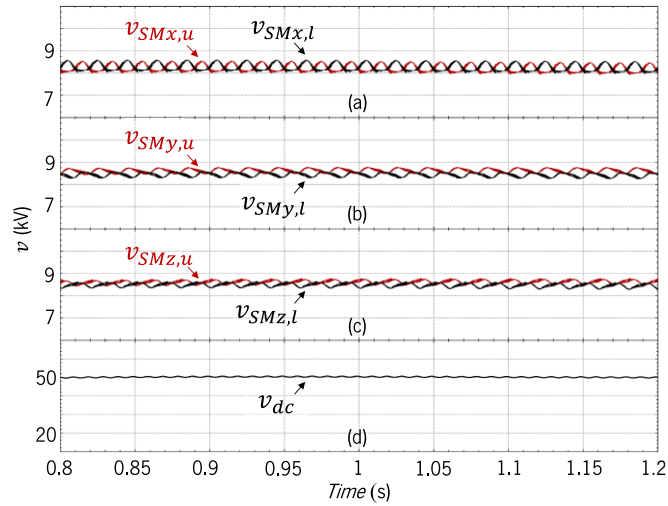


Figure 4.65. TW-MMC3 RPC SM voltages: (a) Phase x ; (b) Phase y ; (c) Phase z ; (d) Main DC-link voltage.

4.9.3 Simplified RPC Based on Half-Bridge Indirect Modular Multilevel Converter

The RPC based on a half-bridge indirect modular multilevel converter (HB-MMC2 RPC) has a simpler hardware structure when compared to the FB-MMC4 RPC and the TW-MMC3 RPC. The half-bridge converters have been used in high-power applications due to their high efficiency, low cost and simple control compared to the full-bridge converters [162]. The half-bridge MMC is a four-quadrant multilevel converter and its drawback is the fact that it requires the double of the phase voltage with respect to the output neutral. Therefore, two large bulk capacitors with a mid-neutral point are required, as shown in Figure 4.66.

However, as shown in Figure 4.67, in the HB-MMC2 RPC, each DC-link capacitor is connected in series with a specific number of SMs, which is half the number of the SMs connected in the case of the FB-MMC4 RPC to generate a half-cycle of the sinusoidal waveform, which means, the power can be transferred to the output terminals during the on-time using half the number of the SMs compared to the case of the FB-MMC4 RPC. This increases the efficiency (due to the lower power losses) of the HB-MMC2 RPC compared to the FB-MMC4 RPC. Since N is the MMC number of levels, $(N-1)$ is the number of SMs in the arm. Table 4.22 presents the components quantities of the HB-MMC2 RPC. In this context, the HB-MMC2 RPC with a V/V power transformer is used in this study [150].

The main disadvantage of the HB-MMC2 RPC is that each of the DC-link voltage capacitor has a voltage ripple frequency similar to the fundamental frequency of the traction power grid, which implies to use two large bulk capacitors with a mid-neutral point. When the MMC level is quite enough to withstand the medium voltage value, then, this solution does not require the use of step-down coupling transformers or isolation transformers to interface the converter with the traction power grid. The switching stress for each switching device in the HB-MMC2 RPC should have double the value of the

applied switching frequency in the TW-MMC3 RPC and FB-MMC4 RPC topologies. Otherwise, higher value of filter inductors is required for the HB-MMC2 RPC because of the high current ripple, as a result of the low equivalent switching frequency. To some extent and although this topology has some drawbacks, it can offer a new attempt for power quality improvement in the railway system, which can expand the research ideas as well [122], [130].

Table 4.22. Components quantities of the HB-MMC2 RPC.

Number of IGBTs	Number of capacitors	Number of inductors	Isolation/coupling transformer
$8(N-1)$	$4(N-1)+2$	4	0

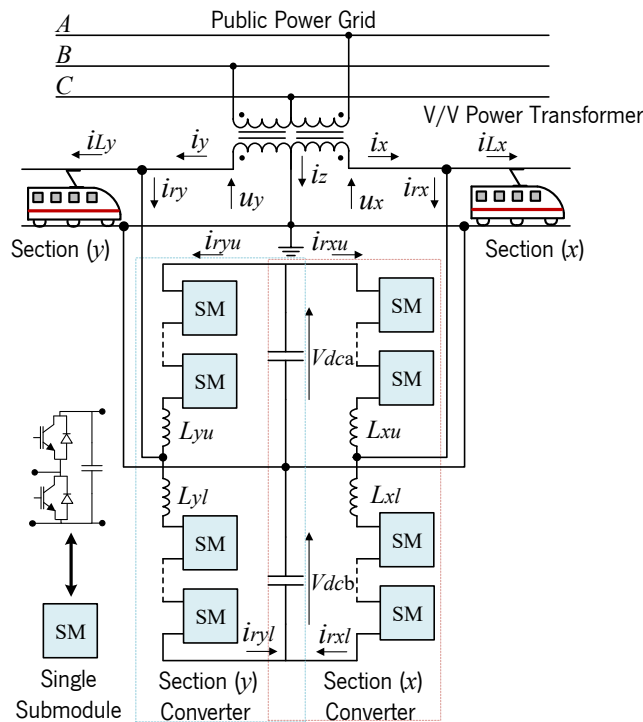


Figure 4.66. HB-MMC2 RPC system with a V/V power transformer.

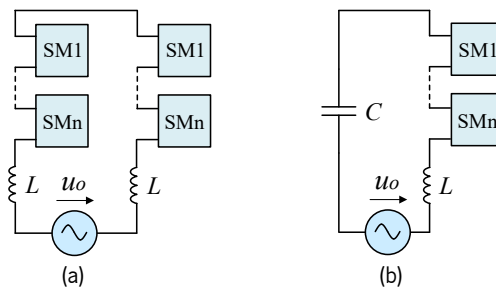


Figure 4.67. Number of SMs connected to the output terminals: (a) FB-MMC4 RPC; (b) HB-MMC2 RPC.

The same previous analysis of the TW-MMC3 RPC can be applied for the HB-MMC2 RPC, then, the AC equivalent circuit of the HB-MMC2 RPC is presented in the Figure 4.68. As a result, and after considering the fact that HB-MMC2 RPC DC-link requires double the voltage with respect to the output neutral, the DC-link voltage should follow the condition presented in (4.40), which is only applicable when using the HB-MMC2 RPC with the V/V power transformer, because the out-of-phase between u_x ,

and u_y is equal to 60° . This solution is applicable in the V/V power transformer and when a high number of MMC levels is implemented to decrease the voltage stress across the power switching devices, considering the maximum voltage blocking power of 6.5 kV of the commercially available power switching devices [112]. The value of $U_{\sigma\sigma}$ refers to the RMS AC output voltage of the HB-MMC2 RPC after considering the voltage drop across the filter inductors [150].

$$V_{dc} \geq 2 \sqrt{2} U_{\sigma\sigma} ; \sigma \in \{x, y\} \text{ for the V/V power transformer} \quad (4.40)$$

However, the condition (4.40) is not applicable when using the Scott power transformer because the out-of-phase between u_x and u_y is equal to 90° . In this case, the DC-link voltage should meet the condition presented in (4.41). Using the HB-MMC2 RPC with the Scott power transformer is not recommended due to the higher DC-link voltage compared to the case when using the HB-MMC2 RPC with the V/V power transformer [150].

$$V_{dc} \geq 4 U_{\sigma\sigma} ; \sigma \in \{x, y\} \text{ for the Scott power transformer} \quad (4.41)$$

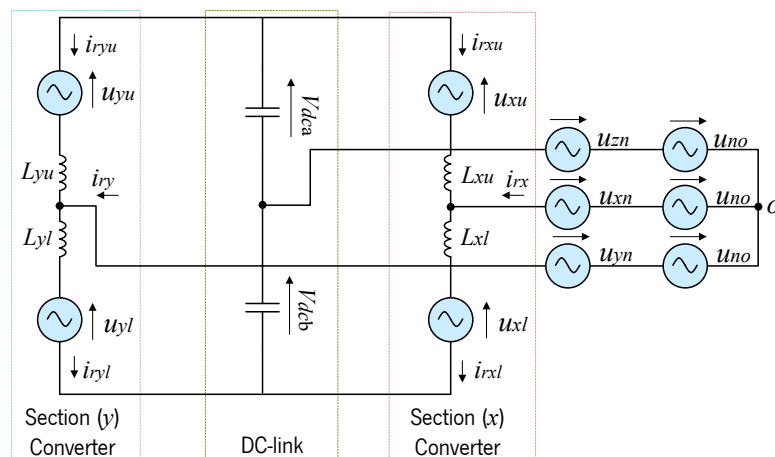


Figure 4.68. AC equivalent circuit of the HB-MMC2 RPC system.

Since this topology saves 50% of FB-MMC4 RPC power devices and it requires lower control complexity, then, an implementation of a reduced-scale workbench was selected to experimentally validate the HB-MMC2 RPC configuration. More details are presented in the Chapter 5.

4.9.3.1. Control Algorithm

The implemented control method in this study is called a digital deadbeat predictive control. Unlike the PI and PR controllers that compile integral errors, deadbeat predictive control is a technique that attempts to extract the required control action during each sample interval through calculations based on the circuit model of the system being controlled. The accuracy of the equivalent circuit is a significant factor to maintain the system output values equal to the reference signals [163].

FB-MMC4 RPC and TW-MMC3 RPC simulation results were obtained by using PR controllers to track the reference signals. This type of controllers compares the compensation current references, i_{rx}^* and i_{ry}^* , with the actual values of i_{rx} and i_{ry} . The main disadvantage of these controllers is the inaccessibility of the MMC circulating current control. It is worthy to mention, the circulating currents do not contribute to the compensation currents synthesized by the converter. However, they circulate between the MMC phases, and they mainly caused by the imbalance between the upper and the lower MMC arm voltages. In addition, the imbalance between the MMC mid-neutral point DC-link voltages will increase the circulating current effect in the HB-MMC2 RPC. A high value of circulating current will not affect the quality of the compensation currents synthesized by the RPC, but it has a distinctive effect on the overall losses and the ratings of the used power components. Therefore, circulating current should be suppressed as possible to reduce the previous impacts [164].

On the other hand, and in some applications, the MMC circulating current can be used in a useful way. For instance, the MMC circulating current is used during the phase-to-ground fault, in which the MMC works in an asymmetrical operation, then the asymmetrical power will flow through the upper and the lower MMC arms, leading to an imbalance of arm capacitor energy. In that case, some improved control strategies were developed based on circulating current injection [156]. Furthermore, it was addressed in [165] that higher harmonic injection in the circulating current improves the MMC operation by reducing the capacitor voltage ripples. In addition, it was addressed in [166] that the existence of a modest circulating current component in the MMC arm current can be useful to have a control freedom, then optimizing the MMC performance. As a result, the interrelation between the compensation currents synthesized by the MMC, the circulating currents, and the SM capacitor voltages complicates the MMC control. The aforementioned quantities may affect each other, then affecting the overall MMC performance.

This item shows that the proposed control method based on deadbeat predictive control has the merits of simplicity and better performance of circulating current suppression than the traditional PI controller. On the other hand, the stationary frame of PI controllers cannot reach the zero steady-state error in controlling the AC signals [167]. PR controllers contain loops and variables that should be tuned [168]. The tuning rules are complex and entail high programming efforts. Authors in [169] proposed MMC circulating current control method using a model predictive control for circulating current suppression, SMs voltage balancing control and to control the AC side currents. However, this method uses a cost function that may overload the processor due to the massive calculations volume. Then, the higher the level of the MMC, the higher control complexity is required [170].

Deadbeat predictive control method can easily be programmed, and it is normally used when a fast-dynamic response is required. However, this control has some disadvantages in terms of existing some errors in the parameter values due to the model assumptions and the unmodeled delay [171]. In this context and according to a comparative study of fixed switching frequency current control techniques presented in [172], the best obtained results that have the smallest error (between the reference and the actual current signals) were the synchronous PI, the *feedforward* [173], the *sliding mode* [174] and the deadbeat predictive control technique presented in [175]. Therefore, a low computational reference equations based on the technique in [175] is developed in the further steps to implement the whole control system in the microprocessor. The results in [175] show a small steady-state error and a fast transient response. Compared with the other current control algorithms, the used deadbeat predictive control algorithm has a shorter code and more time-efficient.

Figure 4.69 shows one MMC leg equivalent circuit (one phase) that helps to obtain the electrical model of the HB-MMC2 RPC. The upper arm current, i_{rxu} , includes two main components: the circulating current component, i_{cir} , and the current related to the compensation current, $i_{rx}/2$, as presented in (4.42). These steps are applicable for the lower arm current as well, i_{rxl} , as presented in (4.43) [160].

$$i_{rxu} = i_{cir} - \frac{i_{rx}}{2} \quad (4.42)$$

$$i_{rxl} = i_{cir} + \frac{i_{rx}}{2} \quad (4.43)$$

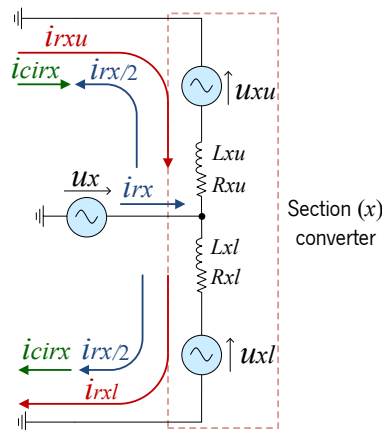


Figure 4.69. HB-MMC2 RPC: one phase equivalent circuit.

From (4.42) and (4.43), the circulating current normally circulates between MMC legs can be expressed as in (4.44). There are two main parts: the double fundamental frequency component of 100 Hz and its even order harmonic contents, and a DC component resulting from the MMC DC-link currents [176], [177]. To keep the MMC losses and the arm currents as lowest as possible, it is necessary that the circulating current should be a pure DC [178].

$$i_{cirx} = \frac{i_{rxu} + i_{rxl}}{2} \quad (4.44)$$

By applying Kirchhoff's voltage law on the equivalent circuit of Figure 4.69, it is possible to obtain the voltage equation of the upper and the lower loops as in (4.45) and (4.46) [160].

$$u_x = -L_{xu} \frac{di_{rxu}}{dt} - u_{xu} - i_{rxu} R_{xu} \quad (4.45)$$

$$u_x = L_{xl} \frac{di_{rxl}}{dt} + u_{xl} + i_{rxl} R_{xl} \quad (4.46)$$

Final control equations based on the deadbeat predictive control are developed using a low computational cost after neglecting the semiconductor conduction and switching losses. This current control strategy is selected since the results in [175] have a small steady-state error and a fast transient response. The further steps are applied for the upper arm of section x converter. The deadbeat predictive current control methodology is determined after knowing the error in the upper arm current of section x converter as in (4.47).

$$i_{rxu_err} = i_{rxu}^* - i_{rxu} \quad (4.47)$$

Due to the low-voltage drop across the internal resistors of the filter inductors, the voltage drop across the MMC arm resistors is neglected to simplify the calculations, without introducing a significant error. By substituting the first equation of (4.45) into (4.47):

$$u_x = -L_{xu} \frac{d(i_{rxu}^* - i_{rxu_err})}{dt} - u_{xu} \quad (4.48)$$

By separating the differential part of (4.48), it is possible to obtain the following equation that gives the upper arm voltage of section x converter.

$$u_{xu} = -L_{xu} \frac{di_{rxu}^*}{dt} + L_{xu} \frac{di_{rxu_err}}{dt} - u_x \quad (4.49)$$

According to the authors in [175] and [172], it is possible to assume a linear variation of $i_{rxu_err}(K)$ with the time (type of $f(x) = xt$), where K , denotes the value at the present sample interval and the next sample interval is denoted as $(K+1)$ [163]. An approximation of $i_{rxu}^*(K)$ derivative in function to the variables values at the instant of (K) and $(K - 1)$ is possible according to (4.50).

$$\frac{dx}{dt} \cong \frac{x(K) - x(K - 1)}{\Delta t} \quad (4.50)$$

Then, it is possible to get (4.51), where T_s is the sampling period.

$$u_{xu}(K) = -\frac{L_{xu}}{T_s} (i_{rxu}^*(K) - i_{rxu}^*(K - 1) - i_{rxu_err}(K)) - u_x(K) \quad (4.51)$$

By substituting (4.47) into (4.51), it is possible to get the equation (4.52).

$$u_{xu}(K) = \frac{L_{xu}}{T_s} [-2 i_{rxu}^*(K) + i_{rxu}^*(K-1) + i_{rxu}(K)] - u_x(K) \quad (4.52)$$

The control algorithm of the HB-MMC2 RPC should calculate the compensation current references, i_{rx}^* and i_{ry}^* , as in (4.10). Therefore, the equation (4.52) as it is, does not serve that purpose, since it computes the compensation current references, i_{rxu}^* and i_{ryu}^* , of the upper and the lower MMC arms. The main purpose of this control is to have circulating currents of i_{cirx} and i_{ciry} between MMC legs close to zero, then from (4.44), the circulating current is significantly reduced when the upper and the lower arm currents are complementary as in (4.53) [160].

$$i_{cirx} = \frac{i_{rxu} + i_{rxl}}{2} \cong 0 \Rightarrow i_{rxu} \cong -i_{rxl} \quad (4.53)$$

By considering the aforementioned assumptions, it is possible to write (4.54).

$$i_{rxu} = -\frac{i_{rx}}{2}, \quad i_{rxl} = +\frac{i_{rx}}{2} \quad (4.54)$$

By substituting (4.54) into (4.52), the equation that calculates the upper arm voltage of u_{xu} in relation with the phase x compensation current reference, i_{rx}^* , is presented in (4.55).

$$u_{xu}^*(K) = \frac{L_{xu}}{2T_s} [2i_{rx}^*(K) - i_{rx}^*(K-1) + 2i_{rxu}(K)] - u_x(K) \quad (4.55)$$

The same previous steps are applicable to conclude the voltage reference final equation for the lower MMC arm of section x as presented in (4.56).

$$u_{xl}^*(K) = -\frac{L_{xl}}{2T_s} [2i_{rx}^*(K) - i_{rx}^*(K-1) - 2i_{rxl}(K)] + u_x(K) \quad (4.56)$$

By applying the same aforementioned steps for section y , the voltage final reference equations for the upper and the lower MMC arms of section y are presented in (4.57) and (4.58).

$$u_{yu}^*(K) = \frac{L_{yu}}{2T_s} [2i_{ry}^*(K) - i_{ry}^*(K-1) + 2i_{ryu}(K)] - u_y(K) \quad (4.57)$$

$$u_{yl}^*(K) = -\frac{L_{yl}}{2T_s} [2i_{ry}^*(K) - i_{ry}^*(K-1) - 2i_{ryl}(K)] + u_y(K) \quad (4.58)$$

Equations (4.55), (4.56), (4.57) and (4.58) are the final voltage reference equations to apply the deadbeat predictive control. The circulating current in this way is significantly reduced but not totally canceled. This because the last is important to achieve the balance between the main DC-links voltages, besides the main role in balancing the SMs voltages. The used control algorithm is divided to three main parts. Figure 4.48 shows the control part of compensation currents acquisition, i_{rx}^* and i_{ry}^* ,

after using an E-PLL and LPF to extract the total DC component from the load currents, i_{Lx} and i_{Ly} . Figure 4.70 shows the part of the DC-link voltage regulation by using two PI controllers and the predictive control to obtain the voltage reference signals, u_{xu}^* , u_{xl}^* , u_{yu}^* and u_{yl}^* . One of the PI controllers is used to compare the actual value of the DC-link voltages ($V_{dca} + V_{dcb}$) with a reference value, then, the output of this controller is multiplied by the correspondent Sine waves to synchronize between the PI output signal and the compensation current waveforms. The second PI controller is mainly used to achieve a DC-link voltage balance between the mid-neutral point capacitors [160].

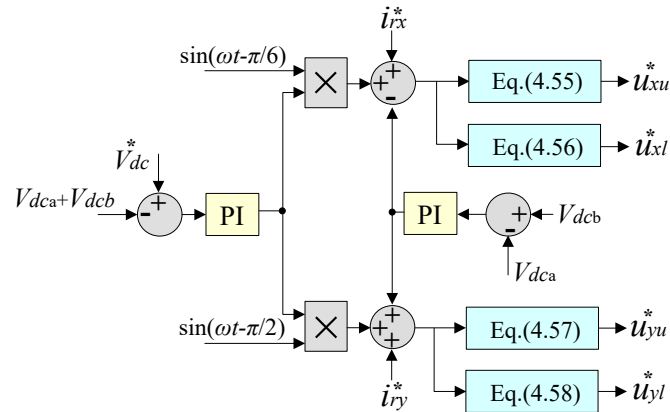


Figure 4.70. DC-link voltage control and calculation of the voltage reference signals of the HB-MMC2 RPC.

Figure 4.71(a) shows an averaging voltage balancing control for SMs capacitors. This control ensures that the voltage of each SM in the leg is close to the average voltage that is provided as a reference. The second PI controller, presented in Figure 4.71(a), allows a low circulating current when it is necessary to balance the SM voltages [100]. Figure 4.71(b) and Figure 4.71(c) indicate the MMC arm averaging voltage control and the individual voltage balancing control, respectively [179], [122]. These controllers force the capacitor voltage of each SM to follow its voltage reference [180], where the output of the controller is multiplied by +1 if the current's direction in the arm is to charge the capacitors, or by -1 if its direction is to discharge the capacitors. These control blocks have been deeply described in the item 4.9.1.

By taking into consideration twenty-four SMs in each MMC leg, so the total SMs number will be divided equally between the upper and the lower arms in the same leg, then the arm will consist of twelve SMs, $N-1 = 12$. Consequently, the PWM triangular carriers are shifted by $360/(N-1)$ degrees between each other. The voltage command generation of each SM applied to a phase-shifted PWM is presented in Figure 4.51. The only difference here is in the input signals of the control block (voltage reference signals), where these signals have to be replaced with the outputs of the deadbeat predictive control (instead of using $u_{r\sigma}^*$ as an input, should be $u_{\sigma(u,l)}^*$, where $\sigma \in \{x, y\}$ and (u, l) means the upper or the lower arms. The resulting modulating signal is to be compared with the phase-shifted PWM

triangular carriers, as presented in Figure 4.51 [160]. It should be declared that all of the above-mentioned explanation is applicable when using the HB-MMC2 RPC with the V/V power transformer. When using the Scott power transformer, several points should be considered in the control blocks and the design parameters of this converter.

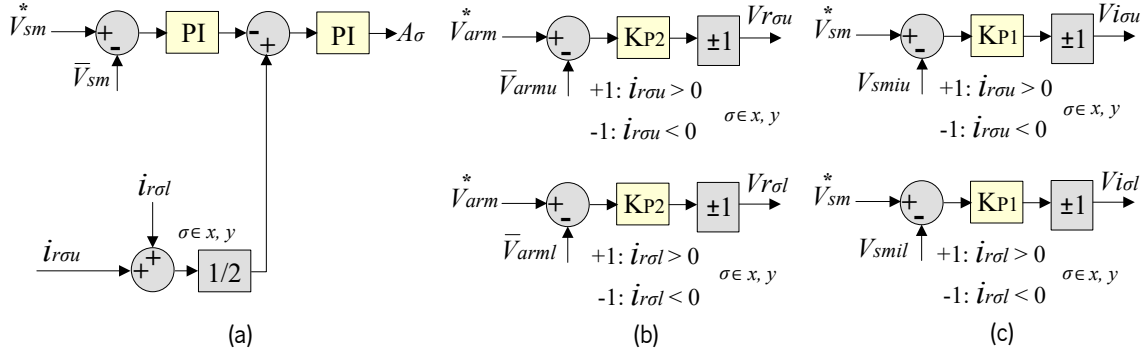


Figure 4.71. SM capacitors voltage control of the HB-MMC2 RPC: (a) MMC leg averaging voltage control; (b) MMC arm averaging voltage control; (c) MMC SM individual voltage control.

4.9.3.2. Simulation Results

An MMC with a few levels is sufficient for a proof of concept of the deadbeat predictive current control, then, the simulation model of the HB-MMC2 RPC consists of twenty-four SMs per each leg (13-levels), and it was developed under *PSIMV.9.1* simulation tool, where the main parameters are presented in Table 4.23 and Table 4.24. The main objective is to perform a comparative study when using the proposed deadbeat predictive control for circulating current reduction in MMC, and when using the conventional PI controller to track the reference signals of i_{rx}^* and i_{ry}^* . The value of the control frequency (of the predictive controller) is equal to the SM switching frequency, f_{isw} .

Since the power factor of the electric locomotives in high-speed trains is close to unitary and the current harmonics are quite small, the high-speed railway electric locomotive is modeled as a resistive-inductive load in parallel with an uncontrollable rectifier bridge connected to the secondary windings of the locomotive transformer, as shown in Figure 4.9. The output of the uncontrollable rectifier bridge is connected to resistor R_2 and inductance L_2 , which are in series. The turns ratio of the locomotive transformer is 25/1.5. The locomotive model parameters are selected as $R_1 = 2 \Omega$, $R_2 = 3.3 \Omega$ and $L_2 = 0.8 \text{ mH}$. At these values, section x load power is close to 1.75 MW. Section y load power is chosen to be 150% higher than section x load power, as presented in the Table 4.23 [160].

This case study presents simulation results for two scenarios: (a) when using the deadbeat predictive current control methodology; (b) when replacing the equations (4.55), (4.56), (4.57) and (4.58) presented in Figure 4.70 by conventional PI controllers. The results for both cases are presented after

considering the same control parameters (similar PI parameters) of the MMC DC-link voltage presented in Figure 4.70, and the PI and KP parameters presented in Figure 4.71.

Table 4.23. Load parameters of the HB-MMC2 RPC converter.

Symbols	Section x	Section y
R_1	2 Ω	1.34 Ω
R_2	3.3 Ω	2.2 Ω
L_2	0.8 mH	0.8 mH
P_L	1.75 MW	2.62 MW

Table 4.24. Parameters of the HB-MMC2 RPC simulation model.

Description	Symbols	Values
Line-to-line PPS voltage	U_{AB}, U_{BC}, U_{CA}	110 kV
Catenary voltage	U_x, U_y	25 kV
RPC filter inductance	$L_{\sigma u}, L_{\sigma nu}, L_{\sigma l}, L_{\sigma nl}$	3 mH
Catenary lumped impedance	Z_L	0.05 + j 0.15 Ω
SM capacitor	C_{SM}	900 μ F
Main DC-link capacitor	$C_{dca} = C_{dcb}$	5 mF
SM Switching frequency	f_{isw}	3 kHz
Equivalent switching frequency	f_{sw}	36 kHz
SM voltage	V_{SM}	6 kV
DC-link voltage	V_{dc}	72 kV
Number of SMs in each arm	$N-1$	12

Figure 4.72(a) shows the three-phase currents before compensation. The currents are imbalanced and have NSC of currents. On the other hand, Figure 4.72(b) presents the same currents after compensating reactive power, harmonics and shifting half of the active power difference between the load sections. In that case, the three-phase currents are balanced and sinusoidal. The load section currents of i_{Lx} and i_{Ly} at unitary load power factor are presented in Figure 4.72(c). It is important to note that the results presented in Figure 4.72 are very similar when using the deadbeat predictive control or the PI controllers. The three-phase currents before compensation, i_A , i_B and i_C , and the catenary section currents, i_{Lx} and i_{Ly} , have no relation with the HB-MMC2 RPC system operation. The three-phase currents after compensation, i_{A2} , i_{B2} and i_{C2} , are resulting after injecting the compensation currents of i_{rx} and i_{ry} . The compensation currents are calculated according to the load section currents of i_{Lx} and i_{Ly} , as in (4.10). In addition, the circulating currents do not contribute to the compensation currents injected by the HB-MMC2 RPC system. Therefore, the three-phase currents after compensation should almost have similar waveforms regardless the used controller [160].

Figure 4.73(I) presents the results when using the proposed deadbeat predictive current control methodology for circulating current suppression. Figure 4.73(I)(a) presents the HB-MMC2 RPC compensation currents. Phase x compensation current, i_{rx} , has a higher value than in phase y compensation current, i_{ry} , because load section y has a higher load value. Figure 4.73(I)(b) and Figure 4.73(I)(c) show the MMC arm currents. Note that subtracting the lower arm current, $i_{r\sigma l}$, from the upper arm current, $i_{r\sigma u}$, gives the MMC compensation current, $i_{r\sigma}$. Figure 4.73(I)(d) shows the circulating currents in MMC legs, $i_{cir\sigma}$. The circulating currents were calculated according to (4.44) and they have an average value of 5 A. This small current component is important to accomplish the balance between the MMC SM voltages.

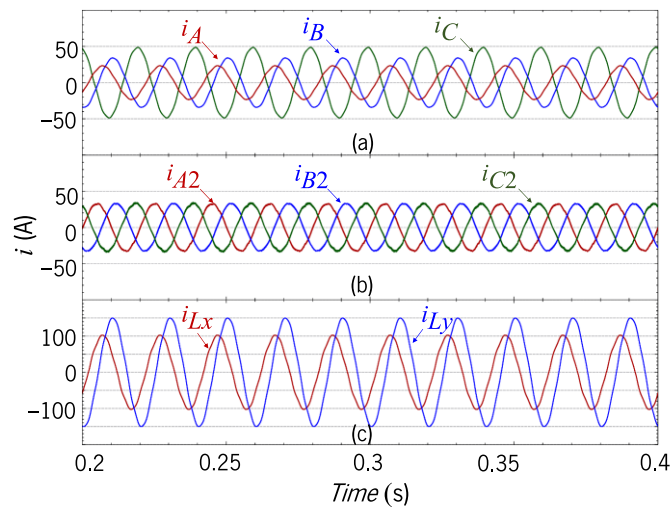


Figure 4.72. HB-MMC2 RPC simulation results: (a) Three-phase grid currents before compensation; (b) Three-phase grid currents after compensation; (c) Catenary section (x and y) currents.

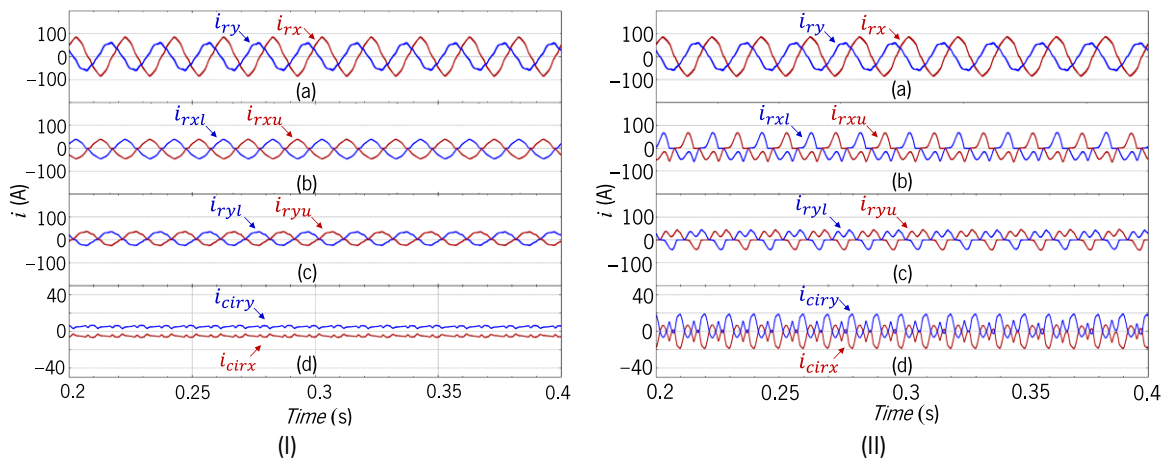


Figure 4.73. HB-MMC2 RPC currents when using the proposed predictive current controller (I) and when using the conventional PI controllers (II): (a) Compensation currents; (b) Upper and lower arm currents of section x converter; (c) Upper and lower arm currents of section y converter; (d) MMC circulating currents.

Figure 4.73(II)(a) presents the simulation results when using well-tuned conventional PI controllers. The compensation currents injected into the power grid presented in Figure 4.73(II)(a) and Figure 4.73(II)(a) are similar, and have no relation with the MMC circulating currents. However, the

upper and the lower arm currents presented in Figure 4.73(II)(b) and Figure 4.73(II)(c) are quite different from the ones presented in Figure 4.73(I)(b) and Figure 4.73(I)(c). In this case, arm currents have higher harmonic contents and higher RMS value due to the circulating currents between the MMC phases, which have an RMS value of 9.8 A, as shown in Figure 4.73(II)(d). As a result, the circulating current component distorts the MMC arm currents.

The frequency spectrum of HB-MMC2 RPC compensation currents when using the proposed deadbeat predictive current control methodology for circulating current suppression is presented in Figure 4.74(I)(a) and Figure 4.74(I)(b), where only fundamental current components of 50 Hz are presenting. In that case, the circulating currents frequency spectrum presented in Figure 4.74(I)(c) and Figure 4.74(I)(d) mainly shows DC components, which are important for the SM voltage balancing control, besides regulating the main DC-link voltage. On the other hand, Figure 4.74(II)(a) and Figure 4.74(II)(b) shows the frequency spectrum of the HB-MMC2 RPC compensation currents when using well-tuned conventional PI controllers. The circulating currents do not contribute to the total compensation currents. Therefore, the frequency spectrum of the compensation currents presented in Figure 4.74(I)(a) and Figure 4.74(I)(b) is similar to the one presented in Figure 4.74(II)(a) and Figure 4.74(II)(b). The circulating currents, in this case, have the multiples of the second-order frequency component (100 Hz), as shown in Figure 4.74(II)(c) and Figure 4.74(II)(d).

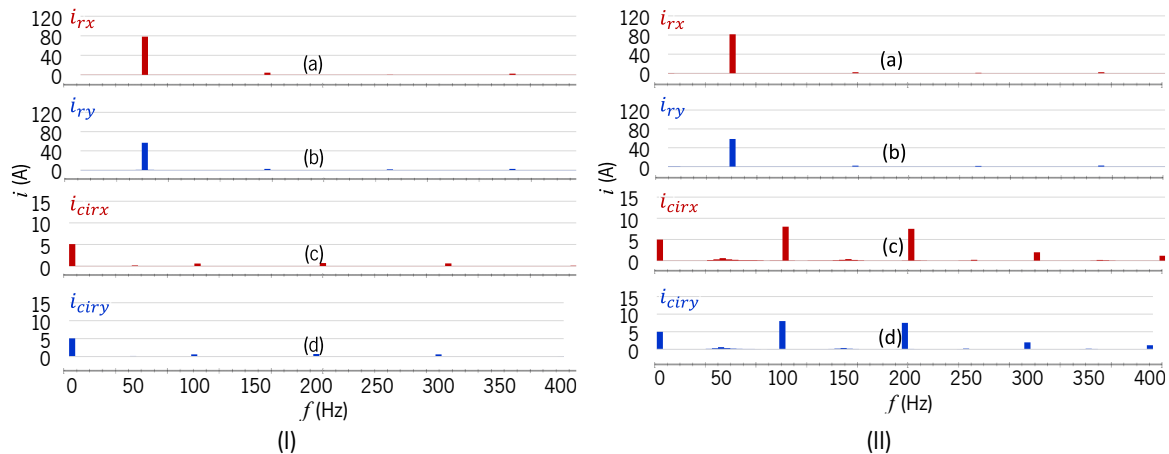


Figure 4.74. HB-MMC2 RPC frequency spectrum of currents when using the proposed predictive current controller (I) and when using the conventional PI controllers (II): (a) Compensation current of section x converter; (b) Compensation current of section y converter; (c) Circulating current of section x converter; (d) Circulating current of section y converter.

Figure 4.75(I)(a), Figure 4.75(I)(b), Figure 4.75(I)(c) and Figure 4.75(I)(d) show the frequency spectrum of the MMC arm currents when using the deadbeat predictive current control methodology for circulating current suppression. There are no second-order components (100 Hz and other even-order harmonics, such as 4th, 6th and 8th) in the MMC arm currents, which proves the effectiveness of the deadbeat predictive control methodology for circulating current suppression. This proposed methodology mainly eliminates the even-order harmonics of the circulating currents, but it

does not eliminate the DC component of the circulating currents, which is important to achieve the SM voltage balancing control. On the other hand, and due to the circulating current harmonics exist when using the conventional PI controllers, then, the frequency spectrum of the MMC upper and lower arm currents, in this case, shows the orders of the even-order harmonics. This is shown in Figure 4.75(II)(a), Figure 4.75(II)(b), Figure 4.75(II)(c) and Figure 4.75(II)(d).

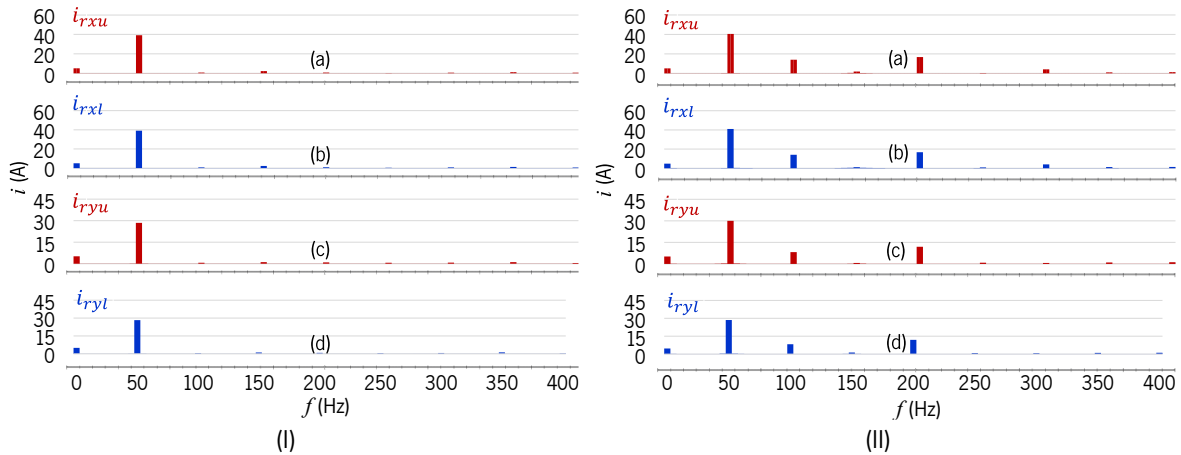


Figure 4.75. HB-MMC2 RPC frequency spectrum of currents when using the proposed predictive current controller (I) and when using the conventional PI controllers (II): (a) Upper arm current of section x converter; (b) Lower arm current of section x converter; (c) Upper arm current of section y converter; (d) Lower arm current of section y converter.

Figure 4.76(I) shows the MMC DC voltages when using the deadbeat predictive current control methodology: the DC-link voltages are presented in Figure 4.76(I)(a), the SM voltages of section x converter and section y converter are presented in Figure 4.76(I)(b) and Figure 4.76(I)(c), respectively. Figure 4.76(II) shows the MMC DC voltages when using the PI controllers and when there are circulating currents in the MMC arms: the DC-link capacitor voltages in Figure 4.76(II)(a), the SM voltages of section x converter and the SM voltages of section y converter in Figure 4.76(II)(b) and Figure 4.76(II)(c), respectively. These waveforms confirm the effectiveness of the voltage balancing control algorithm presented in Figure 4.70 and Figure 4.71.

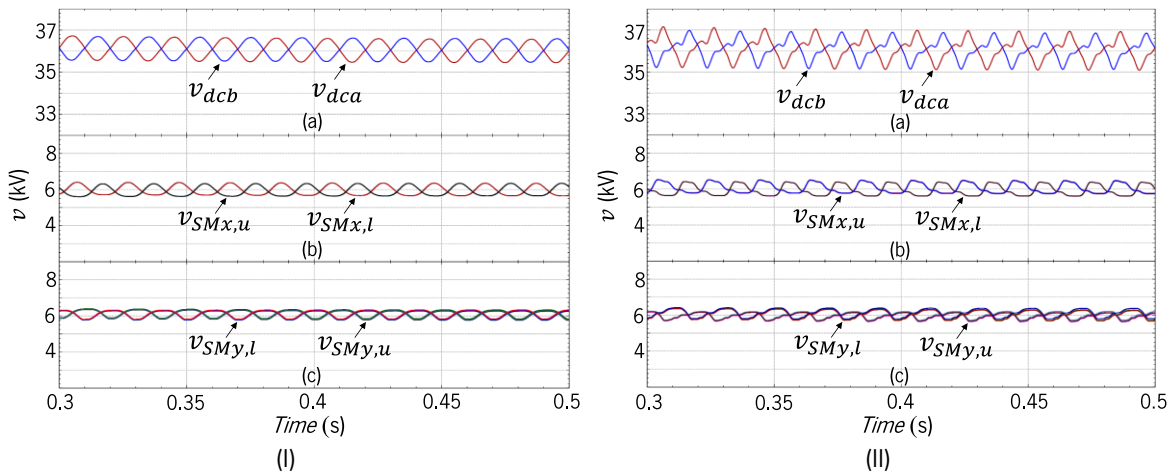


Figure 4.76. HB-MMC2 RPC DC-link voltages when using the proposed predictive current controller (I) and when using the conventional PI controllers (II): (a) Main DC-link voltages; (b) SM voltages of section x converter; (c) SM voltages of section y converter.

A high value of the circulating currents increases the amplitude of the DC voltages ripple, hence, the DC-link voltages waveform of Figure 4.76(I)(a) have lower voltage ripples when using the deadbeat predictive current control methodology. On the contrary, Figure 4.76(II)(a) shows higher voltage ripples of the DC-link voltages when using the conventional PI controllers. On the other hand, the circulating currents may lead to an easier tuning of the SM voltages balancing control and the main DC-link voltage control. As a result, the overflow/over-suppression of the MMC circulating currents is a trade-off between several factors, such as higher/lower MMC power losses, higher/lower MMC equipment power ratings, robust/fragile DC voltages control and higher/lower DC voltage ripples. Therefore, attention must be considered since the over-suppression of MMC circulating current could affect the response of the SM voltage balancing control. The advantages of the deadbeat predictive current control methodology for circulating current suppression can be summarized as follows [160]:

- Removing the AC components of the MMC circulating current, then, the circulating current amplitude is reduced while keeping balanced SM voltages. The DC component of circulating current is essential to keep the SM voltages of MMC around a reference value.
- Reducing the RMS value of the MMC arm currents.
- Reducing the voltage ripples in the SM DC-link capacitor.
- The suppression of circulating current does not disturb the MMC main functionality (in this study, MMC operated as a power quality compensator for electric railway applications).

On the other hand, as specific aspects of the deadbeat predictive current control methodology applied for circulating current suppression can be summarized as follow [160]:

- Being a deadbeat-based control methodology, unmodeled parameters in the HB-MMC2 RPC mathematical model often deteriorates the system performance and its dynamic behavior. These unmodeled parameters may lead to make the calculated voltage references deviate from the expected reference values. However, the one-cycle time delay and arm inductor resistance can be included in a more complex model.
- The presented control methodology is only valid for fixed switching frequency applications.

Besides the operation in steady-state, results showing the HB-MMC2 RPC system performance in transient conditions are presented in [160]. A variable load power was adopted to study the dynamic response of the HB-MMC2 RPC system when using the deadbeat predictive current controller. More information can be found in [160].

4.10 Comparison Between the RPC Topologies

RPC characteristics are not only dependent on the type of the RPC topology, but also the type of the traction power system. In this context, and among the presented RPC topologies in this chapter based on different converters and different types of traction power system (V/V and Scott), a major question must be discussed about the characteristics of these topologies, including advantages, disadvantages, and differences between topologies in V/V and Scott power transformers. In other words, what are the satisfactory conditions for each RPC topology to operate and when can be effectively utilized either in the V/V or in the Scott traction power system. In this framework, RPC characteristics in V/V and Scott power transformers are provided, showing the main differences that must be considered in the design process of the RPC system [150].

For the objective of comparison, V/V and Scott power transformers are both used for all the RPC topologies. In addition, the multilevel RPC topologies are considered with a similar MMC voltage level of N . In this context, Table 4.25 presents the IGBT characteristics of the RPC topologies. Normally, the multilevel RPC topologies, such as the FB-MMC4 RPC and the TW-MMC3 RPC require the highest number of switching devices, but the RPC based on half-bridge topologies, such as the HB-RPC and the HB-MMC2 RPC, needs a lower number of the IGBT switching devices. Other important factors in the IGBT selection are the applied current and voltage stress. Hereafter, and by considering that each of the RPC topologies must synthesize similar compensation current waveforms, the MRPC topology has the lowest IGBT current stress since each RPC module synthesizes only a portion of the total compensation current [150].

Table 4.25. IGBT characteristics of the RPC topologies [150].

	Number of IGBTs	IGBT current stress	IGBT voltage stress	IGBT switching frequency
FB-RPC	8	1 p.u.	$0.5V_{dc}$	f_{isw}
TW-RPC	6	1 p.u.	$0.5V_{dc}$	f_{isw}
HB-RPC	4	1 p.u.	V_{dc}	$2f_{isw}$
MRPC	$8k$	$1/k$ p.u.	$0.5V_{dck}$	f_{isw}
Co-HRPC	8	≈ 1 p.u.	$< 0.5V_{dc}$	f_{isw}
FB-MMC4	$16(N-1)$	1 p.u.	$V_{SM} = V_{dc}/(N-1)$	$f_{isw}/(N-1)$
TW-MMC3	$12(N-1)$	1 p.u.	$V_{SM} = V_{dc}/(N-1)$	$f_{isw}/(N-1)$
HB-MMC2	$8(N-1)$	1 p.u.	$V_{SM} = V_{dc}/(N-1)$	$2f_{isw}/(N-1)$

Regarding the multilevel RPC topologies and by considering an identical MMC voltage level N , and equal SM DC-link voltages V_{SM} , the IGBT voltage stress in the FB-MMC4 RPC, TW-MMC3 RPC and the HB-MMC2 RPC are equal to the SM voltage due to the half-bridge SM topology. In the FB-RPC and the

TW-RPC, the IGBT voltage stress is equal to half of the RPC DC-link voltage, V_{dc} , but it is double of this value in the HB-RPC due to the half-bridge topology. In the hybrid RPC topology with a single or double LC passive filter branch, the IGBT voltage stress is lower than half of the RPC DC-link voltage due to the capacitive coupling structure [150].

In fact, the IGBT switching frequency is an important parameter and has a direct influence on the RPC power losses. By considering the same carrier frequency and equal passive inductors for all of the RPC topologies, the IGBT switching stress in the HB-RPC must be twice the value in the FB-RPC and the TW-RPC to have synthesized compensation currents with similar current ripples. As a result, the switching stress in the half-bridge RPC topologies, such as the HB-RPC and the HB-MMC2 RPC is the double and the associated switching losses are the double as well. In the multilevel RPC topologies, the switching frequency of one IGBT is significantly lower since the switching stress can be divided between several cascade connected SMs in one MMC arm [150].

Table 4.26 presents a quantitative comparison of the RPC topologies after considering the same MMC voltage level, N , for the multilevel topologies. Apparently, FB-MMC4 RPC requires the highest number of capacitors since this topology is based on full-bridge MMC. The number of capacitors in the HB-RPC has double the value in the FB-RPC and the TW-RPC. However, in the MRPC, the number of capacitors is equal to the number of RPC modules.

Table 4.26. Quantitative comparison of the RPC topologies [150].

	Number of capacitors	Number of inductors	Coupling transformers	Isolation transformers
FB-RPC	1	2	Yes (2)	Inherent
TW-RPC	1	2	Yes (2)	Inherent
HB-RPC	2	2	Yes (2)	Inherent
MRPC	k	$2k$	Yes ($2k$)	Inherent
Co-HRPC	2 or 3	3	Yes (1)	Inherent
FB-MMC4	$8(N-1)$	8	No	Yes (2)
TW-MMC3	$6(N-1)+1$	6	No	No
HB-MMC2	$4(N-1)+2$	4	No	No

On the other hand, in the co-HRPC, the number of capacitors depends on whether the co-HRPC has a single or double LC series filter in the two coupling branches, where in the first case, the RPC only contains two capacitors, and in the second case (double capacitive inductive structure), the RPC contains three capacitors. Moreover, the filter inductors are indispensable to smooth the compensation currents produced by the RPC. In this context, and as presented in the Table 4.26, the number of the

filter inductors in most of the RPC topologies is constant. The FB-MMC4 RPC topology needs the highest number of the filter inductors. However, in the MRPC topology, the total quantity of the filter inductors is related to the number of RPC modules, k .

Coupling transformers are essential to step-down the traction power grid voltage and to achieve the necessary galvanic isolation between the RPC converter and the power grid. In this context, the coupling transformers are dispensable in the multilevel RPC topologies (FB-MMC4 RPC, TW-MMC3 RPC and HB-MMC2 RPC) since an MMC with a high level allows a direct interface with the traction power grid. Nevertheless, the FB-MMC4 RPC topology requires two isolation transformers (with turns ratio of 1/1) to prevent short circuits between the MMC SMs. However, when using the FB-MMC4 RPC topology in the co-phase traction grid, the isolation transformers are dispensable. It is worthy to mention that the galvanic isolation is inherent in the RPC topologies that use the coupling transformers [150].

Table 4.27 presents different characteristics of the RPC topologies in the V/V and the Scott power transformers. The most important parameter that makes a difference is the RPC DC-link voltage, which is normally higher in the V/V power transformer than the case when using the Scott power transformer. However, this is only true in the FB-RPC, in the MRPC, in the co-HRPC and in the FB-MMC4 RPC, where the common denominator of these topologies is the four wires back-to-back converter. On the other hand, in the RPC topologies, where a common phase exists, such as the TW-RPC, the HB-RPC, the TW-MMC3 RPC and the HB-MMC2 RPC, the DC-link voltage is higher in the Scott power transformer than the case of the V/V power transformer. As a result, the FB-RPC, the MRPC, the co-HRPC and the FB-MMC4 RPC, are considered as power compensators for general-purpose and they are quite appropriate for the applications of power quality improvement in the V/V or the Scott power transformers. On the contrary, the RPC topologies with a common phase, such as the TW-RPC, the HB-RPC, the TW-MMC3 RPC and the HB-MMC2 RPC, are considered as power compensators for special-purposes. The TW-RPC, the HB-RPC and the TW-MMC3 RPC are only appropriate for the power quality improvement in the V/V traction power system [150].

The control complexity is the highest in the FB-MMC4 RPC, due to the high number of the IGBT switching devices, but the control is the simplest in the HB-RPC topology due to the low number of the hardware components involved. Also, the FB-MMC4 RPC and the TW-MMC3 RPC have the best reliability and performance in the V/V power transformer, then, as the higher the MMC level, the better the performance of the RPC. In the Scott power transformer, the FB-MMC4 RPC has the best reliability and performance, then and after considering the estimated costs of each topology and the required

volume for installation, the TW-MMC3 RPC fulfills the best conditions in the V/V traction power system, whereas the FB-MMC4 RPC provides the best conditions in the Scott traction power system [150].

Table 4.27. Characteristics of the RPC topologies in V/V and Scott transformer [150].

	RPC DC-link voltage	Control complexity	Reliability / performance	Estimated costs	Required volume
V/V power transformer					
FB-RPC	$V_{dc} \geq \sqrt{2} U_{xo(V/V)}$	+++	+++	+++	+++
TW-RPC	$V_{dc} \geq \sqrt{2} U_{xo(V/V)}$	++	+++	++	++
HB-RPC	$V_{dc} \geq 2 \sqrt{2} U_{xo(V/V)}$	+	++	++	++
MRPC	$V_{dc} \geq \sqrt{2} U_{xo(V/V)}$	++++	++++	++++	++++
Co-HRPC	$V_{dc} \leq \sqrt{2} U_{xo(V/V)}$	+++	+++	+++	+++
FB-MMC4	$V_{dc} \geq \sqrt{2} U_{xo(V/V)}$	+++++	+++++	+++++	+++++
TW-MMC3	$V_{dc} \geq \sqrt{2} U_{xo(V/V)}$	++++	+++++	++++	++++
HB-MMC2	$V_{dc} \geq 2 \sqrt{2} U_{xo(V/V)}$	+++	++++	+++	+++
Scott power transformer					
FB-RPC	$V_{dc} \geq \sqrt{2} U_{xo(\text{Scott})}$	+++	+++	+++	+++
TW-RPC	$V_{dc} \geq 2 U_{xo(\text{Scott})}$	++	+++	++++	++++
HB-RPC	$V_{dc} \geq 4 U_{xo(\text{Scott})}$	+	++	+++	+++
MRPC	$V_{dc} \geq \sqrt{2} U_{xo(\text{Scott})}$	++++	++++	++++	++++
Co-HRPC	$V_{dc} \leq \sqrt{2} U_{xo(\text{Scott})}$	+++	+++	+++	+++
FB-MMC4	$V_{dc} \geq \sqrt{2} U_{xo(\text{Scott})}$	+++++	+++++	+++++	+++++
TW-MMC3	$V_{dc} \geq 2 U_{xo(\text{Scott})}$	++++	++++	+++++	+++++
HB-MMC2	$V_{dc} \geq 4 U_{xo(\text{Scott})}$	+++	+++	++++	++++
The symbol "+" reflects the quantification of the parameter.					

According to the Table 4.25, Table 4.26 and Table 4.27, Figure 4.77 shows two radar charts to compare between the multilevel RPC topologies (FB-MMC4 RPC, TW-MMC3 RPC and HB-MMC2 RPC) in the V/V traction power transformer, presented in the Figure 4.77(a) and in the Scott traction power transformer, presented in Figure 4.77(b), considering an equal number of SMs or voltage levels. The presented ratios per characteristic/category, and for different RPC topologies, are proportional between each other. Therefore, any of the presented ratios, in the same characteristic/category, can be considered as a reference [150].

The TW-MMC3 RPC is the best topology to be used in the V/V traction power system, since it does not require isolation transformers and relatively needs a lower number of hardware components with lower IGBT power ratings (voltage and current ratings) compared with the FB-MMC4 RPC. In turn, the FB-MMC4 RPC is the best topology to be used in the Scott traction power system, then, there are

topologies adopted for general-purpose that can be used in the V/V or in the Scott traction power system and show similar performance (FB-RPC, MRPC, co-HRPC and FB-MMC4 RPC). On the other side, there are topologies for special-purposes, such as the TW-MMC3 RPC and the HB-MMC2 RPC which are more appropriate in the V/V traction power system [150].

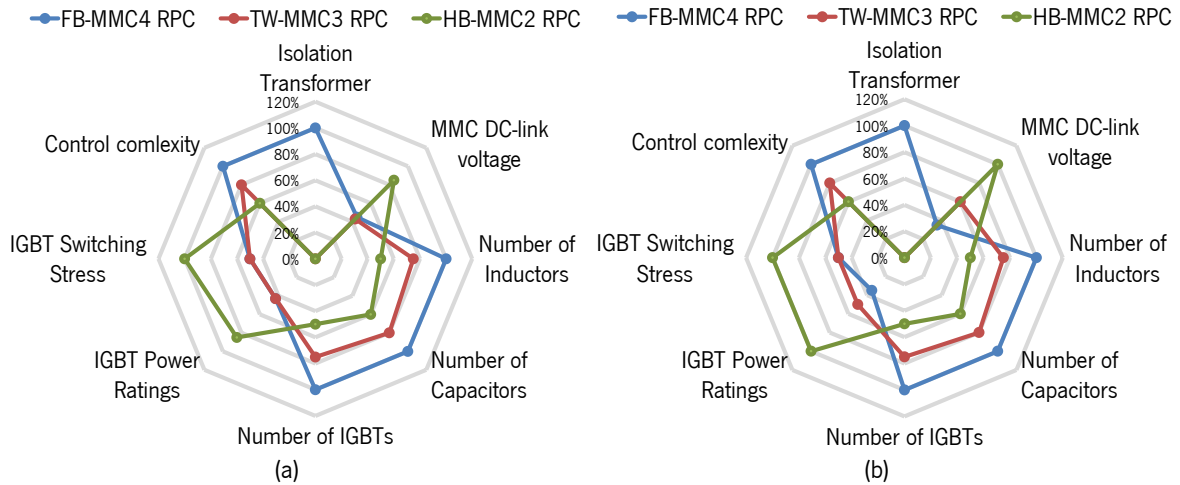


Figure 4.77. Comparison of RPC topologies based on MMC: (a) V/V power transformer; (b) Scott power transformer.

4.11 Conclusion

In this chapter, different topologies of the rail power conditioner (RPC) have been presented and studied, which can be used in the high-speed AC railways to overcome the power quality deterioration. Accordingly, the negative sequence components (NSC) of current and the harmonic contents can be reduced. In addition, reactive power can be exchanged between the traction loads and the RPC, leading to a unitary power factor of the three-phase public power system (PPS). The RPC following topologies were presented:

- RPC based on full-bridge back-to-back two-level converter and V/V power transformer (FB-RPC);
- RPC based on two-phase three-wire converter and V/V power transformer (TW-RPC);
- Simplified RPC based on half bridge two level converter and V/V power transformer (HB-RPC);
- Hybrid co-phase RPC based on full-bridge back-to-back two-level converter and single-phase power transformer (co-HRPC);
- RPC based on Scott power transformer;
- Modular RPC based on full-bridge back-to-back two-level converter and V/V power transformer (MRPC);
- RPC based on full-bridge indirect modular multilevel converter (FB-MMC4 RPC);
- RPC based on two-phase three-wire indirect modular multilevel converter (TW-MMC3 RPC);
- Simplified RPC based on half-bridge indirect modular multilevel converter (HB-MMC2 RPC).

The innovative RPC topologies based on the modular multilevel converter (MMC) have also been presented in this chapter. The MMC total power can be divided among several cascade-connected two-level converters or submodules (SMs), then, the power ratings of the switching devices are much lower. In addition, there is no need for using step-down power transformers to interface the MMC with the traction power system (TPS). However, the case of the FB-MMC4 RPC is an exception, since it requires isolation transformers to interface the converter with the TPS.

This chapter presented a comparative study between the RPC topologies, showing the main characteristics of each topology in the V/V or the Scott power transformer. The main conclusion can be summarized as follows:

- The indirect AC/DC/AC MMC can be used in the high-speed railway application to operate as an RPC without the need for step-down coupling transformers (except for the case of the FB-MMC4 RPC, since this solution requires isolation transformers).
- Switching devices can be used with lower power ratings in the RPC based on MMC topologies.
- Switching devices can be used with lower power ratings in the RPC topologies based on MMC and the MRPC topology.
- The deadbeat predictive current control is quite effective to reduce the MMC circulating currents. However, unmodeled parameters in the HB-RPC mathematical model may deteriorate the system performance.
- The FB-MMC4 RPC can be classified as a general-purpose RPC because it can be used with different types of power transformers (V/V or Scott). However, it requires isolation transformers to interface with the TPS. Then, this solution is quite expensive and bulky.
- The TW-MMC3 RPC and the HB-MMC2 RPC can be classified as special-purpose RPC because they are recommended to be used with only the V/V power transformer. Using these topologies with a Scott power transformer obligates to use higher DC-link voltages and power switching devices with higher power ratings. However, isolation transformers are not mandatory in these solutions.

Chapter 5

Implementation of a Simplified Rail Power Conditioner Based on Modular Multilevel Converter

5.1 Introduction

This chapter presents the main steps for the development of the simplified rail power conditioner based on half-bridge indirect modular multilevel converter (HB-MMC2 RPC). The implemented HB-MMC2 RPC system is a reduced-scale laboratory prototype, developed to validate the RPC based on MMC concept and the associated control algorithm. In addition, the main specifications of the HB-MMC2 RPC are selected according to the available materials and capabilities, then, the components and hardware used in the implementation process are described in this chapter. The options are also justified, considering what is planned and designed, and the materials and components available in the market at the time of development. Furthermore, parameters design of the reduced-scale MMC, such as the size of the MMC submodule (SM) capacitor, the size of the filter inductors, and the size of the MMC main DC-link capacitor are also presented in this chapter.

Additionally, this chapter mainly explains the SM structure of the MMC, the control system hardware, and the supplementary power equipment. In that regard, and as it will be demonstrated along the chapter, each SM consists of three printed circuit boards (PCBs): the driver circuit PCB, the protection circuit PCB and the power circuit PCB. Then, experimental results are presented to validate each of the mentioned PCBs, validating all individual SM before the full implementation of the MMC. It should be noted that some of the components and systems have been oversized, in order to ensure that in the event of abnormal operation, safety is not compromised.

On the other hand, supplementary power equipment, such as V/V power transformer, three-phase power grid, and two-phase traction power system (TPS) are also described in this chapter. Many of supplementary power equipment are important to create the two-phase load sections with 60° out-of-phase, which is essential to obtain a reduced-scale TPS in the laboratory [54].

The control system hardware, including the central control unit, voltage and current sensors, command circuit board, signal conditioning circuit boards, digital-to-analogue converters and analogue-to-digital

converters are also explained in this chapter. The central control unit contains a microcontroller with the respective PCB adapter. In terms of the sensors, the current and the voltage sensors are presented, as well as the signal conditioning PCBs.

It should be noted that some of the PCBs described have been already designed in the Group of Power Electronics and Energy (GEPE) at the University of Minho. However, the PCBs designed and developed under the scope of this Ph.D. thesis will be indicated in the chapter.

5.2 Parameters Design

The HB-MMC2 RPC system, presented in Figure 4.66, designed as a laboratory reduced-scale prototype, will have eight SMs in total (four SMs in one MMC leg). The main aim of the HB-MMC2 RPC implementation is to validate the topology, the proposed control algorithm, and the proposed MMC protection system. Consequently, MMC reduced-scale prototype with a few levels is quite sufficient for a proof of concept. The HB-MMC2 RPC system is implemented considering its operation in a two-phase V/V connection. In addition, the implementation of MMC is carried out considering that the converter will be used for the purpose of power quality improvement.

In the V/V traction system configuration, the main DC-link voltage of the HB-MMC2 RPC should have a value at least twice the load section peak voltages as presented in equation (4.40), then, according to equation (4.31), and when the half-bridge MMC consists of 4 SMs in each leg, the voltage of each DC-link SM should have a value almost half of the main DC-link voltage of the HB-MMC2 RPC. In this item, the main guidelines, and principles to design the MMC filter inductance, main DC-link capacitor and the SM capacitor are presented.

The design of the filter inductance directly influences the control system capability to track the compensation current references. In addition, the current ripples depend on the voltage applied on the inductance, the value of the inductance, and the period that the voltage is applied. The inductance can be designed by considering the factors of current ripples suppression, and the speed of signal tracking [181]. The filter inductance operates as an inner MMC filter to attenuate the high-frequency harmonics in the arm current and to limit the DC-link short circuit current [176]. Moreover, sizing the filtering inductance requires taking into account the suppression of undesired low-frequency harmonics, such as the MMC circulating current that is mainly composed of the 2nd order frequency [182]. In this context and according to [122], [183], [184], the equation that determines the value of the filter inductance, $L_{\sigma(u,l)}$; $\sigma \in \{x, y\}$ is presented in (5.1), where, V_{dc} is the total DC-link voltage of the MMC, V_{SM} is the SM DC-link voltage, f is the traction power grid frequency, $I_{r\sigma(u,l)}$; $\sigma \in \{x, y\}$ is the MMC arm current, f_{sw} is the switching frequency, and $\Delta I_{r\sigma(u,l)}$ is the MMC arm current ripples.

$$\frac{V_{SM}}{8f_{sw} \Delta I_{r\sigma(u,l)}} \leq L_{\sigma(u,l)} \leq \frac{\sqrt{\frac{V_{dc}^2}{4} - V_{SM}^2}}{2\pi f I_{r\sigma(u,l)}} \quad (5.1)$$

A low value of the SM capacitor implies high-voltage ripples. On the other hand, a high value of capacitance results in expensive and bulky MMC prototype [178]. The bulky converter requires a bigger area for installation. From that perspective, the previous principle is taken into account in the selection process of the SM capacitor value, where this value is estimated considering the trade-off between the size, costs and voltage ripples [176]. Furthermore and according to a study presented in [183], there is a resonance point related to the filter inductance and the DC-link capacitor of each SM, in which the maximum value of the resonance angular frequency should always be smaller than the fundamental angular frequency in order to avoid the resonance phenomenon [183]. As a result, the resonance frequency that is related to the filter inductance and the SM capacitor should be considered in the MMC design process. According to [122], [183], the equation that calculates the minimum capacitance of each SM capacitor is presented in (5.2), where, $L_{\sigma(u,l)}$ is the filter inductance, N is the MMC voltage level and f is the grid fundamental frequency.

$$C_{SM} > \frac{3(N-1) + 2(N-1) n^2}{48 (2\pi f)^2 L_{\sigma(u,l)}} \quad (5.2)$$

$$n = \frac{2U_{\sigma(peak)}}{V_{dc}}; \sigma \in \{x, y\} \quad (5.3)$$

Since the main DC-link voltage is always equal to $(N-1)$ times of a single SM voltage as presented in (4.31), in the half-bridge MMC, the size of the main DC-link capacitor should be at least $(N-1)$ times of the SM capacitor value [183]. Choosing the right value of the main DC-link capacitor is important since this value determines the converter power capacity, then, guarantee the HB-MMC2 RPC ability to compensate reactive power, harmonics, and shift half of the active power difference between the load sections. In this regard, the main DC-link power should cover the MMC power losses, p_{losses} , and the AC power of the converter, p_{ac} , as presented in (5.4) [176].

$$p_{dc} = p_{ac} + p_{losses} \implies v_{dc} i_{dc} = \sum_{\sigma = x, y} u_{\sigma} i_{r\sigma} + p_{losses} \quad (5.4)$$

The instantaneous power provided by each capacitor of the main DC-link can be expressed by (5.5), where W_{dca} is the energy stored in the DC-link capacitor, C_{dca} is the capacitance of the DC-link capacitor, and v_{dca} is the DC-link voltage.

$$P_{dca} = \frac{dW_{dca}}{dt} = \frac{d\left(\frac{1}{2} C_{dca} v_{dca}^2\right)}{dt} = v_{dca} C_{dca} \frac{dv_{dca}}{dt} \quad (5.5)$$

Then, it is possible to conclude (5.6) that gives the minimum capacitance of the main DC-link capacitor, where f_d is the DC-link voltage ripple frequency (100 Hz in the full-bridge converter and 50 Hz in the half-bridge converter), $C_{dca(min)}$ is the minimum capacitance of the DC-link capacitor, ΔV_{dca} is the DC-link voltage ripples (peak-to-peak).

$$C_{dca(min)} \geq \frac{P_{dca}}{V_{dca} \Delta V_{dca} f_d} \quad (5.6)$$

By considering the load sections active power difference varies between 0 W and 1500 W. The HB-MMC2 RPC prototype shifts half of the active power difference between sections. Therefore, the worst-case scenario is when only one load section is loaded when the compensator shifts a higher value of active power between the load sections. In this context, it is possible to consider the parameters ($P_{dca} = 750$ W, $f_d = 50$ Hz; $V_{dca} = 200$ V; $\Delta V_{dca} = 30$ V), then, the minimum capacitance for one DC-link capacitor, as presented in (5.6), should be equal to or greater than 2.5 mF.

Reduced-scale MMC prototype final parameters are presented in Table 5.1. They are calculated with regard to (5.1), (5.2) and (5.6). By considering the RMS voltage value of the load section voltages 100 V, fundamental grid frequency of 50 Hz, and by supposing the maximum RMS value of the MMC arm current $I_{r\sigma(u,l)} = 20$ A, then the filter inductance value should be within the range of $0.1 \text{ mH} \leq L_{\sigma(u,l)} \leq 10 \text{ mH}$. Consequently, and by applying this range in (5.2), the SM capacitance should be higher than 100 μF .

In the HB-MMC2 RPC experimental setup, only eight SMs with high switching frequency will be used to reduce the MMC complexity. The used switching frequency is 40 kHz, which allowed to synthesize a sinusoidal waveform with good quality and fast dynamic response when compensating load current harmonics. However, in high-power applications, a few tens of SMs with low switching frequency can be used to achieve the same objectives.

Table 5.1. Reduced-scale MMC parameters.

Parameters	Symbols	Values
Three-phase grid voltage	U_{AC}, U_{BC}	400 V
Load section voltage	U_x, U_y	100 V
Filter inductance of the arm	$L_{\sigma(u,l)}; \sigma \in \{x, y\}$	1.7 mH
Capacitance of the SM capacitor	C_{SM}	987 μF
Capacitance of the main DC-link capacitors	$C_{dca} = C_{dcb}$	2820 μF
Number of SMs in each MMC arm	$N-1$	2
SM Switching frequency	f_{isw}	40 kHz
Equivalent switching frequency	f_{sw}	80 kHz

5.3 Simulation of the Reduced-Scale HB-MMC2 RPC

Simulation models and simulation results of the reduced-scale HB-MMC2 RPC, presented in Figure 4.66, are presented in the following items. The simulation model of the HB-MMC2 RPC was built by using the *PSIMV.9.1* simulation tool, from *Powersim Inc.* This software is dedicated for Power Electronics applications. On the other hand, simulation results of the reduced-scale HB-MMC2 RPC, using the deadbeat predictive current control methodology presented in the Chapter 4, item 4.9.3, are also presented.

5.3.1 Simulation Model

Since *PSIMV.9.1* has a vast set of components and allows *C* programming language, simulation of the HB-MMC2 RPC is useful to test the control algorithm in *C* code environment. All these features were decisive for choosing this simulation tool. Currently, *PSIMV.9.1* can automatically generate *C* language code from the implemented simulation model. The generated *C* code is compatible with the *Texas Instruments F2833X* floating-point microcontrollers [185]. HB-MMC2 RPC simulation model is presented in Figure 5.1, where the system consists of two main parts: leg *x* and leg *y* converters.

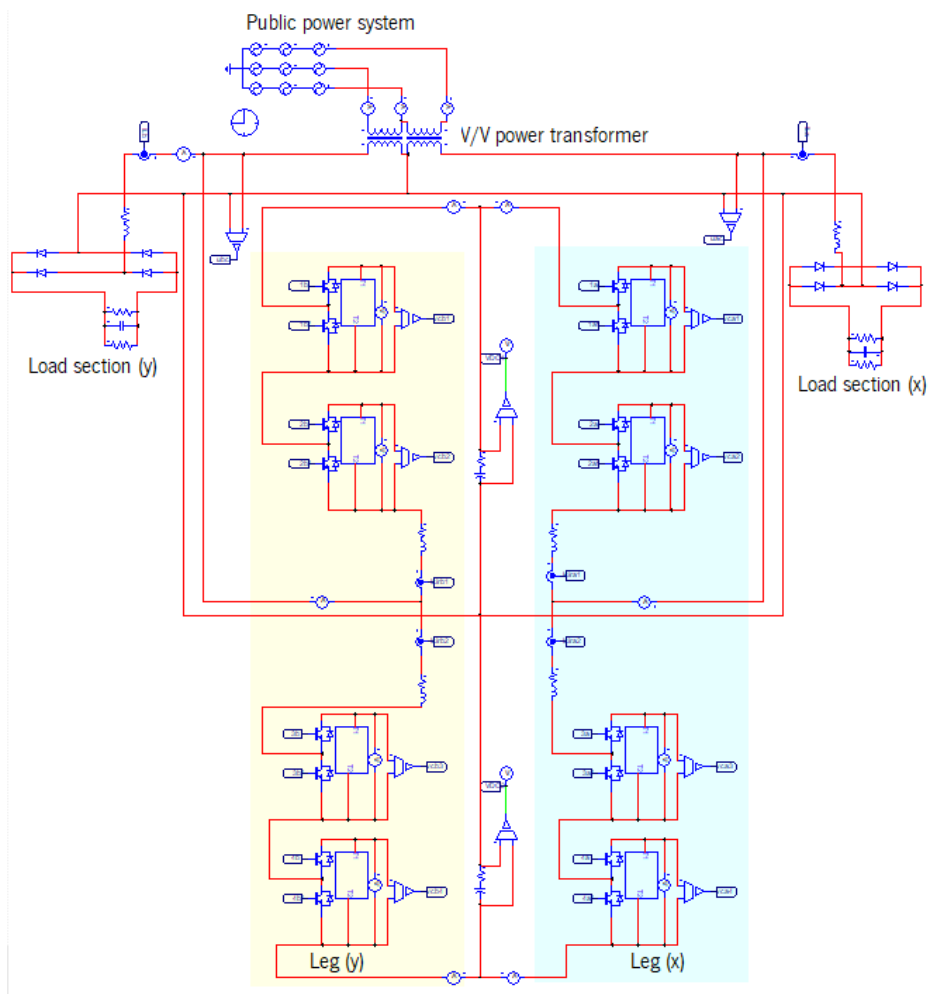


Figure 5.1. HB-MMC2 RPC simulation model using the *PSIMV.9.1*.

Obviously, the power model contains eight SMs, four filter inductors, sixteen insulated-gate bipolar transistors (IGBTs), two load sections and a V/V power transformer. In addition, there are twelve voltage sensors (to measure the SM DC voltages and the load section voltages) and six current sensors (to measure the load section currents and the MMC arm currents).

Figure 5.2 shows the C control blocks used in the simulation. A zero-order hold (ZOH) is used to convert the continuous-time signal to a discrete-time signal, then, this is important to consider the sampling frequency effect. The control part includes eight C blocks to implement the control algorithm of the HB-MMC2 RPC. Two blocks are devoted to implement the enhanced phase-locked loop (E-PLL) (one block for each load section voltage). The calculations of the compensation currents reference signals, besides the main DC-link voltage control of the HB-MMC2 RPC system, are executed in another C control blocks. Two control blocks are used for the purpose of averaging and individual voltage balancing control, which keep balanced SM voltages. On the other hand, two control blocks are used to implement the deadbeat predictive control which has been discussed in the Chapter 4, item 4.9.3.

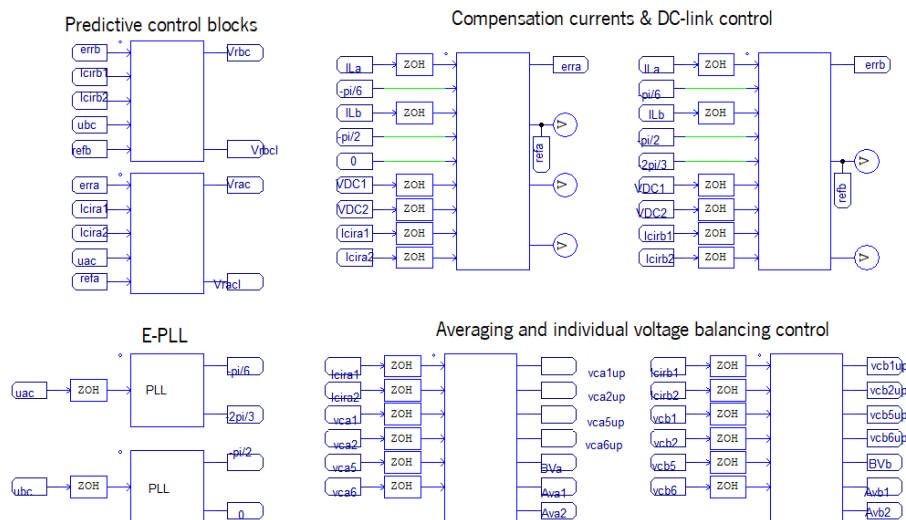


Figure 5.2. HB-MMC2 RPC control blocks using the *PSIM* V.9.1.

5.3.2 Simulation Results

Simulation of the reduced-scale HB-MMC2 RPC is built under the *PSIM* V.9.1 simulation tool. Simulation parameters are presented in the Table 5.1. As shown in Figure 5.1, the simulation model only contains eight SMs in both MMC legs. The main objective is to validate the reduced-scale prototype by simulation before starting in the implementation phase. In this simulation is considered 100 V RMS of the load section voltages, u_x and u_y , 400 V RMS line-to-line three-phase grid voltage, 700 W and 1000 W for section x and section y power, respectively, after considering a unitary load power factor.

Figure 5.3(a) shows the three-phase power grid currents before compensation (before the operation of the HB-MMC2 RPC). The currents are suffering from imbalance and NSC of currents.

Figure 5.3(b) presents the same currents after compensation. In that case and since the HB-MMC2 RPC compensates reactive power and shifts half of the active power difference between the load sections, the three-phase currents are balanced and have sinusoidal waveforms. The load sections currents of i_{Lx} and i_{Ly} , at a unitary load power factor are presented in Figure 5.3(c).

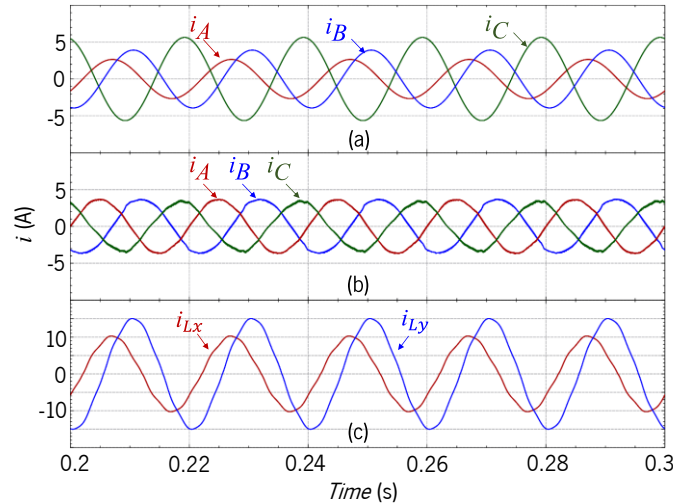


Figure 5.3. HB-MMC2 RPC reduced-scale prototype simulation results: (a) Three-phase grid currents before compensation; (b) Three-phase grid currents after compensation; (c) Catenary section (x and y) currents.

Figure 5.4(a) presents the HB-MMC2 RPC compensation currents. Phase x compensation current, i_{rx} , has a higher value than the phase y compensation current, i_{ry} . This is associated with the loading parameters since the load section y is loaded with a higher power than the load section x loading power. Figure 5.4(b) and Figure 5.4(c) shows the MMC arms currents. Obviously, subtracting the lower arm current from the upper arm current gives the MMC compensation current. Figure 5.4(d) shows the circulating current in the MMC arms. This circulating current has a low value as a result of the proposed deadbeat predictive current control methodology presented in the Chapter 4, item 4.9.3. This current was calculated according to the equation (4.44).

Figure 5.5 shows the MMC DC-link voltages: the main DC-link voltages in Figure 5.5(a), SMs voltages of section x and section y converter in Figure 5.5(b) and Figure 5.5(c), respectively. These waveforms confirm the effectiveness of the voltage balancing control method presented in Figure 4.71. Figure 5.5(a) demonstrates the main DC-link voltages, where the total DC-link voltage, V_{dc} , is calculated by summing both waveforms of V_{dca} and V_{dcb} . The reference signal for each DC-link capacitor is 160 V, then the total main DC-link voltage is around 320 V. Figure 5.5(b) presents the SM voltages of converter x , where $v_{SMx,u}$ indicates the upper arm SM voltages of converter x , and $v_{SMx,l}$ indicates the lower arm SM voltages of converter x . The same is applicable for converter y SM voltages, $v_{SMy,u}$ and $v_{SMy,l}$ in Figure 5.5(c).

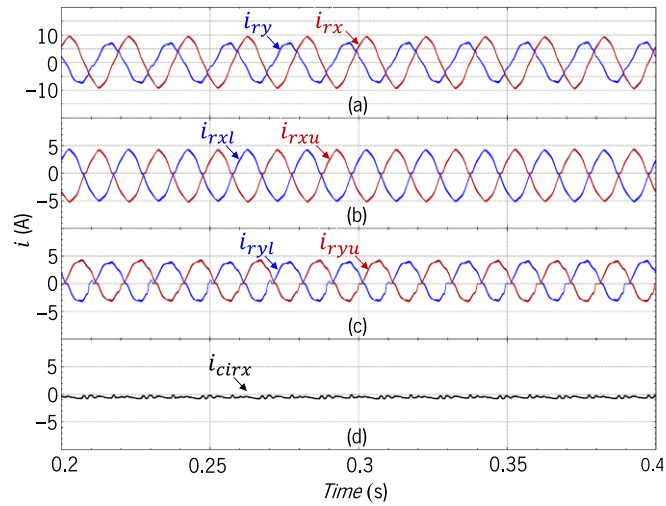


Figure 5.4. HB-MMC2 RPC reduced-scale prototype currents (a) Compensation currents; (b) Upper and lower arm currents of section x converter; (c) Upper and lower arm currents of section y converter; (d) MMC circulating currents.

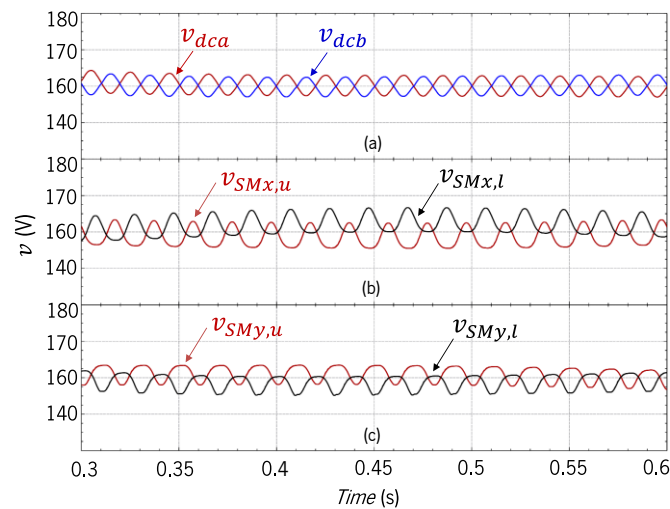


Figure 5.5. HB-MMC2 RPC reduced-scale prototype DC-link voltages: (a) Main DC-link voltages; (b) SM voltages of section x converter; (c) SM voltages of section y converter.

5.4 Supplementary Power Equipment

The implemented HB-MMC2 RPC reduced-scale prototype mainly consists of power system and control system hardware. This item describes the supplementary power hardware used to obtain a reduced-scale TPS workbench. Figure 5.6 shows a diagram of the supplementary power equipment used to get the three-phase public power grid and the two-phase TPS after using a V/V power transformer. The objective is to have two-phase voltages, U_x and U_y with 60° out-of-phase (see the Figure 4.7, chapter 4).

Figure 5.7 shows the supplementary power equipment setup. Three single-phase auto-transformers are used to give the possibility to change the voltage magnitudes of U_x and U_y . The connection must be carried out after respecting the phase order as shown in Figure 5.6. In other words, auto-transformers output voltages (input voltages of the V/V transformer) must be in phase with the line-to-line voltages, U_{AC} and U_{BC} , to have a phase shift of 60° as presented in (5.7).

$$\begin{aligned} \dot{U}_A &= 230 \angle 0^\circ; \dot{U}_B = 230 \angle -120^\circ; \dot{U}_C = 230 \angle -240^\circ \text{ (V)} \\ \dot{U}_{AC} &= 400 \angle -30^\circ; \dot{U}_{BC} = 400 \angle -90^\circ \text{ (V)} \end{aligned} \quad (5.7)$$

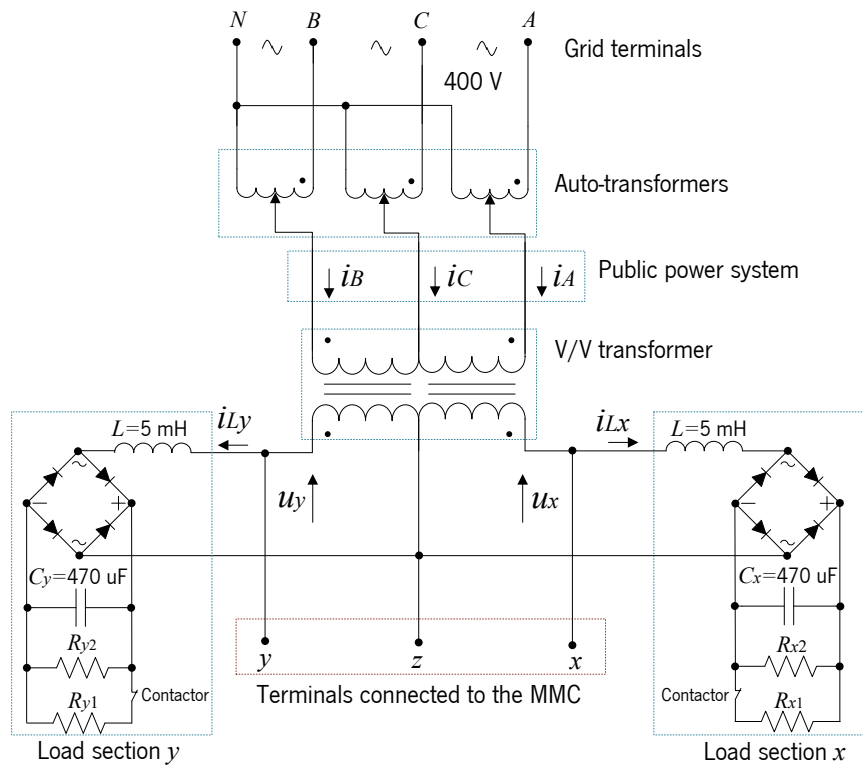


Figure 5.6. Supplementary power equipment diagram.

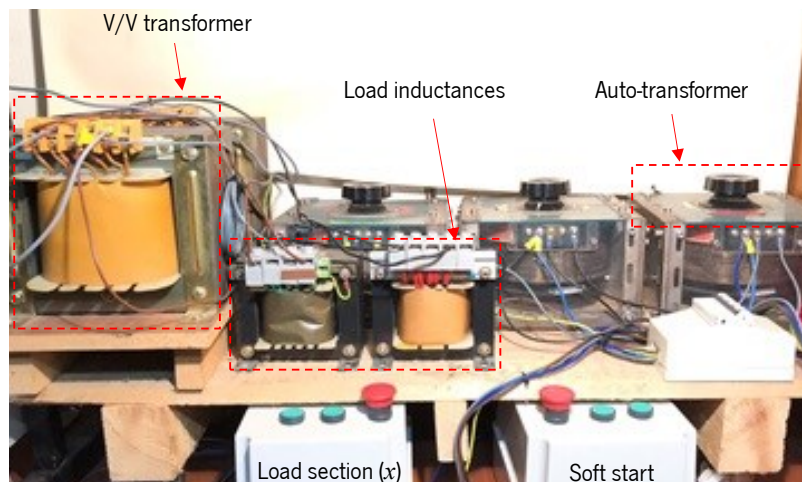


Figure 5.7. Supplementary power equipment setup.

One of the V/V connection advantages is the easy implementation in the laboratory. Hence, single-phase step-down transformers are used to implement the V/V connection and to obtain two-phase voltages, U_x and U_y , as presented in (5.7). Attention to the polarity of the single-phase transformers must be considered to acquire the correct phase shift. These single-phase transformers have turns ratio of 0.5. In this case, the point, z , as shown in the Figure 5.6, is the neutral of the reduced-scale TPS. Each load section is connected to an inductance and a rectifier full-bridge. The inductances are important to represent the non-linear inductive traction load, then, the indicated values in Figure 5.6 are used in the real implementation. However, the values of some parameters are not

presented in Figure 5.6, such as the voltages, U_x and U_y , and the load power values. These parameters, besides the HB-MMC2 RPC experimental results are presented in the chapter 6.

Since the single-phase auto-transformers have a high magnetizing inductance value, then, a soft start is required to avoid high transient currents at the introduce moment to the power supply. This soft start inserts series-connected resistors to the auto-transformers input, then, a timer contactor is used to bypass the series-connected resistors after a predefined period.

The main purpose is to have different load power values to show the HB-MMC2 RPC capability in improving the three-phase grid power quality. The resistors, R_{x1} and R_{y1} , have a small value and they mainly determine most of the consumed power in each load section. On the contrary, the resistors, R_{x2} and R_{y2} have a high value since the main purpose of these resistors is to consume the stored energy in the capacitors after turning-off the power supply or disconnecting the load resistors of R_{x1} and R_{y1} using contactors.

5.5 Implementation of a Reduced-Scale MMC

This item will discuss the implementation steps of the reduced-scale MMC, including the MMC SM, the filter inductors, and the main DC-link capacitors. Initially, the main aim is to implement a well-designed MMC submodule, then replicate the work to have a full MMC. For that purpose, various tests should be employed on the designed SM before reproducing more PCBs. This is essential to guarantee a robust performance under abnormal conditions when several cascade-connected SMs are under operation. Consequently, this item presents the MMC design process, including the MMC SM implementation and validation.

PCB design is performed by using the *PADS* software from *MENTOR GRAPHICS*, which can help to provide powerful PCB layout and easy user interface. In addition, it helps to analyze, test and correct the PCB design before manufacturing. In that regard, Figure 5.8(a) shows the user interface of *PADS Logic* software, which is responsible for building the main electrical scheme/circuit of the PCB. Figure 5.8(b) presents an example of the user interface of *PADS Layout* software, which is responsible for designing the PCB layers, traces, and other technical parameters. There is a communication tool between the *PADS Logic* and the *PADS Layout* software. This tool allows updating the PCB layout design in the *PADS Layout* when changing the electrical scheme in the *PADS Logic* and vice versa [186].

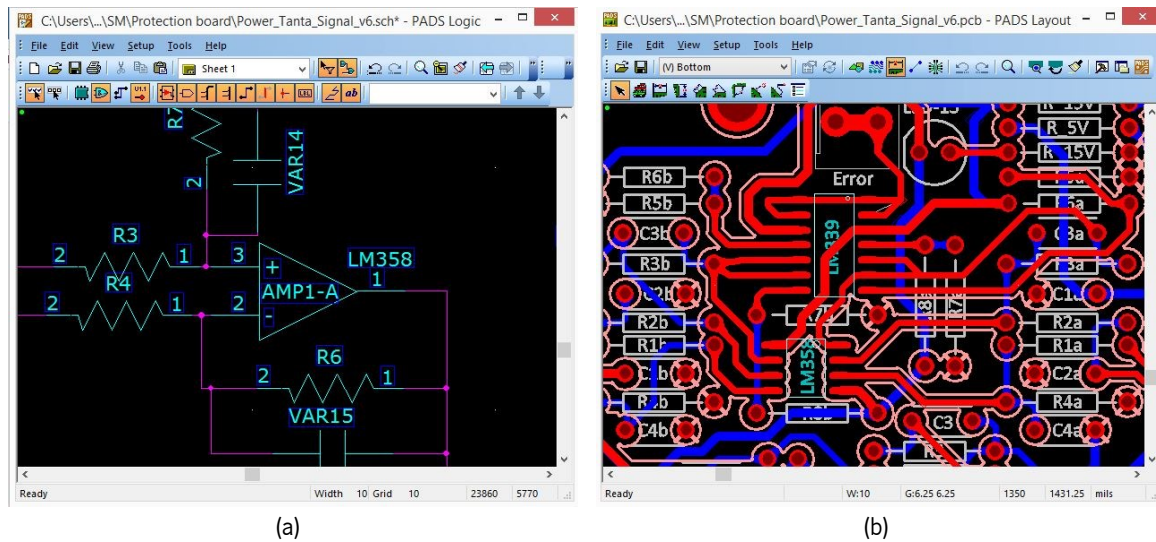


Figure 5.8. User interface of PADS PCB design tool: (a) PADS Logic; (b) PADS Layout.

5.5.1 Driver Circuit PCB

This PCB is designed and implemented under the scope of this Ph.D. thesis. The main application is to drive the SM switching devices. In this context, *Si8244* integrated circuit (IC) from *Silicon Labs* is an isolated driver family that contains two complementary metal-oxide-semiconductor (CMOS) isolated drivers in a single package with a maximum peak current of 4 A [187]. The *Si8244* IC is a high-side/low-side driver specifically targeted to drive complementary switching devices (as the case of half-bridge converter). In addition, its main feature is the integrated deadtime generator between the high-side/low-side drivers. This deadtime allows highly precise control for switching devices, achieving optimal performance and lower distortion [187].

Figure 5.9 shows the internal schematic of the *Si8244* IC. There is one input channel equipped with pulse width modulation (PWM), deadtime, disable, power supply (VDDI) and ground (GND) pins. There are two complementary isolated output channels. Each output channel has its own power supply (VDDA and VDDB), output (VOA and VOB) and ground pins (GNDA and GNDB). In addition to that, Figure 5.9 also shows the IGBT gate protection circuit. This circuit is intended to protect the gates from any voltage spikes (whether positive or negative) or surges that may appear at the IGBTs control terminals. On the other hand, it also prevents from the undesired activation when there is no applied positive signal at the gate. The protection circuit consists of two Zener diodes for transient suppression, Z_1 and Z_2 , and a parallel resistor R_P . The gate resistor value R_g , was selected following the IGBT manufacturer's recommendation. The resistor R_{DT} , presented in Figure 5.9, is used to calibrate the deadtime value. The used IGBT in half-bridge SM is the IKW40N65H5 from *Infineon*. Moreover, additional IGBT for the purpose of protection is used IGW40N65H5 from *Infineon*. Main characteristics of the IKW40N65H5 IGBT and the IGW40N65H5 IGBT can be found in [188] and [189], respectively.

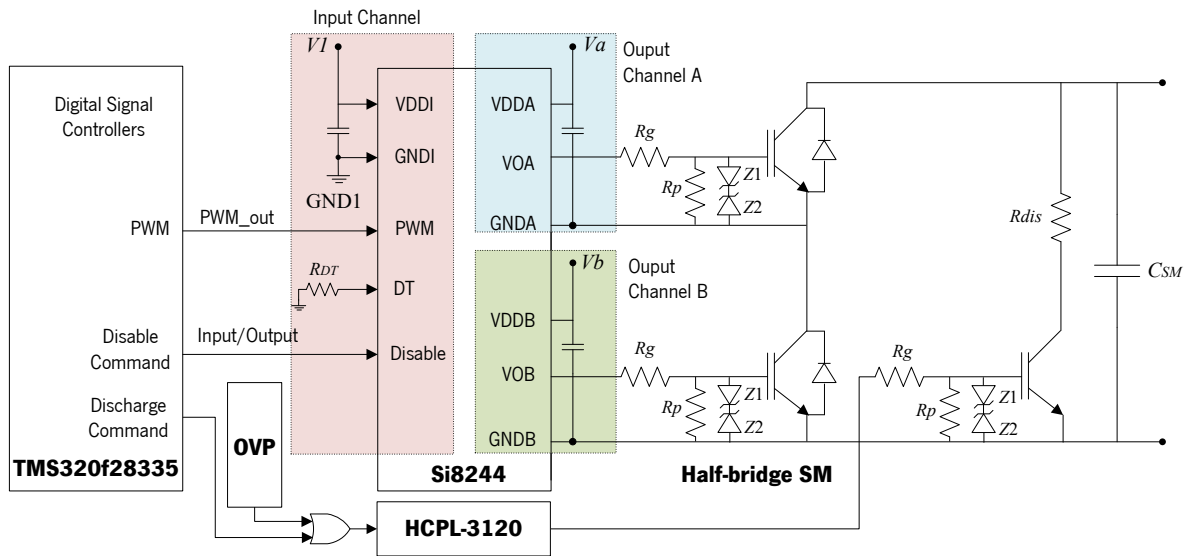


Figure 5.9. Driver circuit PCB scheme: internal schematic of *Si8244* and the connections with the IGBT terminals.

Figure 5.10(a) shows the top layout of the driver circuit PCB design, where the *Si8244* (surface mount IC) is mounted on the top layout of this PCB. On the other hand, Figure 5.10(b) shows the bottom layout of the driver circuit PCB. Since the isolation is essential between the input-to-output channels and output-to-output channels (or between output channels), there are three main isolated copper pours in the top and the bottom layouts, as presented in the Figure 5.10. The maximum values of input-to-output and output-to-output isolation voltages are 2.5 kV RMS and 1.5 kV RMS, respectively. Further details can be found in [187], the *Si8244* datasheet from *Silicon Labs*.

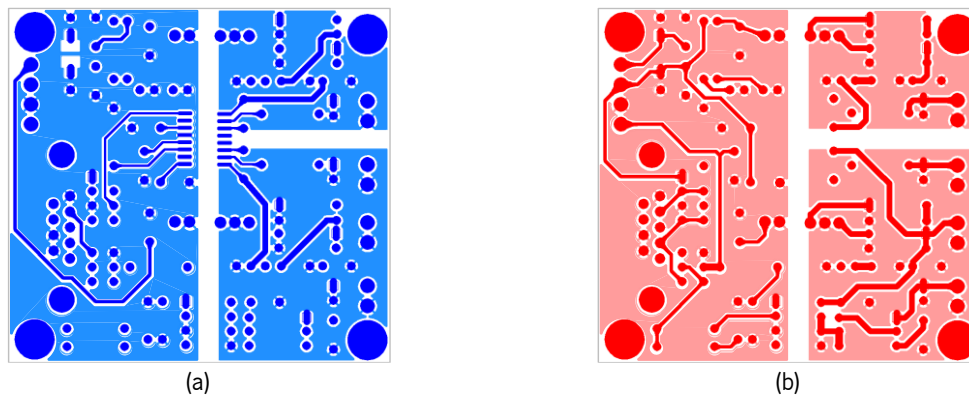


Figure 5.10. Driver circuit PCB layout design: (a) Top layout; (b) Bottom layout.

Figure 5.11 shows the driver circuit PCB hardware (was developed under the scope of this Ph.D. thesis). The PWM input signals of this PCB (the DB9 connector) are supplied from the main central control unit. There are mainly two input PWM signals, the first is considered as an input signal for the *Si8244* IC, and the other signal is to give an order to discharge the SM capacitor by using an additional switching device when it is necessary. Consequently, this PCB has the capability to drive three power switching devices or IGBTs. The main SM switching devices (top and bottom) are driven by the *Si8244* IC, while the additional switching device to discharge the SM capacitor is driven by the *HCPL-3120*

(gate drive optocoupler) from *Avago Technologies* with a maximum peak current of 2.5 A [190]. The *HCPL-3120* input can be supplied either from a discharge command from the controller *TMS320F28335*, or from an overvoltage protection (OVP), as shown in Figure 5.9. Two DC-DC isolated converters from *TRACO Power* are used to accomplish the isolation between input-to-output channels of the *Si8244* IC.

The driver circuit PCB is designed using an optimized layout to reduce the length of the PCB traces. In other words, the design should respect the minimum compulsory dimensions to maintain the isolation between the channels. In addition, the optimized layout is important to minimize the PCB parasitics, such as parasitic inductance and capacitance, then, reducing the noise and improving the PCB performance. Moreover, decoupling capacitors located close to the main power supply signals are used to avoid erroneous operation. On the other hand, extra PCB jumpers are added, giving the possibility to choose the turn-off voltage value (either 0 V or -15 V) of the IGBT switching device (this is due to the bipolar DC-DC isolated converters from *TRACO Power*). The turn-off negative voltage applied to the gate-emitter junction helps to decrease the turn-off time of the IGBT, then, improving the overall performance and obtaining a faster switching device.

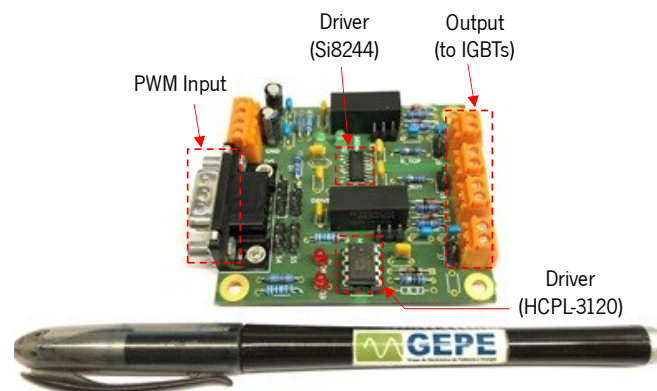


Figure 5.11. Driver circuit PCB (developed under the scope of this Ph.D. thesis).

5.5.1.1. Driver Circuit PCB Experimental Results

Figure 5.12 shows the driver circuit PCB experimental results when a PWM signal (V_{PWM}) is applied on the input terminal of *Si8244* IC. The results are obtained at a switching frequency of 40 kHz, gate resistor $R_g = 20 \Omega$, parallel Zener resistor $R_P = 10 \text{ k}\Omega$, and a dummy load used to simulate the gate-emitter capacitance and resistance. The used IGBT in this project has a gate-emitter capacitance of 2500 pF and a gate-emitter resistance of 20 M Ω . These parameters are used for tuning the dummy load value. On the other side, it is noteworthy to mention that, all the experimental results presented in this Ph.D. thesis are obtained after using the *TPS2000B* series digital storage oscilloscope from *Tektronix*, which has four isolated channels [191]. In that regard, Figure 5.12(a) shows two complementary output signals, V_{OA} and V_{OB} , with an applied deadtime estimated by 1 μs . In this

case, the gate-emitter turn-off voltage value is zero (unipolar). Figure 5.12(b) shows the complementary output signals when using a turn-off voltage value of -15 V (bipolar), VOA and VOB .

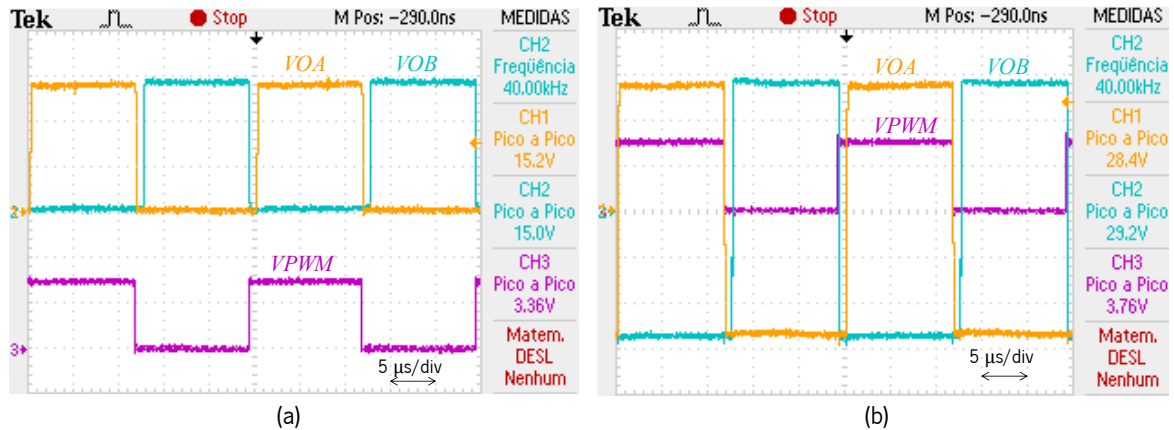


Figure 5.12. Driver circuit PCB experimental results: (a) Unipolar PWM; (b) Bipolar PWM; (VOA , VOB : 5 V/div ; $VPWM$: 2 V/div).

Figure 5.13(a) shows the driver circuit PCB experimental results, demonstrating the deadtime effect when using the same dummy load. The $Si8244$ IC is calibrated to output two complementary signals with deadtime value close to $1\text{ }\mu\text{s}$. However, the results show that deadtime actual value is lower than the adjusted value. This is due to the IGBT switching delay (turn-on time, turn-off time, fall and rise time), and the fact that IGBT turn-off time is higher than the turn-on time, then, the programmed deadtime should be higher than the turn-off time of the IGBT to avoid short circuit in the SM. As a result, the IGBT switching delay should be estimated and considered to have the desired deadtime value. Accordingly, and as shown in Figure 5.13(a), the actual deadtime value is close to $0.75\text{ }\mu\text{s}$.

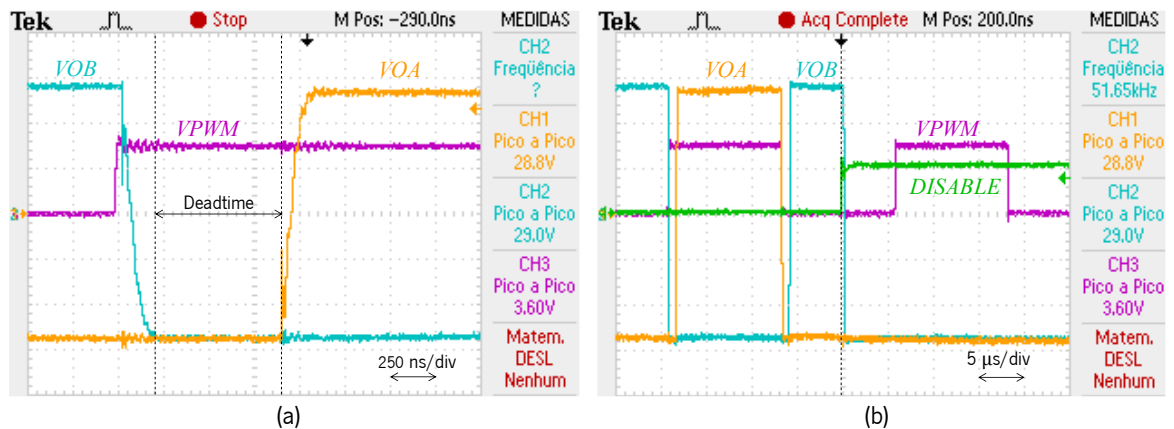


Figure 5.13. Driver circuit PCB experimental results: (a) Deadtime results; (b) Results when $Si8244$ is disabled; (VOA , VOB , $DISABLE$: 5 V/div ; $VPWM$: 2 V/div).

Since the $Si8244$ IC has two complementary output signals, this may bring some complications when a fault is detected. Therefore, *Silicon Labs* has provided the $Si8244$ IC with a disable pin that unconditionally forces the output signals, VOA and VOB , to the turn-off voltage value (0 V or -15 V) regardless the PWM input condition [187]. Figure 5.13(b) shows the experimental results when a disable signal, $DISABLE$, is high at the same aforementioned dummy load conditions. In that case,

the output signals, VOA and VOB , are equal to the turn-off voltage value of -15 V. The shutdown time from disable true and restart time from disable false are estimated by 60 ns [187].

5.5.2 Protection Circuit PCB

MMC reliability and stability are one of the most important demands. This includes the protection against consequences that may appear due to the MMC malfunctioning, bearing in mind that, MMC topology contains many power switching devices such as IGBT, diodes, etc., and each device can be a possible failure point. In this context, and since the MMC is composed of multi cascade-connected SMs, each SM should have its own protection system, then, the developed protection circuit PCB under the scope of this Ph.D. thesis is essential for each MMC SM. However, and before explaining the protection circuit PCB functionality, the following details present the potential MMC faults [192].

There are different faults that may negatively affect the MMC functionality. These faults can be classified according to their origins: external faults caused by an external power source connected to the MMC SMs (such as, the MMC main DC-link or the three-phase power grid faults), as shown in Figure 5.14(a), and internal faults caused by the malfunctioning of one or more SMs (such as, open circuit fault), as shown in Figure 5.14(b), and the deadtime short circuit fault between T_1 and T_2 , as shown in Figure 5.14(c). The current flow due to three-phase power grid fault is not controllable by the half-bridge SM due to the freewheeling diodes [193]. Consequently, it is noteworthy to mention, the proposed protection scheme is only effective against the MMC internal faults, that may occur in any MMC SMs, such as short circuit or open circuit fault caused by the malfunctioning of one or more power switching devices. The short circuit fault may occur due to a defect in one of the SM components, in which the PCB traces may overheat, resulting in an open circuit fault as well.

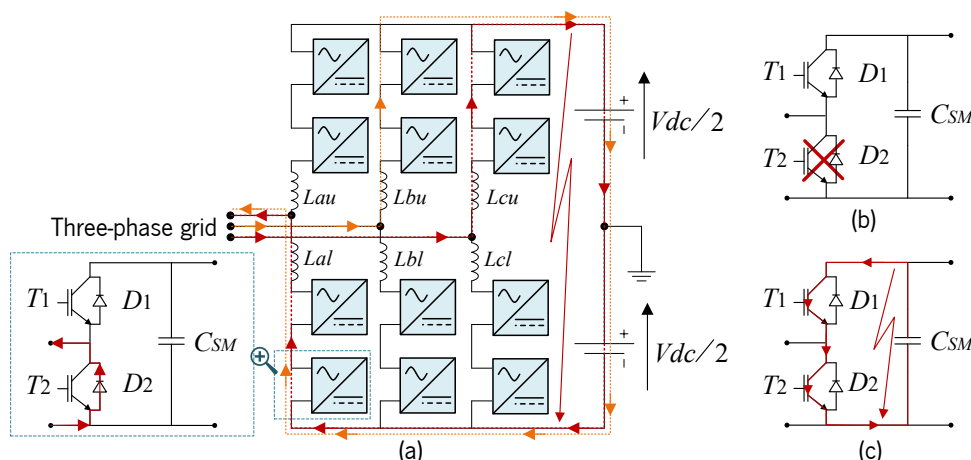


Figure 5.14. MMC faults: (a) External origin faults; (b) (c) Internal origin faults.

When an internal fault in the SM occurs, the consequences may vary between high current flow or DC voltage unbalance of MMC SMs, in which, some SM capacitors can be charged to exceed the capacitor

nominal voltage and others can be simultaneously discharged. Once the SM capacitor is charged with an absolute value higher than its rated voltage, the deterioration in the capacitor performance may increase. For instance, the capacitor overheats, and the failure can be faster, accompanying by explosion effects, or it may be slower with an associated reduction in the capacity, shorter lifespan, and degrading the capacitor main parameters, such as the equivalent series resistor and the equivalent series inductance. Therefore, overvoltage protection is required to avoid detrimental effects, then avoiding the total collapse of the MMC [192].

On the other side, overcurrent protection is extremely required when a failure occurs in any of the power switching devices. In this case, the stored energy in the capacitor of the affected SM releases, leading to a very high current flow, accompanied by overheating of the switching devices [194]. The main aim of the overcurrent protection is to suppress the high currents that usually exceed the maximum working current value of the power switching devices. On the other hand, the overcurrent protection must prevent the fault current to reach the saturation current value of the MMC filter inductors. A high value of inductance can limit the fault current and the circulating currents in the MMC arms [195]. However, using only the filter inductors to overcome the fault currents is not enough, but it can help to dominate the fault location until the protection system is activated. However, using a high value of inductance for high current applications brings a significant voltage drop, which decreases the modulation index of the MMC [194].

The proposed protection scheme is applied on each MMC SM, as shown in Figure 5.15, where this protection consists of two main parts: the overcurrent protection and the overvoltage protection. There are two isolated current sensors *ACS730* IC from *Allegro* that measure the instantaneous current of the collector of each IGBT. The output of these sensors is a differential signal to be less sensitive for noise resulting from electromagnetic interference.

When the actual current value of the IGBT collector, i_{act} , exceeds the reference current value, i_{ref} , this activates the overcurrent protection, as shown in the flowchart presented in Figure 5.16(a). The actuating response of the *ACS730* sensors is very quickly to fault conditions (about 0.7 μ s—without applying signal filtering) [196], which provides robust and reliable protection against short circuit faults. When a high fault current is detected by any of the *ACS730* current sensors, a disable signal will be triggered to stop the commutation of the power switching devices or IGBTs. This leads to bypass the SM capacitors of the MMC. The disable order of the power switching devices is always active until an external reset action is manually released after avoiding the fault origins, such as the deadtime fault that causes a high short circuit current flowing through the IGBTs. A delay function before the reset action is important to prevent the switching stress in the IGBTs. Normally, this protection is calibrated

to be actuated when the fault current value exceeds the freewheeling diodes nominal current. The calibration of the overcurrent protection should also consider the saturation current of the MMC filter inductors, in which the fault current should not exceed the saturation current of the inductors.

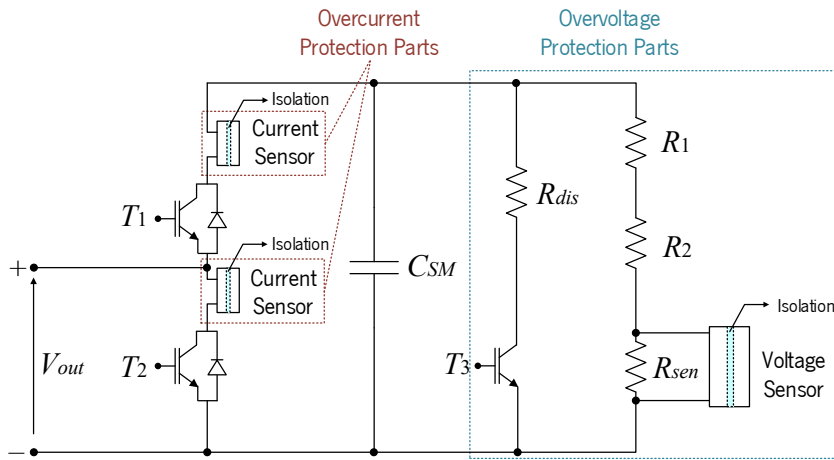


Figure 5.15. Half-bridge SM with the proposed protection scheme.

The proposed overvoltage protection consists of an isolated signal amplifier *Si8920* IC from *Silicon Labs* that measures the DC voltage value across the SM capacitor by using the measuring resistor, R_{sen} , as shown in Figure 5.15. The voltage divider (resistors of R_1 , R_2 and R_{sen}) is used to fit the *Si8920* isolated amplifier nominal input value. The input and the output of this amplifier, besides the signal conditioning process, are differential to reduce the noise resulting from the electromagnetic interference [197]. This isolated signal amplifier has a very low signal delay (about $0.75 \mu\text{s}$ —without applying signal filtering) [197]. According to the overvoltage protection flowchart presented in Figure 5.16(b), the overvoltage protection compares the actual voltage value with its reference value. The overvoltage protection is actuated when the actual voltage value is equal or exceeds the reference signal. In this case, the switching device, T_3 , will be activated to discharge the energy stored in the SM capacitor through a discharge resistor, R_{dis} , until the actual voltage signal is less than the reference voltage signal value, v_{ref} .

Figure 5.17 shows the protection circuit PCB Layout design using the *PADS* software. This PCB is designed to be fixed as close as possible to the SM power circuit PCB. This is important to reduce the parasitics of the SM circuit, particularly, the inductive-resistive parasitics, then, obtaining a low inductive SM DC-link. The protection circuit PCB will be mounted on the top surface of the power circuit PCB, so the connection terminals of the protection circuit PCB and the power circuit PCB are close to each other. The implemented protection circuit PCB is shown in Figure 5.18, where the top layer of the protection circuit PCB has the main terminals of voltage and current sensors, as well as the required components for the signal conditioning of the overvoltage protection, as shown in Figure 5.18(a). On the other hand, the bottom layer of the protection circuit PCB contains the voltage and the current

sensors, besides the ICs that are responsible for the signal conditioning of the overcurrent protection, as shown in Figure 5.18(b).

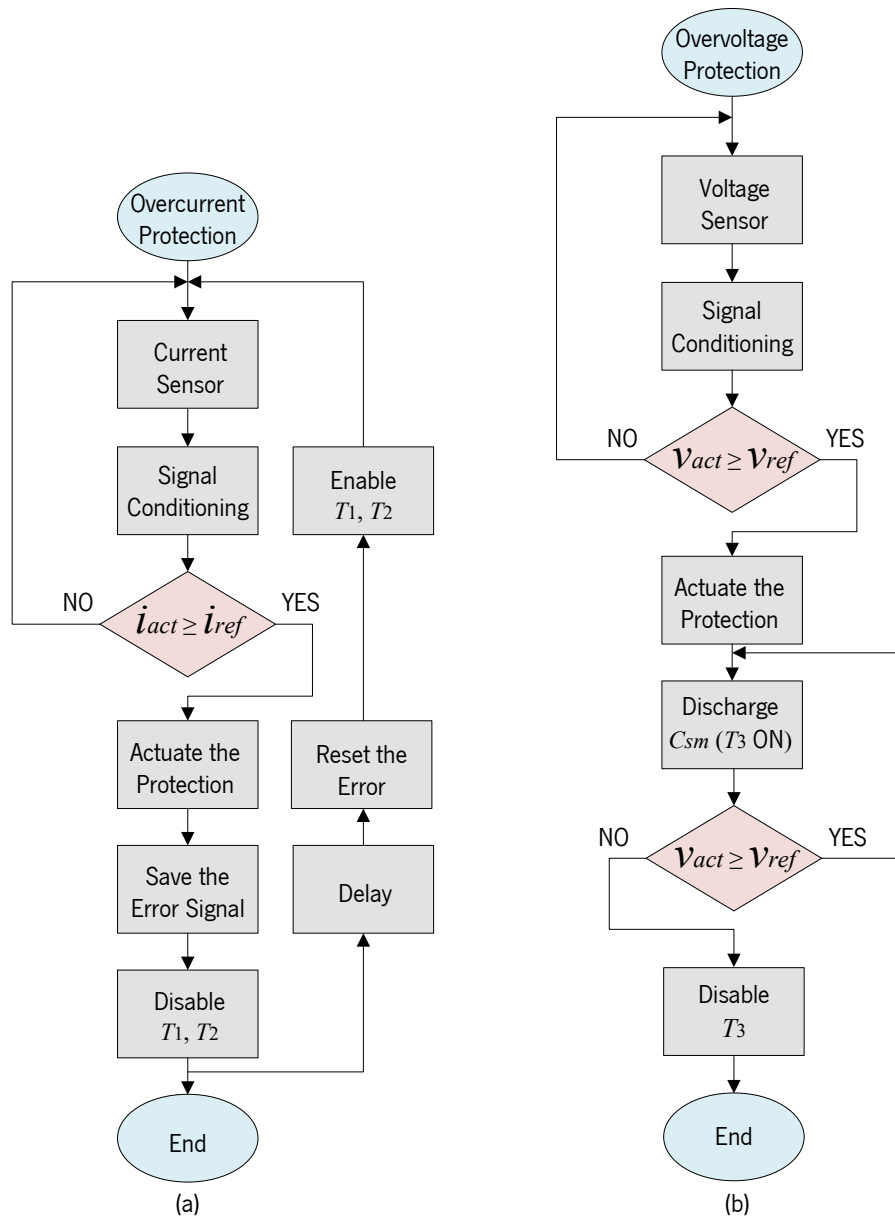


Figure 5.16. Flowchart diagrams of the proposed protection scheme: (a) Overcurrent protection flowchart; (b) Overvoltage protection flowchart.

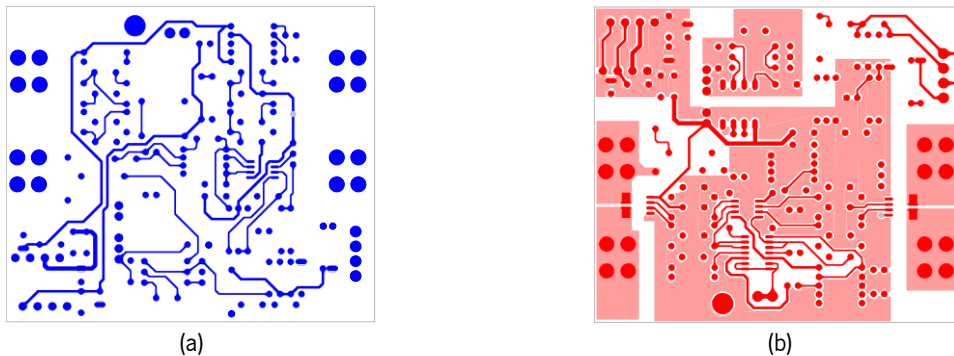


Figure 5.17. Protection circuit PCB layout design: (a) Top layout; (b) Bottom layout.

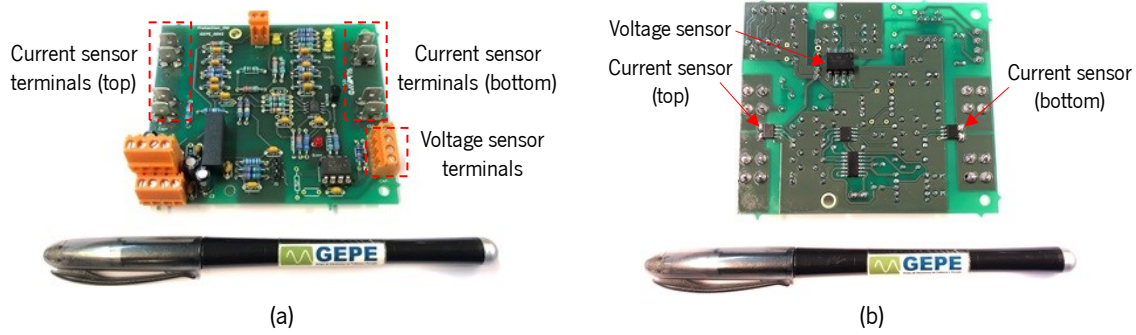


Figure 5.18. Protection circuit PCB: (a) Top; (b) Bottom (developed under the scope of this Ph.D. thesis).

5.5.2.1. Overcurrent Protection Experimental Results

Testing the overcurrent protection of the MMC SM requires to use a test workbench to verify the correct operation of the current sensors *ACS730* under test conditions without damaging other SM components. Therefore, Figure 5.19 presents the circuit schematic of the overcurrent protection test workbench, which consists of an adjustable auto-transformer connected to the primary windings of a step-down transformer. The secondary windings of the step-down transformer can withstand a high current value close to 60 A, which is useful to test the overcurrent protection at tens of Amperes. An uncontrolled rectifier bridge is connected to the secondary windings of the step-down transformer. The electrical impedance, Z , reflects the parasitic elements of the circuit. The isolated current sensor, *ACS730*, is connected in series with an IGBT to the output of rectifier bridge. This series connection is used to create, as real as possible, the conditions when an MMC SM is under operation. The bridge rectifier is used to keep the freewheeling diode in the reverse-biased mode [192].

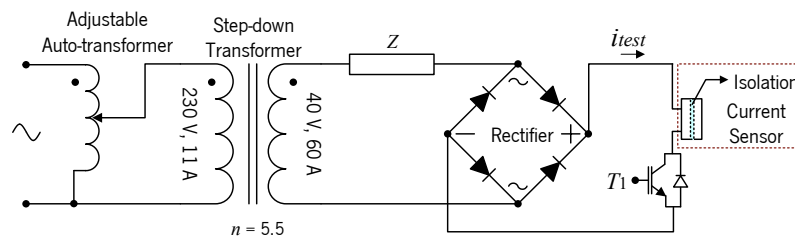


Figure 5.19. Schematic of the circuit implemented for testing the overcurrent protection.

Figure 5.20 shows the overcurrent protection experimental results. The protection is calibrated to actuate when the actual test current exceeds a value higher than ± 28 A (this value is only for experimental testing, and it does not reflect the final considered value for overcurrent protection calibration). The actual test current, i_{test} (in green), has a peak value equal to 32 A, and the overcurrent protection signal, v_{pr} (in purple), is actuated when the actual test current exceeds the reference value of ± 28 A. In that case, the overcurrent protection signal reaches the value of -15 V. The differential output signal of the current sensor, v_{dif} (in orange) has almost the same waveform shape of the actual test current. However, the noise in the v_{dif} waveform is highly reduced after using a differential

amplifier, as seen in v_{amp} signal (in cyan). There is a small delay (less than 1 μ s) between the waveforms of i_{test} and v_{amp} . This delay is resulting from current sensor delay and signal conditioning delay, bearing in mind, there is always a trade-off between the signal fast response and the noise cancellation. The hysteresis amplifier as an example guarantees a cleaner output signal but accompanied with a higher delay [192].

It is noteworthy to mention, the implemented overcurrent protection is a bidirectional one. In other words, it compares the actual current value with its reference value in the positive and the negative cycle of the actual test current waveform. This is important to avoid harmful consequences when the current is flowing through the IGBT or through the freewheeling diode. However, experimental results of the overcurrent protection only show the protection response in the positive half-cycles since a rectifier bridge is used to avoid the current flow through the freewheeling diode.

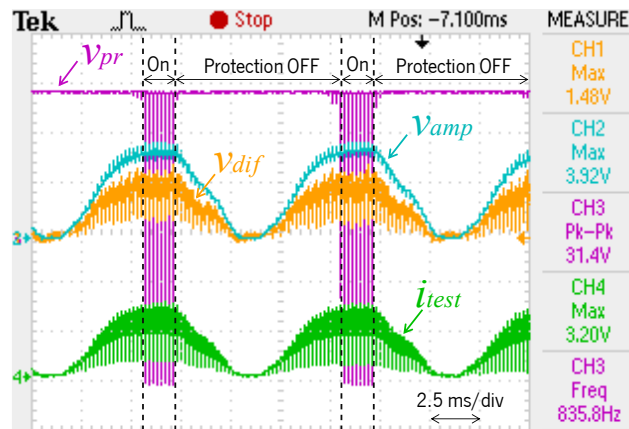


Figure 5.20. Protection circuit PCB experimental results (overcurrent protection): Test current (i_{test} : 20 A/div, 100 mV per 1 A); Overcurrent protection actuation signal (v_{pr} : 5 V/div); Differential output voltage of the current sensor (v_{dif} : 1 V/div); Differential output voltage of the current sensor after using a differential amplifier (v_{amp} : 2 V/div).

5.5.2.2. Overvoltage Protection Experimental Results

Testing the overvoltage protection of the MMC SM requires to use a test workbench to verify the correct operation of the isolated signal amplifier *Si8920* under test conditions without damaging other SM components. Therefore, Figure 5.21 presents the schematic of the overvoltage protection test workbench, which consists of an adjustable auto-transformer connected to the input of an uncontrolled rectifier bridge to obtain DC voltage on the output terminals. The overvoltage protection components are connected to the output terminals of rectifier bridge. The resistors, R_1 , R_2 and R_{sen} , are used as a voltage divider to obtain voltage value across the resistor R_{sen} , below the nominal input voltage value of the isolated voltage sensor *Si8920*. The resistor R_{dis} and the IGBT T_3 , are used to discharge the surplus energy stored in the SM capacitor, then, obtaining lower SM voltage [192].

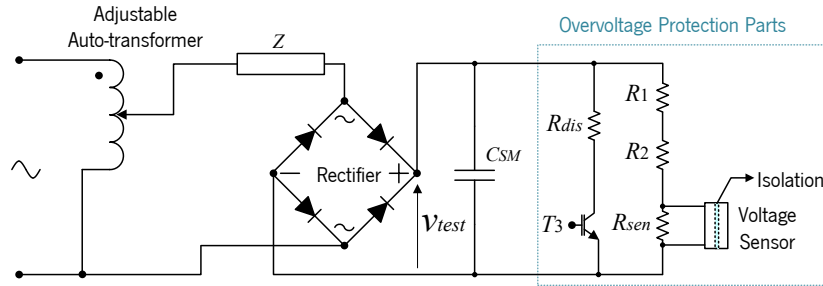


Figure 5.21. Schematic of the circuit implemented for testing the overvoltage protection.

Figure 5.22 shows the overvoltage protection experimental results. The protection is calibrated to actuate when the SM voltage exceeds an absolute value higher than 170 V. The test voltage signal, v_{test} (in orange), has the highest value of 174 V, then, the overvoltage protection signal, v_{pr} (in purple), is actuated when the test voltage exceeds the reference voltage value of 170 V. The differential output signal of the voltage sensor after using a differential amplifier, v_{amp} (in cyan), has a lower noise and very small delay (tens of μs) between v_{test} and v_{amp} signals. This small delay is caused by the voltage sensor delay and the signal conditioning and processing delay. The signal, v_{ref} (in green), denotes the reference signal, in which the protection actuates when the condition, $v_{amp} \geq v_{ref}$, is true. This implemented overvoltage protection is a unidirectional one, then, it only compares the actual voltage value with its reference value in the positive cycles of v_{test} waveform. This is because the MMC SM voltage is always positive, and there is no need to implement a bidirectional overvoltage protection [192].

It is worthy to mention, several protection systems are implemented, either by means of implemented PCBs, such as the protection circuit PCB, or through verification functions in the developed supervision software. In addition, four semiconductor fuses are used as an ultimate protection, where each MMC arm has one semiconductor protection fuse.

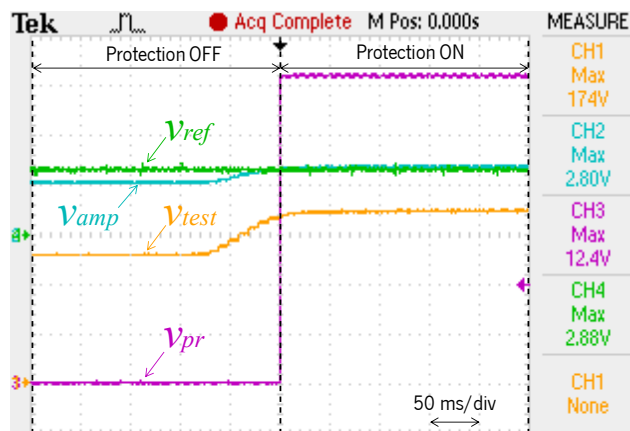


Figure 5.22. Protection circuit PCB experimental results (overvoltage protection): Test voltage (v_{test} : 50 V/div); Voltage protection actuation signal (v_{pr} : 2 V/div); Differential output voltage of the voltage sensor after using a differential amplifier (v_{amp} : 2 V/div); Reference voltage signal (v_{ref} : 2 V/div).

5.5.3 Power Circuit PCB

The power circuit PCB includes the half-bridge SM components, such as DC-link capacitors, coupling capacitors, power switching devices, discharge resistors and power terminals. Three power switching devices, IGBTs, are mounted on the top surface of the power circuit PCB, where two of these switching devices commute under 40 kHz switching frequency to synthesize output waveform signal of 50 Hz. The third switching device is used for the purpose of overvoltage protection. In this context, a fifth-generation high-speed IGBT switching device with fast freewheeling diode from *Infineon* is used in the SM power circuit PCB. The used IGBT has a rated voltage of 650 V and a rated current of 46 A at 100 C°. In addition, it has a rated current of 74 A at 25 C°. The diode forward current can reach up to 21 A at 100 C°. More information of the IGBT (IKW40N65H5 from *Infineon*) can be found in [188].

A bank of aluminum electrolytic capacitors is used to increase the SM capacitor lifetime, and to reduce both of the equivalent series resistance and the equivalent series inductance of the SM capacitor. All aluminum electrolytic capacitors have the same rating, and they are connected in parallel to increase the equivalent SM capacitance, then, storing a greater amount of electrical energy. On the other hand, reducing the total equivalent series resistance of the SM capacitor is important to reduce the power dissipation in the electrolytic capacitors. It also helps to obtain a better stability of the control loop, besides boosting the overall performance and reliability [198]. The full scheme of the power circuit PCB is introduced in Figure 5.23. This PCB contains some power terminals to connect with the driver circuit and the protection circuit PCBs. In addition, these power terminals are beneficial to accomplish the cascade-connection of the MMC SMs. In order to solve the ringing problem in the power circuit PCB, it is essential to use snubber capacitors or transient voltage suppressor (TVS) diodes.

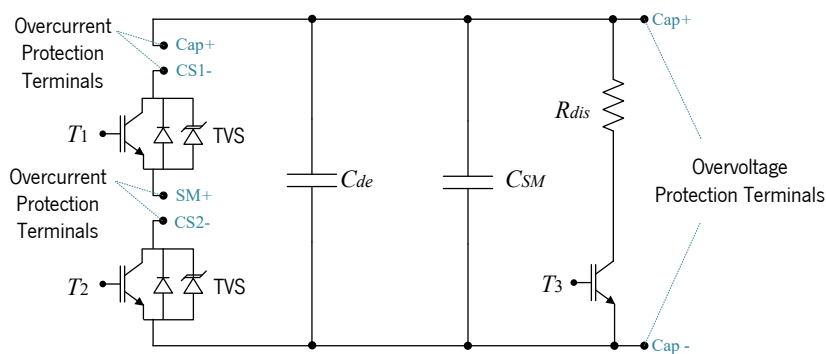


Figure 5.23. Half-bridge SM with the proposed power circuit PCB scheme.

Figure 5.24(a) shows the top layout design of the power circuit PCB, using *PADS Layout* tool. The top layer is mainly used to complete the negative polarity traces. On the contrary, Figure 5.24(b) shows the bottom layout design of the power circuit PCB, which is mainly used to complete the positive polarity traces. Using different polarity traces at the same layout layer is avoided for a better noise and electromagnetic interference cancellation.

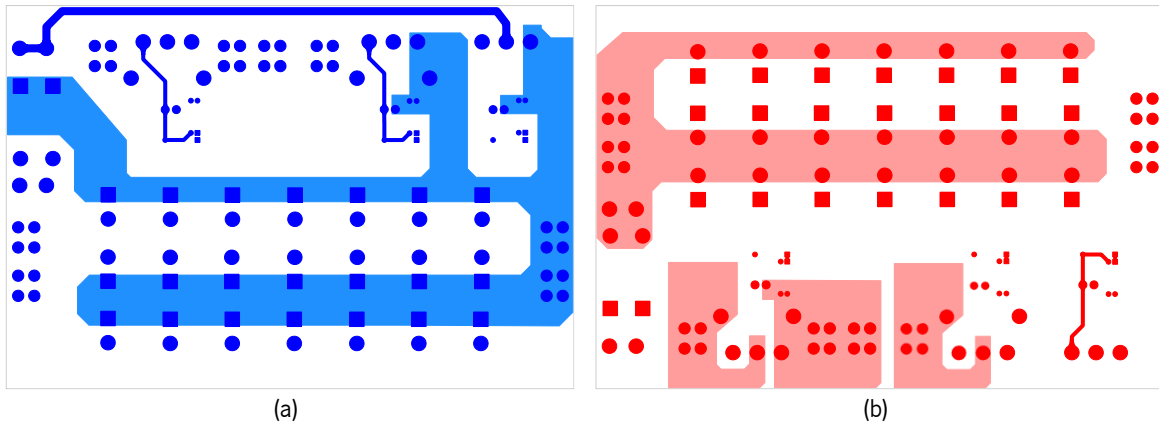


Figure 5.24. Power circuit PCB layout design: (a) Top layout; (b) Bottom layout.

The power circuit PCB is introduced in Figure 5.25. The top layout, presented in Figure 5.25(a), contains the main power terminals and the power switching devices. In addition, protection circuit and driver circuit PCBs are designed to be placed on the top surface of the power circuit PCB. This is important to reduce the connectors length and the related SM parasitics. Moreover, connecting the driver circuit PCB output terminals with the IGBTs gate-emitter terminals should be performed using short connectors. This is essential to reduce the parasitics that may appear as a result of the high switching frequency. Figure 5.25(b) presents the bottom layout of the power circuit PCB, where a bank of electrolytic capacitors is used (21 capacitors connected in parallel). On the other hand, Table 5.2 offers a list of the power circuit PCB components.

Table 5.2. Power circuit PCB components.

Components	Symbols	Values	References
Power IGBTs	T_1, T_2	–	IKW40N65H5 [188]
Overvoltage protection IGBT	T_3	–	IGW40N65H5 [189]
Electrolytic capacitor	C_{sm}	$21 \times 47\mu\text{F} = 987\mu\text{F}$	<i>Nichicon</i> manufacturer [199]
Decoupling capacitor	C_{de}	$0.1\mu\text{F} // 1\mu\text{F} = 1.1\mu\text{F}$	–
Discharge resistors	R_{dis}	$10\text{ k}\Omega // 10\text{ k}\Omega = 5\text{ k}\Omega$	–

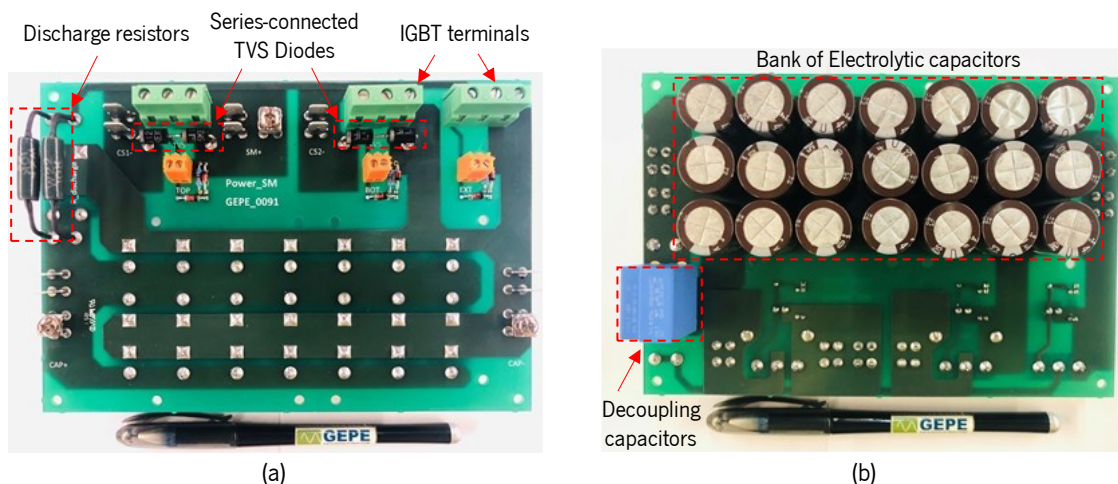


Figure 5.25. Power circuit PCB: (a) Top; (b) Bottom (developed under the scope of this Ph.D. thesis).

5.5.3.1. Power Circuit PCB Experimental Results

After the implementation of one SM, it is important to validate the SM operation conditions before implementing a complete reduced-scale MMC prototype. On the other hand, for the verification of the HB-MMC2 RPC operation and control algorithm, reduced-scale MMC prototype is quite enough [200]. However, the full implementation of an MMC prototype is not a good strategy to test the power circuit PCB, since it is difficult to predict the SMs performance when they are connected in a cascade configuration. In that case, the power switching devices, the electromagnetic and thermal characteristics for each SM is different. Consequently, an experimental setup to test the power circuit PCB of the SM is required.

There are many SM testing schemes that have been presented in the literature [201]–[205]. Some of these testing schemes require an auxiliary half-bridge SM to switch cooperatively with the tested SM, which obligates to use extra hardware and control mechanisms. In this context, a simplified testing scheme of the SM has been proposed in [205], and presented in Figure 5.26. The DC voltage source, V_{dc} , should have an absolute value lower than the rated voltage of the SM capacitor. When the power switching devices, T_1 and T_2 , are switching at a similar duty cycle of 50%, and by neglecting the voltage drop across the resistor R , the SM capacitor voltage V_{SM} , in the ideal case has a value twice the voltage of the DC source, V_{dc} . As a result, and in that case, the half-bridge SM operates as a step-up boost converter.

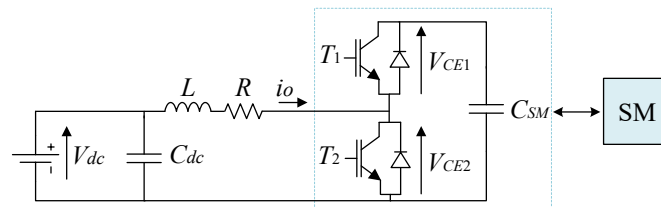


Figure 5.26. Testing scheme of the half-bridge SM.

By commutating the half-bridge SM switches, an alternating output current can be generated at a frequency equal to the SM switching frequency, 40 kHz. This is the main disadvantage of this testing method since the SM output current frequency is not equal to the one when several cascade-connected SMs, as the case of MMC, are commutating. In the case of MMC, the arm currents have a frequency equal to the power grid frequency of 50 Hz. On the other hand, SM output current with a high frequency will pass through the DC source, V_{dc} , which indicates a power demand of the DC source. The main advantage of this method is its simple control, simple structure, and testing the SM switches under frequency stress similar to the one in real operating conditions. In addition, it is possible to predict the transient induced signals across the switching devices due to the parasitic impedance and the thermal behavior of the SM components.

The inductance L is important to generate an alternating current, where this inductance stores energy when the switch T_2 , is closed and the output current i_o , in that case, flows through the IGBT switch T_2 . On the contrary, when the switch T_1 is closed, the output current i_o inverts its direction due to the higher voltage value of the SM capacitor. However, and in order to protect the DC voltage source from the high returning currents, diodes are connected in series with the DC voltage source, and at such a case, the negative currents passing through the capacitor, C_{dc} . The resistor R is added to limit the output current, and in order to avoid the resonance phenomenon.

Figure 5.27 shows the experimental results when testing of one SM without using the TVS diodes or snubber capacitors between the emitter-collector of each IGBT. Table 5.3 presents the parameters used in the half-bridge SM experimental validation. The switching frequency of 40 kHz and a fixed duty cycle of 50% are used during the test. Experimental results show a ringing phenomenon, accompanied by high oscillation with a peak value of 290 V.

This oscillation is caused by the PCB parasitics, bearing in mind that, the longer the PCB traces, the higher the parasitics effect in the circuit. In this context, the ringing phenomenon in short traces is caused by the inductive and capacitive parasitics. On long traces, ringing is not only caused by the inductive and capacitive parasitics, but also by the signal frequency reflection due to the impedance mismatch between the feed and the return long traces. As a result, and in order to solve the ringing problem in the power circuit PCB, it is essential to use snubber capacitors or TVS diodes for a proper operation of the power circuit PCB [206].

Table 5.3. Parameters of single half-bridge SM test.

Parameters	Symbols	Values
Filter inductance	L	18 μ H
Capacitance of the MMC capacitor	C_{SM}	987 μ F
Capacitance of the DC-link capacitor	C_{dc}	470 μ F
Arm resistor	R	52 Ω
PWM switching frequency	f_{sw}	40 kHz
Duty cycle	D	0.5
Deadtime	t	700 ns
DC source voltage	V_{dc}	140 V
SM voltage	V_{SM}	175 V

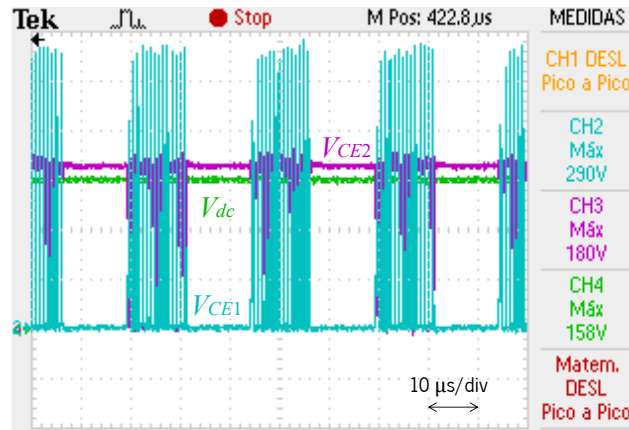


Figure 5.27. Power circuit PCB experimental results without using TVS diodes or snubber capacitors: Collector-emitter voltage of IGBT top (V_{CE1} : 50 V/div); Collector-emitter voltage of IGBT bottom (V_{CE2} : 50 V/div); DC voltage source (V_{dc} : 50 V/div).

To overcome the ringing problem, two series connected unidirectional TVS diodes from *Littelfuse* (1.5KE100A) are used and connected in parallel with the collector-emitter junction of each IGBT [206]. These TVS diodes have a fast time response, typically, lower than 1 ps. On the other hand, decoupling film capacitors of 1 μF and 0.1 μF , are connected in parallel with the electrolytic capacitors bank. Using different values of the film decoupling capacitors connected in parallel with the electrolytic capacitors is recommended to have a wider response for different ringing frequencies. In addition, the parallel connection of capacitors results in lower equivalent series resistance of the SM DC-link capacitor.

Figure 5.28 shows the experimental results when testing of one SM. Alternating current waveform is generated with a frequency equal to the IGBTs switching frequency, 40 kHz. When one of the IGBTs (either the top or the bottom IGBT) is closed, the voltage across its collector-emitter is close to zero. The first pulse in Figure 5.28, is when V_{CE1} of the top IGBT is high, the output current flows through the bottom IGBT or its freewheeling diode. The second pulse is when V_{CE2} of the bottom IGBT is high. The output current i_o , in this case, flows through the top IGBT or its freewheeling diode.

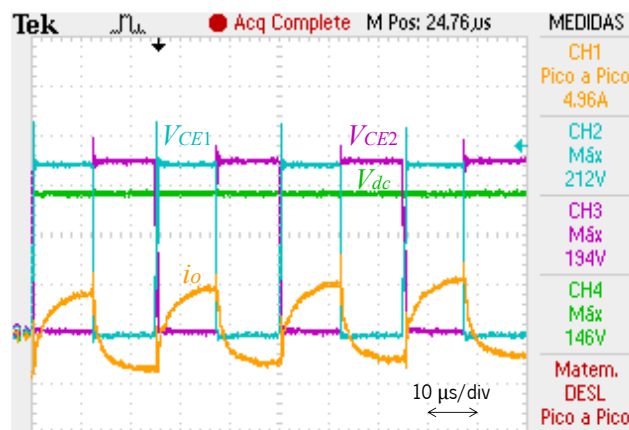


Figure 5.28. Power circuit PCB experimental results: Output current (i_o : 2 A/div); Collector-emitter voltage of IGBT top (V_{CE1} : 50 V/div); Collector-emitter voltage of IGBT bottom (V_{CE2} : 50 V/div); DC voltage source (V_{dc} : 50 V/div).

A deadtime value of 700 ns between PWM pulses is implemented in this experimental test. Consequently, the transient event during the deadtime between the top and the bottom IGBTs is presented in Figure 5.29. The circuit parasitics, in that case (during the deadtime), highly influence the voltage across the collector-emitter of each IGBT.

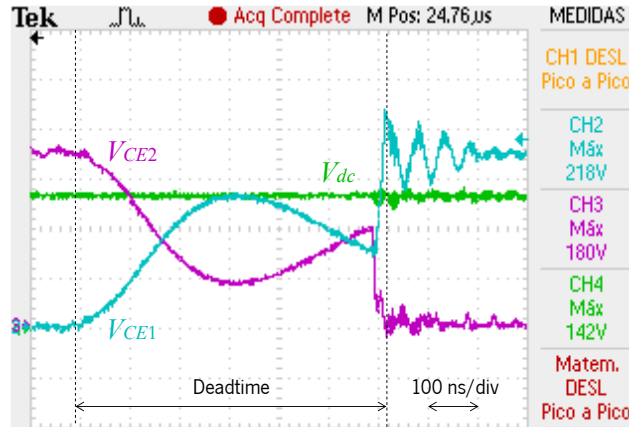


Figure 5.29. Power circuit PCB experimental results during the deadtime: Collector-emitter voltage of IGBT top (V_{CE1} : 50 V/div); Collector-emitter voltage of IGBT bottom (V_{CE2} : 50 V/div); DC voltage source (V_{dc} : 50 V/div).

By calibrating the overcurrent protection to actuate at a current value close to 8 A, and after establishing an overcurrent condition, Figure 5.30 shows that during a time instant t , the output current i_o increases to reach the overcurrent protection reference value of 8 A. At that instant, the overcurrent protection signal, v_{pr} , changes its polarity from 15 V to -15 V, which indicates the actuation of the overcurrent protection. However, the IGBTs are disabled only after a delay time d , estimated by 3.5 μ s. This delay is due to the signal processing delay, such as the signal conditioning delay, the low-pass filters (LPF) delay, the sensors delay, and the delay resulting from the slew rate of the used operational amplifiers.

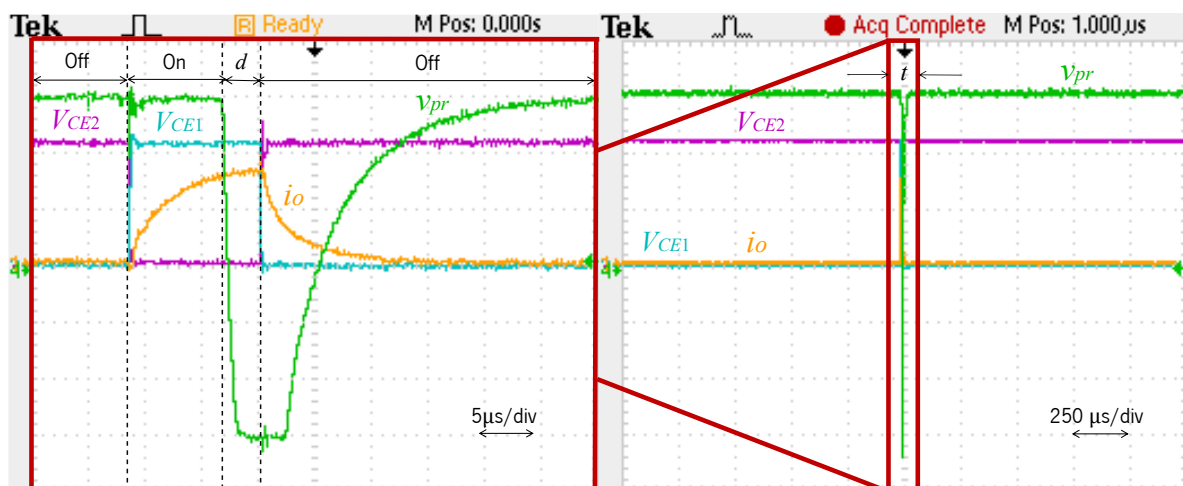


Figure 5.30. Power circuit PCB experimental results when an overcurrent condition is detected by the protection circuit PCB: Collector-emitter voltage of IGBT top (V_{CE1} : 50 V/div); Collector-emitter voltage of IGBT bottom (V_{CE2} : 50 V/div); Overcurrent protection actuation signal (v_{pr} : 5 V/div); Output current (i_o : 5 A/div).

After the IGBTs are disabled, the voltage across the collector-emitter of the bottom IGBT V_{CE2} , is equal to the voltage across the capacitor C_{dc} . On the other hand, the voltage across the collector-emitter

junction of the top IGBT is equal to zero. Additionally, the output current i_o , is gradually decreased to reach the zero value when the voltages across the capacitors, C_{dc} and C_{SM} , have an equal value.

5.5.4 Final SM Structure

Figure 5.31 presents the final SM structure, including the driver circuit PCB, the protection circuit PCB, the power circuit PCB and the IGBTs heatsink. It is worthy to mention, the final SM hardware has a compact, structural, and extensible design to build the reduced-scale HB-MMC2 RPC.



Figure 5.31. Final SM structure.

Four cascade-connected SMs are composing single MMC leg/phase, as shown in Figure 5.32. The total number of SMs for the HB-MMC2 RPC reduced-scale prototype is eight. Chapter 6 presents the experimental results of one MMC leg (when four SMs are commutating), then, the experimental results when all of the SMs are under operation. It is noteworthy to mention that, the MMC operation is validated through the following steps:



Figure 5.32. Single MMC leg/phase (four SMs).

- Single SM validation, including driver circuit, protection circuit and power circuit PCBs (presented in Chapter 5);
- MMC leg/phase validation (presented in Chapter 6);
- Total MMC validation (presented in Chapter 6).

5.5.5 MMC Filter Inductor

The filter inductor is a key component in the MMC. It also has a main influence on the overall MMC size. The inductors are normally used as MMC inner passive filters and they consist of grain-oriented silicon steel sheets core, which is an iron-silicon alloy. Each filter inductor is composed of two windings around the core, as shown in Figure 5.33, which allows to configure the value of the required inductor. In addition, the inductor windings support 20 A RMS value. The coefficient of self-induction for 40 kHz switching frequency is close to 0.8 mH for one coil. However, two windings coils are used and connected in series, so the equivalent inductance is close to 1.6 mH.

To evaluate the saturation current value of the filter inductor, a voltage pulse with an amplitude value close to 15 V is applied to the coil terminals during a short certain time (tens of ms). Consequently, a high current will pass to estimate the saturation point of the coil. In Figure 5.34, it is possible to obtain the saturation test experimental results. The saturation current of the used coil is close to 30 A.



Figure 5.33. Filter inductor used in MMC.

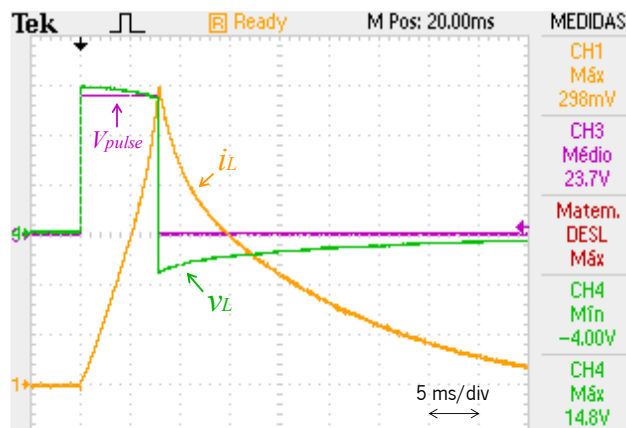


Figure 5.34. Filter inductor saturation test: Pulse voltage (V_{pulse} : 5 V/div); Coil current (i_L : 10 A/div); Coil voltage (v_L : 5 V/div).

5.5.6 MMC Main DC-link Capacitors

Figure 5.35 shows the PCB of the main DC-link capacitor. The same overvoltage protection mechanism, used in the protection circuit PCB, and presented in Figure 5.15, is used in this PCB as well. In that regard, the isolated signal amplifier *Si8920*, the voltage divider resistors, R_1 , R_2 and R_{sen} , the discharge resistor R_{dis} , and the IGBT T_3 , are used to discharge the surplus energy stored in the main DC-link capacitor, then, obtaining lower DC-link voltage when the overvoltage protection is active.

On the other hand, two capacitors with a mid-neutral point should be used in the HB-MMC2 RPC reduced-scale prototype, then, two of the main DC-link capacitor PCB are required. The calibration of the overvoltage protection for both of the main DC-link PCBs should be identical. Otherwise, any voltage variations between both of the mid-neutral point capacitors may lead to higher circulating currents and asymmetric operation of the half-bridge MMC, in which one of the half-bridge MMC legs/phases is loaded with a value higher than the other leg/phase.

Parameter design of the MMC main DC-link has been presented in the item 5.2. A bank of electrolytic capacitors with a total capacitance of $6 \times 470 \mu\text{F} = 2820 \mu\text{F}$ is used. This high value of capacitance helps to reduce the DC-link voltage ripples and gives a higher compensation capability for the converter. In addition, film capacitors are connected in parallel with the electrolytic capacitors bank to reduce the equivalent series resistor of the equivalent capacitor. This is because the film capacitors have a lower internal resistor than the electrolytic capacitors, but their energy storage capacity is limited. In order to reduce the circuit parasitic, it is important to have the power terminals of this PCB close to the electrolytic capacitor poles. Otherwise, it will be more difficult to achieve the voltage balance between the mid-neutral point DC-link capacitors.



Figure 5.35. Main DC-link capacitor (developed under the scope of this Ph.D. thesis).

5.6 Control System Hardware

The control system hardware is fitted in a metallic box, as shown in Figure 5.36. It has several output flat cable connectors to link between the central control unit and the auxiliary control units, such as sensors and actuators. The control system loop always exchanges information between the central control unit and the auxiliary control units (such as signal conditioning unit, sensors unit and the PWM control unit). The metallic box also includes several input/output connectors to interface between the control system and the power system hardware, such as the driver circuit and the protection circuit PCBs. In addition, several power connectors in the metallic box are used to connect the SM DC-link voltages with the associated voltage sensors.

There is also a DC power supply that converts the 230 V AC to a regulated low-voltage (+15 V, +5 V, -15 V) to supply the electronic components of the control system hardware. The MMC control also involves to the MMC protection system, in which the IGBT drivers disable automatically until a reset command is given to erase the error. It is worthy to mention, the majority of the hardware components presented in this item are installed in the metallic box. This is very important to keep the control system hardware quite far from the power system hardware, then reducing the electromagnetic interference effects. The electromagnetic fields generated due to the power system hardware can affect the correct functionality of the central control unit, where these fields may induce currents loops in the electronic ICs.

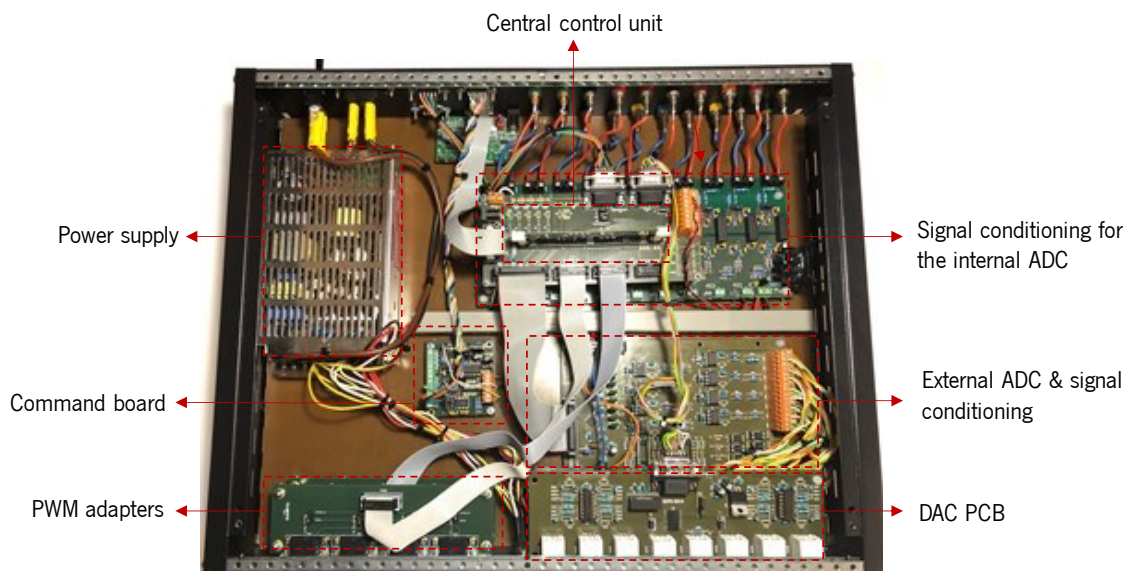


Figure 5.36. Control system hardware fitted in a metallic box.

Figure 5.37 shows the global communication structure of the HB-MMC2 RPC reduced-scale prototype. A depicted hardware architecture of the control system is presented, where a *Delfino* controller from *Texas Instruments TMS320f28335* is used as a central control unit [207]. The HB-MMC2 RPC system requires 18 analogue-to-digital converter (ADC) channels, twelve voltage sensors (ten sensors are

installed for the purpose of MMC DC-links control, and two sensors are installed to implement the E-PLL), six current sensors (four sensors are installed to measure the MMC arm currents and two sensors are installed to measure the load section currents), digital-to-analogue converter (DAC) unit to check the digital signals correctness in the central control unit, and eight PWM channels (one PWM channel is used for each SM, then the driver circuit PCB generates two complementary PWM signals to derive the switching devices).

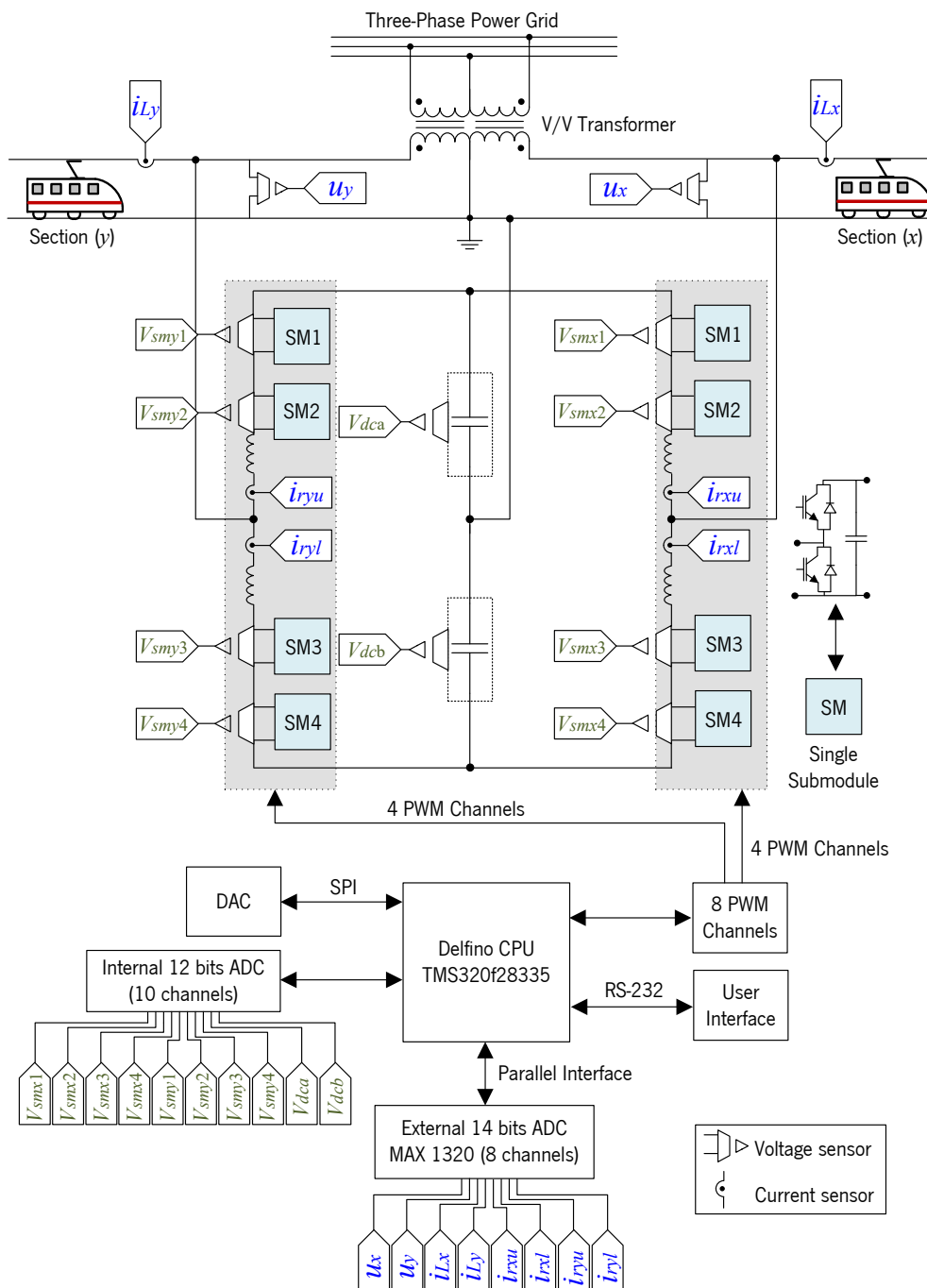


Figure 5.37. Global communication structure of the HB-MMC2 RPC reduced-scale prototype.

There is also a user interface unit based on the RS-232 data interface to send and receive orders, such as pre-charging and discharging of SM capacitors order. There are two ADC units to convert the analogue signals to digital ones. Afterwards, the digital signals can be analyzed and processed by the

central control units. However, the used ADC units have different bit resolution, in which the internal ADC channels of the central control unit are unipolar ones, and they have 12 bits of resolution. Therefore, they have been dedicated for the purpose of DC signals processing, such as the MMC DC-link voltages (SM voltages and main DC-link voltage). On the other hand, the used external ADC IC has 8 bipolar ADC channels with 14 bits of resolution. Therefore, they have been reserved for the purpose of AC signals processing, such as the load section voltages waveforms, as shown in Figure 5.37. The next items demonstrate the main function and tasks of the presented global communication structure.

5.6.1 Central Control Unit

Control algorithm of the HB-MMC2 RPC system is implemented by using a digital signal controller (DSC) *TMS320F28335* from *Texas Instruments*. This controller has the advantage of 32-bit floating-point, which is significant for the calculation's accuracy and robust control implementation. This DSC control unit is used when it is necessary to perform complex operations that require high processing capacity. The major characteristics of the DSC *TMS320F28335* are: clock frequency up to 150 MHz (6.67 ns time cycle); high-performance 32-bit processing unit (*TMS320C28x*); up to 18 PWM channels; 16 ADC channels with 12 bits resolution; 8 external interrupts; up to 88 individually programmable multiplexed of general-purpose input/output pins (GPIO) with input filtering; serial peripheral interface (SPI) port and controller area network communication system, known as CAN communication protocol [207].

The DSC control card, *TMDSCNCD28335*, is a developed tool for the Delfino *F2833x* series. The *TMDSCNCD28335* control card allows the debugging of the programming code, but it needs a base PCB to operate. Subsequently, Figure 5.38 presents the base PCB to support the *TMDSCNCD28335* control card, which is developed and validated in GEPE. This PCB integrates several connectors to facilitate the connection of the different PCBs and the DSC central unit. In addition, it contains the general power supply and it has access for the principal peripherals of the DSC, such as the RS-232 port, the SPI port, the PWM channels and the ADC channels. This PCB involves a connector plug of the *TMDSCNCD28335* control card, which allows replacing the DSC control card when it is necessary. As a conclusion, the DSC, and the other control units integrated in the system can manage, control, and interface with software developed, which allows the user to send/receive commands to/from the HB-MMC2 RPC system.

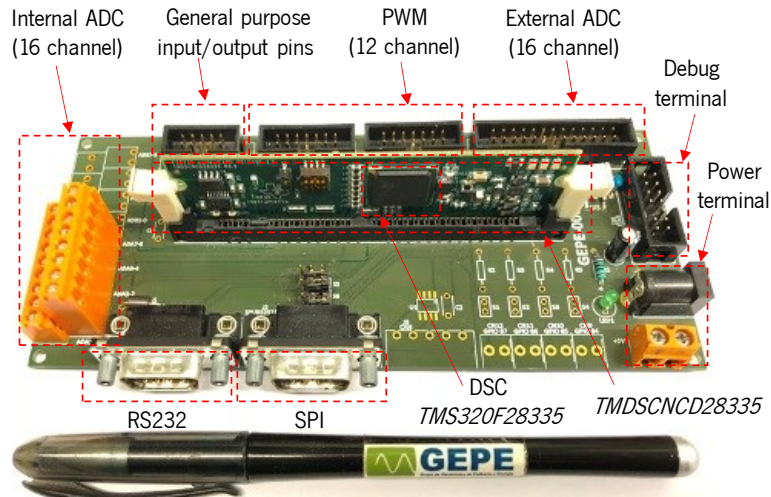


Figure 5.38. Interface board to support the *TMDSCNCD28335* control card.

The control algorithm of the HB-MMC2 RPC system is implemented and uploaded on the DSC, by using the *Code Composer Studio* v5.5.0, which is a tool provided by the *Texas Instruments*, and it enables programming of the microcontroller by using the C++ language. The *Code Composer Studio* user interface is presented in Figure 5.39. This DSC type is chosen considering the number of PWM and ADC channels that are required to switch all the IGBT switching devices (for the PWM), and to acquire all the necessary analogue signals in a digital form (for the ADC). Additional features are the easy programming, the friendly user interface, and the fact that there are many learning resources and numerous example codes, from *Texas Instruments*, available online, which will not imply a long learning process.

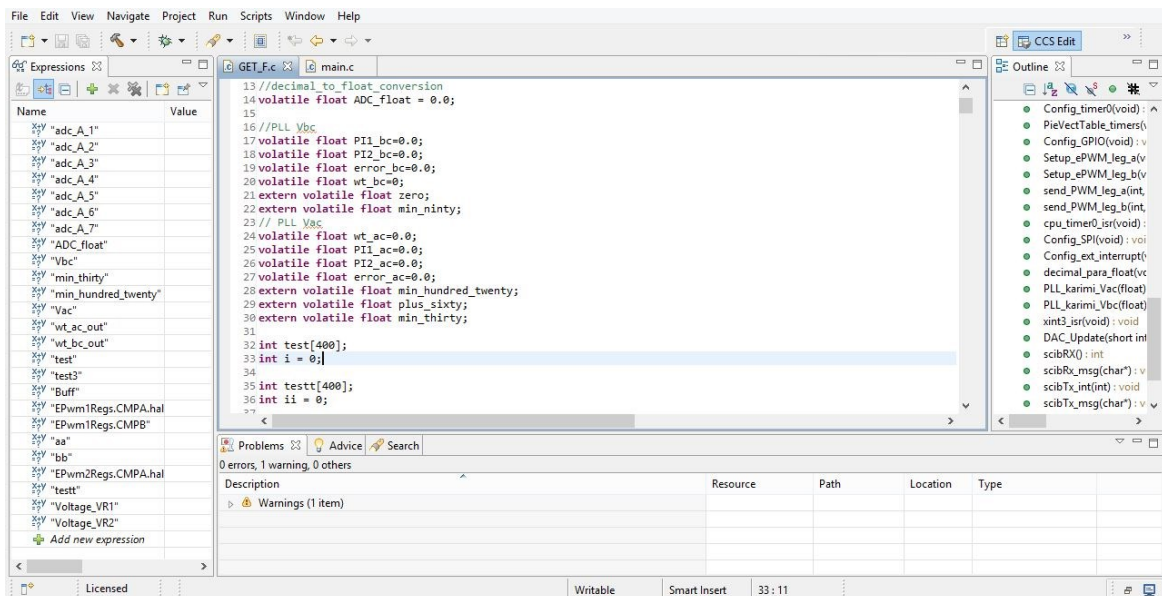


Figure 5.39. User interface of the programming tool *Code Composer Studio* v5.5.0 from *Texas Instruments*.

5.6.2 Sensors

This item presents the sensors used in the HB-MMC2 RPC reduced-scale prototype, namely, the sensors used to measure the associated current and voltage magnitudes, besides the sensors used for the purpose of overcurrent and overvoltage protection.

5.6.2.1. Voltage Sensors

The voltage sensor used in this project was the *CYHVS025A* sensor, manufactured by *ChenYang*. This type of voltage sensor is a Hall effect sensor based on closed-loop and magnetic compensation principles. The *CYHVS025A* can be used for measuring DC and AC voltage waveforms and it has the following advantages: galvanic isolation between the measured voltage and the output signal (2.5 kV RMS); good linearity; good immunity to electromagnetic interference; high bandwidth and voltage measurement up to 500 V [208]. This sensor is mainly used in this Ph.D. thesis to measure the AC grid voltage waveforms, u_x and u_y , which is essential to implement the E-PLL.

Since the output of the *CYHVS025A* sensor is a current signal, the output is less sensitive to the electromagnetic noise. The measurement is performed by using two series-connected measuring resistors, as shown in the voltage sensor PCB that is presented in Figure 5.40. The output terminals of the voltage sensor PCB are connected to the input terminals of the external ADC board, which will be explained in the further items of this chapter.

On the other side, an isolated signal amplifier, *Si8920*, from *Silicon Labs* is used in this Ph.D. thesis to measure the MMC DC-link voltages. This selection is due to the very low power dissipation in this sensor compared to the *CYHVS025A* hall sensor. In other words, the *Si8920* from *Silicon Labs*, works properly at an input current of 100 nA [197], while the *CYHVS025A* hall sensor nominal input current can reach a value between 5 mA–14 mA [208]. The isolated signal amplifier, *Si8920*, is also used for the purpose of overvoltage protection, as presented in the item 5.5.2.

The *Si8920* is a galvanically isolated analogue amplifier, and it provides CMOS isolation between the measured voltage signal and the output (3.75 kV RMS). The differential low-voltage input signal is ideal for measuring the voltage waveforms in a place where a sensor must be isolated from the power system. The output is also a differential analogue signal amplified 16 times. There is a very low signal delay (less than 0.75 μ s) in the *Si8920*, which allows the control system to respond quickly when fault circumstances or any overvoltage conditions occur [197]. The PCB of the *Si8920* sensor also involves the signal conditioning part, and therefore, the PCB of this sensor is described in the item 5.6.4.

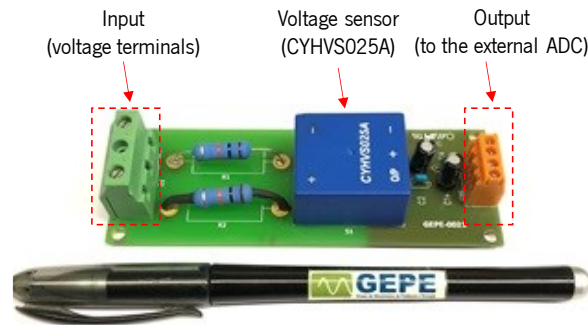


Figure 5.40. PCB of the *CYHVS025A* voltage sensor.

5.6.2.2. Current Sensors

The current sensors used in this Ph.D. thesis are the *LA 100-P* from *LEM* and the *ACS730* from *Allegro*. The *LA 100-P* sensors are important to carry out the measurements of the MMC arm currents and the load section currents. These sensors have a galvanic isolation between the primary and the secondary circuits and they use the closed-loop hall effect technology. The primary nominal RMS current can reach a value up to 100 A, while the measuring range can reach a maximum peak value of 150 A. The secondary nominal RMS current has a value close to 50 mA.

The main advantages of the *LA 100-P* sensor are: good galvanic isolation (up to 2.5 kV), good linearity, high frequency bandwidth (up to 200 kHz) and very good noise immunity [209]. However, filtering capacitors are essential at the input power side. Figure 5.41 presents the PCB of the *LA 100-P* current sensor. The output terminals of this PCB are connected to the input terminals of the external ADC board, as it will be explained in the item 5.6.4. On the other side, the current sensor, *ACS730* from *Allegro*, is only used for the purpose of overcurrent protection, and it has been described in the item 5.5.2. This is due to the wider frequency bandwidth (up to 1 MHz) of the *ACS730*, which makes the response of this sensor much faster and appropriate for the protection application.

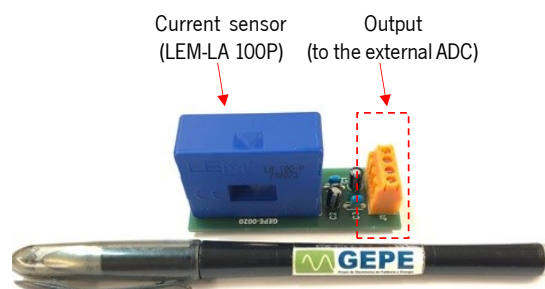


Figure 5.41. PCB of the *LA 100-P* current sensor.

5.6.3 Digital to Analogue Converter

In order to display the unreached control parameters in the real-time domain, which are normally digital parameters resulting from the control calculations in the DSC (such as the compensation current references), DAC is required to perform this transformation. The real-time monitoring of the DSC

internal variables allows checking whether the control system is working properly or not. Figure 5.42 shows a PCB developed and validated in GEPE to perform the DAC transformation by using the DAC TLV5610IC from *Texas Instruments*.

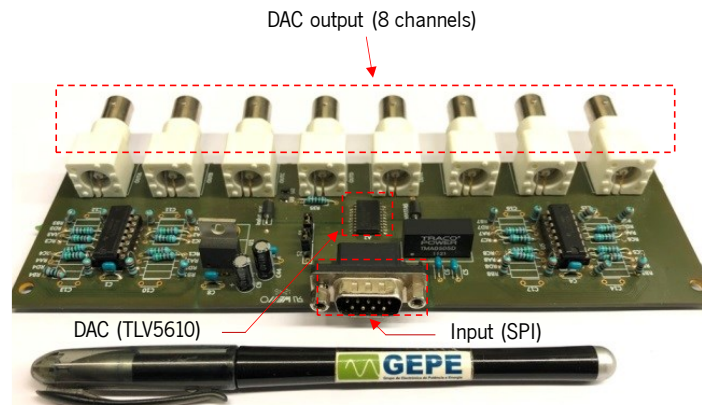


Figure 5.42. Interface PCB between the DSC and the DAC.

The output voltage of the DAC is unipolar and varies between 0.4 V to 2.6 V [210]. However, the PCB contains signal conditioning to adjust the output voltage of the converter to a level between -5 V and 5 V. This DAC has a 12-bits resolution and 8 output channels [210]. These channels can be connected directly to an oscilloscope to monitor any internal digital variable in the DSC. The communication between the DAC and the DSC uses the SPI communication protocol.

5.6.4 Analogue to Digital Converter and Signal Conditioning

This item presents the ADC and signal conditioning PCBs, where usually signal amplification is performed. On the other hand, signal conditioning is important to meet the requirements of the further signal processing steps, which may include voltage signal limiting by using Zener diodes or signal comparators, signal filtering by using active filters to improve the performance and the quality of the signal.

5.6.4.1. Signal Conditioning Board for the External ADC

All the sensors introduced in the control system have analogue output signal, so an ADC is required to convert the analogue output signal to a digital signal. Although the DSC has 16 internal ADC channel, the decision was to use an external ADC IC to perform the analogue-to-digital conversion for the AC signals of voltages and currents, while the internal ADC channels of the DSC were reserved for the DC voltage signals.

Figure 5.43 shows the external ADC and the associated signal conditioning PCB, including the operational amplifiers and the LPF to proceed with the signal conditioning. This PCB contains 8 ADC channels and was developed and validated in GEPE. The used ADC IC is the *MAX1320* from *Maxim*,

with 14-bits of resolution and bipolar input signal of ± 5 V [211]. The internal ADC of the DSC has 12-bits of resolution. Therefore, two steps of the right shift are accomplished to the final binary value to convert the 14-bits resolution to 12-bits. This step is important to equalize the digital binary format of all the control variables in the C code program.

The communication between the signal conditioning PCB for the external ADC and the DSC is performed by using a parallel interface. On the other hand, it is important to refer that, besides the ADC and the signal conditioning components, each ADC channel has its comparator circuit to detect the errors (e.g., in case of overcurrent or overvoltage). In case of error, an isolated signal will be triggered to disconnect the fully controllable power switching devices for better safety and security reasons. However, and due to the implemented overcurrent and overvoltage protection circuit PCB, presented in 5.5.2, the protection circuit (operational comparators) of the signal conditioning PCB for the external ADC is not used in this Ph.D. thesis.

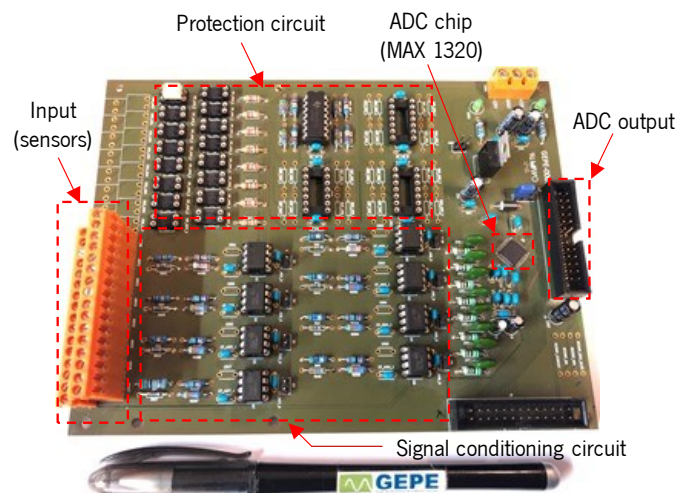


Figure 5.43. Signal conditioning PCB for the external ADC.

5.6.4.2. Signal Conditioning Board for the Internal ADC

The internal ADC channels of the DSC have some limitations, namely, a range of unipolar input values between 0 V and +3 V with 12-bits resolution. Therefore, and due to the unipolar input of the internal ADC channels, the selection was to use these ADC channels for the DC voltage signals, such as the DC-link voltages of the MMC.

Figure 5.44 shows the signal conditioning PCB for the internal ADC, which contains two main parts: the voltage sensors, and the signal conditioning part. This PCB has the capability to process with 10 channels, then, measuring 10 DC signals by using the *Si8920* voltage sensors [197]. In addition, each voltage sensor has its own signal conditioning circuit (channel) to maintain the output signal between 0 V and +3 V, which is the range of the internal ADC. A Zener diode is added at the output of

each channel for the purpose of protection, so the signal cannot reach a value beyond +3 V. The *Si8920* voltage sensors amplify the input voltage (maximum of 0.1 V) to a maximum value of 1.6 V (16 times amplification). The PCB presented in Figure 5.44 is designed and validated under the scope of this Ph.D. thesis.

It is noteworthy to mention, the PCB presented in Figure 5.44 is not appropriate for measuring the AC signals, and it does not have signal comparators to detect the errors. This is unnecessary since there is a protection circuit PCB connected to each MMC SM, which has the ability to actuate the protection in case of any detected errors. The internal ADC and the external ADC are calibrated to have the same sampling frequency of 40 kHz, corresponding to a period of 25 μ s. Therefore, all the calculations in the control loop should be processed during a time-cycle less than 25 μ s.

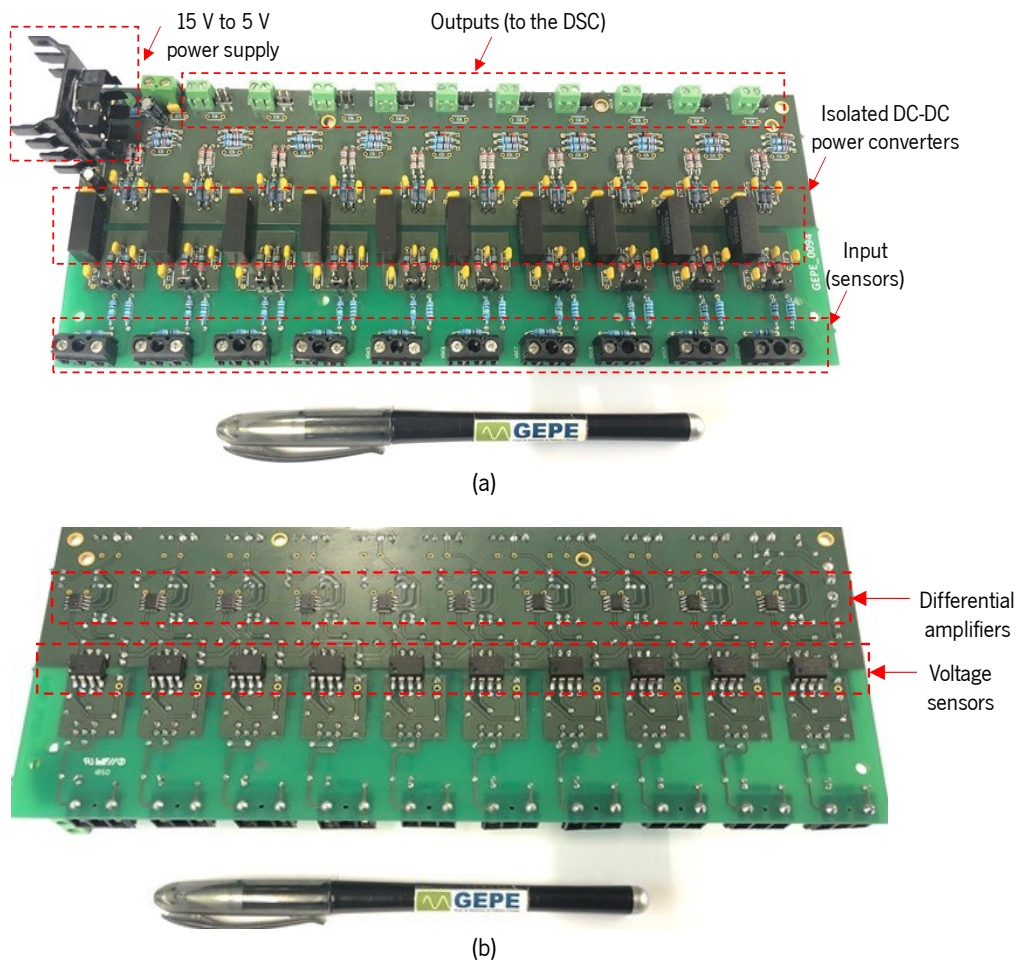


Figure 5.44. Signal conditioning PCB for the internal ADC: (a) Top; (b) Bottom (developed under the scope of this Ph.D. thesis).

On the other hand, differential LPF at the sensor's input and output are required, as shown in Figure 5.45. This gives better signals immunity against high-frequency components. Since the input and output of the *Si8920* are galvanically isolated, DC-DC isolated power supplies are necessary to supply the input and the output of the *Si8920* sensor. The differential output signal of each sensor

after filtering is amplified by using differential amplifiers. This is useful for additional immunity against external noise sources.

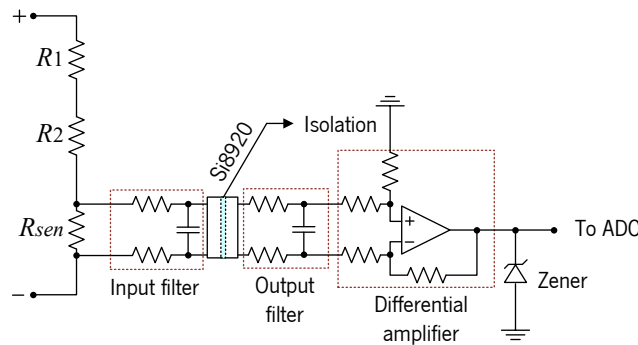


Figure 5.45. Voltage sense application by using *Si8920*, including the signal conditioning.

5.6.5 Command Circuit PCB

This PCB is important to re-enable the PWM channels of the DSC when an error is detected by the protection circuit PCBs. The command circuit PCB main function is to interface between the protection circuit PCB and the driver circuit PCB in the SMs, as shown in the diagram presented in Figure 5.46. There is only one command circuit PCB for the control system that contains numerous logic gates and timers to save the error. One of the logic gates inputs is controlled externally or manually to stop the PWM signals when it is necessary.

There is also an external switch that allows the user to clean the error state after removing the fault origins (reset function). The input and output of this command circuit PCB are isolated from the signal processing parts, as shown in Figure 5.46. This is to keep a safe operation of the other PCBs, and to avoid fault transmission between the PCBs (driver circuit PCBs, protection circuit PCBs and command circuit PCB). As a final conclusion, the PWM signals are transmitted to the drivers when there is no detected error, and when the disable pin is deactivated. Another function of the command circuit PCB is to ensure that, at normal operation conditions and when there is no detected error, all the disable pins of the drivers are grounded to avoid erroneous and undesirable operation due to capacitive noise coupling.

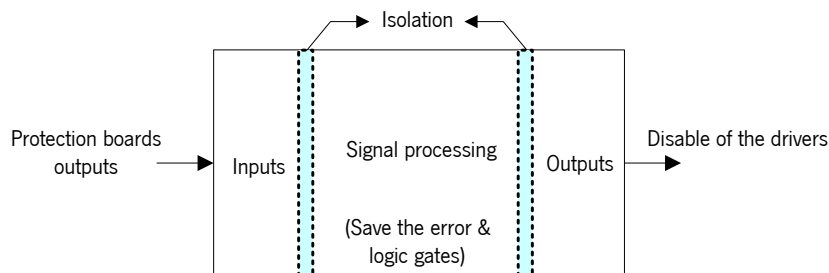


Figure 5.46. Operation principle of the command circuit PCB.

Figure 5.47 shows the command circuit PCB that has been developed and validated in GEPE under the scope of this Ph.D. thesis. The isolation between the inputs and the outputs is a significant concern when designing the command circuit PCB, since most of the response delay in the command circuit PCB is caused by the isolated electronic components, such as the optocouplers. The fault current may rapidly change and increase during some μs , leading to damaging the power switching devices. Therefore, fast protection is required to avoid such situations, and to increase the protection system reliability.

The protection circuit PCBs studied in the item 5.5.2 contain fast voltage and current sensors that quickly respond to fault conditions. Therefore, the design of the command circuit PCB should be aligned with that purpose. In order to achieve the isolation between the inputs and the outputs, optocouplers are used for now, then, it is important to monitor the protection response delay. In this context, Figure 5.48(a) shows that when an error is detected, the protection signal, v_{pr} (in green), should reach to -15 V , then, triggering the drivers disable, $v_{disable}$ (in purple), to reach a value close to $+5\text{ V}$. At that moment, the PWM signals of the top and the bottom IGBTs (in cyan and yellow) should reach a value close to -15 V , then, blocking the switching devices. The experimental results of this case, at no load conditions, are presented in Figure 5.48(a). In this case, the total delay is around $6\ \mu\text{s}$. This is the overall delay that is resulting from sensors, signal processing and optocouplers delay. However, most of this delay is due to the optocoupler devices that have a slow turn-on and turn-off response.

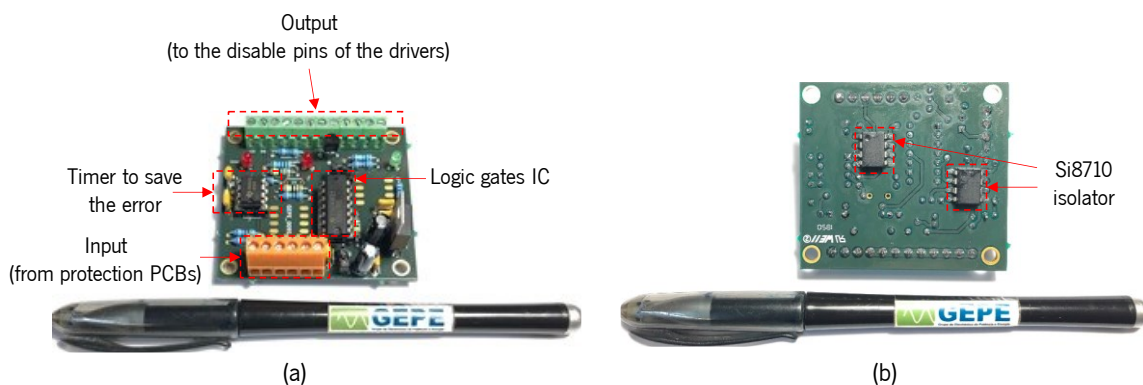


Figure 5.47. Command circuit PCB (developed under the scope of this Ph.D. thesis): (a) Top; (b) Bottom.

The obtained delay time is improper and big enough to damage the electronic components when an error state is detected. This is because during the delay time, one of the top/bottom IGBTs is still switching. Therefore, the optocouplers are substituted by new devices that have LED emulator input, open collector output isolators (*Si8710* from *Silicon labs*). These devices have a faster response and a higher isolation capability than the optocouplers [212]. The results presented in Figure 5.48(b) show a total response delay (from detection, evaluation and actuation) less than $1\ \mu\text{s}$ at no load conditions. This inevitable delay arises from several factors related to hardware propagation, such as sensor lags in the protection circuit PCB, signal processing delay in the command circuit PCB, and the internal

disable delay of the *Si8244* in the driver circuit PCB. It is noteworthy to remember that, Figure 5.13(b) shows the internal disable delay of the *Si8244* IC and Figure 5.30 shows the total response delay under loading conditions. The total delay in that case is close to 3 μs .

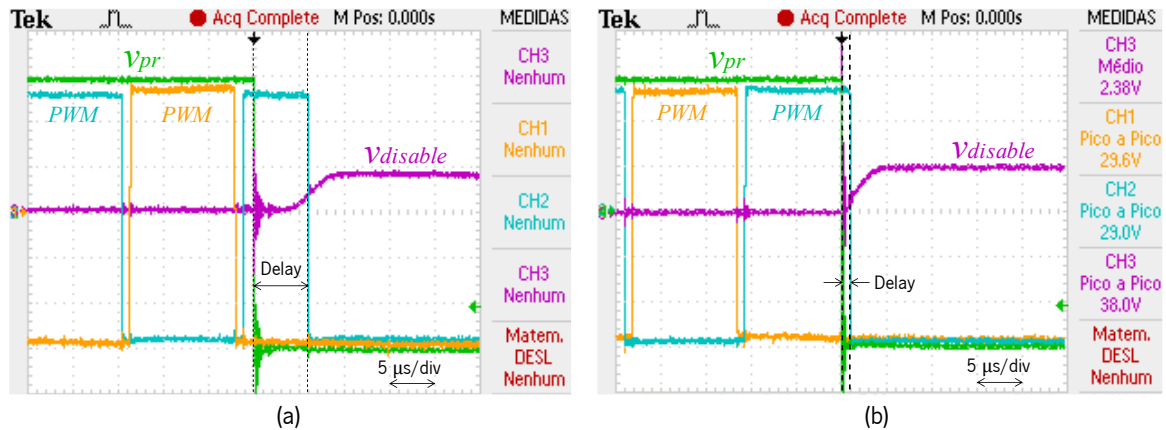


Figure 5.48. The overall delay at no load conditions: (a) When using normal optocouplers; (b) When using *Si8710* isolator from *Silicon labs*; (v_{pr} , $v_{disable}$, PWM: 5 V/div).

5.6.6 PWM Adapter PCB

This PCB has two main functions: the first is to change the plug from a flexible flat cable to a DB9 connector to match the driver circuit PCBs input. The second function is to select the GPIO pins that are in charge to trigger the IGBT T_3 (more details are in Figure 5.23 and Figure 5.15), then, discharging the SM capacitors when an order is given by the DSC. More information about the sequence of PWM registers implemented in the DSC can be found in [207], [213]. Figure 5.49 shows the PWM adapter PCB.

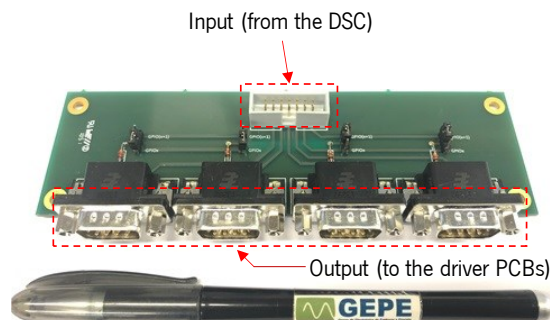


Figure 5.49. PWM PCB adapter (developed under the scope of this Ph.D. thesis).

5.7 Conclusion

This chapter has discussed the modular multilevel converter (MMC) parameters design, and the associated supplementary power equipment (e.g., V/V transformer, auto-transformers, filter inductors) used to obtain a reduced-scale traction power system laboratory workbench. In addition, the simulation model and simulation results of the reduced-scale simplified rail power conditioner based on half-bridge indirect modular multilevel converter (HB-MMC2 RPC), using the *PSIM V.9.1* simulation tool, have also

been presented and discussed. *PSIM* tool was useful to test the control algorithm in *C* code environment.

Moreover, this chapter presented the development process of the HB-MMC2 RPC as a reduced-scale prototype. In this context, the design process of the MMC submodule (SM) is presented, including driver printed circuit board (PCB), protection circuit PCB and power circuit PCB, where each SM is composed by the above-mentioned PCBs. In addition, experimental results are presented to validate each PCB of the driver circuit, protection circuit and power circuit, validating all individual SM before the full implementation of the MMC.

Experimental results of the driver circuit PCB presented the possibility of unipolar or bipolar pulse-width modulation (PWM) pulses. This was important to have a faster performance of the switching devices when using the bipolar PWM. On the other hand, the protection circuit PCB experimental results confirmed the ability to protect against overcurrent and overvoltage faults. The implemented protection was at the SM level and not at the MMC level, which improves the reliability of the implemented protection system. Moreover, experimental results of the power circuit PCB have also been presented at parameters close to the nominal ones, and then, experimental validation of one SM was accomplished.

A detailed explanation of the control system hardware has been presented, including the central control unit, sensors, signal conditioning PCBs, command circuit PCB, PWM adapter PCB, digital-to-analogue and analogue-to-digital converters. As a conclusion, this chapter confirmed the experimental validation of one SM and the associated control system hardware. The next chapter will present the experimental results of the reduced-scale HB-MMC2 RPC system.

Chapter 6

Experimental Results of a Simplified Rail Power Conditioner Based on Modular Multilevel Converter

6.1 Introduction

The experimental validation of all modular multilevel converter (MMC) submodules (SMs), including the driver printed circuit board (PCB), the protection circuit PCB and the power circuit PCB, has been presented in Chapter 5. In this context, this chapter presents the experimental results of the simplified rail power conditioner (RPC) based on half-bridge indirect modular multilevel converter (HB-MMC2 RPC). Figure 6.1 shows the MMC workbench implemented under the scope of this Ph.D. thesis at the University of Minho, within the Group of Power Electronics and Energy (GEPE). The workbench also includes the control system hardware, isolated-channels oscilloscopes, and spare SM to be used in case of failure of any MMC SM. There is a computer device that allows the user interface with the digital signal controller (DSC). The experimental results presented throughout this chapter were obtained using the *TPS2000B* series oscilloscope from *Tektronix* [191]. In addition, a Fluke 434 Power Quality Analyzer was used to measure the total harmonic distortion (THD), the ratio of negative sequence component (NSC), and to show the frequency spectrum of the three-phase currents [214]. It should be noted that some waveforms, as for example those of reference currents, and the angle of the voltage waveform (sawtooth waveform) were obtained using the digital-to-analog converter (DAC), which is connected to the DSC.

The experimental validation of the reduced-scale prototype consists of the following steps:

- Testing the enhanced phase-locked loop (E-PLL) to acquire the signals of the load section voltages, u_x and u_y ;
- Testing the moving average low-pass filter (LPF) to extract the DC current component from the load section currents;
- Generation of the compensation currents reference signals in the DSC;
- Testing of one MMC leg/phase in an open-loop control;
- Testing of one MMC leg/phase in a closed-loop control to operate as a single-phase DC/AC converter;

- Testing two MMC legs/phases in a closed-loop control to operate as two-phase DC/AC converter;
- Testing the MMC to operate as a HB-MMC2 RPC system for the purpose of power quality improvement. In this case, the output terminals of the MMC are connected to the load section voltages (the output of the V/V power transformer).

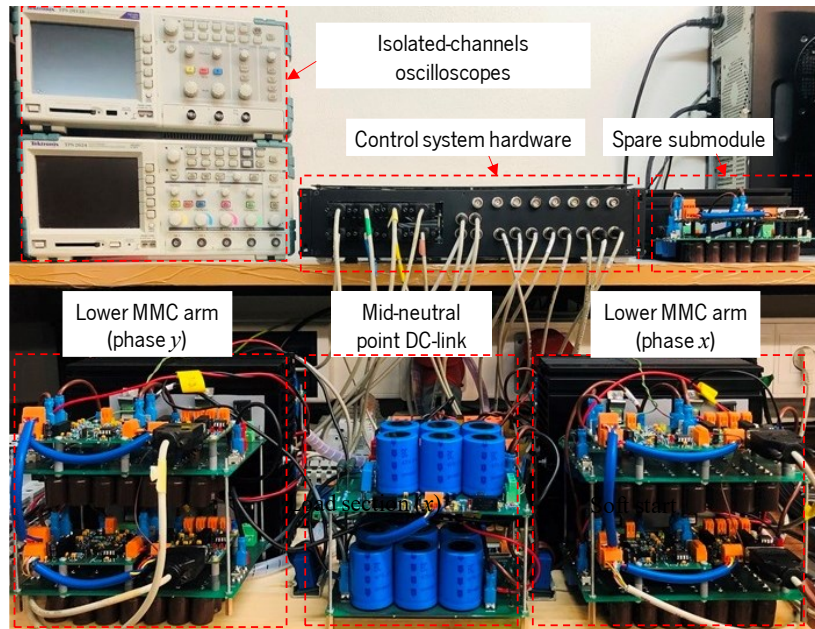


Figure 6.1. MMC workbench developed in GEPE.

6.2 Enhanced Phase-locked Loop (E-PLL) and Moving Average Low-Pass Filter (LPF)

Two single-phase E-PLL (one for each V/V secondary phase voltage) are applied and programmed in the DSC to allow generating the reference waveforms. The E-PLL algorithm is applied in the C programming language, with a sampling frequency of 40 kHz, where the implemented E-PLL in this Ph.D. thesis is proposed by Karimi-Ghartemani et al. [215]. The application of E-PLL is a key step to calculate the references of the compensation currents. It assumes that the fundamental frequency of the input signal is fixed, with performance being compromised when frequency variations occur. Figure 6.2 shows the experimental results of the E-PLL, where the angle of the phase x voltage, θ_x (obtained from the DAC) is in phase with the sinewave voltage of phase x . On the other hand, the angle of the phase y voltage, θ_y (obtained from the DAC) is in phase with the sinewave voltage of phase y . The angle waveforms have a shape similar to a sawtooth with a fixed frequency. It is worthy to mention, the E-PLL output signals, θ_x and θ_y , do not present a significant distortion, which is important to generate the correct references, then E-PLL presents a good response. Consequently, it is possible to determine the frequency and phase angles of the fundamental component of the V/V transformer secondary voltages, u_x and u_y . As shown in Figure 6.2, there are 60° out-of-phase between the V/V transformer secondary voltages.

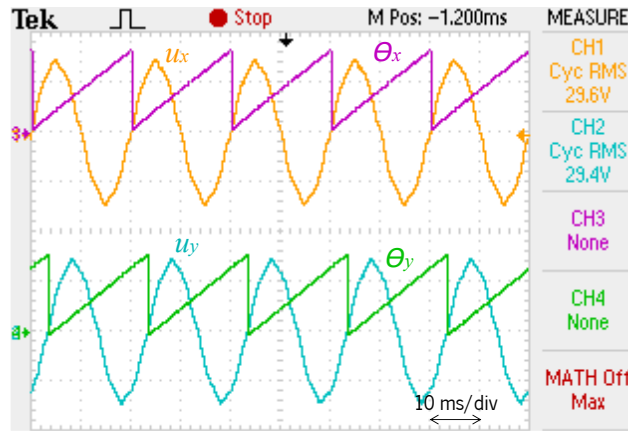


Figure 6.2. Enhanced phase-locked loop (E-PLL) results: Phase x voltage (u_x : 30 V/div); Phase y voltage (u_y : 30 V/div); Phase x voltage angle (θ_x : 10 ms \leftrightarrow 180°); Phase y voltage angle (θ_y : 10 ms \leftrightarrow 180°).

The moving average is the most common LPF used in the digital signal controller (DSC) due to its simple implementation. As the name refers, the moving average LPF operates by averaging a number of samples from the input signal, v_i , to produce each sample in the output signal, v_o , as presented in (6.1). Consequently, it smooths an array of sampled signal by taking M samples of input at a time, making the average of those M samples and produces a single output signal. The number of samples for the ideal digital implementation, M , is the ratio between the time cycle or the period of the processed signal T (it is 20 ms for a signal with 50 Hz frequency) and the analogue-to-digital converter (ADC) sampling periods T_s (it is 25 μ s for a sampling frequency of 40 kHz). Accordingly, the optimal number of samples, M , is equal to 800 samples [216].

$$v_o[k] = \frac{1}{M} \sum_{j=0}^{M-1} v_i[k-j] ; M = \frac{T}{T_s} \quad (6.1)$$

The filter presents a definite amount of delay due to the computation time. Therefore, as the number of samples is higher, the involved delay is also getting higher but the noise in the output signal becomes lower. On the other hand, this type of filters is sufficiently good for time domain signals as it provides the lowest noise possible for a given signal. However, this good performance in the time domain results in a poor performance in the frequency domain, providing limited ability to separate one band of frequencies from another [216].

Figure 6.3 shows the results of the digital moving average LPF when using 200 samples. The main objective is to extract the DC component from the equation (6.2) to implement the control algorithm presented in the Chapter 4, Figure 4.48. In that case, the output signal i_{LPF} contains high-voltage ripples. However, these ripples are getting lower when increasing the number to 600 samples, as shown in Figure 6.4. By adopting the optimal number of samples (800 samples) according to the used sampling frequency (40 kHz), the output signal of the moving average LPF i_{LPF} is almost constant, and

it does not show any voltage ripples, as shown in Figure 6.5. It is worthy to mention, the output signal of the moving average LPF is acquired by using the DAC.

$$I_P = \left[i_{Lx} \sin\left(\omega t - \frac{\pi}{6}\right) \right] + \left[i_{Ly} \sin\left(\omega t - \frac{\pi}{2}\right) \right] \quad (6.2)$$

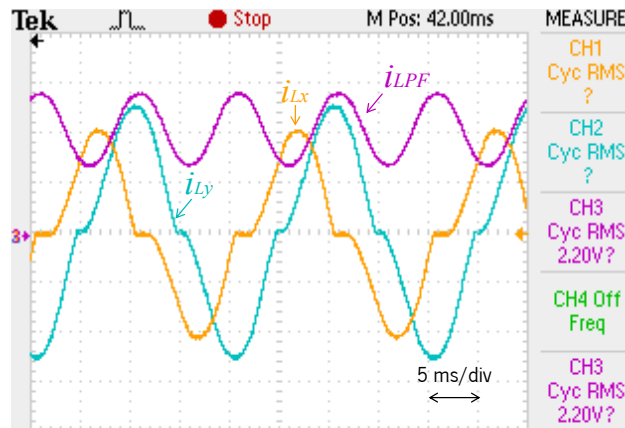


Figure 6.3. Results of the digital moving average LPF at $M = 200$ samples: Load section x current (i_{Lx} : 5 A/div); Load section y current (i_{Ly} : 5 A/div); Moving average LPF output signal (i_{LPF} : 5 A/div).

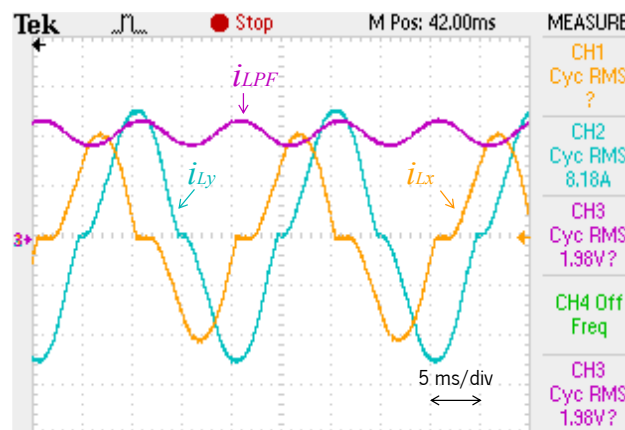


Figure 6.4. Results of the digital moving average LPF at $M = 600$ samples: Load section x current (i_{Lx} : 5 A/div); Load section y current (i_{Ly} : 5 A/div); Moving average LPF output signal (i_{LPF} : 5 A/div).

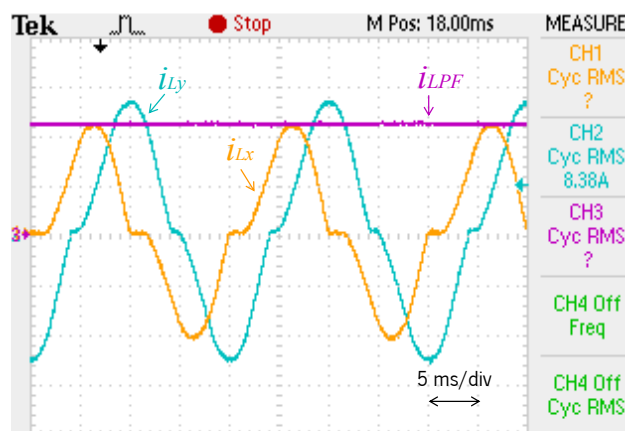


Figure 6.5. Results of the digital moving average LPF at $M = 800$ samples: Load section x current (i_{Lx} : 5 A/div); Load section y current (i_{Ly} : 5 A/div); Moving average LPF output signal (i_{LPF} : 5 A/div).

6.3 Testing One MMC Leg/Phase Using an Open-loop Control

This test is important to study the performance of one MMC leg/phase when several cascade-connected SMs are commutating. In this context, four SMs are used, as presented in Figure 6.6, and the capacitor of each SM is connected to a DC voltage source to maintain a constant voltage across each of the SM capacitors. A sinusoidal waveform is used for the modulation. However, using one MMC leg is not sufficient to have an AC output voltage, then another MMC leg or mid-neutral point capacitors should be used to create a neutral point. Therefore, the output voltage of one MMC leg has a positive average voltage, as presented in Figure 6.7. The parameters of this experimental test are presented in Table 6.1. The SMs in one arm are switching collaboratively. In other words, the pulse width modulation (PWM) carriers are shifted 180 electrical degrees (360° divided by the number of SMs in one MMC arm).

Table 6.1. Parameters of testing one MMC leg/phase in an open-loop control.

Parameters	Symbols	Values
Filter inductance of the arm	L_{xu}, L_{xl}	1.6 mH
Capacitance of the SM capacitor	C_{SM}	987 μ F
SM voltage	V_{SM}	20 V
Load resistor	R	24 Ω
PWM SM switching frequency	f_{isw}	40 kHz
Modulating signal frequency	f	50 Hz
Highest / Lowest duty cycle	-	0.92 / 0.08

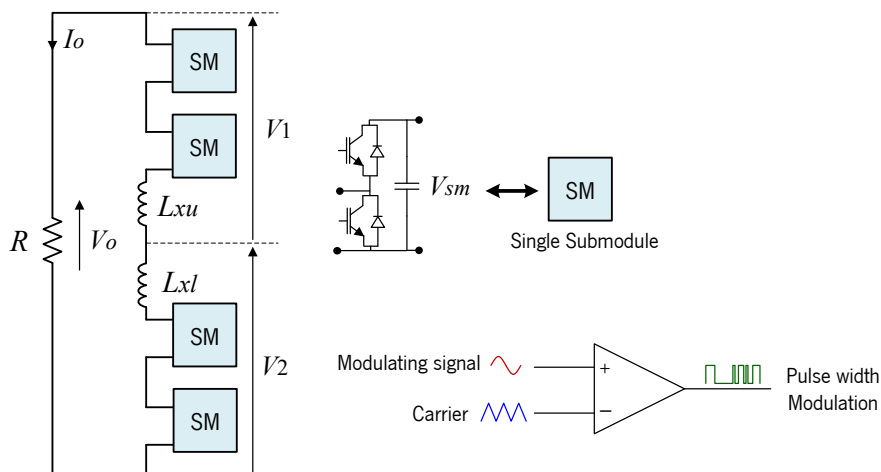


Figure 6.6. Testing of one MMC leg/phase in an open-loop control.

The main objective of this experimental test is to detect whether the MMC leg/phase is able to modulate a sinusoidal waveform. In the ideal case, the upper and the lower arm voltages, v_1 and v_2 , can vary between (V_{sm} and $2V_{sm}$). However, and as presented in Figure 6.7, the peak value of the upper and

the lower arm voltages is lower than $2V_{sm}$ since the peak value of the modulating signal is lower than the value of $2V_{sm}$. In addition, this experimental test gives an idea about the voltage drop in the MMC leg/phase, which is the voltage drop across the insulated-gate bipolar transistor (IGBT) switching devices and the MMC filter inductors. The output voltage of the MMC leg (the voltage across the load) is equal to $v_o = v_1 + v_2$, which is a sinusoidal waveform with a vertical offset equals to the peak value of the upper or the lower arm voltages (v_1 or v_2).

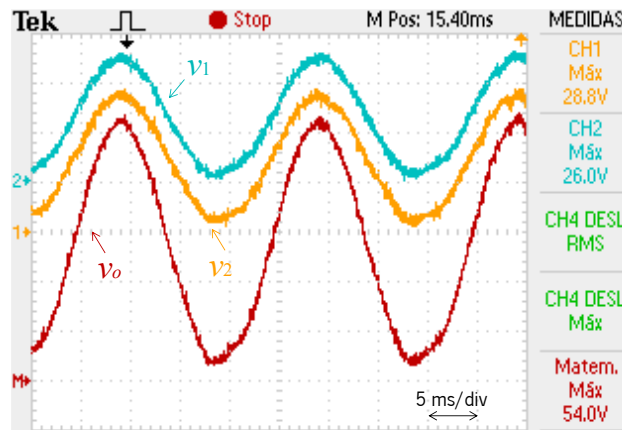


Figure 6.7. Testing of one MMC leg/phase in an open-loop control experimental results: Output voltage (v_o : 10 V/div); Upper arm voltage (v_1 : 10 V/div); Lower arm voltage (v_2 : 10 V/div).

6.4 Testing One MMC Leg/Phase Using a Closed-loop Control

The main objective of this experimental test is to show the performance of the MMC leg averaging voltage control, and the MMC SM individual voltage control (presented in the Chapter 4, Figure 4.71(a) and Figure 4.71(c). The MMC arm averaging voltage control, presented in Figure 4.71(b), is not implemented since the MMC leg averaging voltage control and the MMC SM individual voltage control are quite sufficient to achieve the voltage balance in the SM voltages.

In this test, one of the MMC legs/phases is controlled to output a significant root mean square (RMS) value of current close to 2 A. In this context, a purely resistive load of 9Ω is connected to the MMC output terminals. However, and in order to obtain a neutral point, two capacitors with a mid-neutral point are supplied with a DC voltage of 60 V for each capacitor, as shown in Figure 6.8. For that purpose, two diodes and an adjustable auto-transformer are introduced.

Although the using of an external power source to supply the MMC main DC-link, two proportional-integral (PI) controllers are responsible to achieve the voltage balance between the main DC-link capacitors. Otherwise, if the DC voltage across one of the main DC-link capacitors is much higher than the output voltage of the adjustable auto-transformer, this may damage the diodes due to the high applied blocking voltage. Table 6.2 presents the main parameters of this experimental test.

Two current sensors are dedicated to measuring the currents in the MMC arms, i_{rxu} and i_{rxl} , where subtracting the lower arm current, i_{rxl} , from the upper arm current, i_{rxu} , gives the output current of i_{rx} . Then, PI controller is dedicated to correcting the error between the actual output current of i_{rx} and the reference current. Two PI controllers are employed to achieve the averaging voltage balancing control and the circulating current control, as presented in Chapter 4, Figure 4.71(a). In addition, proportional controllers are used to achieve the individual voltage balancing control for each SM, as presented in Chapter 4, Figure 4.71(c).

Table 6.2. Parameters of testing one MMC leg/phase using a closed-loop control.

Parameters	Symbols	Values
Filter inductance of the arm	L_{xu}, L_{xl}	1.6 mH
Capacitance of the SM capacitor	C_{SM}	987 μ F
Capacitance of the Main DC-link capacitors	$C_{dca} = C_{dcb}$	2820 μ F
SM voltage	V_{SM}	60 V
Main DC-link voltage	$V_{dca} + V_{dcb}$	120 V
Load resistor	R	9 Ω
PWM SM switching frequency	f_{isw}	40 kHz
Modulating signal frequency	f	50 Hz
Highest / Lowest duty cycle	-	0.92 / 0.08

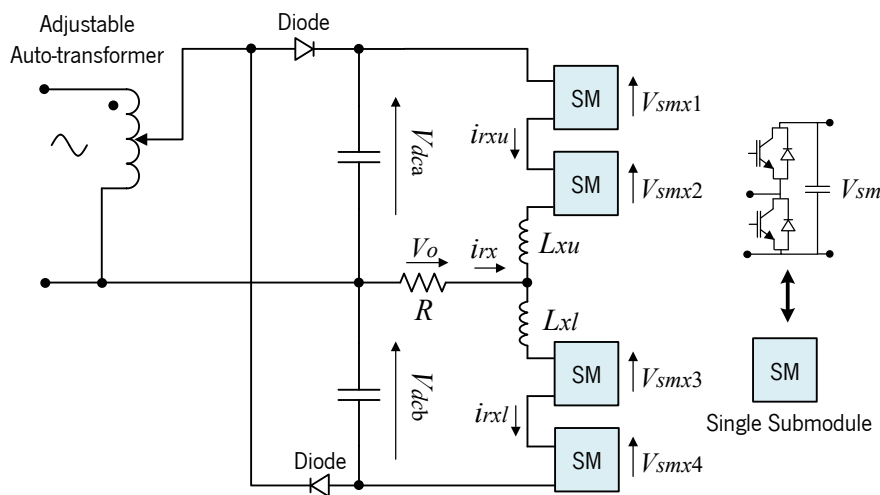


Figure 6.8. Test of one MMC leg/phase using a closed-loop control.

Figure 6.9 shows the voltage waveforms of the MMC SMs before commutation. Each capacitor of the main DC-link is pre-charged to a value close to 60 V, then, each SM capacitor will be pre-charged to a value close to 30 V. The voltages, in that case, are constant without oscillations. On the other hand, Figure 6.10 shows the same voltage waveforms after commutation. In that case, the SM voltages are balanced, and each SM voltage value is around 60 V. However, the lower arm SMs have a DC voltage value higher than the one of the upper arm SMs. This is due to the voltage drop across the MMC filter

inductors and the associated resistors, bearing in mind that, the filter inductors are not ideally identical. The results presented in Figure 6.10 confirm the effectiveness of the averaging and the individual voltage balancing control presented in the Chapter 4, Figure 4.71(a) and Figure 4.71(c), respectively.

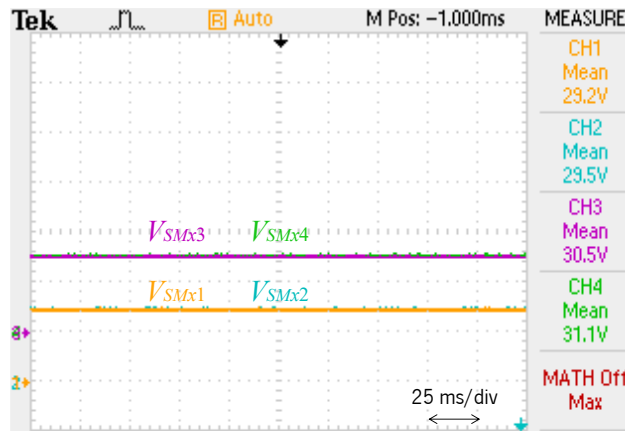


Figure 6.9. MMC SM voltages when testing of one MMC leg/phase without commutation: SM1 voltage (V_{SMx1} : 20 V/div); SM2 voltage (V_{SMx2} : 20 V/div); SM3 voltage (V_{SMx3} : 20 V/div); SM4 voltage (V_{SMx4} : 20 V/div).

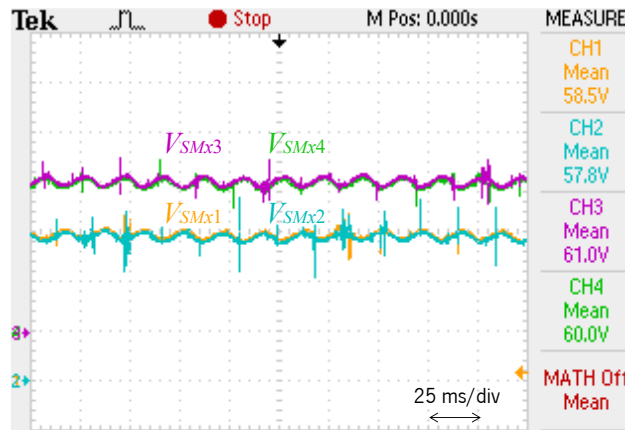


Figure 6.10. MMC SM voltages when testing of one MMC leg/phase with commutation: SM1 voltage (V_{SMx1} : 20 V/div); SM2 voltage (V_{SMx2} : 20 V/div); SM3 voltage (V_{SMx3} : 20 V/div); SM4 voltage (V_{SMx4} : 20 V/div).

Due to the external power supply and the main DC-link voltage control, presented in Chapter 4, Figure 4.70, Figure 6.11 shows balanced main DC-link voltages, V_{dca} and V_{dcb} . The output current of i_{rx} is in phase with its reference i_{ref} , and it has an RMS value close to 2 A as required. It is noteworthy to mention that, the signal i_{ref} is the one calculated in the DSC, then DAC is used to acquire, i_{ref} waveform.

Figure 6.12 shows the upper arm current i_{rxu} , and the lower arm current i_{rxl} of the MMC leg/phase. In addition, the synthesized output current of the MMC leg/phase i_{rx} , is presented in Figure 6.12. Due to the fact that the output current of the MMC leg/phase is resulting from subtracting the lower arm current component from the upper arm current component, the output current of the MMC leg contains lower noise and distortion than the currents of the MMC arms. On the other hand, the currents of the arms have mainly DC components, fundamental frequency current components, and even-order

harmonics that circulate in the main DC-link and the MMC leg. The even-order components, besides the DC current component, do not affect the quality of the MMC output current, but they are important to maintain a balanced voltage between the MMC SMs.

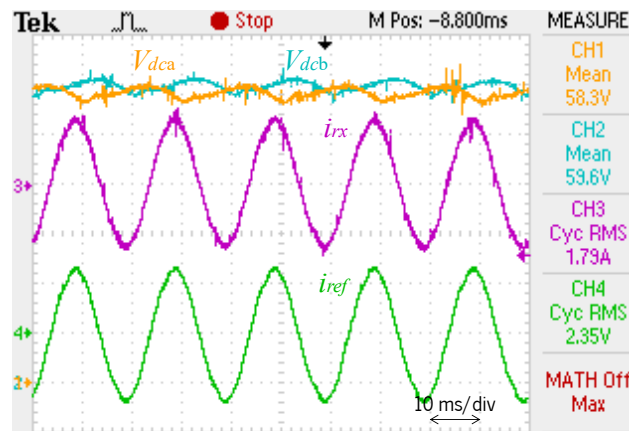


Figure 6.11. Testing of one MMC leg/phase in a closed-loop control: DC-link voltage of the upper capacitor (V_{dca} : 10 V/div); DC-link voltage of the lower capacitor (V_{dcb} : 10 V/div); Reference current waveform (i_{ref} : 2 A/div); Output current waveform (i_{rx} : 2 A/div).

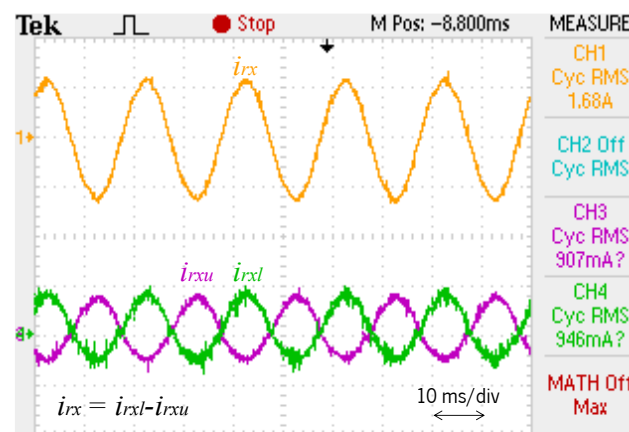


Figure 6.12. Testing of one MMC leg/phase in a closed-loop control: MMC leg/phase output current (i_{rx} : 2 A/div); Upper arm current (i_{rxu} : 2 A/div); Lower arm current (i_{rxl} : 2 A/div).

6.5 Testing Two MMC Legs/Phases Using a Closed-loop Control

The main objective of this experimental test is to study the MMC performance when inserting another leg/phase with additional four SMs. For that purpose, two identical resistive loads are connected between the terminals of each MMC leg/phase and the DC-link capacitors mid-neutral point. The nomenclatures of phase x and phase y are used to indicate the MMC legs/phases, as shown in Figure 6.13. In addition, the evaluation of the MMC leg averaging voltage control and the SM individual voltage balancing control, presented in Figure 4.71(a) and Figure 4.71(c), respectively, is important to validate the MMC control algorithm when all of the SMs are under operation.

In this experimental test, MMC phases are controlled to synthesize two-phase currents, with 120° out-of-phase, and with an RMS value close to 2 A. Two capacitors with a mid-neutral point are supplied

with a DC voltage of 60 V for each capacitor to create a neutral point, as shown in Figure 6.13. For that purpose, two diodes and an adjustable auto-transformer are employed. The parameters presented in Table 6.2 are used in this experimental test as well.

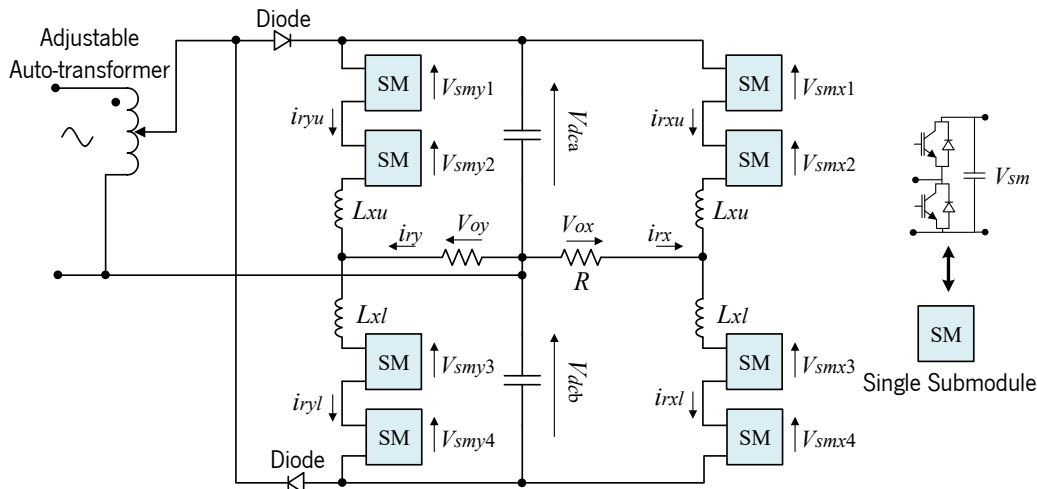


Figure 6.13. Testing two MMC legs/phases using a closed-loop control.

Four current sensors are dedicated to measuring the arm currents in the MMC, i_{rxu} , i_{rxl} , i_{ryu} and i_{ryl} , where subtracting the lower arm current from the upper arm current, gives the output current of the MMC leg/phase. Then, two PI controllers are dedicated to correcting the error between the actual output current and the reference current. On the other hand, two PI controllers are employed to achieve the leg averaging voltage balancing control and the circulating current control for each MMC leg/phase, as presented in the Chapter 4, Figure 4.71(a). In addition to that, proportional controllers are used to proceed with the individual voltage balancing control for each SM, as presented in the Chapter 4, Figure 4.71(c).

Figure 6.14 and Figure 6.15 show the SM voltages under operation (during the commutation) of phase x and phase y , respectively. In that case, the voltages are balanced, and each SM voltage is around its reference value of 60 V. On the other hand, and due to the topology of the half-bridge SM, the voltage ripples have a frequency close to the fundamental frequency of 50 Hz, and the peak-to-peak voltage ripple ratio is close to 8% of the total SM DC-link voltage. The results presented in Figure 6.14 and Figure 6.15 confirm the effectiveness of the leg averaging voltage control and the individual voltage balancing control presented in Chapter 4, Figure 4.71(a) and Figure 4.71(c), respectively. It is worthy to mention, the arm averaging voltage control presented in Figure 4.71(b) is not implemented in this experimental test, since the leg averaging voltage control and the individual voltage balancing control are quite enough to achieve the voltage balance between the MMC SMs.

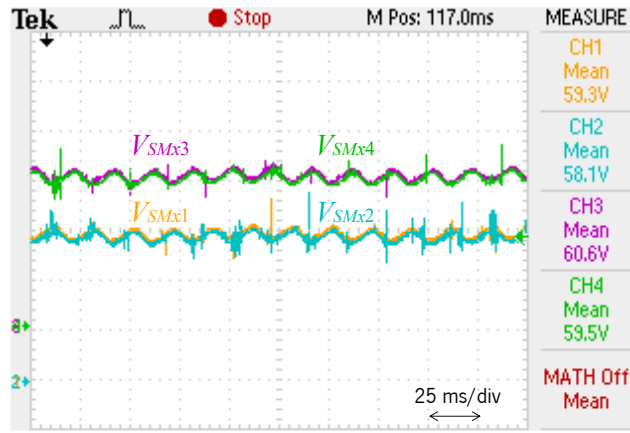


Figure 6.14. SM voltages of phase x under operation, when testing two MMC legs/phases: SM1 voltage (V_{SMx1} : 20 V/div); SM2 voltage (V_{SMx2} : 20 V/div); SM3 voltage (V_{SMx3} : 20 V/div); SM4 voltage (V_{SMx4} : 20 V/div).

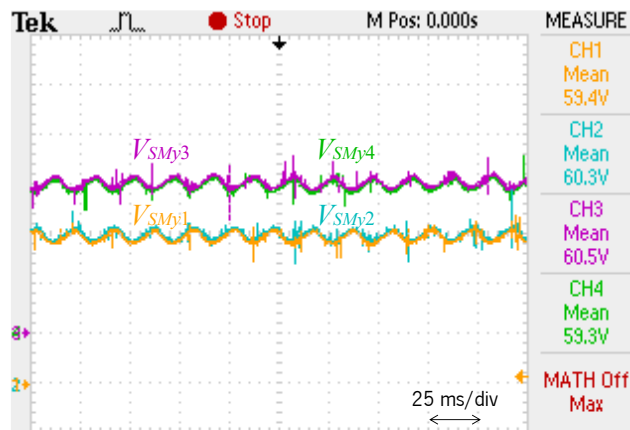


Figure 6.15. SM voltages of phase y under operation, when testing two MMC legs/phases: SM1 voltage (V_{SMy1} : 20 V/div); SM2 voltage (V_{SMy2} : 20 V/div); SM3 voltage (V_{SMy3} : 20 V/div); SM4 voltage (V_{SMy4} : 20 V/div).

The reference current waveforms are calculated in the DSC to obtain two-phase currents, with 120° out-of-phase, and an RMS value close to 2 A. In this context, Figure 6.16 presents the synthesized phase x and phase y output current waveforms of i_{rx} and i_{ry} , which have similar RMS current value and 120° out-of-phase. The currents are sinusoidal and have low harmonic contents due to the fact that phase x and phase y output currents are resulting from subtracting the lower MMC arm current from the upper MMC arm current. Then, if there are harmonic contents that are common to both arm currents, they will be canceled and do not contribute to the MMC output currents. The obtained results in Figure 6.16 and Figure 6.17 are introduced considering the values of filter inductors and SM switching frequency, as presented in Table 6.2.

Figure 6.17 shows the upper arm current i_{rxu} , and the lower arm current i_{rxl} , of the phase x . It also presents the upper arm current i_{ryu} , and the lower arm current i_{ryl} , of the phase y . These currents have mainly fundamental frequency current component which mainly composes the MMC output currents, DC component which is vital for the SM voltage balancing control and the main DC-link voltage control, and even-order harmonics that circulate between the MMC legs/phases. The even-order harmonics besides the DC current component do not affect the quality of the MMC output currents.

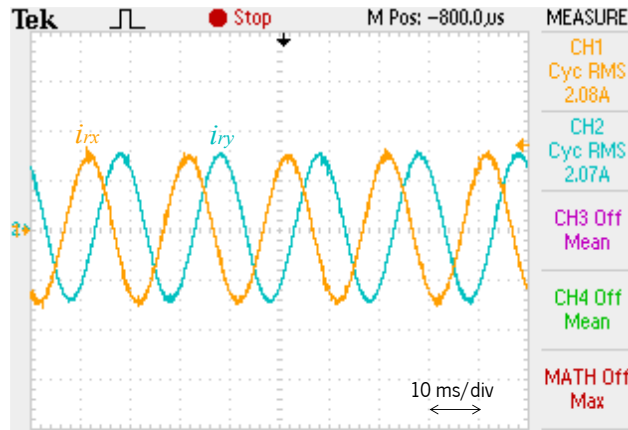


Figure 6.16. Testing two MMC legs/phases using a closed-loop control: Phase x output current (i_{rx} : 2 A/div); Phase y output current (i_{ry} : 2 A/div).

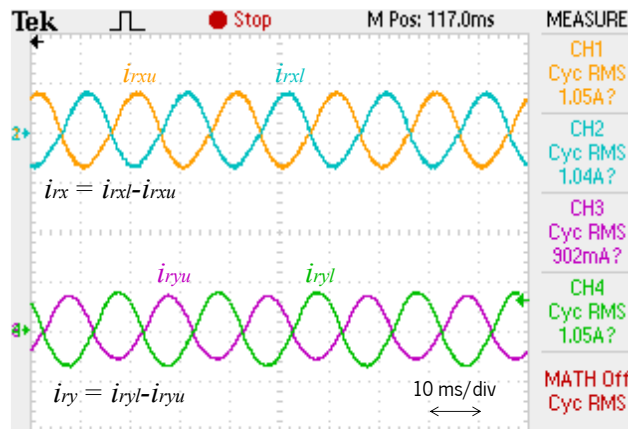


Figure 6.17. Testing two MMC legs/phases using a closed-loop control: Phase x upper and lower arm currents (i_{rxu} , i_{rxl} : 2 A/div); Phase y upper and lower arm currents (i_{ryu} , i_{ryl} : 2 A/div).

6.6 Experimental Results of the HB-MMC2 RPC

This item presents the experimental results of the reduced-scale HB-MMC2 RPC. Figure 6.18 shows the experimental setup scheme, which consists of the supplementary power equipment (auto-transformers, V/V transformer and full-bridge rectifiers) and the HB-MMC2 RPC. For that purpose, full-bridge rectifiers with filtering capacitors are used to create harmonic contents and currents imbalance at the three-phase public power grid. The parameters used in this experimental validation are presented in Table 6.3, where load section y active power is selected to be 150% the active power of the load section x . Therefore, and as presented in Table 6.3, the value of the resistor R_{x1} has 150% the value of the resistor R_{y1} . The resistors of R_{x2} and R_{y2} , have a high value since their main function is to discharge the filtering capacitors after disconnecting the load power resistors, R_{x1} and R_{y1} , by using contactors. On the other hand, the HB-MMC2 RPC consists of eight half-bridge SMs, in which each MMC leg or phase has four SMs. The MMC parameters, such as capacitance of the SM capacitor, capacitance of the main DC-link capacitor, MMC leg filter inductors, and the PWM switching frequency, are presented in Table 6.3. Two case studies are presented in this experimental test: The

first case study is when the load section y active power is 150% of the load section x active power, whereas, the second case study is when only load section y is loaded.

Table 6.3. Experimental parameters of the HB-MMC2 RPC.

Parameters	Symbols	Values
Phase x and phase y RMS voltage	u_x, u_y	40 V
SM voltage	V_{SM}	80 V
MMC main DC-link voltage	$V_{dca} + V_{dcb}$	160 V
Filter inductance of the arm	$L_{xu}, L_{xl}, L_{yu}, L_{yl}$	1.6 mH
Load section inductance	L_x, L_y	5 mH
Load resistor (section x)	R_{x1}	6.5 Ω
Load resistor (section y)	R_{y1}	4.34 Ω
Resistors to discharge the capacitors	R_{x2}, R_{y2}	33 k Ω
Capacitance of the filtering capacitors	C_x, C_y	470 μF
Capacitance of the SM capacitor	C_{SM}	987 μF
Capacitance of the main DC-link capacitors	$C_{dca} = C_{dcb}$	2820 μF
PWM SM switching frequency	f_{isw}	40 kHz
Modulating signal frequency	f	50 Hz
Highest / Lowest duty cycle	–	0.92 / 0.08

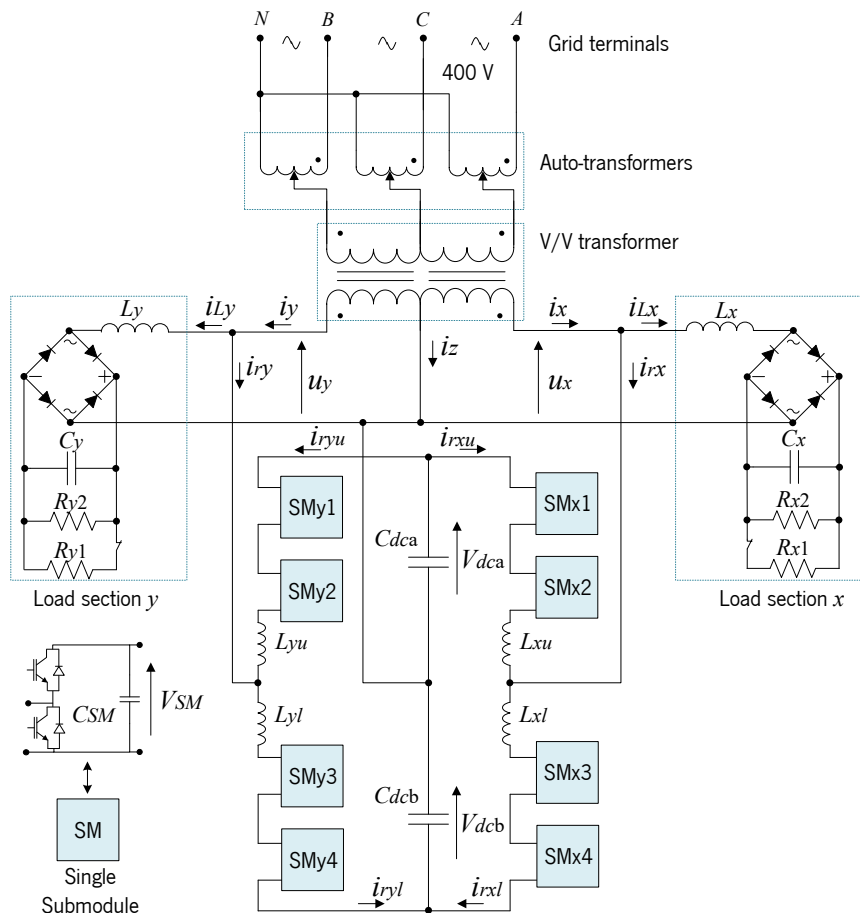


Figure 6.18. Schematic of the HB-MMC2 RPC experimental setup.

6.6.1 Experimental Results when Both Load Sections are Loaded

This item presents the HB-MMC2 RPC experimental results when the load section y active power is 150% the active power of the load section x . In this context, Figure 6.19 shows the three-phase currents at the secondary windings of the V/V transformer before compensation, and when both load sections are unequally loaded. The currents are imbalanced and contain harmonic contents. On the other hand, Figure 6.20 shows the phase difference angle between the phase x , phase y currents or the load section currents before compensation and the phase-to-neutral voltage u_A , which is used as a reference waveform with a phase angle equals to zero. There are almost 30° out-of-phase between u_A and i_x , and nearly 90° out-of-phase between u_A and i_y , as presented in the phasors diagram at the secondary windings of the V/V transformer in the Chapter 4, Figure 4.7.

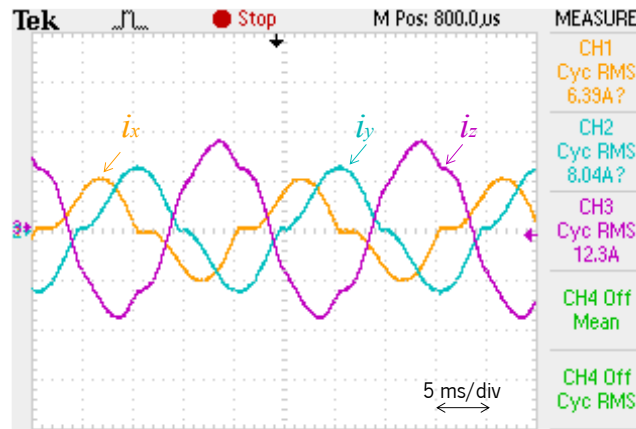


Figure 6.19. HB-MMC2 RPC experimental results (when both load sections are loaded): Phase x current before compensation (i_x : 10 A/div); Phase y current before compensation (i_y : 10 A/div); Phase z current before compensation (i_z : 10 A/div).

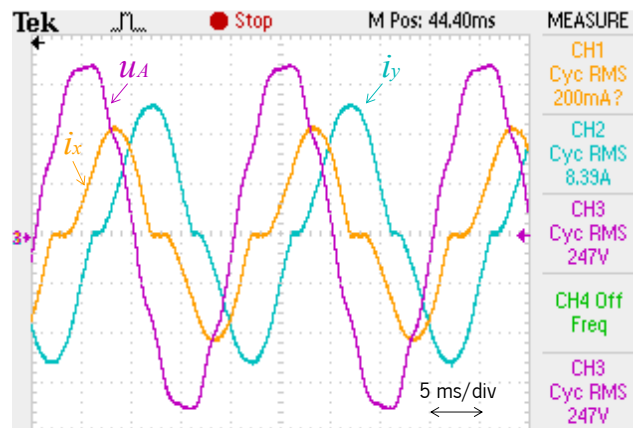


Figure 6.20. HB-MMC2 RPC experimental results (when both load sections are loaded): Phase x current before compensation (i_x : 5 A/div); Phase y current before compensation (i_y : 5 A/div); Phase A voltage (u_A : 100 V/div).

Figure 6.21 presents the three-phase currents at the secondary windings of the V/V transformer after compensation. The currents are balanced with lower harmonic contents and without NSCs. In that case, the RPC compensates reactive power and balance the active power between the load sections.

Consequently, a unitary power factor is obtained at the three-phase power grid. In addition, there are almost 0° out-of-phase between u_A and i_x , and almost 120° out-of-phase between u_A and i_y after compensation, as presented in Figure 6.22. That means that reactive power is totally exchanged between the load sections and the HB-MMC2 RPC and there is no reactive power exchanged with the three-phase power grid.

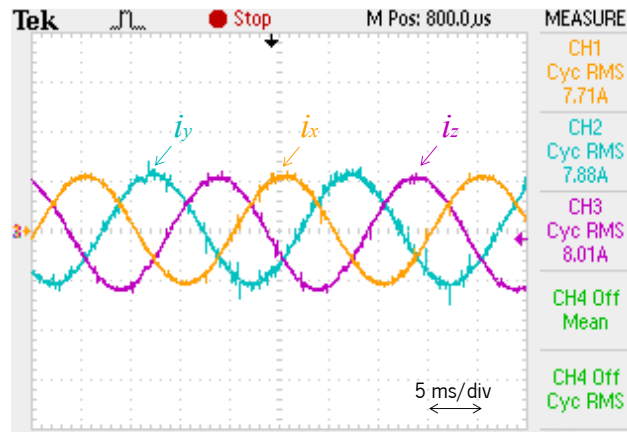


Figure 6.21. HB-MMC2 RPC experimental results (when both load sections are loaded): Phase x current after compensation (i_x : 10 A/div); Phase y current after compensation (i_y : 10 A/div); Phase z current after compensation (i_z : 10 A/div).

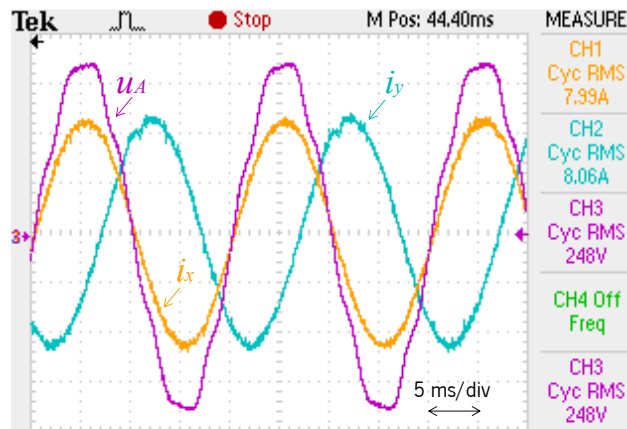


Figure 6.22. HB-MMC2 RPC experimental results (when both load sections are loaded): Phase x current after compensation (i_x : 5 A/div); Phase y current after compensation (i_y : 5 A/div); Phase A voltage (u_A : 100 V/div).

Figure 6.23 presents the frequency spectrum of the three-phase currents at the secondary windings of the V/V transformer. In this context, Figure 6.23(a) shows the harmonic contents before compensation with a THD ratio close to 23.1%. On the other hand, Figure 6.23(b) shows the harmonic contents after compensation with a THD ratio close to 3.1%.

Figure 6.24(a) presents the values of the harmonic contents before compensation. Phase x current i_x , has the highest ratio of THD, with a value close to 22.9%. The third-order harmonic is the highest harmonic content before compensation. Figure 6.24(b) shows the values of the harmonic contents after compensation. In that case, the THD ratio is significantly reduced, especially the third-order and

the fifth-order harmonics. It is worthy to mention, the even-order harmonics circulate between the MMC phases and they do not contribute to the HB-MMC2 RPC compensation currents.

Figure 6.25 shows the phasors diagram and the unbalance ratio (NSC ratio) of the three-phase currents at the secondary of the V/V transformer. The unbalance ratio before compensation is close to 46.8%, as shown in Figure 6.25(a). The phasors diagram, in that case, shows three-phase currents vectors that have different magnitude values. By considering the phase voltage u_A as a reference and due to the nature of the V/V connection, phase x current lags the reference voltage by nearly 30° , while phase y current lags the reference voltage by nearly 90° . On the other hand, Figure 6.25(b) shows the unbalance ratio and the phasors diagram of the three-phase currents after compensation. The unbalance ratio, in that case, is significantly reduced and has a value close to 2.9%. Obviously, the three-phase current phasors are balanced, with similar magnitude values and 120° out-of-phase. The results presented in Figure 6.23, Figure 6.24 and Figure 6.25 are acquired by using the Fluke 434 Power Quality Analyzer [214].

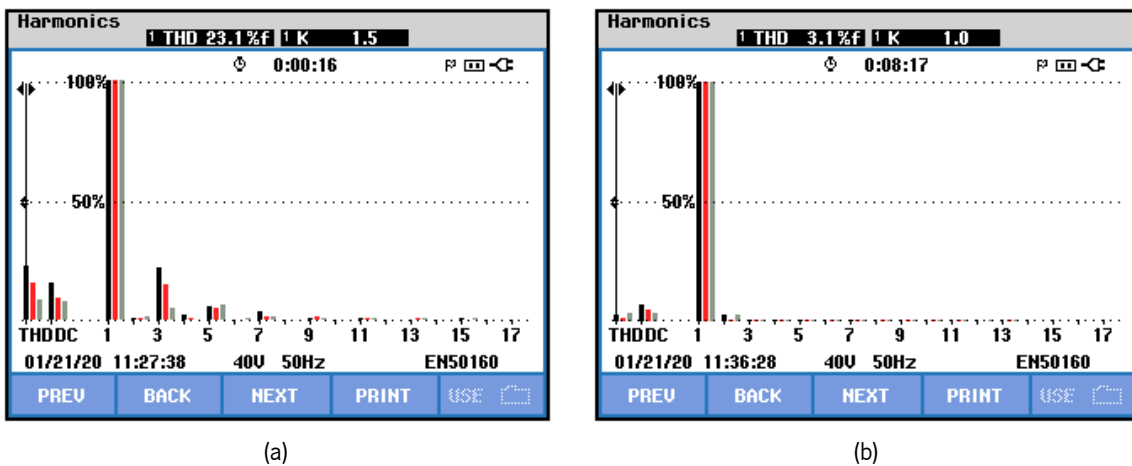


Figure 6.23. Frequency spectrum of the three-phase currents at the secondary windings of the V/V transformer (when both load sections are loaded): (a) Before compensation; (b) After compensation.

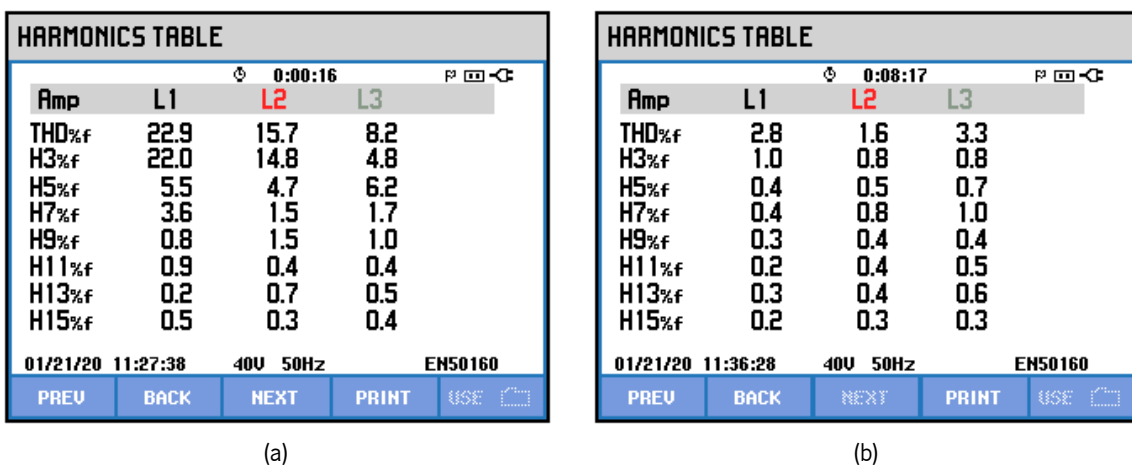


Figure 6.24. Harmonic contents value of the three-phase currents at the secondary windings of the V/V transformer (when both load sections are loaded): (a) Before compensation; (b) After compensation.

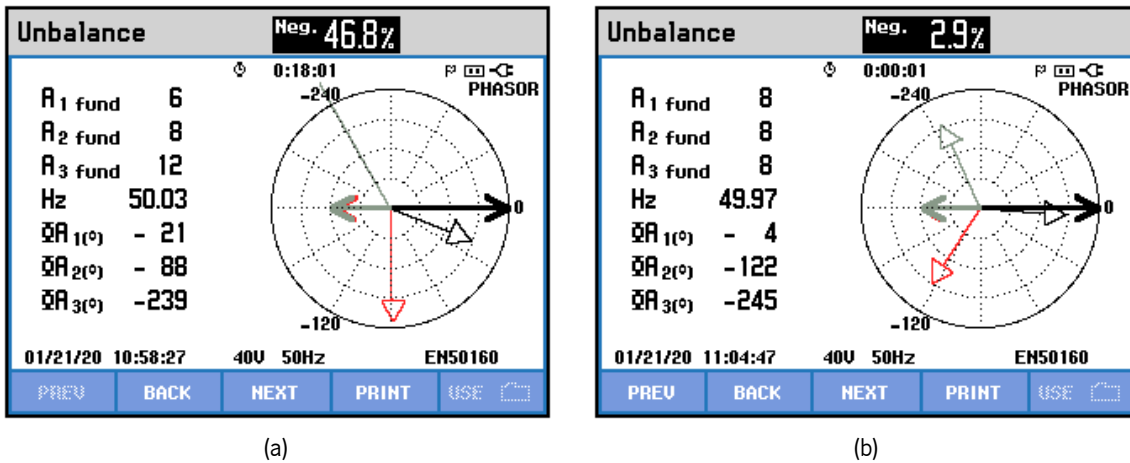


Figure 6.25. Unbalance ratio and phasors diagram of the three-phase currents at the secondary of the V/V transformer (when both load sections are loaded): (a) Before compensation; (b) After compensation.

The compensation currents synthesized by the HB-MMC2 RPC are presented in Figure 6.26. The compensation current of the load section x , i_{rx} , is higher than the compensation current of the load section y , i_{ry} . This is due to the unequal power of the load sections and the fact that section x converter injects higher power than the section y converter. Bearing in mind that, in V/V connection, section x converter compensates a quantity of a capacitive reactive power, whereas section y converter compensates a quantity of an inductive reactive power.

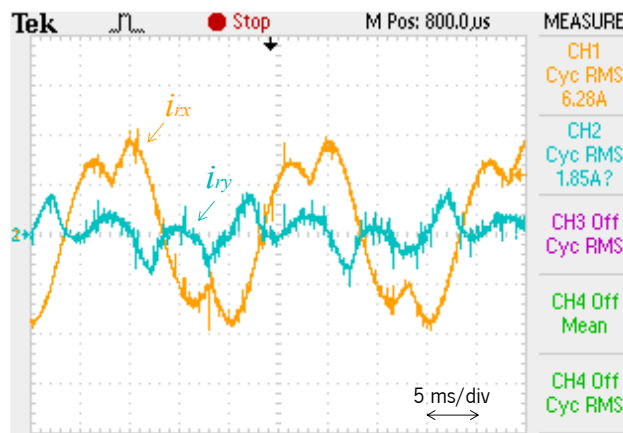


Figure 6.26. HB-MMC2 RPC experimental results (when both load sections are loaded): Phase x compensation current (i_{rx} : 5 A/div); Phase y compensation current (i_{ry} : 5 A/div).

Figure 6.27 and Figure 6.28 show the SM voltage waveforms of the section x converter and the section y converter, respectively. The SM voltages are close to the reference value of 80 V. However, and due to the half-bridge topology of the SM, the voltage ripples frequency is equal to the fundamental frequency of 50 Hz. On the other hand, and since the section x converter injects a higher amount of power, the SM voltages of section x converter V_{SMx1} , V_{SMx2} , V_{SMx3} and V_{SMx4} , have higher voltage ripples than the SM voltages of section y converter V_{SMy1} , V_{SMy2} , V_{SMy3} and V_{SMy4} . These results confirm the effectiveness of the MMC leg averaging voltage balancing control presented in

Figure 4.71(a), and the MMC SM individual voltage balancing control presented in Figure 4.71(c). However, it is worthy to mention that, the MMC arm averaging voltage control, presented in Figure 4.71(b), is not implemented in this experimental test. As a result, the MMC leg averaging voltage balancing control and the MMC SM individual voltage balancing control are sufficient to maintain a balanced voltage of the MMC SMs.

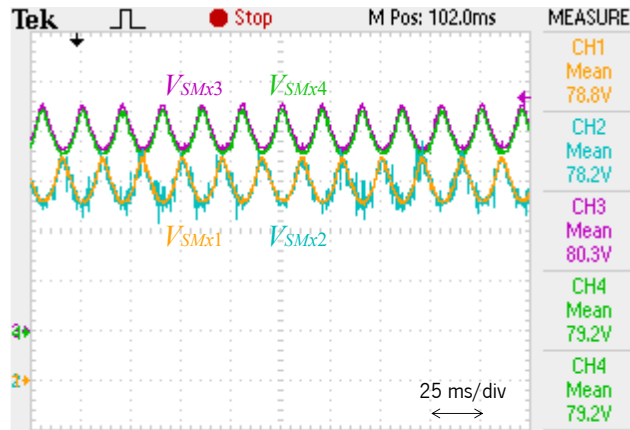


Figure 6.27. HB-MMC2 RPC experimental results – SM voltages of section x converter (when both load sections are loaded): SM1 voltage (V_{SMx1} : 20 V/div); SM2 voltage (V_{SMx2} : 20 V/div); SM3 voltage (V_{SMx3} : 20 V/div); SM4 voltage (V_{SMx4} : 20 V/div).

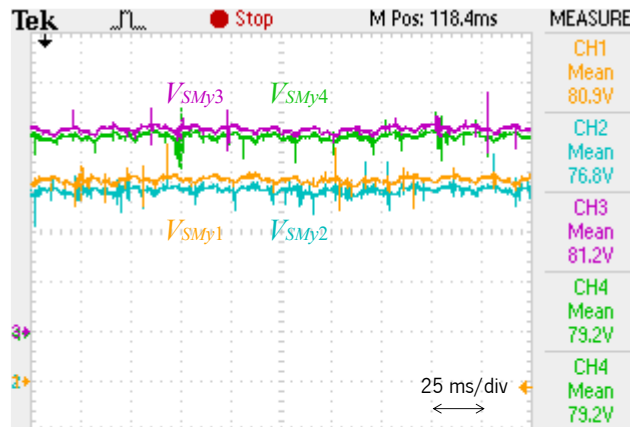


Figure 6.28. HB-MMC2 RPC experimental results - SM voltages of section y converter (when both load sections are loaded): SM1 voltage (V_{SMy1} : 20 V/div); SM2 voltage (V_{SMy2} : 20 V/div); SM3 voltage (V_{SMy3} : 20 V/div); SM4 voltage (V_{SMy4} : 20 V/div).

6.6.2 Experimental Results when One Load Section is Loaded

This item presents the HB-MMC2 RPC experimental results when only the load section y is loaded (load section x has no loads). In this context, Figure 6.29 shows the secondary windings three-phase currents of the V/V transformer before compensation, and when only load section y is loaded. The currents are imbalanced and contain harmonic contents. Phase x current i_x , has a zero RMS value since the load section x is not loaded. Consequently, Phase y current i_y and Phase z current i_z , have

180° out-of-phase. The imbalance ratio, in this case, is higher than the case presented in the item 6.6.1, when both of the load sections were loaded.

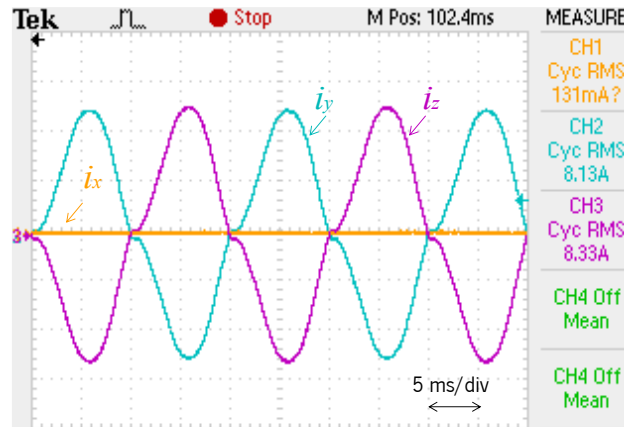


Figure 6.29. HB-MMC2 RPC experimental results (when load section y is loaded): Phase x current before compensation (i_x : 5 A/div); Phase y current before compensation (i_y : 5 A/div); Phase z current before compensation (i_z : 5 A/div).

Figure 6.30 presents the secondary windings three-phase currents of the V/V transformer after compensation. The currents are balanced with lower harmonic contents and NSCs. In that case, the RPC compensates reactive power and balance the active power between the load sections, then, a unitary power factor is obtained at the three-phase power grid.

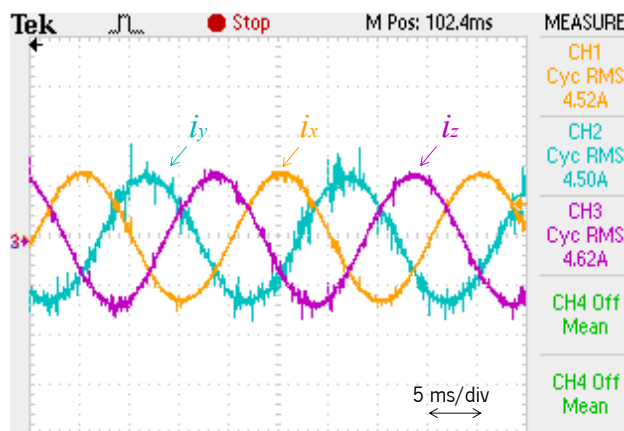


Figure 6.30. HB-MMC2 RPC experimental results (when load section y is loaded): Phase x current after compensation (i_x : 5 A/div); Phase y current after compensation (i_y : 5 A/div); Phase z current after compensation (i_z : 5 A/div).

Figure 6.31 presents the frequency spectrum of the three-phase currents at the secondary windings of the V/V transformer. In this context, Figure 6.31(a) shows the harmonic contents before compensation with a THD ratio close to 15.1%. On the other hand, Figure 6.31(b) shows the harmonic contents after the compensation with a THD ratio near 2.5%. This confirms the effectiveness of the HB-MMC2 RPC system in improving the power quality of the three-phase power grid.

Figure 6.32(a) presents the values of the harmonic contents before compensation. Phase y and phase z currents have 180° out-of-phase, and they have almost the same ratio of the THD. The

third-order harmonic is the highest harmonic content before compensation, with a ratio close to 14.2%. Figure 6.32(b) shows the values of the harmonic contents after compensation. In that case, the THD is significantly reduced, and the third-order harmonics does not exceed the ratio of 2%. It is worthy to mention, the even-order harmonics circulate between the MMC phases and they do not contribute to the HB-MMC2 RPC compensation currents.

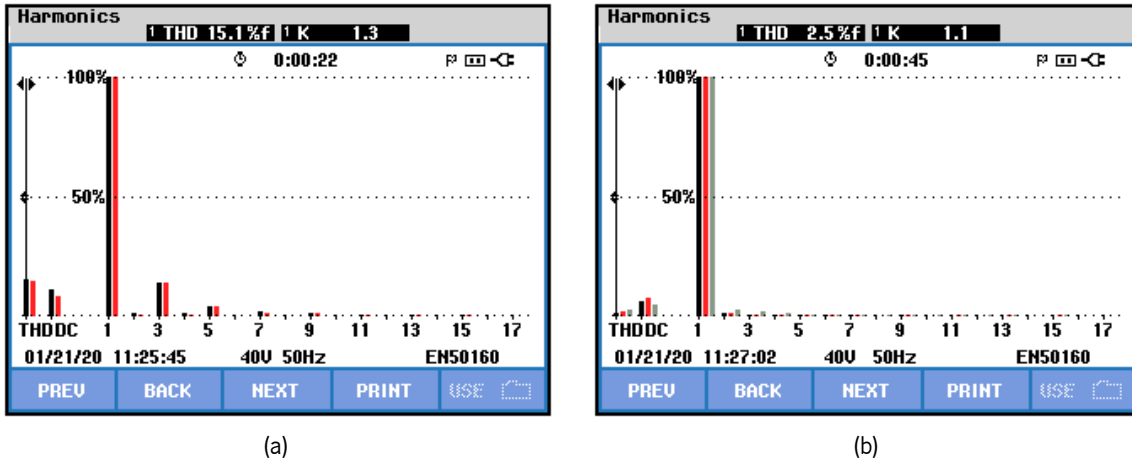


Figure 6.31. Frequency spectrum of the three-phase currents at the secondary of the V/V transformer (when load section y is loaded): (a) Before compensation; (b) After compensation.

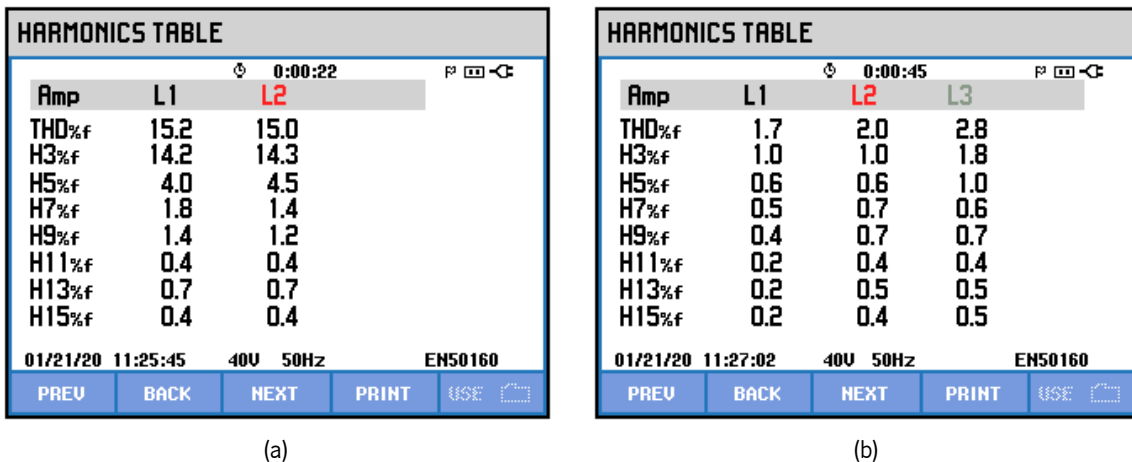


Figure 6.32. Harmonic contents value of the three-phase currents at the secondary of the V/V transformer (when load section y is loaded): (a) Before compensation; (b) After compensation.

Figure 6.33 shows the phasors diagram and the unbalance ratio of the three-phase currents at the secondary windings of the V/V transformer. The unbalance ratio (NSC ratio) before compensation is close to 97.7%, as shown in Figure 6.33(a). The phasors diagram, in that case, shows only two-phase currents that have equal magnitudes and 180° out-of-phase. By considering the phasor of the phase voltage u_A as a reference, and due to the nature of the V/V connection, phase y current lags the reference by nearly 90° , while phase z current lags the reference by nearly 270° . On the other hand, Figure 6.34(b) shows the unbalance ratio and the phasors diagram of the three-phase currents after compensation. The unbalance ratio, in that case, is significantly reduced and has a value close to 1.6%.

Obviously, the three-phase current phasors are balanced, with similar magnitude values and 120° out-of-phase. The results presented in Figure 6.31, Figure 6.32 and Figure 6.33 are acquired by using the Fluke 434 Power Quality Analyzer [214].

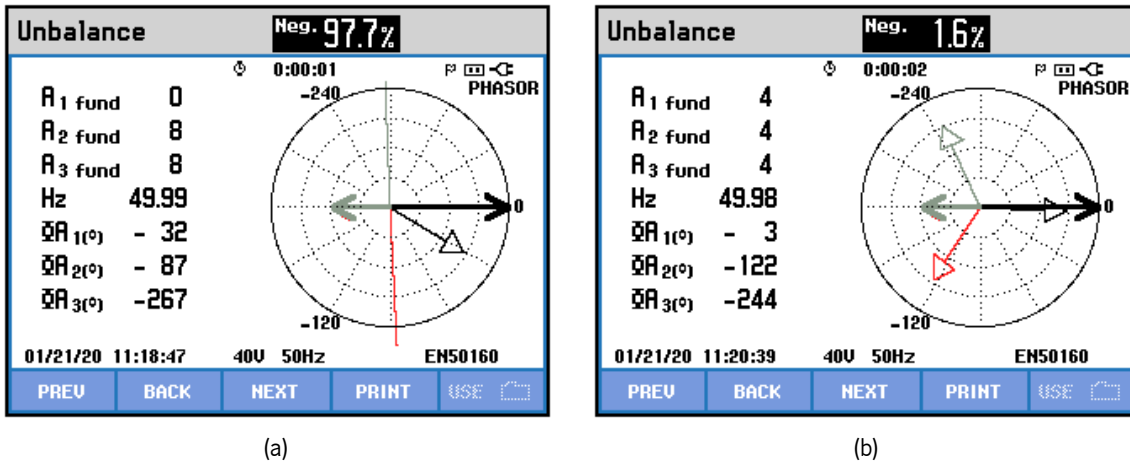


Figure 6.33. Unbalance ratio and phasors diagram of the three-phase currents at the secondary of the V/V transformer (when load section y is loaded): (a) Before compensation; (b) After compensation.

The compensation currents synthesized by the HB-MMC2 RPC are presented in Figure 6.34. The compensation current of the load section x , i_{rx} , is completely sinusoidal since there are no loads connected to the load section x . In that case, section x converter compensates reactive power and balances the active power between the load sections. On the other hand, section y converter compensates harmonic contents, reactive power, and also balances the active power between the load sections.

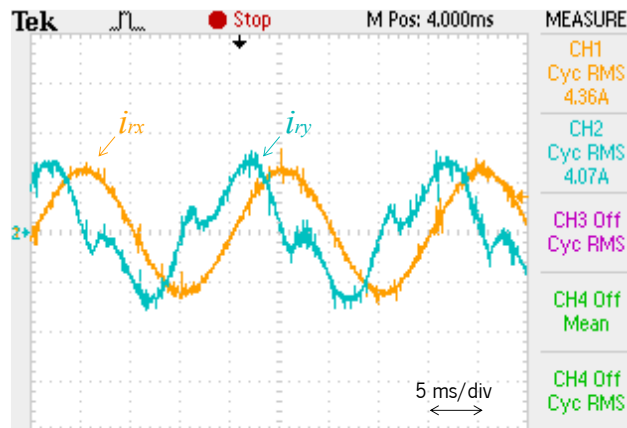


Figure 6.34. HB-MMC2 RPC experimental results (when load section y is loaded): Phase x compensation current (i_{rx} : 5 A/div); Phase y compensation current (i_{ry} : 5 A/div).

Figure 6.35 and Figure 6.36 show the SM voltage waveforms of the section x converter and the section y converter, respectively. The SM voltages are close to the reference value of 80 V. However, and due to the half-bridge topology of the SM, the voltage ripple frequency is equal to the fundamental frequency of 50 Hz. On the other hand, and since the section x converter and the section y converter

compensate almost an equal amount of power, the SM voltages of the MMC have almost an equal voltage ripples for the section x and section y converters. These results confirm the effectiveness of the MMC leg averaging voltage balancing control, and the MMC SM individual voltage balancing control. The control blocks are presented in Chapter 4, Figure 4.71(a) and Figure 4.71(c). However, it is worthy to mention that, the MMC arm averaging voltage control is not implemented in this experimental test. As a result, the MMC leg averaging voltage balancing control and the MMC SM individual voltage balancing control are sufficient to maintain a balanced voltage of the MMC SMs.

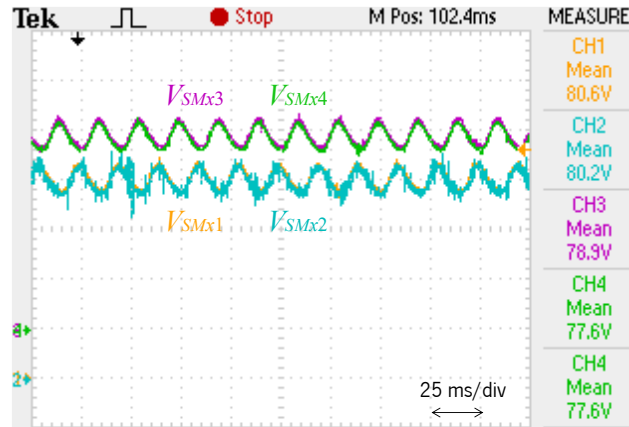


Figure 6.35. HB-MMC2 RPC experimental results – SM voltages of section x converter (when load section y is loaded): SM1 voltage (V_{SMx1} : 20 V/div); SM2 voltage (V_{SMx2} : 20 V/div); SM3 voltage (V_{SMx3} : 20 V/div); SM4 voltage (V_{SMx4} : 20 V/div).

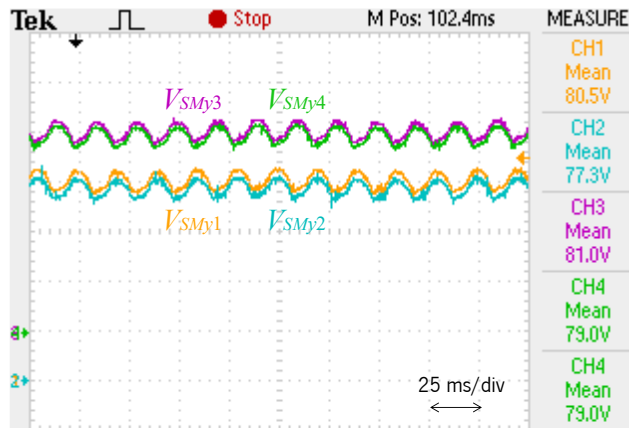


Figure 6.36. HB-MMC2 RPC experimental results – SM voltages of section y converter (when load section y is loaded): SM1 voltage (V_{SMy1} : 20 V/div); SM2 voltage (V_{SMy2} : 20 V/div); SM3 voltage (V_{SMy3} : 20 V/div); SM4 voltage (V_{SMy4} : 20 V/div).

6.7 Conclusion

This chapter presented the experimental results of the simplified rail power conditioner (RPC) based on the half-bridge indirect modular multilevel converter (HB-MMC2 RPC). For that purpose, a developed reduced-scale laboratory workbench prototype of the HB-MMC2 RPC was used to obtain the experimental results. In this context, two case studies were presented: the first is when both of the load

sections are loaded, and the second is when only one load section is loaded. The presented experimental results confirm the rightness of the compensation strategy and the associated voltage balancing control of the modular multilevel converter (MMC) submodules (SMs). Furthermore, the experimental results show that the HB-MMC2 RPC is a viable solution for the purpose of power quality improvement in electrified railway systems.

In the experimental validation, only eight SMs with 40 kHz switching frequency were used. However, and for high-power applications, a few tens of SMs with a lower SM switching frequency should be employed, which allows the MMC to synthesize sinusoidal waveforms with better quality and lower harmonic contents. Subsequently, the case reported in this Ph.D. thesis consists of a low number of SMs with a high SM switching frequency (this choice was made to reduce the MMC complexity). It was verified that the compensation currents synthesized by the HB-MMC2 RPC satisfy the requirements of negative sequence component compensation and harmonics cancelation. As a result, it is important to highlight that in high-power levels, the number of MMC SMs should increase, but the switching frequency could be reduced to achieve the same objectives.

Chapter 7

Conclusion

7.1 Introduction

Flexible AC transmission systems (FACTS) in electrified railway systems could be considered as one of the prominent solutions for a better interface between the three-phase public power system (PPS) and the single-phase traction power system (TPS). As highlighted throughout this Ph.D. thesis, using FACTS devices in railway supply system could bring a series of opportunities and challenges, in which some of these devices operate as active power compensators to achieve power quality improvement at the three-phase PPS. This leads to lower operating costs of the electrified trains, higher power capacity and better efficiency of the three-phase PPS. Thus, the focus of this Ph.D. thesis was on the study and the implementation of a rail power conditioner (RPC), which is one of the FACTS devices used for the purpose of power quality improvement in the electrified railway systems. The novelty of this research work was in the integration of the modular multilevel converter (MMC) to operate as an RPC. In this context, a reduced-scale laboratory prototype of simplified RPC based on half-bridge indirect MMC (HB-MMC2 RPC) has been implemented throughout this work.

This chapter presents the main obtained conclusions of the research and development presented in this Ph.D. thesis. Since the work introduced is in continuous evolution and is quite comprehensive, this chapter also offers an item referring to suggestions for future work.

7.2 General Conclusions

Chapter 1 presented an introduction about the electrified railway systems in Europe, the history and the main challenges that face the European railway sector, as well as the main framework of this Ph.D. thesis, including the main motivations and contributions. This chapter also presented a list of the main scientific articles published under the scope of this Ph.D. thesis in international conferences, international journals, and book chapters.

In Chapter 2, concerning the power quality phenomena in the electrified railway systems, several power quality problems were addressed, such as the imbalance in the three-phase PPS, harmonics distortion, low-frequency voltage fluctuations and voltage arcing. Moreover, this chapter introduced the major

impacts of power quality deterioration in electrified railway systems on both of electric power systems and signaling and communication systems.

Several traditional-based methods for the purpose of power quality improvement in electrified railway systems were presented in Chapter 2. For example, using three-phase electric locomotives to avoid the problem of imbalance in the three-phase PPS, employing three-phase to two-phase balanced power transformers to reduce the effect of imbalance, applying passive power filters that compensate reactive power and harmonics, and taking advantage of the adjacent single-phase power transformers to alternate the supply phases. On the other hand, several AC feeding methods of the single-phase TPS were introduced in Chapter 2. The explanations showed that choosing the suitable feeding system for AC railway electrification is dependent on some fundamental aspects, such as the generated electromagnetic disturbances near the train's surrounding area.

In Chapter 3, were presented the main topologies of active power compensators in the electrified railway systems (e.g., static VAR compensator (SVC), static synchronous compensator (STATCOM), static frequency converter (SFC) and the RPC), showing the main characteristics and the potential abilities for each topology. In this context, it was observed that SFC topology had some distinct advantages over the other FACTS regarding the frequency conversion and the reduction of neutral sections. However, the main disadvantage of the SFC that it had to be designed to transmit all the power required by the traction load, which might increase the implementation costs of the SFC. On the contrary, it was explained that RPC topology had the advantage of overloading capability. In this case, and by using the co-phase RPC topology, the number of neutral sections in front of the traction substations could be reduced by half. Also, the RPC system was able to shift a part of the total load active power from the highly to the lightly loaded section and providing all the load reactive power. More details and explanations can be found in Chapter 3, where a case study to compare between the SFC and the RPC based on indirect AC/DC/AC MMC was presented.

Moreover, and since the main focus of this Ph.D. thesis was on the RPC based on MMC, Chapter 3 explained the MMC characteristics and its fundamental operation principle, excluding the operation scenarios when the MMC is based on the pulse-width modulation (PWM) switching at the fundamental frequency modulation, which is out of the scope of this Ph.D. thesis.

Furthermore, the direct AC/AC MMC and the indirect AC/DC/AC MMC were explained to show the main features and applications of each topology. In that regard, a case study was presented to show the main differences between the direct AC/AC MMC and the indirect AC/DC/AC MMC, when they supposed to operate as an SFC for the 15 kV, 16.7 Hz electrified railway systems. The results showed

that the direct AC/AC MMC (with full-bridge submodules) and the indirect AC/DC/AC MMC (with half-bridge submodules) were the appropriate choices in the 15 kV, 16.7 Hz and the 25 kV, 50 Hz, respectively.

Chapter 4 introduced a comprehensive presentation of the RPC topologies in the electrified railway systems, as well as the possible operation modes of the RPC. Each operation mode could be implemented by using the same converter hardware, but the converter control might be quite different. In that regard, four operation modes were presented:

- SVC mode when one of the traction transformer output phases was disconnected (due to periodic maintenance).
- Catenary voltage regulator mode when the converter was not directly connected to the traction substation, but it was connected to a certain zone of the overhead catenary line (this operation mode is hardly possible since the open-loop voltage in each substation is different and high circulating currents can happen).
- Interface converter between two collateral substations when the converter was used to interface between two phases in the double-side feeding system.
- RPC mode when the TPS was constituted by two traction feeders separated by neutral sections.

In addition, Chapter 4 presented various potential RPC topologies with the associated control algorithms: RPC based on full-bridge back-to-back two-level converter (FB-RPC); RPC based on two-phase three-wire converter (TW-RPC); simplified RPC based on half-bridge two-level converter (HB-RPC); Modular RPC (MRPC); hybrid co-phase RPC (co-HRPC); RPC based on full-bridge indirect modular multilevel converter (FB-MMC4 RPC); RPC based on two-phase three-wire indirect modular multilevel converter (TW-MMC3 RPC); simplified RPC based on half-bridge indirect modular multilevel converter (HB-MMC2 RPC).

Simulation results, using the *PSIM* V.9.1 simulation tool, for each of the RPC topologies were presented. Subsequently, the RPC topologies were evaluated and compared in the V/V and the Scott power transformers, in terms of the number of isolation or coupling transformers required, number of the switching devices, power ratings of the switching devices, number of passive elements required in the RPC system, RPC DC-link voltage value, control complexity, and the required volume for installation. The comparative study proved that the FB-MMC4 RPC could be classified as a general-purpose RPC because it might be used with different power transformers (V/V or Scott). On the other hand, the TW-MMC3 RPC and the HB-MMC2 RPC could be classified as special-purpose RPC because they were recommended to be used with only the V/V power transformer. Moreover, Chapter 4 presented the

simulation results of the deadbeat predictive control for the HB-MMC2 RPC, which had the merits of simplicity and better performance regarding the circulating current suppression in the MMC.

Chapter 5 mainly presented the implementation stages of the HB-MMC2 RPC. It began explaining the parameters design of the MMC, such as the filter inductors and the submodule (SM) capacitors. Then, various supplementary power devices were presented and used to obtain a reduced-scale TPS workbench, including the V/V transformer and the two-phase load sections.

The implementation of the reduced-scale MMC consisted of two main parts: power hardware and control hardware. The power hardware indicated the MMC SM and constituted by three printed circuit boards (PCBs): driver circuit PCB; protection circuit PCB; and power circuit PCB. Each of the mentioned PCBs was implemented and validated, then, Chapter 5 introduced the experimental results of the PCBs involved to assemble the MMC SM.

Experimental results of the driver circuit PCB showed the developed driver was able to provide unipolar or bipolar PWM signals to drive the insulated-gate bipolar transistors (IGBTs) power switching devices. The used integrated circuit (IC) in the driver circuit PCB, *Si8244*, allowed to externally calibrate the deadtime between the PWM signals. On the other hand, experimental results of the protection circuit PCB proved the ability to protect against overvoltage and overcurrent situations. For that purpose, two experimental setups were developed to experiment with the protection under overvoltage and overcurrent conditions, without adversely damaging the MMC components. Moreover, the experimental results of the MMC SM were presented to validate the interface between the driver circuit PCB, the protection circuit PCB, and the power circuit PCB in the SM.

Chapter 5 also presented the control system hardware, which composed by the central control unit or the microcontroller (*Texas Instruments TMS320f28335*), voltage sensors (*ChenYang CYHVS025A*, and *Silicon LAB Si8920*), current sensors (*LEM LA 100 P* and *Allegro ACS730*), digital-to-analogue converter (*Texas Instruments DAC TLV5610*), analogue-to-digital converter (*Maxim MAX1320*), and command circuit PCB.

Chapter 6 showed the HB-MMC2 RPC experimental results. MMC validation was initially performed as a DC/AC converter by testing of one MMC leg/phase with an open-loop control, then repeating the same experiment but with a closed-loop control. Subsequently, the experimental results of the full MMC were presented with a closed-loop control. These experiments were carried out with the help of an adjustable auto-transformer to obtain the required voltage input. Also, two power diodes were used to regulate the input voltage. Accordingly, these experiments were employed to calibrate all the MMC components, such as current and voltage sensors. They also helped to predict the MMC performance

when all the SMs were under operation/commutation, in which passive and active filters were used in the control system for a better noise cancelation. The experimental results of the DC/AC MMC, presented in the items 6.4 and 6.5, showed the ability to synthesize a sinusoidal waveform with low harmonic contents. Moreover, the experimental results of the applied enhanced phase-locked loop and the digital moving average low-pass filter (LPF) with different number of samples were also introduced in the Chapter 6.

Experimental results of the HB-MMC2 RPC were presented considering two case studies: when both load sections x and y were loaded (presented in the item 6.6.1); and when only the load section y was loaded (presented in the item 6.6.2). In the first case study, the load section y active power was 150% the active power of the load section x , whereas, in the second case study, the load section x had no loads and load section y maintained its power value. In both of the case studies, experimental results were carried out for power values below the nominal ones. The voltage of each SM was set to be near 80 V. The presented experimental results, in both of the case studies, proved the effectiveness of the introduced HB-MMC2 RPC control algorithm.

In the first case study, the frequency spectrum of the three-phase PPS currents before compensation showed a total harmonic distortion (THD) ratio of 23.1%. However, the THD ratio of the three-phase currents after compensation was reduced to 3.1%. Negative sequence component (NSC) or the unbalance ratio of the three-phase currents before compensation was close to 46.8%. The phasors diagram of the three-phase currents, in that case, showed unequal magnitudes (6 A, 8 A, 12 A). After reactive power compensation, harmonics cancelation, and active power shifting from the load section y to the load section x , the unbalance or NSC ratio of the three-phase currents was close to 2.9%. In addition, the phasors diagram of the three-phase currents, in that case, showed equal magnitudes (8 A, 8 A, 8 A) and 120° out-of-phase between the phasors.

In the second case study, the frequency spectrum of the three-phase PPS currents before compensation showed the THD ratio of 15.1%. However, the THD ratio of the three-phase currents after compensation was reduced to 2.5%. The unbalance ratio of the three-phase currents before compensation was close to 98%, and the phasors diagram of the three-phase currents, in that case, showed unequal magnitudes (0 A, 8 A, 8 A). After reactive power compensation, harmonics cancelation, and active power shifting from the load section y to the load section x , the unbalance or NSC ratio of the three-phase currents was close to 1.6%. In addition, the phasors diagram of the three-phase currents, in that case, showed equal magnitudes (4 A, 4 A, 4 A) and 120° out-of-phase between the phasors.

The second case study was worse than the first case study since the compensation currents synthesized and injected by the HB-MMC2 RPC were higher in the second case study. Consequently, as the power difference between the load sections was higher, RPC should deal with a higher amount of power.

Since the experimental results were carried out for power values below the nominal, no thermal or efficiency tests were performed on the developed HB-MMC2 RPC reduced-scale prototype. Moreover, in this prototype, only eight SMs with high switching frequency were used to reduce the MMC complexity. The used switching frequency was close to 40 kHz, which allowed to synthesize sinusoidal waveforms with very good quality and fast dynamic response when compensating load current harmonics. However, in high-power applications, a few tens of SMs with low switching frequency should be used to achieve the same objectives. The presented experimental results showed that the HB-MMC2 RPC could be a viable solution for the purpose of power quality improvement in the electrified railway systems.

It should be noted that during this work there was an interest to develop all the power and some control PCBs from scratch, which made the task of building the HB-MMC2 RPC prototype consuming a significant part of the time spent on this Ph.D. thesis, obligating the realization of less usual tasks in the research work, namely, searching for manufacturers and local distributors, comparison between several products and prices, designing and manufacturing several PCBs and the consequent correction of errors, and the implementation of V/V transformer and supplementary power equipment.

The final conclusions of this Ph.D. thesis can be summarized as follows:

- An extensive analysis and comparison of the RPC topologies, for the purpose of power quality improvement in AC electrified railways, was presented in Chapter 4.
- The Scott power transformer helps to reduce the imbalance of the three-phase currents. In other words, when both of the load sections have similar power consumption, no reactive power compensation or active power shifting is required.
- The deadbeat predictive current control methodology for circulating current suppression in MMC was presented in Chapter 4. The results showed reduced circulating currents and sinusoidal MMC arm currents with significantly reduced THD. However, unmodeled parameters in the HB-RPC mathematical model may deteriorate the system performance and wrongly represent the system dynamics.
- The TW-MMC3 RPC and the HB-MMC2 RPC are more adequate to be used with V/V power transformer instead of Scott power transformer. This is due to the DC-link of the TW-MMC3 RPC

and the HB-MMC2 RPC should be designed with respect to the phase-to-phase voltage. Moreover, isolation transformers are not mandatory to interface with the single-phase TPS.

- The FW-MMC4 RPC is a general-purpose topology, and can be used either with the V/V or with the Scott power transformer. This is due to the DC-link of the FB-MMC4 RPC should be designed with respect to the phase-to-neutral voltage. However, isolation transformers are required to interface with the single-phase TPS.
- In the RPC topologies that are designed with respect to the phase-to-neutral voltage (e.g., FB-RPC and FW-MMC4 RPC), using the Scott power transformer could help to reduce the RPC power ratings, since the reactive power compensation is not a vital factor in this case, especially when both of the load sections are equally loaded.
- The simulation results of the HB-MMC2 RPC introduced in Chapter 4, based on its theoretical model, represent the converter behavior under high-power applications.
- The MMC protection system against overvoltage, overcurrent, open and short circuit scenarios, is essential to ensure the safe operation of the MMC. In that regard, a protection system with quick response was proposed and presented in Chapter 5.
- In modular and scalable converters that include several submodules, such as the case of the MMC, it is very important to build and validate the submodule design and its operation before the full implementation of the MMC. In this context, the validation of a single submodule was presented in Chapter 5.
- In the development process of the HB-MMC2 RPC prototype, there were specific measuring errors and assumptions that lay within certain margins. For instance, only eight SMs with high switching frequency were used to reduce the MMC complexity, while in high-power applications a few tens of SMs with low switching frequency should be used to achieve the same objectives.
- Experimental results of the reduced-scale HB-MMC2 RPC prototype, presented in Chapter 6, give an idea about the behavior of the RPC based on MMC system at medium-voltage and high-power applications.
- Experimental results of the HB-MMC2 RPC, presented in Chapter 6, showed the RPC ability to achieve power quality improvement at the three-phase PPS. By other words, the RPC can provide reactive power and compensate harmonic contents of currents.
- Experimental results of the HB-MMC2 RPC, presented in Chapter 6, showed the worse-case scenario when only one load section is loaded. In that case, the RPC system should inject a higher amount of reactive power, as well as shifting a higher amount of active power from the highly to the lightly loaded section. The best operation scenario for the RPC is when both of the load sections have the same power consumption.

- MMC advantages are quite numerous, such as the scalability to different power and voltage levels, reliability to guarantee continuous operation even if few submodules stop working, and filter-less configuration with high synthesized waveforms quality and low THD.
- MMC disadvantages are few, and can be outlined as the high number of switching devices and other power components, besides the high energy stored in the capacitors. This obligates to use a robust protection system to keep the safe operation of the MMC. High costs, complexity and large required area for installation can also be considered as extra disadvantages.

7.3 Significant Contributions

This item presents the significant contributions of this Ph.D. thesis:

- Study, research and comparison between the RPC topologies (presented in Chapter 4);
- Proposal of a new control methodology “deadbeat predictive current control” for the purpose of circulating current reduction in the MMC (presented in Chapter 4, item 4.9.3);
- Design, implementation and validation of an MMC half-bridge SM (presented in Chapter 5);
- Design, implementation and validation of a reduced-scale prototype of a HB-MMC2 RPC (presented in Chapter 6).

7.4 Suggestions for Future Work

The results presented throughout this Ph.D. thesis allowed the validation of the HB-MMC2 RPC topology for the purpose of power quality improvement in the electrified railway systems. However, there are several improvements that can be introduced in the future, as described below:

- Implementing an additional MMC leg/phase to replace the mid-neutral point capacitors, then a three-phase MMC (TW-MMC3 RPC) can replace the half-bridge MMC (HB-MMC2 RPC), which helps to reduce the SM voltages of the MMC, as well as improving the quality of the generated output waveform.
- Boosting the MMC level by inserting extra SMs in the MMC arms. This improvement leads to an increase in the equivalent switching frequency of the MMC. Accordingly, an output waveform with better quality and lower harmonic contents can be generated.
- Using silicon carbide (SiC) switching devices, which have higher efficiency and better performance compared to the IGBT switching devices.
- Studying the RPC based on MMC not only in V/V traction system, but also in the Scott traction system to show that reactive power compensation is not a vital factor in the Scott traction system.

- Improving the MMC control system by changing the digital signal processor (DSP) with a field-programmable gate array (FPGA).
- Implementing the co-phase RPC topology, using a single-phase traction power transformer, which reduces the number of neutral sections by half compared to the conventional RPC connection.

List of References

- [1] European Commission - Directorate-General for Energy and Transport, *Modern Rail Modern Europe: Towards an Integrated European Railway Area*, 1st ed. Belgium: Office for Official publications of the European Communities, 2008.
- [2] A. Verdicchio, P. Ladoux, H. Caron, and C. Courtois, "New Medium-Voltage DC Railway Electrification System," *IEEE Trans. Transp. Electrification*, vol. 4, no. 2, pp. 591–604, Jun. 2018, doi: 10.1109/TTE.2018.2826780.
- [3] M. Rycroft, F. Editor, and E. E. Publishers, "Traction Motors in Diesel Locomotives," *EE Publishers*, 14-Mar-2016. [Online]. Available: <http://www.ee.co.za/article/traction-motors-diesel-locomotives.html>. [Accessed: 29-Jun-2018]
- [4] A. Steimel, "Power-Electronic Grid Supply of AC Railway Systems," in *2012 13th International Conference on Optimization of Electrical and Electronic Equipment (OPTIM)*, Brasov, 2012, pp. 16–25, doi: 10.1109/OPTIM.2012.6231844.
- [5] B. Bhargava, "Railway Electrification Systems and Configurations," in *199 IEEE Power Engineering Society Summer Meeting. Conference Proceedings (Cat. No.99CH36364)*, Edmonton, Alta., Canada, 1999, vol. 1, pp. 445–450, doi: 10.1109/PESS.1999.784389.
- [6] A. Dolara, M. Gualdoni, and S. Leva, "Impact of High-Voltage Primary Supply Lines in the 2x25 kV–50 Hz Railway System on the Equivalent Impedance at Pantograph Terminals," *IEEE Trans. Power Deliv.*, vol. 27, no. 1, pp. 164–175, Jan. 2012, doi: 10.1109/TPWRD.2011.2167635.
- [7] A. M. Freitas, D. Silva, D. C. Amorim, F. M. Cruz, and G. T. Lopes, "Os Comboios em Portugal – A Evolução e as Características dos Comboios de Passageiros," Faculdade de Engenharia – Universidade do Porto, 2011 [Online]. Available: https://paginas.fe.up.pt/~projfeup/cd_2010_11/files/CIV216_relatorio.pdf. [Accessed: 29-May-2018]
- [8] A. Gómez-Expósito, J. M. Mauricio, and J. M. Maza-Ortega, "VSC-Based MVDC Railway Electrification System," *IEEE Trans. Power Deliv.*, vol. 29, no. 1, pp. 422–431, Feb. 2014, doi: 10.1109/TPWRD.2013.2268692.
- [9] Y. Oura, Y. Mochinaga, and H. Nagasawa, "Railway Electric Power Feeding Systems." *Japan Railway & Transport Review* 16, Jun-1998.
- [10] "Technical and Administrative Barriers - Mobility - Siemens." [Online]. Available: <http://www.mobility.siemens.com/mobility/global/en/interurban-mobility/rail-solutions/locomotives/vectron/boundlessness/technical-barriers/pages/technical-barriers.aspx>. [Accessed: 28-Jul-2017]
- [11] "Chronology | CP - Comboios de Portugal," *CP.PT | Comboios de Portugal*. [Online]. Available: <https://www.cp.pt/institucional/pt/cultura-ferroviaria/historia-cp/cronologia>. [Accessed: 29-Nov-2016]
- [12] "The Portuguese Railway: 160 Years and 160 more," *Global Railway Review*. [Online]. Available: <https://www.globalrailwayreview.com/article/30934/portuguese-railway/>. [Accessed: 27-Jul-2017]
- [13] "PORDATA - Extensão da Rede Ferroviária: Total, Explorada e Desactivada - Continente." [Online]. Available: <https://www.pordata.pt/Portugal/Extens%3a3o+da+rede+ferrovi%3a1ria+total++explorada+e+desactivada+++Continente-3108-262527>. [Accessed: 27-Jul-2018]
- [14] "PORDATA - Estações de Comboio e Passagens de Nivel - Continente." [Online]. Available: <https://www.pordata.pt/Portugal/Esta%3a7%3b5es+de+comboio+e+passagens+de+n%3advel+++Continente-3110>. [Accessed: 27-Jul-2018]
- [15] "Rede Ferroviaria Nacional - Page 85 - SkyscraperCity." [Online]. Available: <https://www.skyscrapercity.com/showthread.php?p=57924493>. [Accessed: 27-Jul-2018]

- [16] “Linhas e Ramais com Tráfego Ferroviário 2015.” [Online]. Available: https://wiki.openstreetmap.org/w/images/c/c1/Linhas_e_Ramais_com_Tr%C3%A1fego_Ferrovi%C3%A1rio_2015.png. [Accessed: 27-Jul-2018]
- [17] “PORDATA - Extensão da Rede Ferroviária Explorada: Total, Electrificada e Não Electrificada - Continente.” [Online]. Available: <https://www.pordata.pt/MicroPage.aspx?DatabaseName=Portugal&MicroName=Extens%C3%A3o+da+rede+ferrovi%C3%A1ria+explorada+total++electrificada+e+n%C3%A3o+electrificada+++Continente&MicroURL=3109&>. [Accessed: 27-Jul-2018]
- [18] “Railway in Iberian Peninsula.” [Online]. Available: <http://www.bueker.net/trainspotting/map.php?file=maps/iberian-peninsula/iberian-peninsula.gif>. [Accessed: 24-Sep-2018]
- [19] “Shift2Rail Mission and Objectives.” [Online]. Available: <https://shift2rail.org:443/about-shift2rail/mission-and-objectives/>. [Accessed: 27-Jul-2018]
- [20] “Shift2Rail Members Map.” [Online]. Available: <https://shift2rail.org:443/members-map/>. [Accessed: 27-Jul-2018]
- [21] “Rail Research and Shift2Rail - Mobility and Transport - European Commission,” *Mobility and Transport*. [Online]. Available: /transport/modes/rail/shift2rail_en. [Accessed: 27-Jul-2018]
- [22] “About Shift2Rail.” [Online]. Available: <https://shift2rail.org:443/about-shift2rail/>. [Accessed: 26-Jan-2017]
- [23] L. Zhou and Z. Shen, “Progress in High-Speed Train Technology Around the World,” *J. Mod. Transp.*, vol. 19, no. 1, pp. 1–6, Mar. 2011, doi: 10.1007/BF03325733.
- [24] A. Purba, F. Nakamura, C. N. Dwsbu, M. Jafri, and P. Pratomo, “A Current Review of High Speed Railways Experiences in Asia and Europe,” in *AIP Conference Proceedings*, Palembang, Indonesia, 2017, vol. 1903, p. 060004, doi: 10.1063/1.5011558.
- [25] “DB Deutsche Bahn Group.” [Online]. Available: <https://www.westtours.de/business/en/deutsche-bahnen>. [Accessed: 04-Apr-2018]
- [26] S. Staff, “Aftermath of High-Tech Train Crash: Germany’s Transrapid Project in Doubt After Crash,” *Spiegel Online*, 25-Sep-2006 [Online]. Available: <http://www.spiegel.de/international/aftermath-of-high-tech-train-crash-germany-s-transrapid-project-in-doubt-after-crash-a-438995.html>
- [27] “Photos from the Transrapid in China and Germany.” [Online]. Available: <https://www.hochgeschwindigkeitszuege.com/china/transrapid-foto-galerie.php>. [Accessed: 23-Jul-2018]
- [28] “High speed trains | Comparison tables - SocialCompare.” [Online]. Available: <https://socialcompare.com/en/comparison/high-speed-trains>. [Accessed: 01-Jul-2017]
- [29] “China Introduces New High-Speed Fuxing Train,” *Railway Technology*, 26-Jun-2017. [Online]. Available: <https://www.railway-technology.com/news/newschina-introduces-new-high-speed-train-fuxing-5853452/>. [Accessed: 22-Mar-2017]
- [30] G. Hu *et al.*, “A Sensor-Based Seamless Handover Solution for Express Train Access Networks (ETANs),” *IEEE Commun. Lett.*, vol. 16, no. 4, pp. 470–472, Apr. 2012, doi: 10.1109/LCOMM.2012.030512.112580.
- [31] “China Revs up Bullet Train Revolution with World’s Fastest Service,” *South China Morning Post*, 21-Aug-2017. [Online]. Available: <https://www.scmp.com/news/china/economy/article/2107553/china-rev-bullet-train-revolution-worlds-fastest-service-shanghai>. [Accessed: 13-Jun-2017]
- [32] Y. Luguang, “Progress of the Maglev Transportation in China,” *IEEE Trans. Appl. Supercond.*, vol. 16, no. 2, pp. 1138–1141, Jun. 2006, doi: 10.1109/TASC.2006.871345.
- [33] C. Lee, Y. Sun, J. Jo, J. Lee, and Y. Han, “Investigation on Stray Magnetic Field of High Speed Maglev,” in *2013 International Conference on Electrical Machines and Systems (ICEMS)*, Busan, 2013, pp. 1928–1931, doi: 10.1109/ICEMS.2013.6713232.
- [34] “AVE, Alta Velocidade Española,” *Railway Technology*. [Online]. Available: <https://www.railway-technology.com/projects/spain/>. [Accessed: 23-Feb-2017]

- [35] “The World’s Longest High-Speed Railway Lines,” *Railway Technology*, 19-Dec-2013. [Online]. Available: <https://www.railway-technology.com/features/featurethe-worlds-longest-high-speed-railway-lines-4149752/>. [Accessed: 23-Jul-2017]
- [36] “El AVE Cierra el Año con Un Récord de Casi 31 Millones de Viajeros,” *abc*, 30-Dec-2015. [Online]. Available: https://www.abc.es/economia/abci-cierra-record-casi-31-millones-viajeros-201512301153_noticia.html. [Accessed: 17-Jul-2017]
- [37] “E5 Series Shinkansen Bullet Train,” *Railway Technology*. [Online]. Available: <https://www.railway-technology.com/projects/shinkansen-bullet-train-high-speed-japan/>. [Accessed: 19-Nov-2017]
- [38] “Chuo Shinkansen Maglev Line,” *Railway Technology*. [Online]. Available: <https://www.railway-technology.com/projects/chuo-shinkansen-maglev-line/>. [Accessed: 14-Sep-2017]
- [39] J. McCurry, “Japan’s Maglev Train Breaks World Speed Record with 600km/h Test Run,” *The Guardian*, 21-Apr-2015 [Online]. Available: <http://www.theguardian.com/world/2015/apr/21/japans-maglev-train-notches-up-new-world-speed-record-in-test-run>. [Accessed: 23-Jul-2018]
- [40] L. A. M. Barros, M. Tanta, A. P. Martins, J. L. Afonso, and G. Pinto, “Opportunities and Challenges of Power Electronics Systems in Future Railway Electrification,” presented at the IEEE CPE - POWERENG 2020, Setúbal-Portugal, 8-10 July, pp. 1–6.
- [41] B. F. Exposto, “Development of solutions to compensate for power quality problems based on current source converters,” Doctoral Thesis, University of Minho, 2018 [Online]. Available: <http://repositorium.sdum.uminho.pt/>. [Accessed: 10-May-2020]
- [42] J. G. Pinto, “New UPQC Topology without Transformer to Compensate power quality problems,” Doctoral Thesis, University of Minho, 2012 [Online]. Available: <http://repositorium.sdum.uminho.pt/handle/1822/19822>. [Accessed: 10-May-2020]
- [43] Z. He, Z. Zheng, and H. Hu, “Power Quality in High-Speed Railway Systems,” *Int. J. Rail Transp.*, vol. 4, no. 2, pp. 71–97, Apr. 2016, doi: 10.1080/23248378.2016.1169228.
- [44] I. Krastev, P. Tricoli, S. Hillmansen, and M. Chen, “Future of Electric Railways: Advanced Electrification Systems with Static Converters for AC Railways,” *IEEE Electrification Mag.*, vol. 4, no. 3, pp. 6–14, Sep. 2016, doi: 10.1109/MELE.2016.2584998.
- [45] S. M. M. Gazafrudi, A. T. Langerudy, E. F. Fuchs, and K. Al-Haddad, “Power Quality Issues in Railway Electrification: A Comprehensive Perspective,” *IEEE Trans. Ind. Electron.*, vol. 62, no. 5, pp. 3081–3090, May 2015, doi: 10.1109/TIE.2014.2386794.
- [46] I. Perin, P. F. Nussey, U. M. Cella, T. V. Tran, and G. R. Walker, “Application of Power Electronics in Improving Power Quality and Supply Efficiency of AC Traction Networks,” in *2015 IEEE 11th International Conference on Power Electronics and Drive Systems*, Sydney, NSW, 2015, pp. 1086–1094, doi: 10.1109/PEDS.2015.7203421.
- [47] P. Ladoux, J. Fabre, and H. Caron, “Power Quality Improvement in AC Railway Substations: The Concept of Chopper-Controlled Impedance,” *IEEE Electrification Mag.*, vol. 2, no. 3, pp. 6–15, Sep. 2014, doi: 10.1109/MELE.2014.2331792.
- [48] A. T. Langerudy, A. Mariscotti, and M. A. Abolhassani, “Power Quality Conditioning in Railway Electrification: A Comparative Study,” *IEEE Trans. Veh. Technol.*, vol. 66, no. 8, pp. 6653–6662, Aug. 2017, doi: 10.1109/TVT.2017.2661820.
- [49] M. Tanta, V. Monteiro, T. J. C. Sousa, A. P. Martins, A. S. Carvalho, and J. L. Afonso, “Power quality Phenomena in Electrified Railways: Conventional and New Trends in Power Quality Improvement toward Public Power Systems,” in *2018 International Young Engineers Forum (YEF-ECE)*, Costa da Caparica, 2018, pp. 25–30, doi: 10.1109/YEF-ECE.2018.8368934.
- [50] F. Kiessling, R. Puschmann, A. Schmieder, and E. Schneider, *Contact Lines for Electric Railways: Planning, Design, Implementation, Maintenance, 3rd Edition*. 2018.
- [51] European norm, “Voltage Characteristics of Electricity Supplied by Public Distribution Systems - EN 50160.” European Committee for Electrotechnical Standardization (CENELEC), Jul-2010.

- [52] ENTIDADE REGULADORA DOS SERVIÇOS ENERGÉTICOS, Regulamento n.º 629/2017, “Regulamento da Qualidade de Serviço do Setor Elétrico e do Setor do Gás Natural.” Diário da República, 2.ª série – N.º 243, Dezembro-2017.
- [53] European norm, “Railway Applications - Supply Voltages of Traction Systems, European Standard - EN 50163.” European Committee for Electrotechnical Standardization (CENELEC), 01-Nov-2004.
- [54] A. Luo, C. Wu, J. Shen, Z. Shuai, and F. Ma, “Railway Static Power Conditioners for High-Speed Train Traction Power Supply Systems Using Three-phase V/V Transformers,” *IEEE Trans. Power Electron.*, vol. 26, no. 10, pp. 2844–2856, Oct. 2011, doi: 10.1109/TPEL.2011.2128888.
- [55] D. Serrano-Jiménez, L. Abrahamsson, S. Castaño-Solís, and J. Sanz-Feito, “Electrical Railway Power Supply Systems: Current Situation and Future Trends,” *Int. J. Electr. Power Energy Syst.*, vol. 92, pp. 181–192, Nov. 2017, doi: 10.1016/j.ijepes.2017.05.008.
- [56] V. Monteiro, T. J. C. Sousa, M. Tanta, S. Almeida, R. Gomes, and J. L. Afonso, “A novel two-switch three-level active rectifier for grid-connected electrical appliances in smart grids,” in *2018 International Young Engineers Forum (YEF-ECE)*, Costa da Caparica, Portugal, 2018, pp. 37–42, doi: 10.1109/YEF-ECE.2018.8368936.
- [57] M. Tanta, J. A. Afonso, A. P. Martins, A. S. Carvalho, and J. L. Afonso, “Rail Power Conditioner Based on Indirect AC/DC/AC Modular Multilevel Converter Using a Three-phase V/V Power Transformer,” in *Lecture Notes in Engineering and Computer Science: Proceeding of the World Congress on Engineering, 5-7 July 2017*, London, UK, pp. 289–294.
- [58] European norm, “Railway Applications - Power supply and rolling stock - Technical criteria for the coordination between power supply (substation) and rolling stock to achieve interoperability EN 50388.” CEI Italian Electrotechnical Committee, Mar-2019.
- [59] V. A. Morais, J. L. Afonso, A. S. Carvalho, and A. P. Martins, “New Reactive Power Compensation Strategies for Railway Infrastructure Capacity Increasing,” *Energies*, vol. 13, no. 17, p. 4379, Jan. 2020, doi: 10.3390/en13174379.
- [60] C. Wu, A. Luo, J. Shen, F. J. Ma, and S. Peng, “A Negative Sequence Compensation Method Based on a Two-Phase Three-Wire Converter for a High-Speed Railway Traction Power Supply System,” *IEEE Trans. Power Electron.*, vol. 27, no. 2, pp. 706–717, Feb. 2012, doi: 10.1109/TPEL.2011.2159273.
- [61] R. Bartelt, M. Oettmeier, C. Heising, V. Staudt, and A. Steimel, “Improvement of Low-Frequency System Stability in 16.7-Hz Railway-Power Grids by Multivariable Line-Converter Control in a Multiple Traction-Vehicle Scenario,” in *Railway and Ship Propulsion Electrical Systems for Aircraft*, Bologna, 2010, pp. 1–6, doi: 10.1109/ESARS.2010.5665234.
- [62] J. Li, M. Wu, and Q. Liu, “Measurement and Simulation on Low-Frequency Oscillation in the Traction Network of Xuzhou North Railway Hub,” in *2016 12th World Congress on Intelligent Control and Automation (WCICA)*, Guilin, 2016, pp. 1797–1802, doi: 10.1109/WCICA.2016.7578509.
- [63] X. Jiang, H. Hu, Z. He, H. Tao, and Q. Qian, “Study on Low-Frequency Voltage Fluctuation of Traction Power Supply System Introduced by Multiple Modern Trains,” *Electr. Power Syst. Res.*, vol. 146, pp. 246–257, May 2017, doi: 10.1016/j.epsr.2017.01.033.
- [64] S. Midya, D. Bormann, A. Larsson, T. Schutte, and R. Thottappillil, “Understanding Pantograph Arcing in Electrified Railways - Influence of Various Parameters,” in *2008 IEEE International Symposium on Electromagnetic Compatibility*, Detroit, MI, 2008, pp. 1–6, doi: 10.1109/IEMC.2008.4652112.
- [65] S. Midya, D. Bormann, T. Schutte, and R. Thottappillil, “Pantograph Arcing in Electrified Railways-Mechanism and Influence of Various Parameters-Part I: With DC Traction Power Supply,” *IEEE Trans. Power Deliv.*, vol. 24, no. 4, pp. 1931–1939, Oct. 2009, doi: 10.1109/TPWRD.2009.2021035.
- [66] B. Wang *et al.*, “Pantograph Arc’s Energy Characters Under Various Load,” in *2011 IEEE 57th Holm Conference on Electrical Contacts (Holm)*, Minneapolis, MN, 2011, pp. 1–5, doi: 10.1109/HOLM.2011.6034811.
- [67] S. Durantou, A. Audier, J. Hazan, M. P. Langhorn, and V. Gauche, “The 2017 European Railway Performance Index.” [Online]. Available: <https://www.bcg.com/publications/2017/transportation-travel-tourism-2017-european-railway-performance-index.aspx>. [Accessed: 28-Jul-2017]

- [68] Y. Hu, J. Huang, Z. Wang, and Y. Tao, "Research on the Impact of Electrified Railway on Power Grid," in *CICED 2010 Proceedings*, Nanjing, 2010, pp. 1–9.
- [69] P. M. Kalla-Bishop, *Italian Railways (Railway Histories of the World)*. England: David and Charles, 1971 [Online]. Available: https://books.google.com/books/about/Italian_Railways.html?id=JFcSAAAAMAAJ
- [70] "Corcovado - Wikiwand." [Online]. Available: <https://www.wikiwand.com/en/Corcovado>. [Accessed: 10-May-2020]
- [71] "History - Le Train de la Rhune," <https://www.rhune.com/>. [Online]. Available: <https://www.rhune.com/en/all-about-the-train/history/>. [Accessed: 10-May-2020]
- [72] G. Keenor, "Overhead Line Electrification for Railways 4th Edition." Railways Archive UK, Nov-2016 [Online]. Available: <http://www.railwaysarchive.co.uk/ocs4rail/download/Overhead-Line-Electrification-for-Railways-4th-edition.pdf>. [Accessed: 12-Jun-2020]
- [73] V. P. Joseph and J. Thomas, "Power Quality Improvement of AC Railway Traction Using Railway Static Power Conditioner a Comparative Study," in *2014 International Conference on Power Signals Control and Computations (EPSCICON)*, Thrissur, 2014, pp. 1–6, doi: 10.1109/EPSCICON.2014.6887509.
- [74] L. Abrahamsson, T. Schütte, and S. Östlund, "Use of Converters for Feeding of AC Railways for all Frequencies," *Energy Sustain. Dev.*, vol. 16, no. 3, pp. 368–378, Sep. 2012, doi: 10.1016/j.esd.2012.05.003.
- [75] Bin-Kwie Chen and Bing-Song Guo, "Three-Phase Models of Specially Connected Transformers," *IEEE Trans. Power Deliv.*, vol. 11, no. 1, pp. 323–330, Jan. 1996, doi: 10.1109/61.484031.
- [76] C. Dai and Y. Sun, "Investigation of the Imbalance Current Compensation for Transformers Used in Electric Railways," in *2010 Asia-Pacific Power and Energy Engineering Conference*, Chengdu, 2010, pp. 1–4, doi: 10.1109/APPEEC.2010.5448337.
- [77] Z. Xu, L. Luo, Z. Zhang, and Y. Li, "A Novel Asymmetrical Connection Balance Transformer for Traction Power Supply," *Turk. J. Electr. Eng. Comput. Sci.*, vol. 23, no. 5, p. 1284, Aug. 2015, doi: 10.3906/elk-1304-195.
- [78] Cheng-Ping Huang, Chi-Jui Wu, Yung-Sung Chuang, Shih-Kai Peng, Jung-Liang Yen, and Ming-Hong Han, "Loading Characteristics Analysis of Specially Connected Transformers Using Various Power Factor Definitions," *IEEE Trans. Power Deliv.*, vol. 21, no. 3, pp. 1406–1413, Jul. 2006, doi: 10.1109/TPWRD.2005.864076.
- [79] S. Yousefi, H. Biyouki, M. M. A. Zaboli, H. Askarian Abyaneh, and S. H. Hosseinian, "Harmonic Elimination of 25 kV AC Electric Railways Utilizing a New Hybrid Filter Structure," *AUT J. Electr. Eng.*, vol. 49, no. 1, pp. 3–10, Jun. 2017, doi: 10.22060/ej.2016.811.
- [80] M. Salehifar, M. Ranjbar, A. Amirahmadi, and A. Shoulaie, "A Combined System of Passive Filter and TCR for Power Quality Improvement in a 25-kV Electrified Railway System," in *2009 International Conference for Technical Postgraduates (TECHPOS)*, Kuala Lumpur, 2009, pp. 1–5, doi: 10.1109/TECHPOS.2009.5412115.
- [81] P. Ladoux, G. Raimondo, H. Caron, and P. Marino, "Chopper-Controlled Steinmetz Circuit for Voltage Balancing in Railway Substations," *IEEE Trans. Power Electron.*, vol. 28, no. 12, pp. 5813–5822, Dec. 2013, doi: 10.1109/TPEL.2013.2242492.
- [82] L. Sainz, J. Pedra, and M. Caro, "Steinmetz Circuit Influence on the Electric System Harmonic Response," *IEEE Trans. Power Deliv.*, vol. 20, no. 2, pp. 1143–1150, Apr. 2005, doi: 10.1109/TPWRD.2004.834339.
- [83] T. K. Ho, Y. L. Chi, L. K. Siu, and L. Ferreira, "Traction Power System Simulation in Electrified Railways," *J. Transp. Syst. Eng. Inf. Technol.*, vol. 5, pp. 93–107, 2005.
- [84] G. Varju, "Comparison of the Booster Transformer and Auto-Transformer Railway Feeding Systems, Feeding Features and Induction to Telecom Lines," Budapest University of Technology & Economics, Jul-2004.
- [85] G. Séguier and F. Notelet, *Electrotechnique Industrielle*, Edité par TECHNIQUE&DOC, 2000., 1 vols. TECHNIQUE ET DOCUMENTATION.

- [86] L. Abrahamsson, T. Kjellqvist, and S. Ostlund, "High-Voltage DC-Feeder Solution for Electric Railways," *IET Power Electron.*, vol. 5, no. 9, pp. 1776–1784, Nov. 2012, doi: 10.1049/iet-pel.2011.0219.
- [87] L. Abrahamsson, "Railway Power Supply Models and Methods for Long-Term Investment Analysis," Licentiate Thesis, Royal Institute of Technology, Stockholm, Sweden, 2008.
- [88] K. W. Lao, M. C. Wong, and S. Santoso, "Recent Advances of FACTS Devices for Power Quality Compensation in Railway Traction Power Supply," in *2018 IEEE/PES Transmission and Distribution Conference and Exposition (T D)*, Denver, CO, 2018, pp. 1–5, doi: 10.1109/TDC.2018.8440270.
- [89] V. Monteiro, N. Tashakor, M. Tanta, J. A. Afonso, J. S. Martins, and J. L. Afonso, "A Proposed Single-Phase Five-Level PFC Rectifier for Smart Grid Applications: An Experimental Evaluation," in *IECON 2019 - 45th Annual Conference of the IEEE Industrial Electronics Society*, Lisbon, Portugal, 2019, vol. 1, pp. 3436–3441, doi: 10.1109/IECON.2019.8926971.
- [90] T. Uzuka, "Faster than a Speeding Bullet: An Overview of Japanese High-Speed Rail Technology and Electrification," *IEEE Electrification Mag.*, vol. 1, no. 1, pp. 11–20, Sep. 2013, doi: 10.1109/MELE.2013.2271839.
- [91] M. Tanta, V. Monteiro, J. G. Pinto, A. P. Martins, A. S. Carvalho, and J. L. Afonso, "Efficiency and Cost Estimation for a Static Frequency Converter and a Rail Power Conditioner Based on an Indirect Modular Multilevel Converter in Railways Applications," in *ICEE International Conference on Energy and Environment: Bringing Together Engineering and Economics*, Porto, Portugal, 2017, pp. 313–319.
- [92] ABB, "Static Var Compensation (SVC)." [Online]. Available: [https://new.abb.com/facts/static-var-compensation-\(svc\)](https://new.abb.com/facts/static-var-compensation-(svc)). [Accessed: 01-Nov-2020]
- [93] N. Y. Dai, K. Lao, and C. Lam, "Hybrid Railway Power Conditioner with Partial Compensation for Converter Rating Reduction," *IEEE Trans. Ind. Appl.*, vol. 51, no. 5, pp. 4130–4138, Sep. 2015, doi: 10.1109/TIA.2015.2426134.
- [94] L. Gyugyi, "Dynamic Compensation of AC Transmission Lines by Solid-State Synchronous Voltage Sources," *IEEE Trans. Power Deliv.*, vol. 9, no. 2, pp. 904–911, Apr. 1994, doi: 10.1109/61.296273.
- [95] J. G. Pinto, M. Tanta, V. Monteiro, L. A. M. Barros, and Joao. L. Afonso, "Active Power Conditioner Based on a Voltage Source Converter for Harmonics and Negative Sequence Components Compensation in Electrified Railway Systems," presented at the Transport Research Arena TRA 2018, Vienna, Austria, 2018, pp. 1–10, doi: 10.5281/zenodo.1491309.
- [96] L. A. M. Barros, M. Tanta, A. P. Martins, J. L. Afonso, and J. G. Pinto, "STATCOM Evaluation in Electrified Railway Using V/V and Scott Power Transformers," in *Sustainable Energy for Smart Cities, SESC 2019*, Cham, 2020, pp. 18–32, doi: 10.1007/978-3-030-45694-8_2.
- [97] X. He, J. Peng, P. Han, Z. Liu, S. Gao, and P. Wang, "A Novel Advanced Traction Power Supply System Based on Modular Multilevel Converter," *IEEE Access*, vol. 7, pp. 165018–165028, 2019, doi: 10.1109/ACCESS.2019.2949099.
- [98] M. Aeberhard, C. Courtois, and P. Ladoux, "Railway Traction Power Supply from the State of the Art to Future Trends," in *SPEEDAM 2010*, Pisa, 2010, pp. 1350–1355, doi: 10.1109/SPEEDAM.2010.5542093.
- [99] J. Ranneberg, "Transformerless Topologies for Future Stationary AC-Railway Power Supply," in *2007 European Conference on Power Electronics and Applications*, Aalborg, 2007, pp. 1–11, doi: 10.1109/EPE.2007.4417330.
- [100] M. Zhang, L. Huang, W. Yao, and Z. Lu, "Circulating Harmonic Current Elimination of a CPS-PWM-Based Modular Multilevel Converter With a Plug-In Repetitive Controller," *IEEE Trans. Power Electron.*, vol. 29, no. 4, pp. 2083–2097, Apr. 2014, doi: 10.1109/TPEL.2013.2269140.
- [101] H. M. P. and M. T. Bina, "A Transformerless Medium-Voltage STATCOM Topology Based on Extended Modular Multilevel Converters," *IEEE Trans. Power Electron.*, vol. 26, no. 5, pp. 1534–1545, May 2011, doi: 10.1109/TPEL.2010.2085088.
- [102] J. Moon, C. Kim, J. Park, D. Kang, and J. Kim, "Circulating Current Control in MMC Under the Unbalanced Voltage," *IEEE Trans. Power Deliv.*, vol. 28, no. 3, pp. 1952–1959, Jul. 2013, doi: 10.1109/TPWRD.2013.2264496.

- [103] S. Kouro *et al.*, "Recent Advances and Industrial Applications of Multilevel Converters," *IEEE Trans. Ind. Electron.*, vol. 57, no. 8, pp. 2553–2580, Aug. 2010, doi: 10.1109/TIE.2010.2049719.
- [104] S. i Hamasaki, K. Hadano, M. Tsuji, and R. Rizzo, "Control of Modular Multilevel Converter for AC/AC Conversion," in *2016 International Symposium on Power Electronics, Electrical Drives, Automation and Motion (SPEEDAM)*, Anacapri, 2016, pp. 984–989, doi: 10.1109/SPEEDAM.2016.7525970.
- [105] H. J. Knaak, "Modular multilevel Converters and HVDC/FACTS: A Success Story," in *Proceedings of the 2011 14th European Conference on Power Electronics and Applications*, Birmingham, 2011, pp. 1–6.
- [106] A. Nami, J. Liang, F. Dijkhuizen, and G. D. Demetriades, "Modular Multilevel Converters for HVDC Applications: Review on Converter Cells and Functionalities," *IEEE Trans. Power Electron.*, vol. 30, no. 1, pp. 18–36, Jan. 2015, doi: 10.1109/TPEL.2014.2327641.
- [107] M. Tanta, L. A. M. Barros, G. Pinto, A. P. Martins, and J. L. Afonso, "Modular Multilevel Converter in Electrified Railway Systems: Applications of Rail Static Frequency Converters and Rail Power Conditioners," in *2020 International Young Engineers Forum (YEF ECE)*, Caparica Portugal, 2020, pp. 1–6.
- [108] L. A. M. Barros, M. Tanta, A. P. Martins, J. L. Afonso, and J. G. Pinto, "Submodule Topologies and PWM Techniques Applied in Modular Multilevel Converters: Review and Analysis," in *Sustainable Energy for Smart Cities, SESC 2020*, 2020, pp. 1-20 (Accepted for publication).
- [109] Z. Yan, H. Xue-hao, T. Guang-fu, and H. Zhi-yuan, "A Study on MMC Model and its Current Control Strategies," in *The 2nd International Symposium on Power Electronics for Distributed Generation Systems*, Hefei, 2010, pp. 259–264, doi: 10.1109/PEDG.2010.5545924.
- [110] M. Ishfaq *et al.*, "A New Adaptive Approach to Control Circulating and Output Current of Modular Multilevel Converter," *Energies*, vol. 12, no. 6, p. 1118, Jan. 2019, doi: 10.3390/en12061118.
- [111] M. Vasiladiotis, A. Christe, T. Geyer, and A. Faulstich, "Decoupled Modulation Concept for Three-to-Single-Phase Direct AC/AC Modular Multilevel Converters for Railway Interties," in *2017 19th European Conference on Power Electronics and Applications (EPE'17 ECCE Europe)*, Warsaw, 2017, p. P.1-P.9, doi: 10.23919/EPE17ECCEurope.2017.8099033.
- [112] J. Feng, W. Q. Chu, Z. Zhang, and Z. Q. Zhu, "Power Electronic Transformer-Based Railway Traction Systems: Challenges and Opportunities," *IEEE J. Emerg. Sel. Top. Power Electron.*, vol. 5, no. 3, pp. 1237–1253, Sep. 2017, doi: 10.1109/JESTPE.2017.2685464.
- [113] D. Ronanki and S. S. Williamson, "Modular Multilevel Converters for Transportation Electrification: Challenges and Opportunities," *IEEE Trans. Transp. Electrification*, vol. 4, no. 2, pp. 399–407, Jun. 2018, doi: 10.1109/TTE.2018.2792330.
- [114] G. R and O. D, "Use of Modular Multilevel Converter (MMC) Technology in Rail Electrification," presented at the AusRAIL PLUS 2014, Doing it Smarter. People, Power, Performance, 24-26 November 2014, Melbourne, Vic, Australia, 2014 [Online]. Available: <https://trid.trb.org/view.aspx?id=1341047>
- [115] S. Norrga, L. Ångquist, K. Ilves, L. Harnefors, and H. P. Nee, "Frequency-Domain Modeling of Modular Multilevel Converters," in *IECON 2012 - 38th Annual Conference on IEEE Industrial Electronics Society*, Montreal, QC, 2012, pp. 4967–4972, doi: 10.1109/IECON.2012.6389570.
- [116] M. A. Perez, S. Bernet, J. Rodriguez, S. Kouro, and R. Lizana, "Circuit Topologies, Modeling, Control Schemes, and Applications of Modular Multilevel Converters," *IEEE Trans. Power Electron.*, vol. 30, no. 1, pp. 4–17, Jan. 2015, doi: 10.1109/TPEL.2014.2310127.
- [117] M. Winkelkemper, A. Korn, and P. Steimer, "A Modular Direct Converter for Transformerless Rail Interties," in *2010 IEEE International Symposium on Industrial Electronics*, Bari, 2010, pp. 562–567, doi: 10.1109/ISIE.2010.5637826.
- [118] D. Ronanki and S. S. Williamson, "Modular Multilevel Converters for Transportation Electrification: Challenges and Opportunities," *IEEE Trans. Transp. Electrification*, vol. 4, no. 2, pp. 399–407, Jun. 2018, doi: 10.1109/TTE.2018.2792330.
- [119] T. Uzuka, S. Ikeda, and K. Ueda, "A Static Voltage Fluctuation Compensator for AC Electric Railway," in *2004 IEEE 35th Annual Power Electronics Specialists Conference (IEEE Cat. No.04CH37551)*, Aachen, Germany, 2004, vol. 3, pp. 1869-1873 Vol.3, doi: 10.1109/PESC.2004.1355401.

- [120] S. Tamai, "Novel Power Electronics Application in Traction Power Supply System in Japan," in *2014 16th International Power Electronics and Motion Control Conference and Exposition*, Antalya, 2014, pp. 701–706, doi: 10.1109/EPEPEMC.2014.6980579.
- [121] Y. Horita, N. Morishima, M. Kai, M. Onishi, T. Masui, and M. Noguchi, "Single-Phase STATCOM for Feeding System of Tokaido Shinkansen," in *The 2010 International Power Electronics Conference - ECCE ASIA*, Sapporo, 2010, pp. 2165–2170, doi: 10.1109/IPEC.2010.5544532.
- [122] M. Tanta *et al.*, "Simplified Rail Power Conditioner Based on a Half-Bridge Indirect AC/DC/AC Modular Multilevel Converter and a V/V Power Transformer," in *IECON 2017 - 43rd Annual Conference of the IEEE Industrial Electronics Society*, Beijing, China, 2017, pp. 6431–6436, doi: 10.1109/IECON.2017.8217120.
- [123] Ch. Zhao, C. Banceanu, Th. Schaad, Ph. Maibach, S. Aubert, "Static Frequency Converters: a Flexible and Cost Efficient Method to Supply Single-Phase Railway Grids in Australia," in *AusRAIL PLUS 2015, ABB Switzerland Ltd*, Australia, 2015.
- [124] F. Chang, Z. Yang, and F. Lin, "Research on Control Strategy of AC-DC-AC Substation Based on Modular Multilevel Converter," *Math. Probl. Eng.*, p. 14, 2017, doi: 10.1155/2017/4157165.
- [125] M. Tanta, J. A. Afonso, A. P. Martins, A. S. Carvalho, and J. L. Afonso, "Comprehensive Study for a Rail Power Conditioner Based on a Single-Phase Full-Bridge Back-to-Back Indirect Modular Multilevel Converter," in *Transactions on Engineering Technologies*, Singapore, 2019, pp. 263–279.
- [126] K. k Lee, "Advances in the Application of Power Electronics to Railway Traction," in *2015 6th International Conference on Power Electronics Systems and Applications (PESA)*, Hong Kong, 2015, pp. 1–4, doi: 10.1109/PESA.2015.7398960.
- [127] C. Meidan and W. Mingli, "The Switching Transient Simulation of SVC Used in Electric Railway Traction Substation," in *2009 International Conference on Sustainable Power Generation and Supply*, Nanjing, 2009, pp. 1–5, doi: 10.1109/SUPERGEN.2009.5348348.
- [128] H. Morimoto *et al.*, "Development of railway static power conditioner used at substation for Shinkansen," in *Proceedings of the Power Conversion Conference-Osaka 2002 (Cat. No.02TH8579)*, Osaka, Japan, 2002, vol. 3, pp. 1108–1111 vol.3, doi: 10.1109/PCC.2002.998127.
- [129] D. Zhang, Z. Zhang, W. Wang, and Y. Yang, "Negative Sequence Current Optimizing Control Based on Railway Static Power Conditioner in V/V Traction Power Supply System," *IEEE Trans. Power Electron.*, vol. 31, no. 1, pp. 200–212, Jan. 2016, doi: 10.1109/TPEL.2015.2404934.
- [130] F. Ma, A. Luo, X. Xu, H. Xiao, C. Wu, and W. Wang, "A Simplified Power Conditioner Based on Half-Bridge Converter for High-Speed Railway System," *IEEE Trans. Ind. Electron.*, vol. 60, no. 2, pp. 728–738, Feb. 2013, doi: 10.1109/TIE.2012.2206358.
- [131] H. Oso, T. Kaneko, and A. Suzuki, "Railway Static Power Conditioner for Shin-Kurobe Substation of Hokuriku Shinkansen," *Fuji Electr. Rev.*, vol. 61, no. 1, pp. 52–57, 2015.
- [132] K. Aoki, K. Kikuchi, M. Seya, and T. Kato, "Power Interchange System for Reuse of Regenerative Electric Power," *Hitachi Rev.*, vol. 67, no. 7, pp. 71–75, 2018.
- [133] G. Cui *et al.*, "Supercapacitor Integrated Railway Static Power Conditioner for Regenerative Braking Energy Recycling and Power Quality Improvement of High-Speed Railway System," *IEEE Trans. Transp. Electrification*, vol. 5, no. 3, pp. 702–714, Sep. 2019, doi: 10.1109/TTE.2019.2936686.
- [134] European norm, "Railway applications - Fixed installations - Requirements for the validation of simulation tools used for the design of traction power supply systems - EN 50641." British Standards Institution (BSI), Aug-2017.
- [135] M. Ohmi and Y. Yoshii, "Validation of Railway Static Power Conditioner in Tohoku Shinkansen on Actual Operation," in *2010 International Power Electronics Conference - ECCE ASIA*, Sapporo, 2010, pp. 2160–2164, doi: 10.1109/IPEC.2010.5544563.
- [136] C. Zhang *et al.*, "A Novel Collaboration Compensation Strategy of Railway Power Conditioner for a High-Speed Railway Traction Power Supply System," in *Proceedings of 2012 UKACC International Conference on Control*, Cardiff, 2012, pp. 731–736, doi: 10.1109/CONTROL.2012.6334720.

- [137] N. Ding, Z. Shu, and Y. Guo, "A Railway Power Quality Conditioner Based on Chain Circuit Using Impedance-Matching Balance Transformers," in *2011 International Conference on Advanced Power System Automation and Protection*, Beijing, 2011, vol. 1, pp. 374–377, doi: 10.1109/APAP.2011.6180430.
- [138] H. J. Kaleybar, H. M. Kojabadi, M. Brenna, F. Foadelli, and S. S. Fazel, "A two-phase three-wire quasi-Z-source based railway power quality compensator for AC rail networks," in *2017 IEEE International Conference on Environment and Electrical Engineering and 2017 IEEE Industrial and Commercial Power Systems Europe (EEEIC / I CPS Europe)*, Milan, 2017, pp. 1–6, doi: 10.1109/EEEIC.2017.7977713.
- [139] H. M. Roudsari, A. Jalilian, and S. Jamali, "A Z-source railway static power conditioner for power quality improvement," in *2016 7th Power Electronics and Drive Systems Technologies Conference (PEDSTC)*, Tehran, 2016, pp. 261–267, doi: 10.1109/PEDSTC.2016.7556871.
- [140] M. Tanta, G. Pinto, V. Monteiro, A. P. Martins, A. S. Carvalho, and Joao. L. Afonso, "A Comprehensive Comparison of Rail Power Conditioners Based on Two-level Converters and a V/V Power Transformer in Railway Traction Power Systems," in *7th Transport Research Arena (TRA 2018)*, Vienna, 2018, pp. 1–10, doi: 10.5281/zenodo.1483284.
- [141] S. Hu *et al.*, "A New Railway Power Flow Control System Coupled With Asymmetric Double LC Branches," *IEEE Trans. Power Electron.*, vol. 30, no. 10, pp. 5484–5498, Oct. 2015, doi: 10.1109/TPEL.2014.2369132.
- [142] Z. Shu *et al.*, "Digital Detection, Control, and Distribution System for Co-Phase Traction Power Supply Application," *IEEE Trans. Ind. Electron.*, vol. 60, no. 5, pp. 1831–1839, May 2013, doi: 10.1109/TIE.2012.2190959.
- [143] N. Dai, M. Wong, K. Lao, and C. Wong, "Modelling and control of a railway power conditioner in co-phase traction power system under partial compensation," *IET Power Electron.*, vol. 7, no. 5, pp. 1044–1054, May 2014, doi: 10.1049/iet-pel.2013.0396.
- [144] K. Lao, M. Wong, N. Dai, C. Lam, L. Wang, and C. Wong, "Analysis of the Effects of Operation Voltage Range in Flexible DC Control on Railway HPQC Compensation Capability in High-Speed Co-phase Railway Power," *IEEE Trans. Power Electron.*, vol. 33, no. 2, pp. 1760–1774, Feb. 2018, doi: 10.1109/TPEL.2017.2684427.
- [145] B. Chen, C. Zhang, W. Zeng, C. Tian, and J. Yuan, "An electrical-magnetic hybrid power quality compensation strategy for V/V traction power supply system," in *2014 IEEE Energy Conversion Congress and Exposition (ECCE)*, Pittsburgh, 2014, pp. 3774–3779, doi: 10.1109/ECCE.2014.6953914.
- [146] Q. Xu *et al.*, "Analysis and Comparison of Modular Railway Power Conditioner for High-Speed Railway Traction System," *IEEE Trans. Power Electron.*, vol. PP, no. 99, pp. 6031–6048, 2016, doi: 10.1109/TPEL.2016.2616721.
- [147] Z. Shu, S. Xie, and Q. Li, "Single-Phase Back-To-Back Converter for Active Power Balancing, Reactive Power Compensation, and Harmonic Filtering in Traction Power System," *IEEE Trans. Power Electron.*, vol. 26, no. 2, pp. 334–343, Feb. 2011, doi: 10.1109/TPEL.2010.2060360.
- [148] K.-W. Lao, M.-C. Wong, and N. Dai, *Co-phase Traction Power Supply with Railway Hybrid Power Quality Conditioner*. Springer, 2018.
- [149] M. Tanta, G. Pinto, V. Monteiro, A. P. Martins, A. S. Carvalho, and Joao. L. Afonso, "Cost Estimation of Rail Power Conditioner Topologies based on Indirect Modular Multilevel Converter in V/V and Scott Power Transformers," presented at the 4th International Conference on Energy and Environment: bringing together Engineering and Economics, Guimarães, Portugal, 2019, pp. 365–370.
- [150] M. Tanta, J. G. Pinto, V. Monteiro, A. P. Martins, A. S. Carvalho, and J. L. Afonso, "Topologies and Operation Modes of Rail Power Conditioners in AC Traction Grids: Review and Comprehensive Comparison," *Energies*, vol. 13, no. 9, p. 2151, Jan. 2020, doi: 10.3390/en13092151.
- [151] H. Jafari Kaleybar and R. Kazemzadeh, "A Comprehensive Study on Performance of YD Transformer in AC Electrified Railway Systems," *J. Electr. Eng.*, vol. 16, pp. 1–8, 2016.
- [152] M. Tanta, "Simulation and implementation of power electronics for educational purposes: with SEPIC converter for MPPT," 2014 [Online]. Available: <http://repositorium.sdum.uminho.pt/>. [Accessed: 06-Nov-2020]

- [153] S. Hu, S. Li, Y. Li, O. Krause, and F. Zare, "A Comprehensive Study for the Power Flow Controller Used in Railway Power Systems," *IEEE Trans. Ind. Electron.*, vol. 65, no. 8, pp. 6032–6043, Aug. 2018, doi: 10.1109/TIE.2017.2786201.
- [154] F. Ma, X. Wang, L. Deng, Z. Zhu, Q. Xu, and N. Xie, "Multi-Port Railway Power Conditioner and Its Management Control Strategy with Renewable Energy Access," *IEEE J. Emerg. Sel. Top. Power Electron.*, pp. 1–1, 2019, doi: 10.1109/JESTPE.2019.2899138.
- [155] B. Xie *et al.*, "A Compensation System for Cophase High-Speed Electric Railways by Reactive Power Generation of SHC SAC," *IEEE Trans. Ind. Electron.*, vol. 65, no. 4, pp. 2956–2966, Apr. 2018, doi: 10.1109/TIE.2017.2748063.
- [156] M. Lu, J. Hu, R. Zeng, and Z. He, "Fundamental-Frequency Reactive Circulating Current Injection for Capacitor Voltage Balancing in Hybrid-MMC HVDC Systems During Riding Through PTG Faults," *IEEE Trans. Power Deliv.*, vol. 33, no. 3, pp. 1348–1357, Jun. 2018, doi: 10.1109/TPWRD.2017.2755505.
- [157] F. Ma *et al.*, "A Railway Traction Power Conditioner Using Modular Multilevel Converter and Its Control Strategy for High-Speed Railway System," *IEEE Trans. Transp. Electrification*, vol. 2, no. 1, pp. 96–109, Mar. 2016, doi: 10.1109/TTE.2016.2515164.
- [158] F. Deng and Z. Chen, "A Control Method for Voltage Balancing in Modular Multilevel Converters," *IEEE Trans. Power Electron.*, vol. 29, no. 1, pp. 66–76, Jan. 2014, doi: 10.1109/TPEL.2013.2251426.
- [159] R. Teodorescu, F. Blaabjerg, M. Liserre, and P. C. Loh, "Proportional-Resonant Controllers and Filters for Grid-Connected Voltage-Source Converters," *IEE Proc. - Electr. Power Appl.*, vol. 153, no. 5, pp. 750–762, Sep. 2006, doi: 10.1049/ip-epa:20060008.
- [160] M. Tanta, J. G. Pinto, V. Monteiro, A. P. Martins, A. S. Carvalho, and J. L. Afonso, "Deadbeat Predictive Current Control for Circulating Currents Reduction in a Modular Multilevel Converter Based Rail Power Conditioner," *Appl. Sci.*, vol. 10, no. 5, p. 1849, Jan. 2020, doi: 10.3390/app10051849.
- [161] M. Hagiwara, R. Maeda, and H. Akagi, "Control and Analysis of the Modular Multilevel Cascade Converter Based on Double-Star Chopper-Cells (MMCC-DSCC)," *IEEE Trans. Power Electron.*, vol. 26, no. 6, pp. 1649–1658, Jun. 2011, doi: 10.1109/TPEL.2010.2089065.
- [162] K. H. Ahmed and A. A. Aboushady, "Modified half-bridge modular multilevel converter for HVDC systems with DC fault ride-through capability," in *IECON 2014 - 40th Annual Conference of the IEEE Industrial Electronics Society*, Dallas, TX, 2014, pp. 4676–4682, doi: 10.1109/IECON.2014.7049207.
- [163] J. Rogers, "Comparative Analysis of Current Control Methods for Modular Multilevel Converters," University of South Carolina, 2016 [Online]. Available: <https://scholarcommons.sc.edu/etd/3419>. [Accessed: 22-Oct-2018]
- [164] L. Ben-Brahim, A. Gastli, M. Trabelsi, K. A. Ghazi, M. Houchati, and H. Abu-Rub, "Modular Multilevel Converter Circulating Current Reduction Using Model Predictive Control," *IEEE Trans. Ind. Electron.*, vol. 63, no. 6, pp. 3857–3866, Jun. 2016, doi: 10.1109/TIE.2016.2519320.
- [165] J. Li, G. Konstantinou, H. R. Wickramasinghe, J. Pou, X. Wu, and X. Jin, "Impact of Circulating Current Control in Capacitor Voltage Ripples of Modular Multilevel Converters Under Grid Imbalances," *IEEE Trans. Power Deliv.*, vol. 33, no. 3, pp. 1257–1267, Jun. 2018, doi: 10.1109/TPWRD.2017.2747079.
- [166] X. Li, Q. Song, W. Liu, S. Xu, Z. Zhu, and X. Li, "Performance Analysis and Optimization of Circulating Current Control for Modular Multilevel Converter," *IEEE Trans. Ind. Electron.*, vol. 63, no. 2, pp. 716–727, Feb. 2016, doi: 10.1109/TIE.2015.2480748.
- [167] C. Zou, B. Liu, S. Duan, and R. Li, "Stationary Frame Equivalent Model of Proportional-Integral Controller in dq Synchronous Frame," *IEEE Trans. Power Electron.*, vol. 29, no. 9, pp. 4461–4465, Sep. 2014, doi: 10.1109/TPEL.2013.2296789.
- [168] L. F. A. Pereira and A. S. Bazanella, "Tuning Rules for Proportional Resonant Controllers," *IEEE Trans. Control Syst. Technol.*, vol. 23, no. 5, pp. 2010–2017, Sep. 2015, doi: 10.1109/TCST.2015.2389655.
- [169] J. Qin and M. Saedifard, "Predictive Control of a Modular Multilevel Converter for a Back-to-Back HVDC System," *IEEE Trans. Power Deliv.*, vol. 27, no. 3, pp. 1538–1547, Jul. 2012, doi: 10.1109/TPWRD.2012.2191577.

- [170] A. Dekka, B. Wu, V. Yaramasu, R. L. Fuentes, and N. R. Zargari, "Model Predictive Control of High-Power Modular Multilevel Converters—An Overview," *IEEE J. Emerg. Sel. Top. Power Electron.*, vol. 7, no. 1, pp. 168–183, Mar. 2019, doi: 10.1109/JESTPE.2018.2880137.
- [171] P. Cortes, M. P. Kazmierkowski, R. M. Kennel, D. E. Quevedo, and J. Rodriguez, "Predictive Control in Power Electronics and Drives," *IEEE Trans. Ind. Electron.*, vol. 55, no. 12, pp. 4312–4324, Dec. 2008, doi: 10.1109/TIE.2008.2007480.
- [172] V. D. F. Monteiro, "Development of Bidirectional Charging Systems for Electric Vehicles with New Modes of Operation for Smart Grid, in Portuguese: Desenvolvimento de sistemas de carregamento bidirecionais para veiculos elétricos com novos modos de operação para Smart Grids," Doctoral Thesis, University of Minho, 2016 [Online]. Available: <http://repositorium.sdum.uminho.pt/handle/1822/43448>. [Accessed: 22-Oct-2018]
- [173] M. Chen and J. Sun, "Feedforward Current Control of Boost Single-Phase PFC Converters," *IEEE Trans. Power Electron.*, vol. 21, no. 2, pp. 338–345, Mar. 2006, doi: 10.1109/TPEL.2005.869746.
- [174] S. Tan, Y. M. Lai, C. K. Tse, and C. K. Wu, "A Pulsewidth Modulation Based Integral Sliding Mode Current Controller for Boost Converters," in *2006 37th IEEE Power Electronics Specialists Conference*, Jeju, 2006, pp. 1–7, doi: 10.1109/pesc.2006.1712005.
- [175] S. Orts-Grau, F. J. Gimeno-Sales, A. Abellan-Garcia, S. Segui-Chilet, and J. C. Alfonso-Gil, "Improved Shunt Active Power Compensator for IEEE Standard 1459 Compliance," *IEEE Trans. Power Deliv.*, vol. 25, no. 4, pp. 2692–2701, Oct. 2010, doi: 10.1109/TPWRD.2010.2049033.
- [176] S. Debnath, J. Qin, B. Bahrani, M. Saeedifard, and P. Barbosa, "Operation, Control, and Applications of the Modular Multilevel Converter: A Review," *IEEE Trans. Power Electron.*, vol. 30, no. 1, pp. 37–53, Jan. 2015, doi: 10.1109/TPEL.2014.2309937.
- [177] L. He, K. Zhang, J. Xiong, and S. Fan, "A Repetitive Control Scheme for Harmonic Suppression of Circulating Current in Modular Multilevel Converters," *IEEE Trans. Power Electron.*, vol. 30, no. 1, pp. 471–481, Jan. 2015, doi: 10.1109/TPEL.2014.2304978.
- [178] K. Sharifabadi, L. Harnefors, H.-P. Nee, S. Norrga, and R. Teodorescu, *Design, Control and Application of Modular Multilevel Converters for HVDC Transmission Systems*. Wiley-IEEE press, 2016.
- [179] M. Hagiwara, K. Nishimura, and H. Akagi, "A Medium-Voltage Motor Drive with a Modular Multilevel PWM Inverter," *IEEE Trans. Power Electron.*, vol. 25, no. 7, pp. 1786–1799, Jul. 2010, doi: 10.1109/TPEL.2010.2042303.
- [180] G. Liu, Q. Jiang, and Y. Wei, "Study on Capacitor Voltage Balancing Control of Modular Multilevel Converter at Low Frequency," *Int. J. Comput. Electr. Eng.*, pp. 196–200, 2013, doi: 10.7763/IJCEE.2013.V5.694.
- [181] N. Dai and M. Wong, "Design Considerations of Coupling Inductance for Active Power Filters," in *2011 6th IEEE Conference on Industrial Electronics and Applications*, Beijing, 2011, pp. 1370–1375, doi: 10.1109/ICIEA.2011.5975801.
- [182] Q. Tu, Z. Xu, H. Huang, and J. Zhang, "Parameter Design Principle of the Arm Inductor in Modular Multilevel Converter Based HVDC," in *2010 International Conference on Power System Technology*, Hangzhou, 2010, pp. 1–6, doi: 10.1109/POWERCON.2010.5666416.
- [183] L. Liu and N. Dai, "Hybrid Railway Power Conditioner Based on Half-Bridge Modular Multilevel Converter," in *2016 IEEE Energy Conversion Congress and Exposition (ECCE)*, Milwaukee, WI, 2016, pp. 1–7, doi: 10.1109/ECCE.2016.7855177.
- [184] Y. Zhao, N. Dai, and BaoAn, "Application of Three-Phase Modular Multilevel Converter (MMC) in Co-Phase Traction Power Supply System," in *2014 IEEE Conference and Expo Transportation Electrification Asia-Pacific (ITEC Asia-Pacific)*, Beijing, 2014, pp. 1–6, doi: 10.1109/ITEC-AP.2014.6941064.
- [185] "PSIM Electronic Simulation Software | Powersim," *Powersim Inc.* [Online]. Available: <https://powersimtech.com/>. [Accessed: 23-May-2020]
- [186] "PADS." [Online]. Available: <https://www.pads.com/>. [Accessed: 22-May-2020]

- [187] Silicon Labs, "Si824x - Class D Audio Driver with Precision Dead-Time Generator," 2014. [Online]. Available: <https://www.silabs.com/documents/public/data-sheets/Si824x.pdf>. [Accessed: 09-Oct-2018]
- [188] Infineon Technologies AG, "High Speed Switching Series Fifth Generation IGBT-IKW40N65H5," 06-May-2015. [Online]. Available: https://www.infineon.com/dgdl/Infineon-IKx40N65H5-DS-v02_01-EN.pdf?fileId=db3a30433af5291e013afa8ba6fb6078. [Accessed: 22-Jul-2019]
- [189] Infineon Technologies AG, "High Speed Switching Series Fifth Generation IGBT-IGW40N65H5," 30-Apr-2015. [Online]. Available: https://pt.mouser.com/datasheet/2/196/Infineon-IGP40N65H5_IGW40N65H5-DS-v02_01-EN-1226015.pdf. [Accessed: 22-Jul-2019]
- [190] Avago Technologies, "HCPL-3120/J312, HCNW3120-Output Current IGBT Gate Drive Optocoupler," 2008. [Online]. Available: https://www.promelec.ru/pdf/HCPL-3120-J312_HCNW3120.pdf. [Accessed: 02-Nov-2019]
- [191] "TPS2000 | Tektronix." [Online]. Available: <https://www.tek.com/oscilloscope/tps2000>. [Accessed: 23-May-2020]
- [192] M. Tanta, J. Cunha, V. Monteiro, A. P. Martins, A. S. Carvalho, and J. L. Afonso, "A Novel Hardware Protection Scheme for a Modular Multilevel Converter Half-Bridge Submodule," in *IECON 2019 - 45th Annual Conference of the IEEE Industrial Electronics Society*, Lisbon, Portugal, 2019, vol. 1, pp. 6043–6048, doi: 10.1109/IECON.2019.8927361.
- [193] A. A. Aboushady, K. H. Ahmed, and D. Jovcic, "Analysis and Hardware Testing of Cell Capacitor Discharge Currents During DC Faults in Half-Bridge Modular Multilevel Converters," in *11th IET International Conference on AC and DC Power Transmission*, Birmingham, 2015, pp. 1–7, doi: 10.1049/cp.2015.0010.
- [194] P. Asimakopoulos, K. Papastergiou, and M. Bongiorno, "Design of a Modular Multilevel Converter As an Active Front-End for a Magnet Supply Application," in *2014 16th European Conference on Power Electronics and Applications*, Lappeenranta, 2014, pp. 1–10, doi: 10.1109/EPE.2014.6910790.
- [195] Y. Li, E. A. Jones, and F. Wang, "Circulating Current Suppressing Control's Impact on Arm Inductance Selection for Modular Multilevel Converter," *IEEE J. Emerg. Sel. Top. Power Electron.*, vol. 5, no. 1, pp. 182–188, Mar. 2017, doi: 10.1109/JESTPE.2016.2617865.
- [196] Allegro Micro-Systems, LLC, "ACS730, Galvanically Isolated Current Sensor IC in Small Footprint SOIC8 Package.," 2017. [Online]. Available: <https://www.allegromicro.com/~media/Files/Datasheets/ACS730-Datasheet.ashx>. [Accessed: 02-Dec-2018]
- [197] Silicon Labs, "Si8920 Data Sheet, Isolated Amplifier for Current Shunt Measurement," Apr-2018. [Online]. Available: <https://www.silabs.com/documents/public/data-sheets/si8920-datasheet.pdf>. [Accessed: 18-Oct-2018]
- [198] H. Wang and F. Blaabjerg, "Reliability of Capacitors for DC-Link Applications in Power Electronic Converters—An Overview," *IEEE Trans. Ind. Appl.*, vol. 50, no. 5, pp. 3569–3578, Sep. 2014, doi: 10.1109/TIA.2014.2308357.
- [199] Nichicon, "Aluminum Electrolytic Capacitors." [Online]. Available: <http://www.nichicon.co.jp/english/products/pdfs/e-ucs.pdf>. [Accessed: 12-Jun-2018]
- [200] L. Harnefors, A. Antonopoulos, S. Norrga, L. Angquist, and H. Nee, "Dynamic Analysis of Modular Multilevel Converters," *IEEE Trans. Ind. Electron.*, vol. 60, no. 7, pp. 2526–2537, Jul. 2013, doi: 10.1109/TIE.2012.2194974.
- [201] Y. Tang, L. Ran, O. Alatise, and P. Mawby, "A Model Assisted Testing Scheme for Modular Multilevel Converter," *IEEE Trans. Power Electron.*, vol. 31, no. 1, pp. 165–176, Jan. 2016, doi: 10.1109/TPEL.2015.2411694.
- [202] T. Modeer, S. Norrga, and H. Nee, "Resonant Test Circuit for High-Power Cascaded Converter Submodules," in *2013 15th European Conference on Power Electronics and Applications (EPE)*, Lille, 2013, pp. 1–5, doi: 10.1109/EPE.2013.6631990.
- [203] T. Yuan, "Modular Multilevel Converter: Submodule Dimensioning, Testing Method, and Topology Innovation," Doctoral Thesis, University of Warwick, 2015 [Online]. Available: <http://webcat.warwick.ac.uk/record=b2864277~S1>. [Accessed: 23-Apr-2019]

- [204] Y. Tang, L. Ran, O. Alatise, and P. Mawby, "Improved Testing Capability of the Model-Assisted Testing Scheme for a Modular Multilevel Converter," *IEEE Trans. Power Electron.*, vol. 31, no. 11, pp. 7823–7836, Nov. 2016, doi: 10.1109/TPEL.2016.2514439.
- [205] F. Gruson *et al.*, "Design, Implementation and Testing of a Modular Multilevel Converter," *EPE J.*, vol. 27, no. 4, pp. 153–166, Oct. 2017, doi: 10.1080/09398368.2017.1417785.
- [206] Littelfuse, "Transient Voltage Suppressors (TVS Diode) Applications Overview," *Application Note*, 2015. [Online]. Available: https://m.littelfuse.com/~media/electronics/application_notes/littelfuse_tvs_diode_overview_application_note.pdf.pdf. [Accessed: 02-May-2020]
- [207] Texas Instruments, "TMS320F2833x, TMS320F2823x Digital Signal Controllers (DSCs)," 2016. [Online]. Available: <http://www.ti.com/lit/ds/symlink/tms320f28335.pdf>. [Accessed: 18-Oct-2018]
- [208] J. Liu, "Hall Effect Voltage Sensor CYHVS025A," May-2016. [Online]. Available: <http://www.hallsensors.de/CYHVS025A.pdf>. [Accessed: 21-Feb-2020]
- [209] LEM, "Current Transducer LA 100-P," Jan-2016. [Online]. Available: https://www.lem.com/sites/default/files/products_datasheets/la_100-p_e_.pdf. [Accessed: 26-Jan-2020]
- [210] Texas Instruments, "8-Channel, 12-/10-/8-BIT, 2.7-V TO 5.5-V Low Power Digital-TO-Analog Converter with Power Down," 2008. [Online]. Available: <http://www.ti.com/lit/ds/symlink/tlv5610.pdf>. [Accessed: 25-Jul-2019]
- [211] MAXIM, "8-/4-/2-Channel, 14-Bit, Simultaneous Sampling ADCs with $\pm 10V$, $\pm 5V$, and 0 to +5V Analog Input Ranges," Oct-2008. [Online]. Available: <https://www.maximintegrated.com/en/ds/MAX1316-MAX1326.pdf>. [Accessed: 26-Jan-2019]
- [212] Silicon Labs, "Si87xx - LED Emulator Input, Open Collector Output Isolators," 2018. [Online]. Available: <https://www.silabs.com/documents/public/data-sheets/Si87xx.pdf>. [Accessed: 17-Oct-2018]
- [213] L. A. M. Barros, M. Tanta, T. J. C. Sousa, J. L. Afonso, and J. G. Pinto, "New Multifunctional Isolated Microinverter with Integrated Energy Storage System for PV Applications," *Energies*, vol. 13, no. 15, p. 4016, Jan. 2020, doi: 10.3390/en13154016.
- [214] "Fluke 434 / 435 Power Quality and Energy Analyzers." [Online]. Available: <https://www.fluke.com/en-us/product/electrical-testing/power-quality/434-435>. [Accessed: 30-May-2020]
- [215] M. Karimi-Ghartemani and M. R. Iravani, "A nonlinear adaptive filter for online signal analysis in power systems: applications," *IEEE Trans. Power Deliv.*, vol. 17, no. 2, pp. 617–622, Apr. 2002, doi: 10.1109/61.997949.
- [216] A. J. Roscoe and S. M. Blair, "Choice and properties of adaptive and tunable digital boxcar (moving average) filters for power systems and other signal processing applications," in *2016 IEEE International Workshop on Applied Measurements for Power Systems (AMPS)*, Aachen, 2016, pp. 1–6, doi: 10.1109/AMPS.2016.7602853.